Synthesis, characterization and industrial applicability of combined sorbent-catalyst materials for sorption enhanced steam methane reforming

Andrea Di Giuliano

UNIVERSITÉ DE STRASBOURG

UNIVERSITÀ DEGLI STUDI DELL'AQUILA

École Doctorale des Sciences Chimiques, ICPEES UMR CNRS 7515 - ECED

Dipartimento di Ingegneria Industriale e dell'Informazione e di Economia

THÈSE en cotutelle

présentée par :

Andrea DI GIULIANO

soutenue le : **19 décembre 2017**

pour obtenir le grade de : **Docteur de l'Université de Strasbourg**

Discipline / Spécialité : Chimie / Catalyse hétérogène

pour obtenir le grade de : **Dottore di Ricerca dell'Universià degli Studi dell'Aquila**

Discipline / SSD : Ingegneria industriale e dell'Informazione e di Economia / ING-IND/24, ING-IND/27

Synthesis, characterization and industrial applicability of Combined Sorbent-Catalyst Materials for Sorption Enhanced Steam Methane Reforming

THÈSE dirigée par :

Mme Claire COURSON	Maître de conférences, Université de Strasbourg
M Pier Ugo FOSCOLO	Professeur, Università degli Studi dell'Aquila

RAPPORTEURS :

Mme Catherine BATHIOT-DUPEYRAT	Professeur, Université de Poitiers
M Gianpiero GROPPI	Professeur, Politecnico di Milano

MEMBRES DU JURY :

Mme Nathalie TANCHOUX	Chargé de recherches, Université de Montpellier
Mme Mirella VIRGINIE	Maître de conférences, Université de Lille 1
Mme Maria Cristina ANNESINI	Professeur, Università degli Studi di Roma La Sapienza
M Renzo DI FELICE	Professeur, Università degli Studi di Genova

EDSC
École Doctorale des
Sciences Chimiques

Università degli Studi dell'Aquila
Dipartimento di Ingegneria Industriale e dell'Informazione e d'Economia

Université de Strasbourg
École Doctorale des Sciences Chimiques
(ED 222)

THESIS
presented to obtain the degree of

Dottore di ricerca
dell'Università degli Studi dell'Aquila
in
Ingegneria industriale e dell'informazione e d'economia. XXX ciclo
SSD: ING-IND/24, ING-IND/27

Docteur
de l'Univesité de Strasbourg
en
Chimie
Spécialité: Catalyse hétérogène

Synthesis, characterization and industrial applicability of Combined Sorbent-Catalyst Materials for Sorption Enhanced Steam Methane Reforming

Author
Andrea DI GIULIANO

Supervisor
Prof. Pier Ugo FOSCOLO

Supervisor
Dr. Claire COURSON

Coordinator of the PhD in Industrial and information engineering and economics
Prof. Roberto CIPOLLONE

Director of the Doctoral school of chemical sciences (ED 222)
Prof. Jean-Serge REMY

Jean-Serge REMY
Directeur
École Doctorale des Sciences Chimiques

Academic year 2016/2017

Do what I do:
hold tight and pretend it's a plan!
Matt Smith, as the 11th Doctor
BBC Doctor Who

It ... could ... WORK!!!
Gene Wilder, as Doctor F. Frankenstein
Young Frankenstein

Where is the wisdom we have lost in knowledge?
Where is the knowledge we have lost in information?
T. S. Eliot
The Rock

Abstract

Sorption enhanced steam methane reforming (SESMR), i.e. steam methane reforming (SMR) with in situ CO_2 sorption by a high temperature solid sorbent, can lead to a sustainable and economical exploitation of natural gas to produce high purity H_2 for power generation and production of chemicals, with simultaneous sequestration of greenhouse gases. The European research project ASCENT (Advanced Solid Cycles with Efficient Novel Technologies), active from March 2014 for four years, among several goals, aims to give a solid proof-of-concept of SESMR industrial applicability by a Combined Sorbent Catalyst Material (CSCM).

This thesis, as part of ASCENT project, deals with Ni-mayenite SMR catalysts, CaO-mayenite CO_2 sorbents, and Ni-CaO-mayenite CSCM for SESMR. These materials were successfully synthesized by wet mixing and wet impregnation methods, to study the effect of Ni fraction, its precursor salt (Ni-nitrate or Ni-acetate), and free CaO fraction. ICP-AES, XRD, BET and BJH methods, SEM-EDS, TEM-EDS, TPR and TGA were largely used as characterization techniques. The reactivity of synthesized material was evaluated by tests in a packed-bed microreactor, which served also as a screening tool to choose the most promising materials. Their industrial applicability was further assessed by multicycle SESMR/regeneration tests in an automated packed-bed bench scale rig.

Microreactor scale tests indicated that: (i) Ni-acetate shows lower reactivity towards reforming than Ni-nitrate, with both Ni-mayenite catalysts and Ni-CaO-mayenite CSCM; (ii) CaO presence causes a depletion of Ni reactivity in CSCM, and even in raw mixing of Ni-mayenite and CaO-mayenite; (iii) the detrimental effect of CaO can be faced by a sufficiently high Ni fraction.

Based on these evidences, a CSCM with high Ni fraction (10 wt%) from Ni-nitrate, deriving from a sorbent with low CaO excess (15 wt%) was chosen for multicycle tests. This material performed satisfactorily in 205 consecutive SESMR/regeneration cycles, with mild regeneration conditions (pure N_2 at 850 °C), showing a very stable behaviour. On the other hand, with more severe regeneration conditions (pure CO_2 at 925 °C), the same material suffered an important deactivation, attributed by post-test characterization to a textural decay and Ni rearrangement.

***

Il sorption enhanced steam methane reforming (SESMR), cioè lo steam methane reforming (SMR) con cattura in situ di CO_2 per mezzo di un sorbente solido ad alta temperatura, è considerato un processo interessante al fine di un utilizzo sostenibile ed economicamente conveniente del gas naturale per la produzione di H_2 di elevata purezza, da usare per la generazione di energia elettrica e/o di composti chimici, con un simultaneo sequestro di gas serra. Il progetto di ricerca europeo ASCENT (Advanced Solid Cycles with Efficient Novel Technologies), attivo da marzo 2014 per quattro anni, tra i suoi obiettivi, mira a fornire una concreta dimostrazione dell'applicabilità industriale del SESMR con materiali combinati sorbenti catalizzatori (CSCM).

Questa tesi è stata svolta nell'ambito del progetto di ricerca ASCENT: riguarda catalizzatori Ni-mayenite per SMR, sorbenti CaO-mayenite per la cattura di CO_2 e CSCM Ni-CaO-mayenite per il SESMR. Questi materiali sono stati sintetizzati con successo tramite i metodi wet mixing e wet impregnation, per studiare l'effetto della frazione di Ni, del sale precursore di Ni utilizzato (acetato di Ni o nitrato di Ni), della frazione di CaO libero. Le tecniche ICP-AES, XRD, metodi BET e BJH, SEM-EDS, TEM-EDS, TPR e TGA sono state largamente utilizzate per la caratterizzazione dei materiali sintetizzati. La loro reattività, invece, è stata valutata tramite test in micro-reattore a letto fisso, che sono anche serviti per una selezione dei materiali più promettenti per uno studio di applicabilità industriale con test multi-ciclici di SESMR/rigenerazione in un impianto a letto fisso da banco.

I test in micro-reattore hanno indicato che: (i) l'acetato di Ni conferisce alla Ni-mayenite e ai CSCM Ni-CaO-mayente una reattività inferiore verso il reforming rispetto al nitrato di Ni; (ii) la presenza di CaO causa una diminuzione della reattività del Ni nei CSCM, ma anche in miscele eterogenee di Ni-mayenite e CaO-mayenite; (iii) gli effetti negativi ascrivibili al CaO possono essere contrastati con una frazione di Ni sufficientemente alta.

In base a tali evidenze, è stato scelto per i test multi-ciclici un CSCM ad alta frazione di Ni (10 wt%) da nitrato, derivante da un sorbente a basso tenore di CaO libero in eccesso (15 wt%). Questo materiale ha garantito una prestazione soddisfacente e molto stabile per 205 cicli consecutivi di SESMR/rigenerazione, applicando condizioni di rigenerazione temperate (N_2 puro a 850 °C). Con una rigenerazione più severa in CO_2 pura a 925 °C, invece, lo stesso materiale ha subito un'importante disattivazione, che tramite le caratterizzazioni post-test è stata attribuita al decadimento delle proprietà strutturali e al ri-arrangiamento del Ni.

***

Le procédé SESMR (Sorption Enhanced Steam Methane Reforming), c'est-à-dire le SMR (Steam Methane Reforming) avec capture de CO_2 in-situ par un adsorbant solide à haute température, peut amener à une exploitation durable et économique du gaz naturel pour la production de H_2 à haute pureté pour générer de l'énergie électrique, en capturant le gaz à

effet de serre. Le projet de recherche européen ASCENT (Advanced Solid Cycles with Efficient Novel Technologies), actif depuis février 2014 pour une durée de 4 ans vise à fournir, entre autres, une démonstration concrète de l'applicabilité industrielle du SESMR par des matériaux combinés adsorbants-catalyseurs (CSCM).

La thèse, partie du projet de recherche ASCENT, concerne le développement d'un catalyseur Ni-mayenite pour le SMR, d'adsorbants CaO-mayenite pour la capture de la CO_2, et de CSCM Ni-CaO-mayenite pour le SESMR. Ces matériaux ont été synthétisés avec succès par mélange humide et par imprégnation par voie humide, aux fins d'étudier les influences dues à la fraction de Ni, aux sels précurseurs du Ni (Ni-acétate ou Ni-nitrate), et à la fraction de CaO disponible. Les techniques ICP-AES, XRD, BET/BJH, SEM/EDS, TEM/EDS, TPR et TGA ont été largement utilisés pour caractériser les matériaux synthétisés. Leur réactivité a été évaluée par des tests en lit fixe à l'échelle du microréacteur, qui ont aussi permis une sélection des matériaux les plus prometteurs pour une étude de l'applicabilité industrielle par tests multi cycliques SESMR/régénération de solides par un réacteur automatisé à lit fixe.

Les tests en microréacteur ont indiqué que : (i) le Ni-acétate donne aux catalyseurs Ni-mayenite et aux CSCM Ni-CaO-mayenite une réactivité envers le vaporeformage beaucoup plus basse que le Ni-nitrate ; (ii) la présence du CaO cause une diminution de la réactivité du Ni des CSCM, mais aussi en mélanges bruts de Ni-mayenite et CaO-mayenite ; (iii) les effets négatifs du CaO peuvent être combattus par une fraction de Ni suffisamment élevée.

En se basant sur ces évidences, on a choisi, pour les tests multi cycliques, un CSCM avec une grande fraction de Ni (10 wt%) issu du nitrate, et un adsorbant à faible teneur de CaO en excès (15 wt%). Ce matériau a garanti une performance satisfaisante et très stable pendant 205 cycles de SESMR/régénération du solide, sous des conditions de régénération modérées (sous N_2 pur à 850 °C). Par une régénération plus dure sous CO_2 pur à 925 °C, au contraire, le même matériau a subi une importante désactivation, qui a été attribuée, par caractérisation après-test, à une dégradation texturale et à un réarrangement du Ni.

Résumé de la thèse

1 Introduction

La thèse s'intègre dans le cadre du projet de recherche ASCENT (Advanced Solid Cycles with Efficient Novel Technologies), financé par l'Union Européenne (numéro du projet 608512) et qui a débuté en mars 2014, impliquant 16 partenaires (universités européennes, instituts de recherche, petites et moyennes entreprises). ASCENT étudie différents procédés de production d'énergie décarbonée, basés sur l'utilisation d'un matériau solide absorbant de CO_2 à haute température, permettant l'élimination simultanée de CO_2 et la conversion des autres gaz carbonés (c'est-à-dire CO ou CH_4) en H_2, en orientant les recherches vers un futur développement commercial [1]. H_2 est actuellement principalement produit par SMR (Steam Methane Reforming) à l'échelle industrielle. Il existe différents matériaux capables de catalyser la réaction de SMR, néanmoins, des raisons économiques soutiennent le choix de catalyseurs au Ni supportés [2].

L'Université de L'Aquila participe aux recherches concernant le procédé SESMR (Sorption Enhanced Steam Methane Reforming) mis en œuvre par une boucle chimique au calcium, c'est à dire utilisant des absorbants à base de CaO pour la capture in situ de CO_2. Les réactions principales sont la réaction de SMR (Réaction 1) associée à la réaction de Water Gas Shift (WGS, Réaction 2) et la carbonatation de CaO (Réaction 3) [3] :

$CH_{4(g)} + H_2O_{(v)} \leftrightarrow CO_{(g)} + 3H_{2(g)}$ $\quad \Delta H^0_{298\,K} = 206.2\ kJ\ mol^{-1}$ *Réaction 1*

$CO_{(g)} + H_2O_{(v)} \leftrightarrow CO_{2(g)} + H_{2(g)}$ $\quad \Delta H^0_{298\,K} = -41.2\ kJ\ mol^{-1}$ *Réaction 2*

$CaO_{(s)} + CO_{2(g)} \leftrightarrow CaCO_{3(s)}$ $\quad \Delta H^0_{298\,K} = -175.7\ kJ\ mol^{-1}$ *Réaction 3*

La Réaction 3 déplace l'équilibre du WGS (Réaction 2) vers la droite, en éliminant le CO2 gazeux, de sorte que la fraction gazeuse d'H_2 augmente (d'où le nom « amélioration par absorption »).

Les conditions opérationnelles appropriées pour effectuer les réactions 1 et 2 catalysées par le nickel (Ni), conjointement à la Réaction 3, sont de 650 °C et 1 ATM. Néanmoins,

CaO étant finalement saturé, le matériau absorbant doit être régénéré pour continuer le processus : la stratégie la plus commune consiste en une augmentation de la température vers 800-900 ° C, à 1 atm, afin d'inverser la Réaction 3 et de récupérer CaO [4]. Par conséquent, du point de vue du solide, le procédé SESMR peut fonctionner comme une alternance d'absorption de CO_2 et de régénération de l'absorbant : le double lit circulant fluidisé est une configuration appropriée, avec un réacteur opérant comme reformeur et l'autre comme régénérateur de l'absorbant [5].

En ce qui concerne la stabilité de la capacité d'absorption de CO_2 pendant les multicycles de carbonatation/calcination, les absorbants à base de CaO posent un problème, car la capacité de sorption de CaO diminue fortement avec l'augmentation du nombre de cycles [6]. Ceci est principalement dû au frottage de CaO, qui peut être limité en intégrant CaO dans un matériau inerte [7]. La mayenite ($Ca_{12}Al_{14}O_{33}$) et d'autres aluminates de calcium (par exemple, $Ca_9Al_6O_{18}$ ou $Ca_3Al_2O_6$) sont largement utilisés comme dispersant dans des matériaux synthétiques [7]. La stabilité de l'activité catalytique au long de ce processus cyclique constitue un autre problème.

La faisabilité du procédé SESMR par des systèmes contenant un mélange brut de catalyseur et d'absorbant est prouvée dans la littérature [8]. Afin d'éviter une résistance mutuelle entre les réactions endothermiques et exothermiques, la notion de CSCM (Combined Sorbent Catalyst Materials), c'est-à-dire l'utilisation d'un seul matériau contenant, à la fois une phase absorbante de CO_2 et une phase catalytique pour la réaction de SMR, a été proposé [9]. En outre, l'utilisation de CSCM au lieu d'un système équivalent de mélange brut de catalyseur et d'absorbant réduit considérablement la quantité totale de solide dans le réacteur. Dans ce cadre, diverses synthèses de matériaux CSCM de type Ni-CaO-$Ca_xAl_yO_z$ et leurs performances expérimentales sont rapportées dans la littérature [10].

Finalement, la thèse rapporte une étude de catalyseurs Ni-mayenite de SMR, d'absorbants de CO_2 CaO mayenite et de CSCM Ni CaO mayenite concernant leur :

- Synthèse par mélange humide (pour produire la mayenite ou CaO mayenite) et par imprégnation par voie humide (pour ajouter du Ni aux produits des mélanges humides, afin de produire, respectivement du Ni- mayenite ou du Ni-CaO-mayenite) [8] ;
- La caractérisation par les méthodes ICP-AES, XRD, BET et BJH, SEM et TEM combinées avec EDS, TPR pour étudier la réductibilité et TGA ;
- La réactivité à l'échelle du microréacteur en lit fixe pour le procédé de SESMR (dont les données sont également utilisées pour la validation des modèles mathématiques du procédé SESMR [11]).

Cette étude expérimentale s'est concentrée sur les facteurs suivants :

- Le précurseur de Ni ($Ni(NO_3)_2 \cdot 6H_2O$ ou $Ni(CH_3COO)_2 \cdot 4H_2O$) ;
- La fraction de Ni (valeur nominale comprise entre 3 et 10% en masse) ;
- La fraction de CaO (valeur nominale dans la gamme 0-54% en masse) ;

- La « proximité » de Ni et CaO (lits séparés de Ni-mayenite et de CaO-mayenite par rapport à leur mélange brut et par rapport aux matériaux mixtes CSCM).

Les résultats expérimentaux ont conduit au choix des matériaux les plus prometteurs, qui ont ensuite été examinés pour une applicabilité industrielle, comme d'autres matériaux fournis par d'autres partenaires d'ASCENT.

2 Résultats et discussions

2.1 Caractérisation de matériaux synthétisés

Les méthodes de synthèse appliquées se révèlent appropriées à la production des catalyseurs de SMR Ni-mayenite, des absorbants de CO_2 CaO-mayenite et des matériaux mixtes CSCM Ni-CaO-mayenite, comme cela a pu être confirmé par les analyses ICP-AES et XRD (quelques exemples en Figure 1).

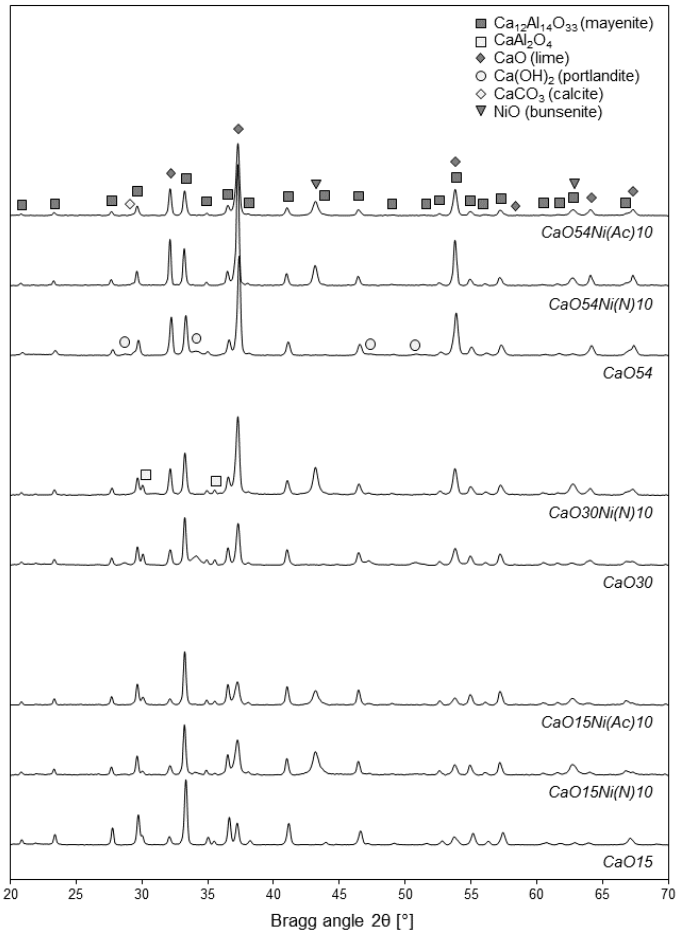

Figure 1 : Diffractogrammes RX de CSCM contenant 10% en masse de Ni par rapport aux absorbants parents correspondants contenant 15 à 54% en masse de CaO.

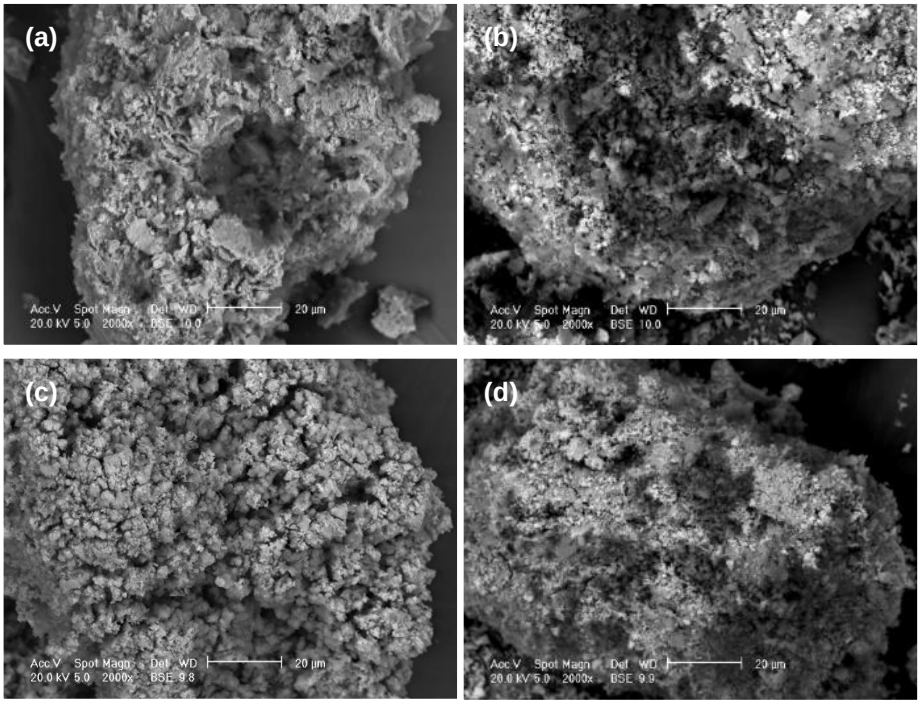

Figure 2 : Micrographies SEM au grossissement 2000x de CaO15Ni(N)10 (a), CaO15Ni(Ac)10 (b), CaO54Ni(N)10 (c), CaO54Ni(Ac)10 (d).

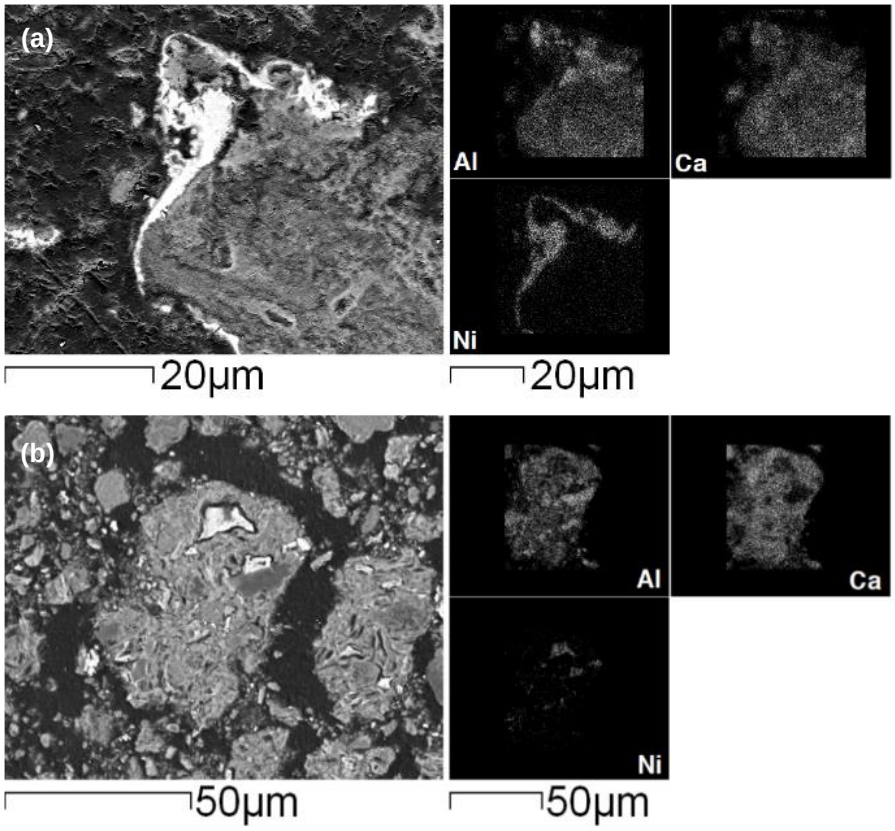

Figure 3 : Cartographies SEM-EDS de CaO15Ni(N)10 (a)et CaO15Ni(Ac)10 (b).

Les analyses morphologiques par SEM/EDS montrent une structure externe microgranulaire commune pour tous les types de matériaux synthétisés (quelques exemples en Figure 2). L'analyse SEM/EDS sur des sections transversales internes de particules de Ni-mayenite et de CSCM révèle une distribution de Ni non uniforme. E, effet, le Ni est principalement situé dans des coquilles externes ou des veines internes (quelques exemples en Figure 3).

Aucune différence n'est détectée entre les matériaux contenant du Ni provenant de $Ni(NO_3)_2 \cdot 6H_2O$ ou de $Ni(CH_3COO)_2 \cdot 4H_2O$.

En ce qui concerne les propriétés de texture (méthodes BET et BJH), tous les matériaux synthétisés partagent une structure méso- et macroporeuse commune avec des pores irréguliers, comme en témoigne la forme des isothermes d'adsorption/désorption de N_2. Ces courbes conduisent à une surface spécifique comprise entre 30 et 5 m^2g^{-1} et un volume de pores de 0,14-0,02 cm^3g^{-1}. La fraction de CaO, la fraction de Ni et le précurseur de Ni influent sur les propriétés de texture (Figure 4).

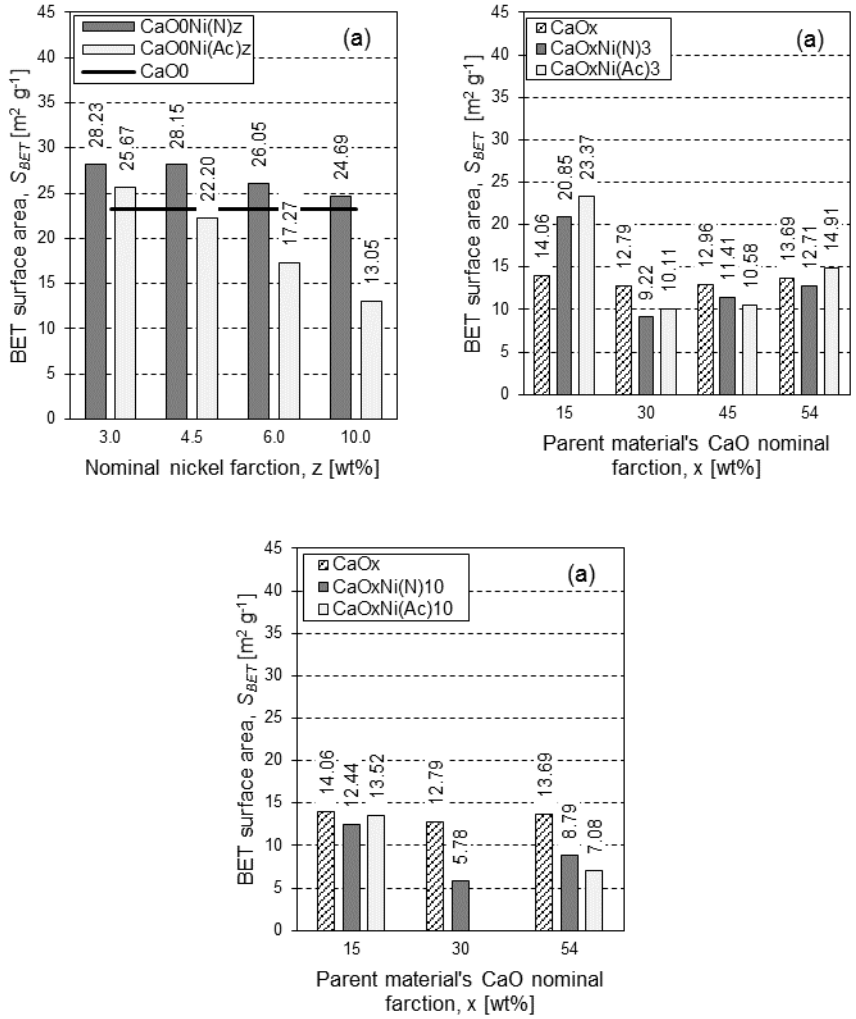

Figure 4 : surfaces spécifiques BET.

Si l'on considère les propriétés de réductibilité, les profils de TPR de Ni-mayenite témoignent d'interactions Ni-support plus fortes dans le cas du précurseur nitrate, pour toutes les fractions de Ni explorées de 3 à 10 % en masse, avec des températures de réduction allant de la réduction de NiO (environ 400 °C) à celle de $NiAl_2O_4$ (au-delà de 800 °C). Pour les matériaux mixtes CSCM, l'effet de CaO est totalement prédominant, ce qui affaiblit l'interaction Ni-support quelle que soit l'origine du Ni ou sa teneur.

2.2 Tests de réactivité en microréacteur

Les matériaux Ni mayenite sont testés pour vérifier leur réactivité en SMR, à trois niveaux de température (850-750-650 °C, 1 atm, WHSV = 0,24 $Nl_{CH4,in}$ $gcat^{-1}$ h^{-1}, masse de lit = 500 mg, rapport molaire vapeur/carbone = 3). Les catalyseurs SMR issus du nitrate de Ni ont toujours une très bonne réactivité, proche de l'équilibre thermodynamique ; d'autre part, la réactivité des catalyseurs dérivés de l'acétate de Ni est très inférieure, approchant l'inactivité à 650 °C, température du procédé de SESMR (Figure 5).

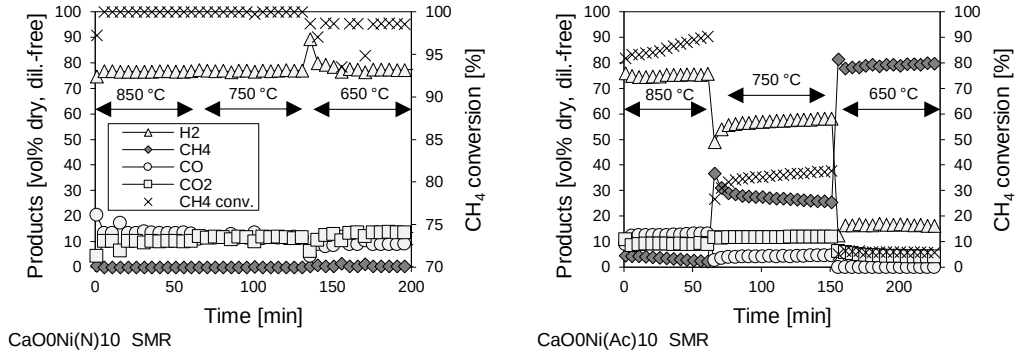

Figure 5 : Tests de SMR sur le catalyseur Ni-mayenite avec 10% en masse de Ni.

Pour cette raison, seuls les catalyseurs Ni mayenite dérivant du nitrate de Ni ont été utilisés pour des essais combinés avec des absorbants CaO mayenite. Les essais avec des lits séparés, c.-à-d. avec un catalyseur Ni mayenite (200 mg) précédant l'absorbant CaO mayenite (300 mg) selon le sens du flux de gaz, ont mis en évidence la fonctionnalité complète des deux types de matériaux dans des conditions choisies pour le procède SESMR (650 °C, 1 atm, WHSV = 0.60 $Nl_{CH4,in}$ $gcat^{-1}$ h^{-1}, rapport molaire vapeur/carbone = 3). Dans la configuration de mélange brut (mêmes conditions de tests qu'en lits séparés), un rôle préjudiciable de l'absorbant sur l'activité catalytique du catalyseur Ni mayenite a été détecté pour les catalyseurs à faible teneur en Ni (Figure 6).

Les deux preuves principales obtenues à partir des tests décrits ci-dessus sont confirmées dans les tests SESMR sur CSCM (650 °C, 1 atm, WHSV = 0,24 $N_{lCH4,in}$ g_{cat}^{-1} h^{-1}, masse du lit = 500 mg, rapport molaire vapeur/carbone =3). En fait, tous les autres facteurs étant égaux :

- Les matériaux issus du nitrate de Ni sont nettement plus actifs que ceux issus de l'acétate de Ni ;

- L'excès de CaO dans le CSCM réduit l'activité du Ni vis-à-vis du SMR : le CSCM issu de l'absorbant contenant un excès de 15 % en masse de CaO est totalement actif à la fois avec 3 % et 10 % en masse de Ni à partir du nitrate de Ni, tandis que pour 30 % ou 54 % en masse de CaO libre, une teneur massique en Ni de 10 % à partir du nitrate de Ni est suffisante pour garantir une réactivité complète en SESMR, mais 3 % en masse ne suffit pas (Figure 7).

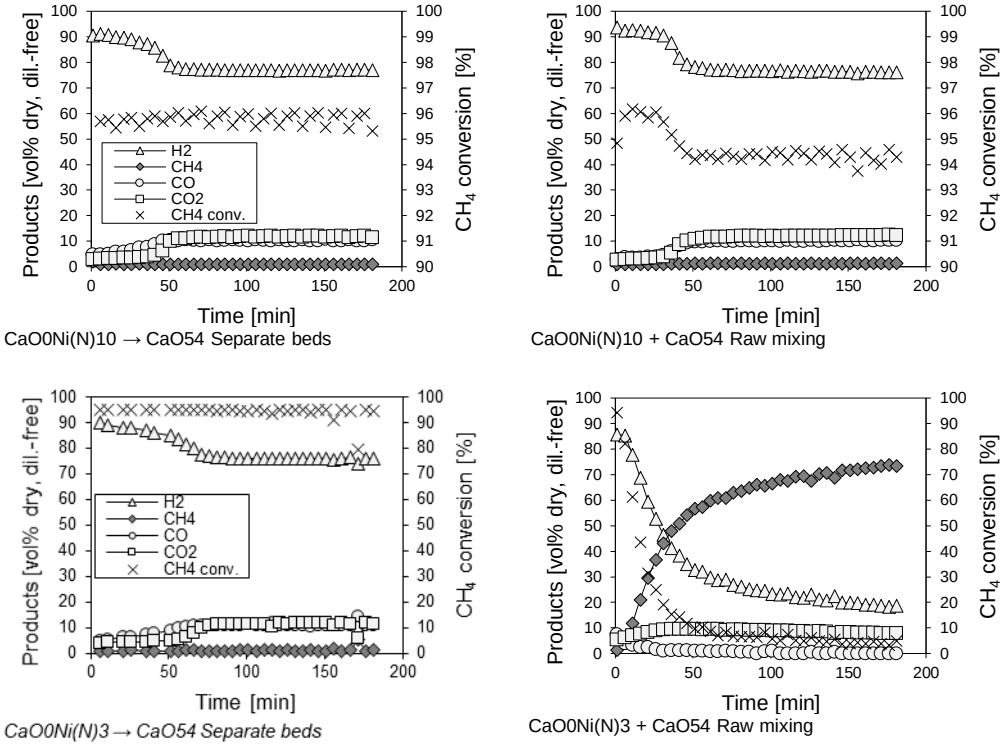

Figure 6 : Tests de reformage avec les 2 types de matériaux dans des lits séparés et en mélange brut, en utilisant des catalyseurs de Ni-mayenite avec 3% ou 10% en masse de Ni à partir du nitrate de Ni et de l'absorbant de CaO-mayenite avec 54% en masse d'excès de CaO.

Les matériaux sont également caractérisés après ces tests, de manière à mieux comprendre les phénomènes de réactivité observés : la DRX, les méthodes BET et BJH, l'apparition de la carbonatation (Réaction 3) confirmée par MEB dans tous les matériaux issus de tests SESMR à haute réactivité.

En se basant sur les résultats du SESMR de l'échelle du microréacteur, le CSCM le plus prometteur pour une applicabilité industrielle est CaO15Ni(N)10 (c'est-à-dire CaO mayenite avec 15% en masse d'excès de CaO, imprégnée du nitrate de Ni pour obtenir 10% en masse de Ni).

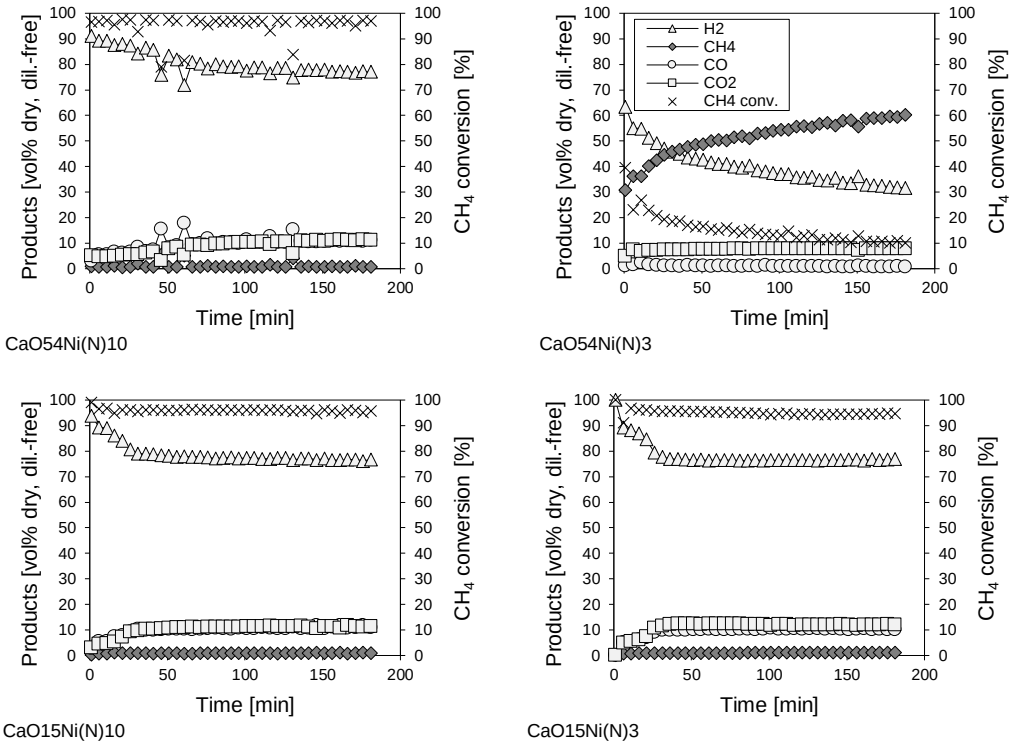

Figure 7 : Tests de SESMR sur CSCM issus des absorbants avec 54% et 15% en masse d'excès de CaO, imprégnés de $Ni(NO_3)_2 \cdot 6H_2O$ pour obtenir 3% ou 10% en masse de Ni.

2.3 Étude d'applicabilité industrielle

L'étude d'applicabilité industrielle est basée sur des tests multi cycliques SESMR/régénération de solides par un réacteur automatisé à lit fixe. Pour l'étape SESMR, les mêmes conditions utilisées pour les tests à l'échelle du microréacteur sur des CSCM sont adoptées, avec une mise à l'échelle sur la masse de lit de 6-7 g. Différents types de variation de température sont utilisés pour l'étape de régénération.

Dans un premier test, CaO15Ni(N)10 subit 205 cycles (durée totale 16 jours), avec régénération sous N_2 pur (de 650 °C à 850 °C, 10 °C min^{-1} avec un palier à 850 °C), donnant une performance très stable, en gardant son activité catalytique et ses fonctionnalités d'absorption, comme on peut le déduire de la différence constante entre les concentrations de produits avant et après la saturation de l'absorbant (Figure 8).

Par la suite, plus de 205 cycles sont effectués sur un échantillon frais du même matériau (durée totale 19 jours), avec des conditions de régénération plus dures sous CO_2 pur (de 650 °C à 925 °C, 10 °C min^{-1} avec un palier à 925 °C), plus proche d'un processus à l'échelle commerciale. Dans ce cas, la performance est moins satisfaisante, car le matériau présente une désactivation progressive pendant les 140 premiers cycles. Dans le but de restaurer l'activité catalytique pour les cycles restants, une forte réduction (850 °C, 30 min, 50 % en volume de H_2 dans N_2) est ajoutée après celle à 925 °C. Seule une récupération

partielle de production d'H_2 et une augmentation modérée de la conversion du CH_4 (Figure 8) sont récupérées.

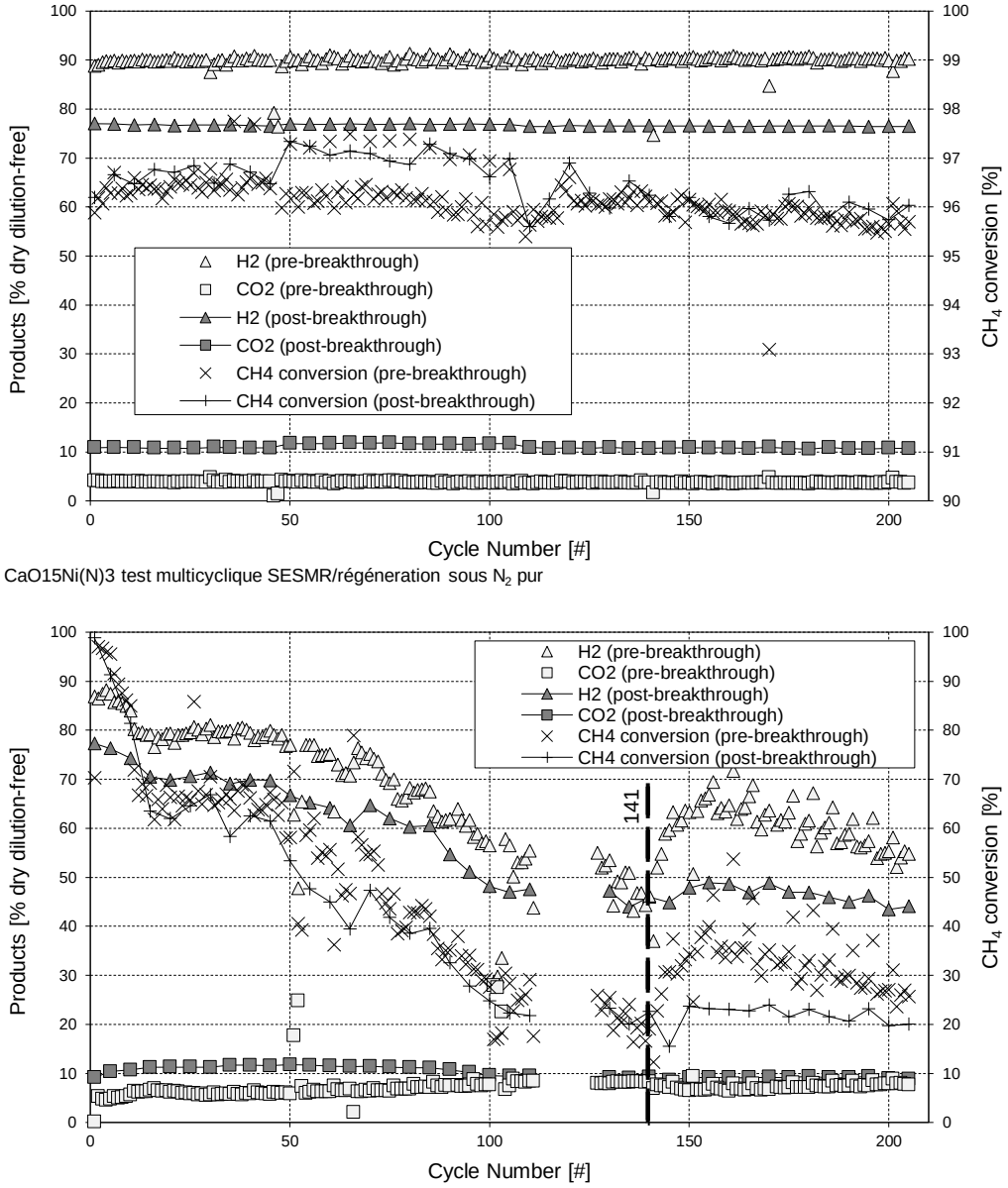

Figure 8 : Tests multicycles SESMR/régénération sur CaO15Ni(N)10.

De plus, des tests multi cycliques sur des matériaux d'autres partenaires du projet ASCENT (IFE, CSIC et Marion Technologies) sont rapportés dans la thèse, synthétisés par agglomération mécanique d'un catalyseur industriel à base de Ni et d'un absorbant CaO mayenite. Ils ont été testés directement avec la régénération sous CO_2 à 925 °C suivie d'une réduction sous 50 % en volume de courant H_2, à 850 °C, avec une performance satisfaisante (Figure 9).

Un autre aspect important pour l'applicabilité industrielle, dans l'hypothèse d'une configuration de réacteur à double lit fluidisé à plus grande échelle, est la résistance mécanique des particules à l'attrition. Cette propriété est évaluée pour les matériaux les plus prometteurs, selon la norme ASTM D5757-11 (Méthode d'essai standard pour la détermination de l'attrition et l'abrasion des catalyseurs en poudre par Air Jets).

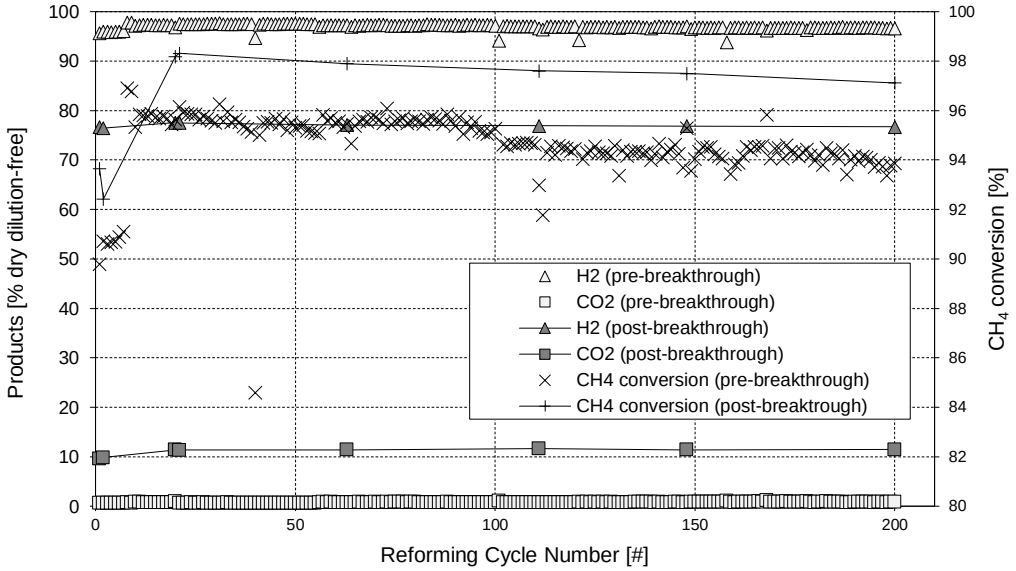

Figure 9 : Tests multicycles SESMR/régénération sur un matériel synthétisé par Marion Technologies (France) selon la méthode de IFE (Norvège) at CSIC (Espagne), autres partenaires du projet ASCENT.

3 Conclusion générale

Le procédé SESMR est d'un grand intérêt dans le cadre de la production d'hydrogène et la limitation des changements climatiques. L'utilisation de CSCM à base de Ni pour la catalyse du SMR et CaO pour la capture de CO_2 est rapportée dans la littérature, en utilisant des aluminates de calcium comme dispersants inertes. L'hypothèse d'un procédé à l'échelle industrielle réalisé dans un double lit fluidisé semble possible, car l'un des lits pourrait agir en tant que reformeur et l'autre comme régénérateur de l'absorbant par une variation de la température.

Une méthode de synthèse comprenant le mélange humide et l'imprégnation par voie humide s'est révélée efficace dans la production de catalyseurs de SMR Ni mayenite, des absorbants de CO_2 CaO mayenite et des CSCM Ni CaO mayenite. Tous les matériaux synthétisés partagent une morphologie microgranulaire, avec des vides internes répartis dans la gamme des méso- et macroporosité.

Pour Ni mayenite, le précurseur de Ni (nitrate ou acétate) influence principalement les propriétés texturales et la réductibilité. La réactivité en SMR est également très différente entre les deux cas, avec des matériaux dérivés de l'acétate de Ni présentant une activité catalytique très faible.

Les résultats des essais sur Ni mayenite et CaO mayenite ont prouvé l'efficacité de cette dernière pour la capture de CO_2 dans les conditions de SESMR, mais également un effet néfaste sur l'activité du Ni lorsque les deux matériaux sont en contact direct et que la fraction de Ni est suffisamment faible.

Ces deux comportements principaux se répercutent sur l'efficacité du CSCM. Les tests en SESMR sur CSCM avec différents précurseurs de Ni, différentes teneurs en Ni et différents excès de CaO, ont mis en évidence que le nitrate de Ni et une faible teneur en CaO favorisent l'activité en SESMR.

Tout cela considéré, nous avons choisi Ni-CaO-mayeinite avec 10 % en masse de Ni provenant du nitrate ajouté par imprégnation humide sur un absorbant CaO mayenite avec 15 % en masse d'excès de CaO, pour une étude d'applicabilité industrielle, consistant en tests multicycles de SESMR/régénération. Différentes conditions de régénération donnent des résultats différents, car le matériau a des performances très bonnes et stables pour 205 cycles avec des régénérations sous N_2 à 850 °C, alors qu'il subit une désactivation progressive lorsqu'il est régénéré sous CO_2 à 925 °C.

D'autre part, les matériaux provenant d'autres partenaires du projet ASCENT ont eu des performances satisfaisantes dans un test de 205 cycles avec régénération sous CO_2 suivie d'une période de réduction. Ceci a permis de valider une nouvelle étape vers le développement du procédé SESMR.

4 Références

[1] "ASCENT project," 2014. [Online]. Available: http://www.ascentproject.eu/. [Accessed: 23-Sep-2016].

[2] L. Barelli, G. Bidini, F. Gallorini, and S. Servili, "Hydrogen production through sorption-enhanced steam methane reforming and membrane technology: A review," Energy, vol. 33, no. 4, pp. 554–570, 2008.

[3] M. R. Cesário, B. S. Barros, C. Courson, D. M. A. Melo, and A. Kiennemann, "Catalytic performances of Ni-CaO-mayenite in CO2 sorption enhanced steam methane reforming," Fuel Process. Technol., vol. 131, pp. 247–253, 2015.

[4] C. S. Martavaltzi and A. A. Lemonidou, "Hydrogen production via sorption enhanced reforming of methane: Development of a novel hybrid material-reforming catalyst and CO2 sorbent," Chem. Eng. Sci., vol. 65, no. 14, pp. 4134–4140, 2010.

[5] J. Meyer, J. Mastin, T.-K. Bjørnebøle, T. Ryberg, and N. Eldrup, "Techno-economical study of the Zero Emission Gas power concept," Energy Procedia, vol. 4, pp. 1949–1956, 2011.

[6] B. Dou, C. Wang, Y. Song, H. Chen, B. Jiang, M. Yang, Y. Xu, "Solid sorbents for in-situ CO2 removal during sorption-enhanced steam reforming process : A review," Renew. Sustain. Energy Rev., vol. 53, pp. 536–546, 2016.

[7] M. Shokrollahi Yancheshmeh, H. R. Radfarnia, and M. C. Iliuta, "High temperature CO2 sorbents and their application for hydrogen production by sorption enhanced steam reforming process," Chemical Engineering Journal, vol. 283. pp. 420–444, 2016.

[8] A. Di Giuliano, J. Girr, R. Massacesi, K. Gallucci, and C. Courson, "Sorption enhanced steam methane reforming by Ni–CaO materials supported on mayenite," Int. J. Hydrogen Energy, vol. 42, no. 19, pp. 13661–13680, 2017.

[9] I. Aloisi, A. Di Giuliano, A. Di Carlo, P. U. Foscolo, C. Courson, and K. Gallucci, "Sorption enhanced catalytic Steam Methane Reforming: Experimental data and simulations describing the behaviour of bi-functional particles," Chem. Eng. J., 2016.

[10] F. Micheli, "Risparmio energetico e micro generazione distribuita, Clean Coal Technologies: CO2 capture," University of L'Aquila and Universtiy of Strasbourg, 2014.

[11] I. Aloisi, N. Jand, S. Stendardo, and P. U. Foscolo, "Hydrogen by sorption enhanced methane reforming: A grain model to study the behavior of bi-functional sorbent-catalyst particles," Chem. Eng. Sci., vol. 149, pp. 22–34, 2016.

Synthesis, characterization and industrial applicability of Combined Sorbent-Catalyst Materials for Sorption Enhanced Steam Methane Reforming

Andrea DI GIULIANO

Supervisor
Prof. Pier Ugo FOSCOLO

Supervisor
Dr. Claire COURSON

Contents

List of figures

List of tables

List of symbols

Symbols

$c^{ABB}_{i,out}$	outlet volumetric percentages measured by ABB system (Equation 2.10) [vol%]
$c^{GC}_{i,out}$	outlet species concentrations measured by GC (Equation 2.4) [vol%]
$C_{i,out}$	products percentage on dry and inert-free basis (Equation 2.8) [vol% dry, dil.-free]
$D_{av,BJH}$	BJH averaged cylindrical pore diameter [nm]
$F_{i,in}$	inlet molar flowrate of species "i" (Equation 2.4, Equation 2.5) [Nml min^{-1}]
$F_{i,out}$	outlet molar flowrate of species "i" (Equation 2.4, Equation 2.8) [Nml min^{-1}]
F_{out}	overall dry product flowrate (Equation 2.10) [Nml min^{-1}]
K	Scherrer equation (Equation 2.1) constant [#]
L	average crystallite sizes, calculated by Scherrer equation (Equation 2.1) [nm]
m	packed-bed mass (Equation 2.5 , Equation 2.6) [mg]
$m^{(i)}$	mass at the beginning of the i^{th} cycle, TGA multicycle CO_2 capture test (Equation 2.3) [mg]
m_0	mass at the end of cleaning, TGA CO_2 capture test (Equation 2.2) [mg]
$m_{fines}(1\ h)$	attrition tests recovered fines mass after 1 h (Equation 2.11) [g]
$m_{fines}(5\ h)$	attrition tests recovered fines mass after 1 h (Equation 2.12, Equation 2.13) [g]
m_r	attrition test residual mass (Equation 2.13) [g]
m_s	attrition test initial sample mass (Equation 2.11, Equation 2.12, Equation 2.13) [g]
$N_{C,in}$	total elemental C moles entering the reactor (Equation 2.9) [mol]
$N_{C,out}$	total elemental C moles leaving the reactor (Equation 2.9) [mol]
O_i"	extra-framework oxygen ion in mayenite

O_O^x	framework oxygen ion in mayenite
P	BET experimental equilibrium pressure
P/P_0	BET equilibrium relative pressure
P_0	N_2 vapour pressure at BET operating temperature
p_{CO2}	CO_2 partial pressure [atm]
$p_{CO2,eq}$	CO_2 equilibrium partial pressure (Equation 1.1, Equation 1.2, Equation 1.3) [atm]
S_{BET}	BET surface area [$m^2\ g^{-1}$]
T	absolute temperature (Equation 1.1, Equation 1.2, Equation 1.3) [K]
t	time [min]
t^*	breakthrough completion time [min]
V_{BJH}	BJH cumulative pore volume [$cm^3\ g^{-1}$]
V_i^x	empty cage in mayenite crystalline structure

Greek letters

λ	wavelength of CuKα_1 radiation (Equation 2.1) [nm]
β	FWMH of the reference peak (Equation 2.1) [rad]
$\gamma_{CO2}^{(i)}$	captured CO_2 at the i^{th} cycle, TGA multicycle CO_2 capture test (Equation 2.3) [g_{CO2} 100 $g^{-1}_{calcined\ material}$]
Γ_{CO2}	experimental maximum CO_θ sorption capacity (Equation 2.2) [g_{CO2} 100 $g^{-1}_{calcined\ material}$]
δ_{CaO}^0	average initial diameter of CaO grains in the PGM [nm]
ΔC	C-balance deviation in terms of percentage error (Equation 2.9) [%]
Δm	7 h mass increase, TGA CO_2 capture test (Equation 2.2) [mg]
$\Delta m^{(i)}$	mass increase during the i^{th} cycle, TGA multicycle CO_2 capture test (Equation 2.3) [mg]
ΔS_{BET}	BET surface area percentage variation with respect to the as-synthesized state [$m^2\ g^{-1}$]
ΔV_{BJH}	BJH cumulative pore volume percentage variation with respect to the as-synthesized state [$cm^3\ g^{-1}$]
2θ	Bragg angle (Equation 2.1) [rad]
χ_{CH4}	CH_4 conversion (Equation 2.7) [%]
ω_{Ni}	Ni fraction (Equation 2.6) [wt%]

List of acronyms

ADPFR	Axial Dispersion Plug Flow Reactor
AISI	American Iron and Steel Institute
AJI	Air Jet Index
ASCENT	Advanced Solid Cycles for Novel Efficient technologies
ASTM	American Society for Testing and Materials
ASU	Air Separation Unit
BET	Brunauer-Emmett-Teller
BFB	Bubbling Fluidized-Bed
BJH	Barrett-Joyner-Halenda
BSE	Back Scattering Electron
CCS	Carbon Capture and Storage
CFB	Circulating Fluidized Bed
CFBC	Circulating Fluidized Bed Combustion
CFC	ChloroFluoroCarbons
CLC	Chemical Looping Combustion
CSCM	Combined Sorbent-Catalyst Material
CSIC-ICB	Consejo Superior de Investigaciones Cientificas – Instituto de Carboquimíca
DBFB	Dual Bubbling Fluidized-Bed
EDS	Energy Dispersive X-ray Spectrometry
EU	European Union
FCC	Fluid Catalytic Cracking
F-gases	Fluorinated gases
FWHM	Full Width at Half Maximum

GC	Gas Chromatograph
GHG	GreenHouse-Gases
GWP	Global Warming Potential
HRTEM	High-Resolution Transmission Electron Microscopy
ICDD	International Centre of Diffraction Data
ICP-AES	Inductively Coupled Plasma - Atomic Emission Spectroscopy
IFE	Institutt For Energiteknikk
IGGC	Integrated Gasifier Combined Cycle
IPCC	United Nations Intergovernmental Panel on Climate Change
IUPAC	International Union of Pure and Applied Chemistry
JCPDS	Joint Committee on Powder Diffraction Standards
LHV	Lower Heating Value
MEA	MonoEthanolAmmine
NDIR	Non-Dispersive InfraRed
Ni(Ac)	Nickel Acetate tetrahydrate, $Ni(CH_3COO)_2 \cdot 4H_2O$
Ni(N)	Nickel Nitrate hexahydrate, $Ni(NO_3)_2 \cdot 6H_2O$
Ni-WHSV	Nickel Weight Hourly Space Velocity
PDF	Powder Diffraction Files
PGM	Particle Grain Model
PSA	Pressure Swing Adsorption
SEM	Scanning Electron Microscopy
SESMR	Sorption Enhanced Steam Methane Reforming
SMR	Steam Methane Reforming
SOFC	Solid Oxide Fuel Cells
STEM	Scanning Transmission Electron Microscopy
TCD	Thermal Conductibility Detector
TEM	Transmission Electron Microscopy
TGA	Thermo-Gravimetric Analysis
TPD	Temperature Programmed Desorption
TPR	Temperature Programmed Reduction
USA	United States of America
WGS	Water Gas Shift

WHSV	Weight Hourly Space Velocity
WI	Wet Impregnation
WM	Wet Mixing
XRD	X-Ray Diffraction

Chapter 1

Introduction to the research subject and issues

This chapter gathers information about the subject of this thesis, the sorption enhanced steam methane reforming, providing a background and raising the research issues faced in the next chapters.

1.1 Climate change

Earth climate has changed throughout history, for instance by seven glaciation in the last 650000 years, the last abruptly ending 7000 years ago, leading to the modern climate era and therefore to human civilization [1].

Nonetheless, the global warming trend measured since the second half of 20th century is of noteworthy relevance, as it shows an unprecedented rate over decades to millennia and is extremely likely the result of contribution from human activities to the greenhouse-effect [2–5].

The causality relationship between human activities and climate-warming trend over the past century is acknowledged by the 97 % percent of climate scientists, and most of the leading scientific organizations worldwide have publicly endorsed this position [1,4].

1.1.1 Causes of climate change

The phenomenon popularly known as greenhouse-effect (Figure 1.1) consists in the trapping of long-wave (4-100 μm) radiations emitted by Earth's surface, mainly brought about by water vapor, with a substantial contribution from CO_2 and smaller contributions by other gases, e.g. CH_4, N_2O, O_3 [6]. The presence in Earth's atmosphere of these radiatively active gases, also known as greenhouse-gases (GHG), has made so far our planet habitable by life as we know it, since they rise the average global surface temperature by roughly 30 °C, as opposed to the estimated -15 °C in the absence of an atmosphere [6].

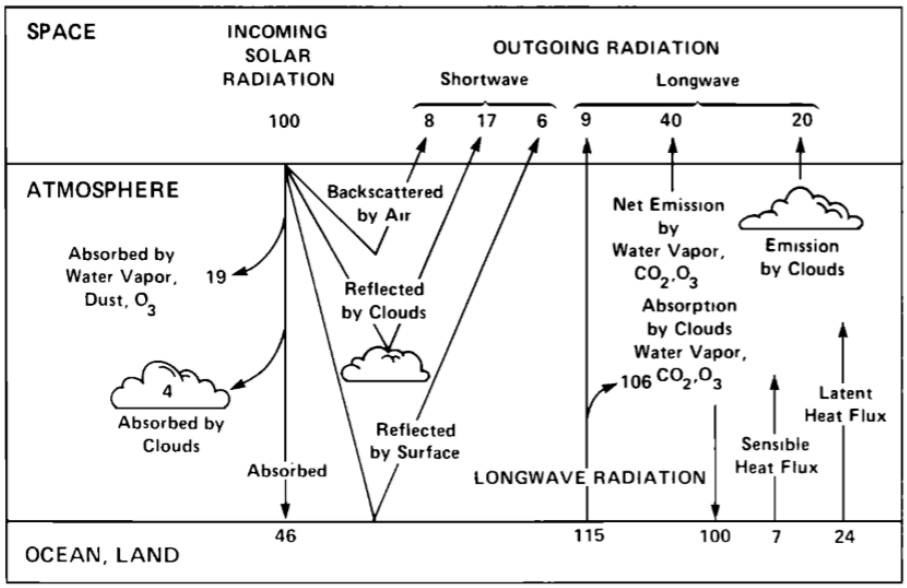

Figure 1.1: Schematic representation of the atmospheric heat balance (units are percent of incoming solar radiation): the solar fluxes are shown on the left-hand side, and the longwave (thermal infrared) fluxes are on the right-hand side [6,7]

Most of the scientific community recognizes anthropogenic contribution to the greenhouse-effect as the main cause of the current global warming trend underpinning climate change [4,8,9]. This contribution consists in the augmentation of CO_2, CH_4, N_2O concentrations in the atmosphere (Figure 1.2a, Figure 1.2b, Figure 1.3), together with the emission of synthetic GHG as chlorofluorocarbons (CFC) or other fluorinated gases (F-gases) [1,2].

In fact, anthropogenic GHG emissions have increased since the pre-industrial era, driven largely by economic and population growth, and are now higher than ever, so that atmospheric concentrations of CO_2, CH_4 and N_2O are unprecedented in at least the last 800000 years [8].

Table 1.1: GHG characteristics: "anthropogenic sources" from [1]*; numerical data from* [10]*, with Global Warming Potential at 100 year horizon (GWP_{100}) defined as the number of times the referred GHG is more warming than CO_2 in 100 years*

Gas	Anthropogenic sources	GWP_{100}	Atmospheric lifetime [years]	Increased radiative forcing [W m^{-2}]
CO_2	Deforestation Land-use changes Burning fossil-fuels Manufacture of cement	1	100-300	1.94
CH_4	Decomposition of wastes in landfills Ruminant digestion Manure management associated with domestic livestock	28	12.4	0.50
N_2O	Soil cultivation practices (commercial fertilizers); Burning fossil-fuels; Nitric acid production; Biomass combustion	265	121	0.20

Table 1.1 summarizes anthropogenic sources of main GHG, evidencing how the two branches of human activities most affecting climate are the primary sector, causing land-usage change (Figure 1.2c), and the production of energy, nowadays still mainly based on fossil-fuels burning (Figure 1.2d).

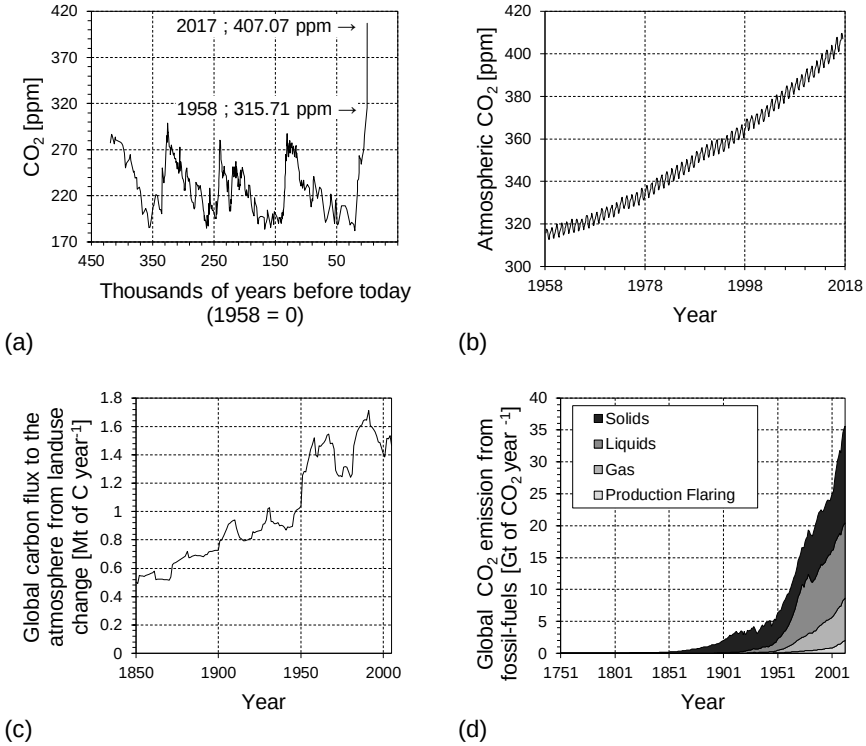

Figure 1.2: CO_2 emissions: historical series of CO_2 level (a), with data until 2342 years ago reconstructed from Vostok Ice Core indirect measurements [11]*, and those between 1958 and 2017 directly measured at Mauna Loa Observatory, Hawaii* [1]*, magnified in (b); global net carbon flux to atmosphere from land-usage change, data from* [11] *(c); global CO_2 emissions from fossil-fuels burning, data from* [11] *(d);*

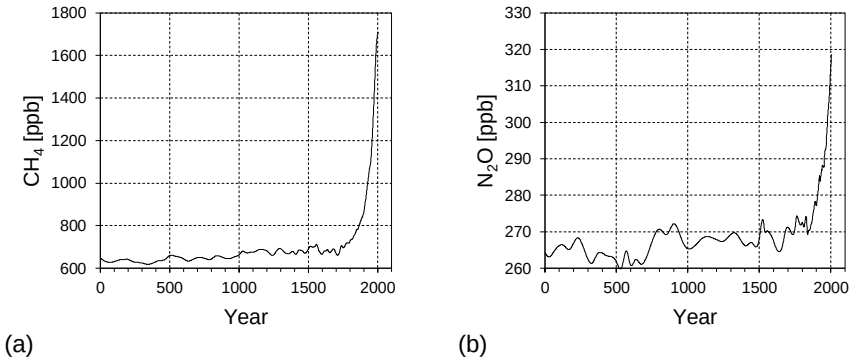

Figure 1.3: CH_4 and N_2O concentration series from Law Dome ice core records, data from [11]

1.1.2 Evidences of climate change

Tangible phenomena related to climate change, currently occurring on Earth, are:

- Global temperature rise: planet's average surface temperature has increased of 1.1 °C since the late 19th century, the most happening in the last 35 years [1]

(Figure 1.4, other data bringing similar conclusions can be consulted in [12] or [13]); at the Earth's surface, each of the last three decades has been successively warmer than any preceding decade since 1850 [14] and 16 of the 17 warmest years on record has occurred since 2001 [1];

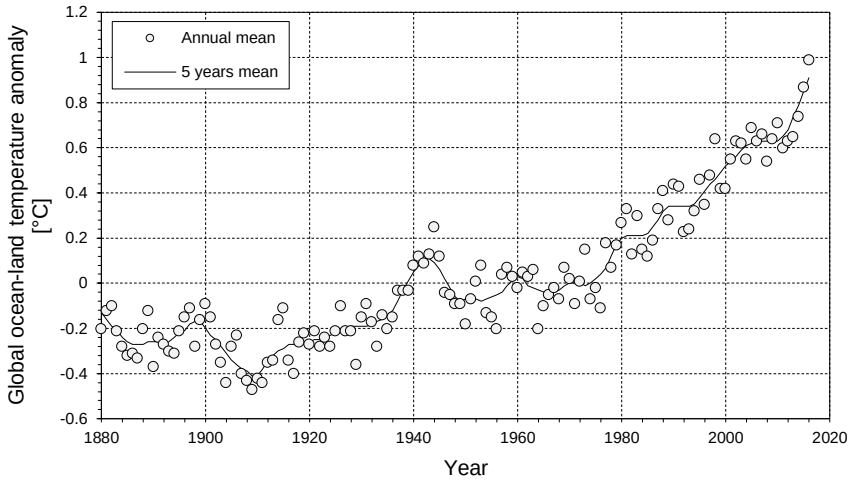

Figure 1.4: Change in global ocean-land surface temperature, relative to 1951-1980 average temperature (NASA's Goddard Institute for Space Studies) [1]

- Warming oceans: they store most of the global heat surplus due to greenhouse-effect, because of their heat capacity (90 % of the energy accumulated by the climate system between 1971 and 2010 [14]), with an increase of their subsurface (0-700 m) temperature [15];
- Oceans acidification: because of humans emissions into the atmosphere since the beginning of industrial era, oceanic uptake of CO_2 has increased, resulting in acidification of the oceanic waters [14,16]
- Shrinking ice sheets: Greenland and Antarctica ice sheets have been losing mass in the las two decades (Figure 1.5a) [1];
- Declining Artic sea-ice: its annual mean extent has decreased over the period 1979 to 2012, with a rate very likely in the range 3.5 % to 4.1 % per decade [14], also accompanied by a thickness lowering [17];
- Glacial retreat [18] and decreased snow cover [19];
- Sea level rise: it is primarily due to the added water from melting ice sheets and glaciers and the expansion of sea water as it warms; the rise rate since the mid-19th century has been larger than the mean rate during the previous two millennia; furthermore, the rise rate of the last two decades (Figure 1.5b) doubles the one of the last century [1,20];
- Extreme events: weather or climate events, considered rare at particular places and time of the year, have increased their frequency and/or intensity, e.g.: heat waves, cold waves, heavy rains, periods of drought and flooding, severe storms and cyclones, wildfires [14,21,22].

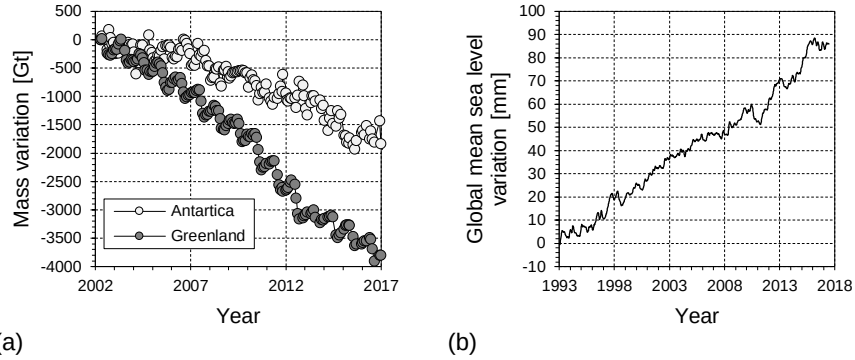

Figure 1.5: Mass variation of Antarctica and Greenland land ice (data from NASA's GRACE satellites) (a); change in sea level observed by satellites (data from NASA Goddard Space Flight Centre) (b) [1]

1.1.3 Dealing with climate change

In the light of §1.1.1, it is reasonable to assume that a continued GHG emissions would cause further warming, with long-lasting impact on the whole Earth climate system, along the lines of current situation depicted in §1.1.2 [1,8]

Anthropogenic GHG emissions depend on economic and population growth, lifestyle and associated use of energy, land and technology, together with adopted climate policy [8]. World population is expected to grow up to 11.2 billion people by 2100 (more than 50 % increase on today's 7.3 billions) and this expansion of humanity is substantially anticipated in the least developed regions of south and west Asia and north Africa [23,24]. Global energy consumption is more than doubled in the period from 1973 to 2014 [25], with a sharing among countries somehow reflecting forecasted trends of world population growth (Figure 1.6); furthermore, the world sharing of fuels usage highlights the still dominating role of fossil-fuels as coal, oil and natural gas (Figure 1.7). In this context, efforts for anthropogenic GHG containment must be directed towards the change of lifestyle, energy usage and technologies, under the aegis of a new world climate policy.

Signals of this efforts come from the past, firstly with 1987 Montreal Protocol on substances that deplete the ozone layer [26], followed by 1997 Kyoto Protocol on the containment of GHG emissions for environmental protection [27] and the 2010 Europe2020 strategy, which addressed EU members to reduce GHG emissions by at least 20 % compared to 1990 levels, increase the share of renewable energy sources in EU final energy consumption to 20 %; and increase by 20 % energy efficiency, all by 2020 [28].

In December 2015, 195 countries have signed the Paris Agreement and nowadays 160 have ratified it, accepting their first legal binding climate deal; in its Article 2, point 1 (a), it is clearly stated that the parties have committed to a limitation of the increase in the average global temperature to well below 2 °C above pre-industrial levels and to pursue efforts to limit the temperature increase to 1.5 °C above pre-industrial levels [29].

IPCC (United Nations Intergovernmental Panel on Climate Change) simulated a great number of future scenarios, until 2100: only those leading to CO_2-equivalent concentrations (i.e. CO_2 concentration causing the same radiative forcing as a given actual mixture of CO_2 and other components) of about 450 ppm or lower are likely to maintain global warming

below 2 °C relative to pre-industrial levels [2], not so far from current levels, so that the limitation of GHG emissions is of paramount importance to contain global warming. In other words, the world is running out of time.

A socio-economic comment could give an optimistic conclusion to this discussion: many investors are wondering whether the time has come for the 6th Kondratieff cycle, a name indicating a long-term period (40-60 years) usually characterized at its beginning by some economy-depressive events, followed by prosperity gained by means of knowledge and technological breakthroughs (Figure 1.8); the last economic crisis could be seen as the trigger event of this hoped 6th cycle and inventions in the areas of healthcare, nanotechnologies, biotechnologies and climate protection could constitute the prosperity-driving breakthroughs [30].

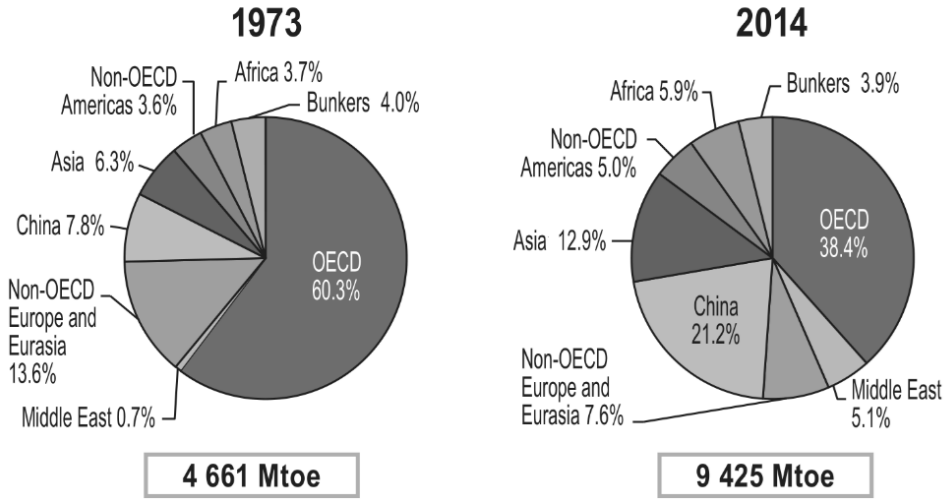

Figure 1.6: World total final energy consumption by region; "Asia" excludes China and countries belonging to the Organisation for Economic Co-operation and Development (OECD) of Asia; "Bunkers" includes international aviation and international marine bunkers [25]

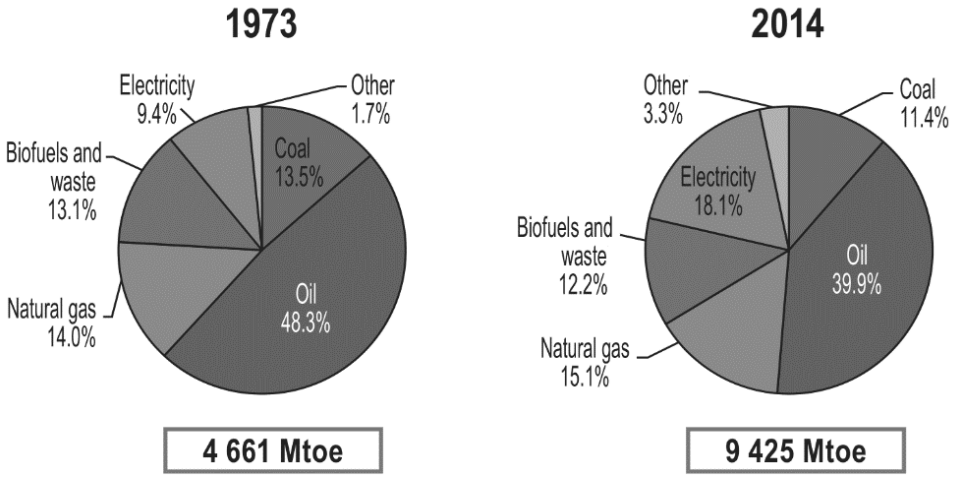

Figure 1.7: World total final energy consumption by fuel; "Coal" includes coal, peat and oil shale; data for "Biofuels and waste" final consumption have been estimated for a number of countries; "Others" includes geothermal, solar, wind, heat, etc. [25]

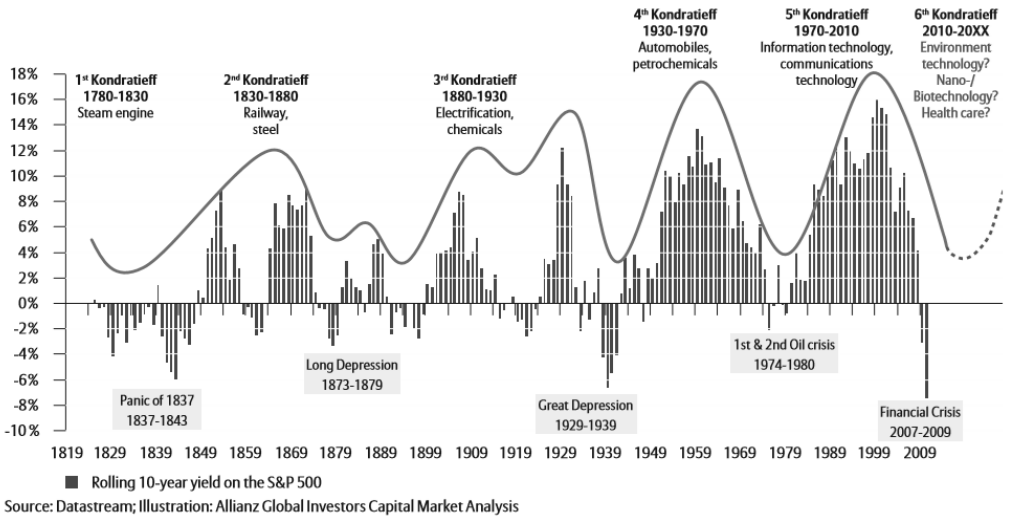

Figure 1.8: Kondratieff cycles-long wave of prosperity, rolling 10-year yield on the S&P 500 since 1814 to March 2009 [30]

1.2 Hydrogen

H_2 has been claimed since some decades as an alternative to carbon containing fossil-fuels [31,32]. Besides its long-term potential to reduce carbon emissions from the transport sector, hydrogen also has the advantage of its high Lower Heating Value (LHV) equal to 122 MJ kg^{-1}, which is approximatively 2.8 times higher than those of gasoline and diesel-fuel [33]. On the other hand, H_2 low density has made technically difficult its storage and provision, hampering its widespread use as an energy carrier [34].

Currently, as an important industrial feedstock, H_2 is widely used in petroleum refining, production of commodity chemicals as ammonia and methanol (Figure 1.9b), as well as metal refining and food industry, anticipating also a renewed interest in Fisher–Tropsch technology [35–38].

However, as a benign energy carrier, H_2 also has great potential in all sectors of the economy, including transportation, buildings and industry [35,39], in other words the potential to develop the so called "hydrogen economy" (expression introduced by General Motors Co. in 1970 [33]).

1.2.1 Demand and production

H_2 is essentially not available as such in nature [33]. World H_2 production rate in 2008 was approximatively 50 Mt $year^{-1}$ [36], divided by origin and usage as shown in Figure 1.9. Its demand is expected to increase in the near future as sour, heavy crude is increasingly replacing sweet, light crude, and in anticipation of the shift towards a more decarbonized energy market [38].

At present, steam reforming, auto-thermal reforming, partial oxidation and coal gasification are the main commercially developed routes for H_2 production, all based on

fossil-fuels [36,40,41]. A minor share of H_2 world production is covered by water electrolysis [40], the first available commercial technology in 1920s [41].

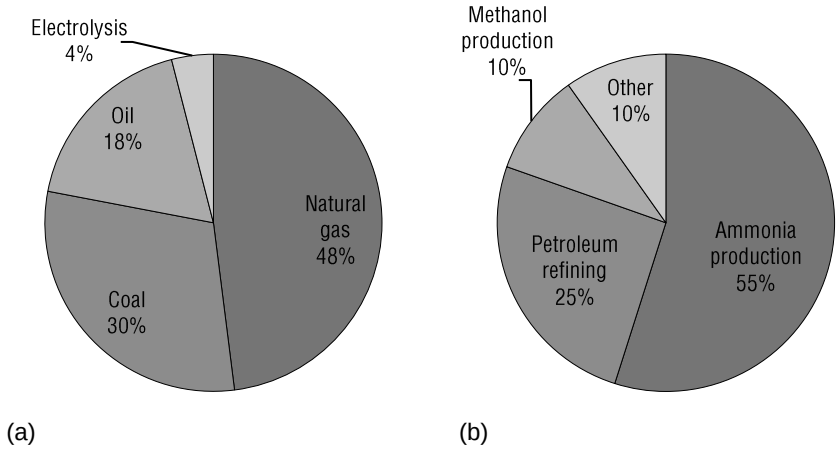

Figure 1.9: Estimated world H_2 production sources (a) and usage (b) in 2008; data from [36]

Several processes are under study and considered as emerging, even though nowadays they are not competing with above mentioned technologies: plasma hydrocarbons reforming [42,43], hydrocarbons pyrolysis [44], biomass gasification coupled with catalytic processes [45–48], thermochemical water splitting [49] and biological routes (e.g. direct water photolysis or dark fermentation of carbohydrate substrates) [40].

Catalytic Steam Methane Reforming (SMR), using natural gas (CH_4 with traces of C_2-C_6 hydrocarbons [50,51]) as a feedstock, is currently the dominating industrial technology for the production of H_2 [40,41,52–54], in so far it covers nearly half of the world H_2 demand [33]. There are different materials able to catalyse SMR, nevertheless economic reasons drive the choice to metallic nickel (Ni) as an active phase, supported on modified alumina [37,55].

The proper SMR (Reaction 1.1) is always accompanied by Water Gas Shift (WGS, Reaction 1.2) [56–58], which leads to an higher H_2 yield, although produces also CO_2 [59,60].

$$CH_{4(g)} + H_2O_{(v)} \leftrightarrow CO_{(g)} + 3H_{2(g)} \qquad \Delta H^0_{298\,K} = 206.2\ kJ\ mol^{-1} \qquad \textit{Reaction 1.1}$$

$$CO_{(g)} + H_2O_{(v)} \leftrightarrow CO_{2(g)} + H_{2(g)} \qquad \Delta H^0_{298\,K} = -41.2\ kJ\ mol^{-1} \qquad \textit{Reaction 1.2}$$

In addition, Boudouard reaction (Reaction 1.3) and CH_4 cracking (Reaction 1.4) may occur, leading to the formation of solid carbon [61,62]:

$$2CO_{(g)} \leftrightarrow C_{(s)} + CO_{2(g)} \qquad \Delta H^0_{298\,K} = -172.4\ kJ\ mol^{-1} \qquad \textit{Reaction 1.3}$$

$$CH_{4(g)} \leftrightarrow C_{(s)} + 2H_{2(g)} \qquad \Delta H^0_{298\,K} = 74.9\ kJ\ mol^{-1} \qquad \textit{Reaction 1.4}$$

The enthalpy balance of Reaction 1.1 and Reaction 1.2 results in a strongly endothermic transformation. In fact, industrial SMR is an energy intensive process, typically operated

at severe conditions (800-1000 °C and 1.5-3.0 MPa) in a vertical array of tubes placed in a furnace and filled with the catalyst, so to form a packed-bed reactor, fed by natural gas and steam in stoichiometric excess (inlet steam to carbon molar ratio between 2.5 and 5 [63]), in order to avoid carbon deposition (Reaction 1.3, Reaction 1.4), which causes Ni deactivation, tubes obstruction and consequent pressure drop increase [55,61,64,65]. Downstream, two reactors in series respectively operate a high-temperature shift (350-400 °C, Fe_3O_3-Cr_2O_3 as a catalyst [66]) and a low-temperature shift (180-350 °C, ZnO-CuO-Al_2O_3 as a catalyst [66]), taking advantage of WGS equilibrium at lower temperature (exothermic reaction, Reaction 1.2) [38,67]. The typical gas composition on dry basis leaving the second shift reactor is 76 vol% H_2, 3 vol% CO, 17 vol% CO_2 and 4 vol% of unreacted CH_4 [38]. High purity H_2 is eventually obtained by a CO_2 removal processes [38,67].

Notwithstanding its matureness as H_2 production technology, the SMR whole process presents some disadvantages, becoming more and more alarming in view of the current climate situation (§1.1) [38]:

- Tubular furnace intensively requires heat, generally provided by burning part of the same natural gas employed as a feedstock, so determining CO_2 net emissions;
- Temperature lowering associated with shift steps determines poor energy integration efficiency.

1.2.2 Hydrogen as a fuel

A fuel cell is a static device operating the conversion of chemical energy from a fuel gas directly in electrical energy, and heat as by-product, without intermediate steps as combustion, heat transfer or momentum transfer [35,68,69].

Fuel cells are compatible with renewable sources and modern energy carriers as H_2, with high conversion efficiency even at small scale, so that they are regarded as efficient and clean devices for sustainable energy conversion in the future, in the fields of power generation and transport [69,70].

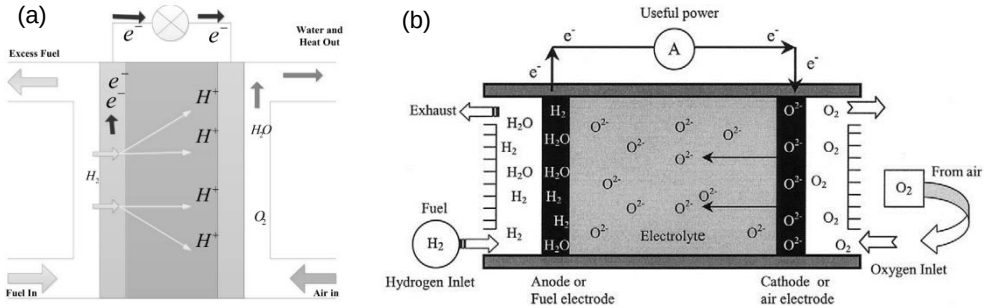

Figure 1.10: Representation of a generic fuel cell with H^+ ion conduction (picture from [69]*) (a), and of a SOFC (picture from* [68]*) (b)*

Their operating principles are basically the same of a battery (Figure 1.10): a fuel (generally H_2) and an oxidant (generally O_2 from air) are respectively supplied to an anode and a cathode, which are put in contact by a ion conduction electrolyte [68]. However,

unlike a battery, a fuel cell works as long as both fuel and oxidant are fed, without running down or requiring recharging [68,69].

Fuel cells are classified on the basis of their electrolyte material, differing in their power outputs, operating temperatures, electrical efficiencies, and typical applications [68–70]. A detailed list of fuel cells types can be found in [70].

In general, they have many inherent advantages over conventional combustion-based systems: reduced harmful emissions, higher efficiency, modularity, static nature, flexibility [69,70]. Nevertheless, they also have some disadvantages requiring further research and development: high cost per generated energy unit, low durability, lack of infrastructures for economical and safe H_2 distribution and storage, water by-product management, low dynamics, poor voltage profile against current density, lack of codes and standards [69,70]. As a matter of fact, the overall commercialization of fuel cell has not yet come, the two biggest drawbacks for commercialization being life time and expensiveness [69,71].

Solid Oxide Fuel Cells (SOFC, Figure 1.10b) are among the most efficient and environmentally friendly technologies available for power generation from H_2, also in distributed form [69,72].

Their main components are [68,70]:

- A non-porous electrolyte, which can be constituted by a variety of oxides combinations, the most common being yttria-stabilized zirconia (Y_2O_3-ZrO_2), which exhibits a pure oxygen ionic conduction (O^{2-});
- An anode, made of a porous composite mixture of the electrolyte material and nickel oxide (NiO), added to inhibit sintering;
- A cathode, with several materials available, depending on the specific application (e.g. perovskite-like strontium-doped lanthanum manganite, $LaSrMnO_3$ for temperatures above 800 °C).

SOFC have the highest operative temperature range of all fuel cells (600-1000 °C), therefore furnishing high-grade heat, and are uniquely made of solid materials, so that there are no fundamental restrictions on their design configuration [68,70]. Moreover, SOFC accept CO and CH_4 as a fuel, besides H_2 [68,70], so they can be coupled to SMR plant for power generation [72].

Intensive research in SOFC has taken place worldwide for twenty years, because of their high electric efficiency, e.g. as compared to traditional gas turbine power plants (30-40 %) [73], with possible application technologies in Table 1.2.

Table 1.2: Application of SOFC technology (adapted from [72]*)*

Application	**Power**	**Efficiency**
SOFC-Gas turbine combined cycle	Several MW	> 60 %
SOFC-Steam turbine combined cycle	Several MW	Up to 67 %
Cogeneration with SOFC	200-300 kW (small scale applications) Several MW (industrial application)	> 80 %
Trigeneration with SOFC	200-300 kW (small scale applications) Several MW (industrial application)	Increasing by at least 22 %
Transportation	2 kW l^{-1}	50 %
Residential	1-300 kW	Up to 83 %

Important steps towards the hydrogen economy have been done in the transportation sector too. Nowadays, the first fuel cell electrical vehicles have been commercialized [74–76], simultaneously with the first instalment worldwide of automotive hydrogen fuelling stations [77]; moreover, Western Europe and USA have been deploying the first fuel cell electric buses, with several government funded programs aiming the same in Canada, Japan, China, Australia, and South America [70].

1.3 Carbon capture

Carbon Capture and Storage (CCS) is defined as a process in which a relatively pure CO_2 stream from industrial and energy-related sources is separated (i.e. captured), conditioned, compressed and transported to a storage location for long term isolation from the atmosphere, so to avoid increments of greenhouse-effect [2].

One approach to reach the goal of keeping global warming below 2 °C is the coupling of CCS technology with fossil-fuel energy system, whereas other strategies are energy efficiency increasing, or the use of nuclear energy, bioenergy, wind power, and solar energy [78]. IPCC evaluated the first approach together with these strategies, assessing various scenarios: when CCS is excluded, only half of hypothesized scenarios brings to a global warming lower than 2 °C, anyway causing higher costs than those predicted when CCS is included (138 % more expensive on average) [2,78].

Therefore, CCS is expected to have a significant role in the battle against climate change in a cost-effective manner [78]. Unfortunately, immediate direct costs associated with CCS technology deployment have been an obstacle to its widespread, so that further researches are needed [78], even though the concept of CCS as a strategy to face global warming was first suggested 40 years ago [79]. Particularly, the CO_2 capture step contributes to around 70-80 % of the total cost of the full CCS chain [80].

1.3.1 CO_2 capture technologies

On the basis of the energy conversion process with which they are coupled, CO_2 capture technologies are classified as follows [80–82]:

- Post-combustion;
- Pre-combustion;
- Oxyfuel combustion.

1.3.1.1. Post-combustion technologies

Post-combustion CO_2 capture is operated on the flue gas produced by a combustion process [80–82].

Its main quality is the adaptability towards existing combustion plants, while a relevant constrain is the low concentration of CO_2 in the flue gas (e.g. 7-14 vol% for coal-fired boilers, 4 vol% for gas-fired turbines), which causes high costs to reach the high purities required by subsequent steps of transport and storage (above 95.5 vol%) [80–82].

Absorption by amine aqueous solutions, mainly monoethanolamine (MEA) [83], is a lead contending technology for post-combustion CO_2 separation [80,84], allowing to obtain a high purity CO_2 stream, ready for compression, conditioning and storage, stripped from the liquid sorbent by a pressure and/or temperature swing [81,83]. Main process issues are [81,84]:

- The energy duty for solvent regeneration affecting thermal efficiency of the coupled plant (approximately 4 MJ per kg of captured CO_2 for MEA [83]);
- The high solvent rates required by the low CO_2 concentration in the flue gas;
- Amines degradation in the presence of CO_2, O_2 and SO_x or due to temperature, with an environmental and health concern about nitrosamines developing.

Fluor Daniel's ECONAMINE process [85] or Mitsubishi KS-1 process [86] are applied since 1980s to remove CO_2 in methane combustion plants [87], proving the maturity for commercial employment of this technique. The commercialization is close for coal-fired plants too, with more than 25 pilots (0.1-5 MW_e) testing amine absorption/stripping on coal-fired flue gas, and 7 prototype systems operated at 10-33 MW with coal-fired flue gas and compression of the CO_2 [87].

Long-term research on post-combustion technologies is focusing on several alternative CO_2 separation methods [80], as: membrane separation [88], hydrate-based separation [81], physical and chemical adsorption [89], absorption by ionic liquids [90], cryogenic distillation [81].

1.3.1.2. Pre-combustion technologies

A pre-combustion system processes a fuel to obtain syngas (roughly a mixture of H_2 and CO with minor fractions of CH_4, CO_2), e.g. by gasification of coal or steam reforming of natural gas; afterwards, the syngas reacts with steam in a WGS reactor to form additional H_2 and CO_2 (approximately 55 vol% and 40 vol% respectively), so that resulting CO_2 has a high partial pressure, which improves the driving force for separation, leaving high-purity H_2 ready as a fuel [80–82].

Pre-combustion configuration allows to reach higher CO_2 concentrations than post-combustion ones, however it has a more restricted application area and causes relevant changes in the conversion chain from the primary fuel to the final power or heat production with consequent issues related to energy efficiency [80–82].

Amine scrubbing is also an option for pre-combustion technologies, for instance applied to SMR [38]. However, for SMR, the Pressure Swing Adsorption (PSA) on multiple packed-bed reactors (filled with molecular sieves, silica gels or activated carbons) is mainly adopted, obtaining H_2 purities higher than 99 vol% and recycling the tail gas to the reformer burner [38,55].

Other current state-of-the-art processes for pre-combustion CO_2 capture, applied to Integrated Gasifier Combined Cycle (IGCC) fed with coal, are physical or physical/chemical absorption by glycol-based solvent like Selexol™, or methanol-based Rectisol® [80,91–93].

Mid-term to long-term opportunities to reduce pre-combustion CO_2 capture costs could come from membranes and solid sorbents, coupled with processes for the production of H_2 as gasification or reforming, currently studied at laboratory or pilot scale [80,94,95].

1.3.1.3. Oxyfuel combustion

In oxyfuel combustion systems, oxygen is used as a oxidant agent instead of air, avoiding N_2 within the reactor and therefore producing an undiluted flue gas, mainly composed by CO_2, H_2O, SO_2 and particulate; after conventional electrostatic precipitation, desulfurization and water condensation, highly concentrated CO_2 (80-98 vol%) can be obtained, compressed, transported and stored [80–82].

For an improvement in CO_2 concentration levels, economic constrains come from the expensive Air Separation Unit (ASU) for the production of pure oxygen, and from corrosion issues due to SO_2 [80–82].

At present, the process has been operated not beyond the pilot scale in pulverized coal-fired boilers (< 100 MW_{th}), with the variant named oxyfuel Circulating Fluidized Bed Combustion (CFBC) explored at an even lower scale (< 100 kW) [87].

An alternative new concept emerging from the literature, named Chemical Looping Combustion (CLC), can be classified as oxyfuel combustion: a metal oxide is used instead of pure oxygen, burning (i.e. oxidizing) the fuel in one reactor, by its reduction to metallic state, therefore producing highly concentrated CO_2; afterwards, the metal is re-oxidized by air in a second reactor and sent again to the burner, closing the loop and avoiding the direct contact between air and fuel, so the dilution of CO_2 [80,81].

1.3.2 CaO-based high-temperature solid sorbents

Adsorption by solid sorbents for CO_2 capture is considered a promising technology that offers potential energy savings with lower capital and operating costs, as compared to current state-of-the-art physical absorption by solvents [93].

Most available works in the open literature focus on high-temperature (450-700 °C) sorbents, for which the following characteristics are required [63]:

- Thermal stability at operating temperatures;
- High CO_2 sorption capacity and kinetics;
- Easiness of sorbent regeneration;
- Reasonable production costs;
- Long-term cyclic stability.

Examples of investigated high-temperature sorbents are lithium zirconate (Li_2ZrO_3), sodium zirconate (Na_2ZrO_3), lithium silicate (Li_4SiO_4) and especially sorbents based on calcium oxide (CaO) [63].

1.3.2.1. The reactive system $CaO/CO_2/CaCO_3$

CaO is largely known as a CO_2 high-temperature sorbent, as it is easily available in nature in its low cost mineralized forms of limestone ($CaCO_3$) and dolomite ($CaMg(CO_3)_3$), and

also because of its high sorption capacity (78.6 g_{CO2} per 100 g_{CaO}) and kinetics in the high-temperature range [63,96].

CaO sorption occurs by carbonation (Reaction 1.5), whereas its regeneration is commonly obtained by calcination, i.e. reversing Reaction 1.5 equilibrium by raising the temperature beyond a threshold depending on CO_2 partial pressure (p_{CO2}) in the surrounding gas [63].

$$CaO_{(s)} + CO_{2(g)} \leftrightarrow CaCO_{3(s)} \qquad \Delta H^0_{298\,K} = -175.7\ kJ\ mol^{-1} \qquad \text{Reaction 1.5}$$

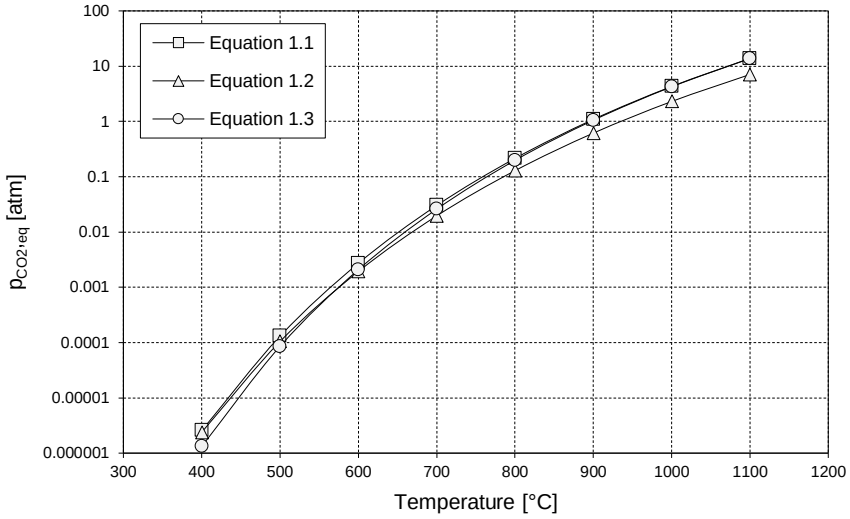

Figure 1.11: Equilibrium curves for Reaction 1.5

Several relations are available in literature for the quantification of equilibrium p_{CO2} of Reaction 1.5 ($p_{CO2,eq}$) as a function of temperature (e.g. Equation 1.1 [97], Equation 1.2 [98], Equation 1.3 [99]), among which Equation 1.1 is typically adopted [97].

From the kinetics point of view, Reaction 1.5 occurs firstly by a fast step, followed by a slower one: the first step is controlled by the chemical reaction between CaO and CO_2, during which "isles" of $CaCO_3$ begin to from on CaO grains (i.e. nucleation); as CaO conversion increases, the freshly produced $CaCO_3$ layer entirely covers the remaining CaO grain, constituting a diffusional resistance for CO_2 to get in direct contact with CaO, switching the reaction to the slow kinetic step, controlled by gas diffusion [63,100–106].

$$p_{CO_2,eq} = 4.137 \cdot 10^7 \exp\left(-\frac{20474}{T}\right) \qquad \text{Equation 1.1}$$

$$p_{CO_2,eq} = 1.186 \cdot 10^7 \exp\left(-\frac{19680}{T}\right) \qquad \text{Equation 1.2}$$

$$p_{CO_2,eq} = \exp\left(17.74 - 0.00108 \cdot T + 0.332 \ln T - \frac{22020}{T}\right) \qquad \text{Equation 1.3}$$

1.3.2.2. CaO cyclical sorption stability

As far as the list at the beginning of §1.3.2 is concerned, long-term cyclic stability is the issue raising the most relevant concerns about long-term CaO industrial utilization [63], since CO_2 sorption capacity of CaO undergoes a strong reduction with the increase of carbonation/calcination cycle number [100,104,107,108]. Moreover, the transition between the fast and slow regimes takes place at a level of CaO conversion which decreases when the number of carbonation/calcination cycles increases [108].

CaO sintering, i.e. the progressive agglomeration of its grains so to cause pore deformation and shrinkage (Figure 1.12), is recognized as the main cause of this sorption capacity drop [63,109].

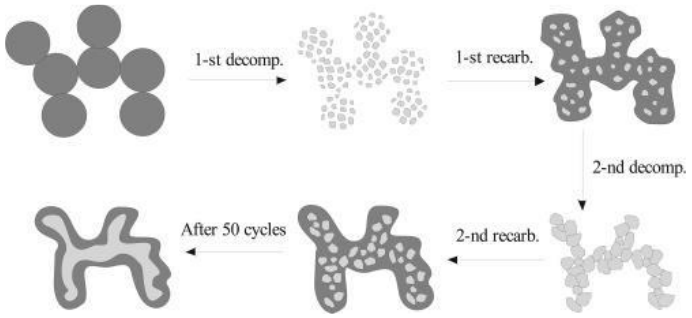

Figure 1.12: Representation of sintering phenomena in CaO (light grey) $CaCO_3$ (dark grey) system (picture from [109]*)*

Grasa and Abanades [108] measured by thermogravimetric analysis (TGA) limestone sorption capacity in many hundreds consecutive carbonation/calcination cycles, concluding that the decay of maximum CO_2 capture capacity is a feature not depending on limestone type; at atmospheric pressure, for temperatures lower than 950 °C, a dramatic decrease of capture capacity occurs in the first 20 cycles, after which a stable residual CaO conversions, equal to 7.5-8 %, is measured until cycle 500; for temperatures higher than 950 °C and/or extended calcination times a faster decay happens.

Sun et al. [110] performed similar measurements on limestone for more than 1000 cycles, reporting a stable residual non-zero CaO conversion after 150 cycles (4-17 %, depending on the carbonation time).

Dolomite shows better properties than limestone in the limitation of CaO sorption capacity decay: Silaban et al. [111] observed through 6 carbonation/calcination cycles a CaO conversion decrease in limestone from 61 % to 35 % and an immediate stabilization at 40 % for dolomite; Bandi et al. [112] performed 47 carbonation/calcination cycles on dolomite and calcite, finding a preservation of 55 % of initial capacity for dolomite and of 38 % for calcite. This behaviour is ascribed to MgO, acting as an inert phase at carbonation and calcination temperatures of CaO, therefore giving a higher structural stability [63].

Being established that natural CaO-based sorbent decay in multicyclic operation is inevitable, strategies for the improvement of CaO carbonation/calcination cyclical performances have been studied [63]:

- Choice of CaO sources: organometallic CaO precursors, especially calcium acetates, are reported to confer better CO_2 sorption properties than inorganic

precursors, in connection with the development of mesoporous and macroporous structures with higher specific surface areas, as experimentally proved in [113–115];

- CaO reactivation procedures: hydration in different steps of carbonation/calcination cycles has been investigated, the more relevant being steam introduction after CaO regeneration [63,116]; thermal pre-treatments (800-1300 °C) improve CaO capture capacity, also with self-activation throughout cycles, because of phenomena describable with a pore-skeleton model [63,117];
- Integration of inert stabilizers: following MgO positive effects in dolomite compared to lime, synthetic CaO-based sorbents integrated with inert materials have been studied, with the aim to distribute inert particles between CaO grains, preventing CaO sintering thanks to inert high Tammann temperature; examples of utilized inert materials are SiO_2 [118,119], ZrO_2 [120], MgO [121], TiO_2 [122], Y_2O_3 [123] and, above all, Al_2O_3 or calcium aluminates ($Ca_xAl_yO_z$); for the latter a thorough compendium can be found in [63], in which mayenite ($Ca_{12}Al_{14}O_{33}$) is indicated as the most employed.

1.3.2.3. Mayenite

Among several calcium aluminates (Figure 1.13) utilized as CaO stabilizers for multicycle carbonation/calcination operation, mayenite (noted as $C_{12}A_7$ in Figure 1.13) holds a predominant position.

Discovered as a rare natural mineral in 1964 near Mayen (Germany), this compound has been actually well known in concrete researches since the second decade of the 20th century [124,125]. Only in 1988 mayenite was reported as a surprisingly good oxygen ions conductor [126,127], arousing the interest for scientific applications. Mayenite has, indeed, peculiar structural properties: from the crystallographic point of view, it has a body centred cubic structure with cell parameter 11.99 Å; however, the chemical composition of its unit cell (Figure 1.14a) can be expressed as $[Ca_{12}Al_{14}O_{32}]_2O_2$«V»$_{10}$, where the first part in square brackets forms a rigid lattice framework with 12 cages, in which two extra-framework oxygen ions are randomly distributed (O_2), while the remaining 10 cages («V»$_{10}$) are vacant [124,128]. Extra-framework oxygen ions are weakly bonded to the crystal framework and their diameter smaller by ~50% than the diameter of cages, so that they can freely move through the crystal lattice, providing considerable oxide ion conductivity [124,129]. There are three possible oxygen migration mechanisms (Figure 1.14b) [127]:

a) Interstitialcy (exchange) mechanism: an extra-framework oxygen ion O_i" kicks a framework oxygen O_O^x into an empty cage V_i^x , taking its place in the framework; this mechanism has been experimentally proved to be the energetically favoured;
b) Interstitial (direct) mechanism: an extra-framework oxygen O_i" moves directly into a neighbouring empty site V_i^x through an opening in a cage wall caused by a perpendicular displacement of framework ions;

c) Vacancy mechanism: a framework oxygen O_O^x directly jumps into a framework vacancy $V_O^{\bullet\bullet}$.

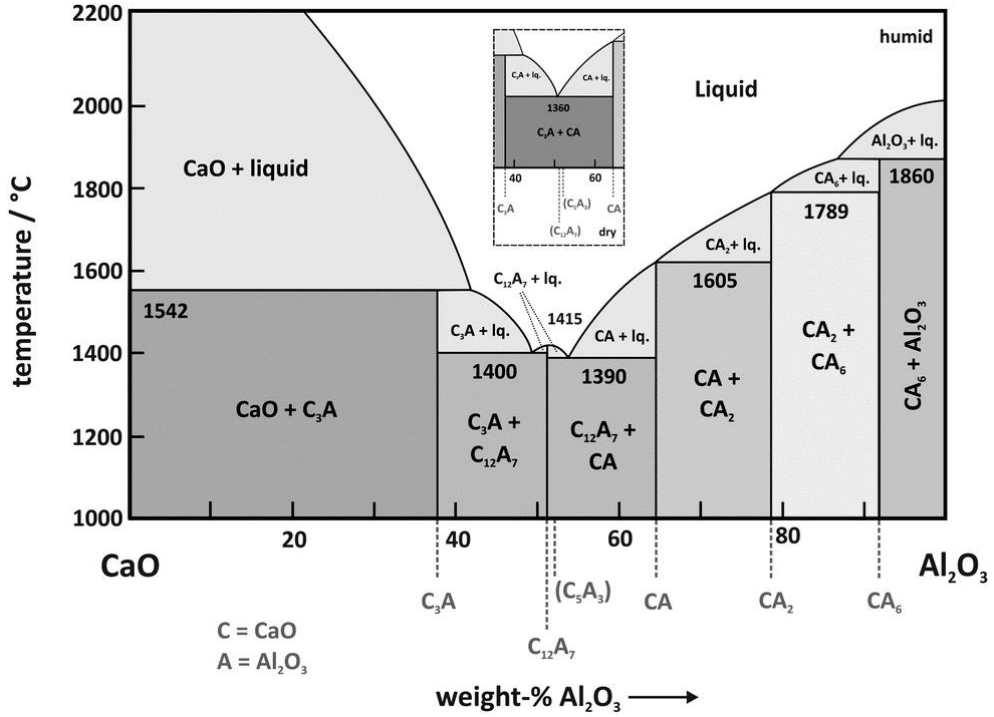

Figure 1.13: Calcium aluminate phase diagram for humid conditions; Inset: section of the phase diagram around the mayenite composition ($C_{12}A_7$) for dry condition; phases in brackets are considered as metastable [127]

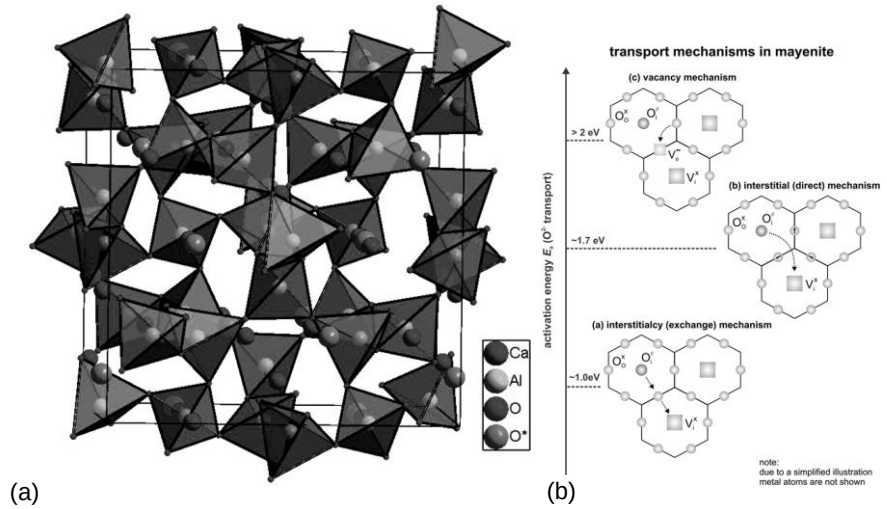

Figure 1.14: Representation of $[Ca_{12}Al_{14}O_{32}]_2O_2$«V»$_{10}$ unit cell (a), with cage cantered oxygen ions marked as O, and schematization of possible oxygen ions conduction mechanisms (b)* [127]

The presence of this "free oxygen" gives to mayenite special ion exchange properties, its defect chemistry being influenced by surrounding steam and gaseous oxygen partial pressures; moreover, the partial pressure of surrounding water vapour affects the stability of mayenite phase itself, as it has been found to be clearly not stable under dry conditions (< 100 ppm H_2O) at temperatures above 1050 °C, vanishing from the calcium aluminate phase diagram (insert of Figure 1.13) [127].

An application exploiting these "free oxygen" is Ni addition to form Ni-mayenite catalysts for tar reforming in biomass gasifiers [130,131]: mayenite was proven to avoid carbonaceous deposition on Ni, with the proposed explanation of a migration of superoxide radicals from mayenite towards Ni sites, to gasify the surface carbon deposed on metallic Ni to CO [130,132].

1.4 Sorption enhanced steam methane reforming

In order to start an effective transition towards a "hydrogen economy", it is crucial to get technical improvements in H_2 production, so to reduce its environmental footprint; however, this production must be kept economical, so that SMR and natural gas (§1.2.1) are still a relevant process and a strategic feedstock, which cannot be abandoned yet [55,133]. Moreover, IPCC evaluations emphasize the role of coupling fossil-fuels exploitation with CCS for an affordable containment of average global temperature to well below 2 °C above pre-industrial levels, the Paris agreement minimum target (§1.1.3 and §1.3).

For these reasons, a good candidate for the sustainable conversion of natural gas in high purity H_2 is the Sorption Enhanced Steam Methane Reforming (SESMR), a process intensification of traditional SMR (Reaction 1.1 and Reaction 1.2, §1.2.1) by means of in-situ CO_2 capture, carried out by a high-temperature solid sorbent (§1.3.2) [38,55,134,135]. In-situ CO2 sorption occurrence pushes WGS (Reaction 1.2) equilibrium, and then SMR (Reaction 1.1), towards supplementary H_2 production by subtracting CO_2 from the gaseous reaction phase, i.e. the so-called sorption enhancing (Figure 1.15) [60,63,136,137].

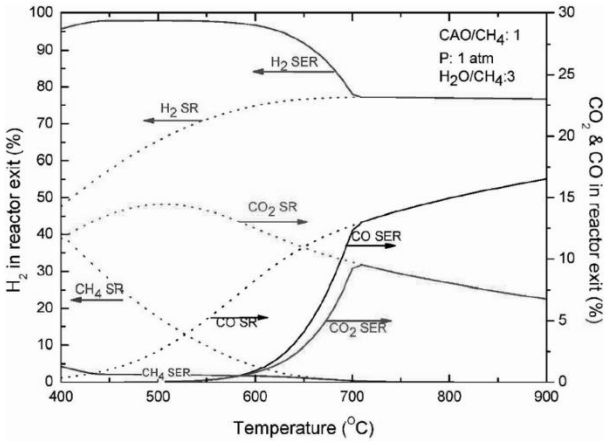

Figure 1.15: Simulation results for products of steam methane reforming (SR in figure) and sorption enhanced steam methane reforming (SER in figure), as a function of temperature; picture and simulative study from [137]

When the sorbent is saturated, or before its saturation as well, it is regenerated so to produce highly concentrated or pure CO_2, ready for other disposal strategies [78,138] or as a chemical feedstock (e.g. for synthesis of methanol or dimethyl ether [139,140]).

The complete SESMR process can be divided in three parts (Figure 1.16) [141,142]:

- pre-breakthrough, in which the sorbent is fully available to provide the in-situ CO_2 sorption (Reaction 1.5), simultaneously with SMR (Reaction 1.1) and WGS (Reaction 1.2), therefore increasing overall H_2 concentration beyond equilibrium levels of standard SMR;
- breakthrough, due to the progressive lack of sorption rate as a consequence of sorbent reaching its saturation, resulting in a transition towards the standard SMR;
- post-breakthrough, corresponding to the end of any relevant sorbent action, so that only catalytic SMR can occur.

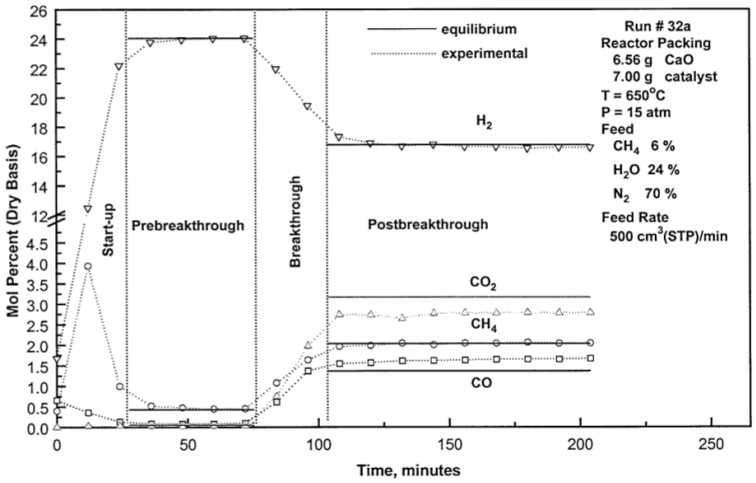

Figure 1.16: Typical breakthrough curve for a completely developed SESMR, picture from [141]

The chosen sorbents are usually CaO-based ones, as they assure (§1.3.2.1):

- satisfactory CO_2 sorption capacity and rate [96];
- carbonation (Reaction 1.5) at 600-700 °C and atmospheric pressure, conditions compatible with a simultaneous catalytic SMR conversion [143] and at which CaO is thermodynamically favoured in comparison to other high-temperature sorbents [144];
- calcination (reverse of Reaction 1.5) at atmospheric pressure and roughly 800-950 °C, depending on surrounding p_{CO2}, temperatures relatively close to those of carbonation (§1.3.2.1) [142,143].

From here onwards, SESMR is established as the set of Reaction 1.1, Reaction 1.2, Reaction 1.5. This process is still not developed in a commercial scale, nevertheless several researchers have been working on it to favour its development.

1.4.1 2-Material systems in literature

Different studies prove the feasibility of SESMR at laboratory or pilot scale by systems containing raw mixings of solo-catalyst and solo-sorbent particles (i.e. 2-material systems); some of them are summarized in the following, with corresponding experimental details in Table 1.3.

Table 1.3: Summary of different experimental conditions found in literature for 2-material systems

Catalyst	Sorbent	SESMR	Regeneration	Ref.
Ni-based commercial 1.5 g in packed-bed	CaO-mayenite (85:15 wt) 3-6 g in packed-bed	550-650 °C 11-44 ml min^{-1} CH_4 Steam/C = 3.4	/	[143]
Ni-$NiAl_2O_4$ (10 wt% (NiO)	CaO-$Ca_xAl_yO_z$ (90:10 wt)	600-700 °C 760 h^{-1} CH_4 30 cm^3 bed volume Steam/C = 1.6-5	/	[145]
Ni-based commercial	CaO-mayenite (85:15 wt)	650 °C 11 ml min^{-1} CH_4 25 ml min^{-1} He Steam/C = 3.4	850 °C He	[137]
Ni-based commercial 3 g in the packed-bed	CaO-mayenite (75:25 wt) 9 g in the packed-bed	630 °C 70 ml min^{-1} CH_4 Steam/C = 3	780 °C N_2	[146]
Ni-hydrotalcite 1.6 g in packed-bed	CaO-mayenite or limestone 6 g in packed-bed	550 °C 0.56 l min^{-1} total 10 vol% dry CH_4 in N_2 Steam/C = + 4	750 °C 0.8 l min^{-1} N_2	[37]
Ni-based commercial 2214 g in fluidized bed	Calcined dolomite 886 g in fluidized bed	600 °C Superficial velocity = 3.2 mm/s inlet: CH_4, steam Steam/C = 3	850 °C N_2	[147]

Martavaltzi et al. [143] tested mixtures of a commercial Ni-based catalyst and a synthetic CaO-mayenite sorbent in a packed-bed reactor at atmospheric pressure, varying temperature, CH_4 inlet flow and sorbent/catalyst ratio. They found 650 °C to be the optimal temperature for SESMR, measuring pre-breakthrough CH_4 conversion and H_2 concentration of 93-96 % and 93 vol% dry, diluent-free, respectively; furthermore, no significant variation of reactive performance occurred at 650 °C because of changing space velocity in the explored range, whereas the duration of the pre-breakthrough period was almost twice when the sorbent mass was doubled within the packed-bed, keeping constant the other operating parameters.

García-Lario et al. [145] tested at atmospheric pressure several mixings of purposely synthesized Ni-$NiAl_2O_4$ catalyst and CaO-calcium aluminate sorbent in a packed-bed reactor, finding 650 °C to be the optimal temperature for SESMR and 4 as the steam/C molar ratio to maximize CH_4 conversion and H_2 concentration (94 % and 96 vol% dry, diluent-free basis, respectively), with good performances at different catalyst/sorbent mass ratios from 1.6 to 6.2.

Martavaltzi et al. [137] tested in a packed-bed reactor at atmospheric pressure a mixing of a Ni-based commercial catalyst and a purposely synthesized CaO-mayenite sorbent for 13 consecutive SESMR/regeneration cycles. Pre-breakthrough H_2 concentration was slightly higher than 92 vol% for all cycles, with CH_4 conversions higher than 93 % and a moderate progressive decrease of sorption capacity.

Kim et al. [146] tested a mixture of a CaO-mayenite sorbent and a commercial Ni-based catalyst in a packed-bed facility at atmospheric pressure for 4 SESMR/regeneration cycles. H_2 concentration was around 95 vol% during the pre-breakthrough period, with no

significant variation in the shape of breakthrough curves, confirming the positive influence of mayenite in CaO stabilization throughout CO_2 capture/regeneration cycles.

Broda et al. [37] tested a Ni-hydrotalcite catalyst mixed with a synthetic CaO-mayenite sorbent or a natural limestone, in a packed-bed reactor at atmospheric pressure for 10 SESMR/calcination cycles, producing a stream of high-purity H_2 (99 vol % dry, diluent-free) and estimating a capture capacity in the synthetic sorbent equal to 46 g of CO_2 per 100 g of CaO after 10 cycles, which was more than double the value achieved by limestone.

Johnsen et al. [147] tested a mixture of commercial Ni-based catalyst and dolomite as a sorbent in an atmospheric-pressure bubbling fluidized bed reactor (10 cm diameter) operated batchwise for 4 SESMR/calcination cycles; H_2 concentration in pre-breakthrough is constantly 98-99 vol% dry in all cycles, but the breakthrough occurs earlier with cycle number increase because of dolomite sorption capacity drop.

1.4.2 Combined sorbent-catalyst materials in literature

In order to avoid inter-particle and intra-particle diffusivity resistances [101,146,148,149] and to allow a more intimate mutual coupling between endothermic and exothermic reactions, the concept of CSCM (Combined Sorbent Catalyst Materials), i.e. a single particle with both CO_2 sorption and SMR catalytic active phases, was proposed [134]. Furthermore, the use of CSCM instead of equivalent solo-catalyst plus solo-sorbent system, drastically reduces the total solid hold-up in the reactor [133], also avoiding the problem of synchronization of solo-sorbent and solo-catalyst lifetimes or of their separation for the removal from the reactor in the absence of this synchronization [146].

Table 1.4: Summary of different experimental conditions found in literature for CSCM

CSCM	SESMR	Regeneration	Ref.
Ni-CaO-mayenite (5 wt% of Ni) (75:25, 90:10, 100:0 in parent sorbent) 1 g in the packed-bed	650 °C 26 ml min^{-1} Ar 1 ml min^{-1} CH_4 Steam/C = 3	/	[150]
Ni-CaO (12.5 wt% of Ni) 0.8 g in the packed-bed	600 °C 50 ml min^{-1} total 10 ml min^{-1} CH_4 Steam/C = 3	/	[149]
Ni-CaO-mayenite (70 wt% of free CaO; 8, 11, 16, 20 wt% for Ni) 5 g in the packed-bed	650 °C 11 ml min^{-1} CH_4 25 ml min^{-1} He Steam/C = 3.4	/	[142]
Ni-CaO-mayenite (18.5 wt% of NiO) 0.5 g in the packed-bed	650 °C 500 h^{-1} CH_4 Steam/C = 3	875 °C, air + 650 °C, 10 vol% H_2	[151]
Ni-CaO-mayenite (3, 5, 7, 10 wt% of Ni) (75:25 wt in the parent sorbent) 12 g in the packed-bed	630 °C 70 ml min^{-1} CH_4 Steam/C = 3	780 °C N_2	[146]

In this framework, various syntheses for Ni-CaO-$Ca_xAl_yO_z$ CSCM and corresponding experimental performances are reported in literature, with some examples summarized in the following and in Table 1.4.

Cesário et al. [150] synthesizes Ni-CaO-mayenite CSCM by a wet impregnation of CaO-mayenite sorbents, prepared by a microwave assisted self-combustion method or a wet mixing method; the final content of Ni was 5 wt% for all materials, while parent sorbents had 90 wt% or 75 wt% of free CaO on mayenite; in addition, pure CaO was also impregnated with 5 wt% of Ni. They confirmed the positive influence of mayenite on CaO cyclical performances in CO_2 capture for both CaO-mayenite sorbents and Ni-CaO-mayenite CSCM, also noting an influence on Ni reducibility properties from different parent sorbent synthesis methods and CaO fractions. Best SESMR performance, at atmospheric pressure in a packed-bed micro-reactor, were achieved by the CSCM with the lower CaO excess content, derived from microwave method: 100 vol% dry, diluent-free of H_2 was detected in the pre-breakthrough products and a stable catalytic activity, with nearly total CH_4 conversion, was measured during the whole 15 h test; on the other hand, the higher the CaO fraction in CSCM, the higher the deactivation towards CH_4 conversion with time.

Chanburanasiri et al. [149] produced CSCM by incipient wet impregnation with Ni nitrate hexahydrate on CaO with several Ni loads (8 wt%, 10 wt% and 12.5 wt% of Ni), testing them for SESMR in a packed-bed reactor at atmospheric pressure. Ni load resulted as a key parameter to ensure reforming catalytic activity, reaching a pre-breakthrough H_2 concentration of 80 vol% only with the highest Ni/CaO ratio, progressively loosing CH_4 conversion in the other cases, therefore proving high sorbent quantity being useless in the absence of a sufficiently developed catalysis.

Martavaltzi and Lemonidou [142] synthesized several Ni-CaO-mayenite CSCM by a wet mixing method, nominally containing 70 wt% of free CaO, from 8 to 20 wt% of Ni and the rest being mayenite. In SESMR tests in packed-bed reactor at atmospheric pressure, the material with 16 wt% of Ni expressed the best performance, with pre-breakthrough H_2 concentration at about 90 vol% and CH_4 conversion at about 80 %; this last value, significantly lower than SESMR and SMR equilibrium conversion at the conditions tested experimentally, was related by the authors to the low affinity between Ni and CaO, resulting in worse catalytic properties than traditional Ni-based reforming catalysts supported on alumina.

García-Lario et al. [151] synthesized several Ni-CaO-calcium aluminates by a wet mixing method applied on powdery CaO derived from limestone calcination, NiO and commercial cement, varying the NiO/CaO ratio. Process thermal treatments made the cement result in mayenite, so to eventually get Ni-CaO-mayeinte CSCM. Their best CSCM, containing 18.5 wt% of NiO, was tested for 7 SESMR/regeneration/reduction cycles: pre-breakthrough H_2 concentration of about 90 vol% resulted for all cycles, but the increase of cycle number brought a slight decrease of pre-breakthrough step duration and a partial catalytic deactivation, even though Ni reduction was performed at the end of each cycle, as the post-breakthrough H_2 concentration became lower and lower with repeated cycles.

Kim et al. [146] synthesized by a wet mixing method Ni-CaO-mayenite CSCM, with several Ni fractions from 3 wt% to 10 wt%. They found all the Ni loadings to be active for 4 SESMR/regeneration cycles, with pre-breakthrough H_2 concentration always at around

95 vol%, with no significant variation of breakthrough durations. Anyway, they judged the 7 wt% of Ni as the most reliable CSCM, as it showed no fluctuation in CH_4 conversion (as for CSCM with 5 wt% and 3 wt% of Ni) or Ni agglomeration (as for CSCM with 10 wt%).

1.4.3 Process configuration

The inherent cyclical nature of SESMR process, due to sorbent saturation and regeneration, represents a significant feature influencing the configuration of a hypothetical continuous process on commercial scale.

Li et al. [152] successfully experimented the continuous production of H_2 via SESMR by two packed-beds operated in parallel (75:25 mass ratio between Ni-Al_2O_3 catalyst and CaO-mayenite), alternating feed and temperatures at constant atmospheric pressure to carry out Reaction 1.1, Reaction 1.2, and Reaction 1.5 in one reactor (SESMR), and reverse Reaction 1.5 in the other (calcination). Waldron et al. [153] used the same configuration to operate continuous H_2 production via SESMR, but using K_2CO_3 as a sorbent and applying a pressure swing as a regeneration strategy, keeping a unique constant temperature for both reactors.

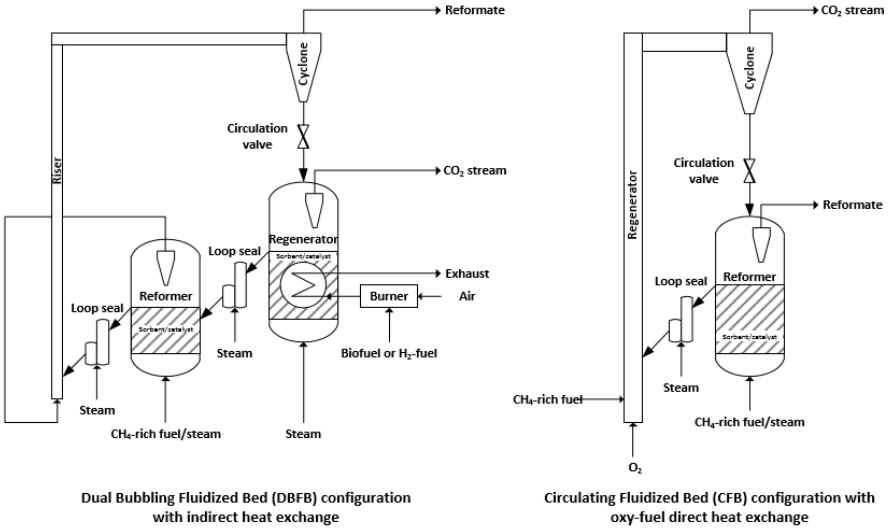

Figure 1.17: Representation of possible SESMR configurations based on the concept of solids circulation between two fluidized bed reactors [154]

Meyer et al. [154] proposed two configurations based on the concept of solids circulation between two fluidized-bed reactors operating in steady state, one serving as a reformer and the other as a calciner (Figure 1.17), also considering the issue of heat provision for the calcination step:

- in their Circulating Fluidized Bed (CFB) configuration the reformer is a Bubbling Fluidized-Bed (BFB) and the regenerator is an oxyfuel combustion riser;
- in their Dual Bubbling Fluidized-Bed (DBFB) configuration, heat in the calcination bed is provided by a submerged heat exchanger; design, realization

and trial of a DBFB prototype with a nominal H_2 production of 10 $Nm^3 h^{-1}$ is also presented in the same publication.

As far as the energetic aspects are concerned, the enthalpy compensation of Reaction 1.1, Reaction 1.2, and Reaction 1.5 results in a potential nearly autothermic process, so that CH_4 conversion by SESMR is less energy intensive than in standard SMR [38,155–157]. Moreover, from an exergetic point of view, SESMR and consequent heat-consuming sorbent regeneration are more advantageous than SMR and relative downstream purification processes (§1.2.1), needed to get the same H_2 yield [138,156].

Meyer et al. [158] evaluated, by an Aspen HYSYS® simulative study, the coupling of a DBFB system with a SOFC (§1.2.2), which is fed by produced high concentrated H_2 to yield power, and provides its high-temperature waste heat to the calciner by indirect heat exchange; power efficiencies close to 77 % with 100 % CO_2 capture could be obtained and a net present value (NPV) analysis (based on 8000 operating h $year^{-1}$, 25 years operation and 7.5 % interest rate) proves this technologies to be advantageous in comparison to a reference case counting conventional pre-combustion available technologies.

1.5 Research issues

On the basis of the literature survey presented so far, SESMR results worthy of research efforts, as much as possible oriented towards the development of the process at industrial scale. The European research project ASCENT (Advanced Solid Cycles for Novel Efficient technologies) [95] has met this request. It has been funded by European Union Seventh Framework Program FP7 (agreement n. 608512), it started in March 2014 and is scheduled to last for 48 months.

ASCENT aims to develop new low carbon power generation processes, improving energy efficiency associated to CO_2 capture, orienting researches to future commercial development. It involves 16 partners (European universities, research institutes, small and medium enterprises), from Italy, France, UK, Norway, Spain, Netherlands, Switzerland.

ASCENT studies three different decarbonized processes to produce H_2 as a fuel for high efficiency gas turbines and fuel cells:

- combined Ca-Cu chemical loop (work package 2);
- fast sorbent mediated WGS (work package 3);
- sorption enhanced reforming looping cycles (work package 4).

These processes share the concept of using a solid sorbent material for high temperature CO_2 removal simultaneously with the conversion of other carbon-containing gases into H_2. The high-temperature (> 300 °C) CO_2 capture can increase energy efficiency because of a better heat integration, in comparison to current low temperature capture technologies.

ASCENT lead technical objective for each of the three technologies is to provide a robust proof-of-concept with industrially relevant conditions and materials at a scale where a platform for future demonstration is established.

University of L'Aquila, as a partner of ASCENT in the work package 4, has been involved in researches about SESMR. This PhD thesis, in co-tutelle between University of L'Aquila and University of Strasbourg, describes the share of contributions to the work package 4 from these two institutions, dealing with synthesis, characterization and study for industrial applicability of Ni-CaO-mayenite CSCM for SESMR. Tasks of work package 4, together with the planned co-tutelle PhD activities, also include SESMR mathematical modelling study and experimental tests on materials developed by other ASCENT partners; results and methodologies described in this thesis were used for the achievement of these additional tasks too, as described in Addenda and scientific publications mentioned there. Specific issues faced in the related research work are summarized in the following.

1.5.1 Ni fraction

As already stated in §1.2.1, metallic Ni is the catalytic active phase of choice for SMR, and the same results about SESMR are revealed from §1.4.1 and §1.4.2.

What clearly emerges from §1.4.2 is the influence of Ni fraction on materials catalytic activity, in some cases with an optimum for CSCM, so that this parameter must be certainly considered.

1.5.2 Ni salt precursor

An additional interesting feature, noted during the writing up of §1.4.1 and §1.4.2, is that Ni nitrate hexahydrate is always the chosen Ni salt precursor for purposely synthesized SMR catalysts or CSCM. In fact, for transition metals ranging from Mn to Zn, metal nitrates are generally selected as precursors, since they are generally available and cheap, highly soluble in water (more than 4 mol l^{-1}), and decompose at moderate temperatures (below 300 °C) [159].

Nevertheless, literature shows that different properties and catalytic performances can result, being equal all other parameters, only because of a change of the Ni salt precursor.

Estellé et al. [160] produced NiO by thermal decomposition of Ni nitrate hexahydrate, Ni hydroxide and Ni acetate tetrahydrate: in the first case, highly crystalline NiO with octahedral structures was obtained; in the second, a more amorphous NiO resulted; in the third, together with crystalline NiO, metallic Ni was developed too, because of CO and H_2 developing during acetate decomposition.

Ren et al. [161] demonstrated Ni/γ-Al_2O_3 catalysts derived from Ni acetate to be much more active than Ni nitrate derived ones in the hydrogenation of α-pirene, being equal their Ni fraction; moreover, the former were more easily reducible than the latter thanks to a higher Ni^{2+} positioning in γ-Al_2O_3 octahedral sites rather than tetrahedral ones.

Wu et al. [162] synthesized 15 wt% of Ni catalysts for glycerol steam reforming, by wet impregnation of commercial γ-Al_2O_3 using Ni nitrate, Ni chloride, Ni acetate and Ni acetylacetonate as precursors. Acetate derived catalysts showed the best performances in terms of catalytic activity and H_2 yield, with the lower quantity of deposited carbon.

All this considered, effects of Ni acetate tetrahydrate and Ni nitrate hexahydrate as Ni precursors are going to be studied in this thesis.

1.5.3 CaO influence on Ni

Some influences on Ni properties from CaO have emerged from §1.4.2.

The use of alkali and alkali earths as dopants on Ni-based reforming catalysts, to avoid solid carbon deposition, is well known [61], however there is a lack of information about Ca-doping in literature.

Dias and Assaf [163] studied effects of CaO doping on Ni/γ-Al_2O_3 catalysts for dry reforming of CH_4. They found an optimum dose of CaO at about 3 wt%, which maximized catalytic activity, with an abrupt worsening of CH_4 conversion due to a small increase up to 7 wt% of CaO, being all other parameters equal. They attributed this effect to the increased electron density around active metallic Ni particles due to Ca, affecting its ability to adsorb CH_4 which is related to a Ni electron deficiency.

Similar results were determined by Choong et al. [164], in the different context of ethanol steam reforming on Ni/γ-Al_2O_3 catalysts doped with Ca. An optimum of catalytic performances was found by doping their catalyst with 3 wt% of Ca, while dosages of 7 wt% and 10 wt% of Ca caused deactivation, the more dramatic the higher the Ca content. By valence-band photoelectron spectra, they related this effect to a valence electronic enhancement of Ni surface atoms in their 3d orbitals, due to Ca.

These findings, even though coming from studies on processes other than SMR, suggest a detrimental role of CaO on metallic Ni activity, so that effects on SESMR from the dosage of these two phases must be investigated, especially for CSCM.

1.5.4 Industrial applicability

In this thesis, some important aspects related to industrial applicability of CSCM are considered, with reference to both CO_2 capture and catalytic activity, on one side, and the effect of attrition (envisaging utilization in fluidized bed reactors), on the other side. Aspects beyond material properties, such as process and plant design, which are equally important in order to perform global techno-economic analyses, are not studied.

With the aim of a continuous H_2 production via SESMR (§1.4.3), the cyclical stability of CaO and Ni respective functions is a crucial aspect to be studied: materials suitable for industrial applications should assure a long lifetime, which turns into acceptable performances for a high number of SESMR/regeneration cycles. As a matter of fact, literature examined in §1.4 goes in this direction, as well as this thesis does.

With regard to industrial applicability, another interesting feature is the regeneration procedure. Realistic regeneration conditions should involve high CO_2 concentrations, so to favour downstream CCS strategies by a sufficiently high CO_2 fraction; this means that dilution permanent gases should be avoided in the sorbent regeneration step. On the other hand, the use of steam as a diluent for CO_2 in the sorbent regeneration step could decrease p_{CO2} (allowing a lower calcination temperature), with the drawback of an additional energy demand related to steam separation from CO_2 by condensation and its production by evaporation. In addition, it is advantageous to operate close to atmospheric pressure, so to contain as much as possible within acceptable values the calcination temperature (Figure

1.11) [114], therefore protecting active materials from further sintering. This brings additional issues:

- CaO-based sorbents have a more dramatic decrease of CO_2 sorption capacity in these relevant conditions, compared to milder one (low or null CO_2 concentration, lower temperatures) [63,114];
- Higher temperature may determine Ni sintering [165];
- CO_2 in the regeneration step is supposed to partially re-oxidize metallic Ni to NiO, negatively affecting catalytic activity and collaterally forming CO [166]; as a matter of fact, as Ni is a highly oxophilic metal which favours CO_2 dissociation to CO [167].

Therefore, effects of more realistic regeneration conditions are going to be examined.

As far as the application in fluidized beds is concerned, another important feature to be taken into account is the mechanical resistance of SESMR materials to attrition. The main consequence of attrition is the generation of fines eventually passing through the dust recovery system, then causing a loss of valuable material; main attrition sources in a system with solid recirculation, as the one hypothesized for SESMR (§1.4.3), are bottom grid jets, bubbles within the bed and cyclones/solid recovery facilities, the first being more important at lower superficial velocities, the third at higher velocities because of solid entrainment [168]. This aspect is investigated in the thesis too.

1.6 Thesis outline

Research issues are tackled in the next chapters of this manuscript, organized as follows:

- Chapter 2 “Materials and methods”, describing materials synthesis procedures, employed characterization techniques, as well as experimental test rigs and data elaboration methodologies used in microreactor scale and for the studies about industrial applicability;
- Chapter 3 “As-synthesized materials”, summarizing all results from characterization of synthesized Ni-mayenite SMR catalysts, CaO-mayenite CO_2 sorbents and Ni-CaO-mayenite CSCM for SESMR;
- Chapter 4 “Reactivity tests”, presenting all experimental results collected by reforming tests in the packed-bed microreactor rig on Ni-mayenite materials, 2-material systems made of Ni-mayenite and CaO-mayenite, and Ni-CaO-mayenite CSCM, also with post-test characterizations;
- Chapter 5 “Study for industrial applicability”, in which stability in multicycle SESMR/reaeration and resistance to attrition are verified for the most promising materials, selected by evidences from Chapter 4;
- General conclusions, containing a general sum up about main results achieved, points needing more efforts and suggestions for the future work;

- Addendum A "Other materials in the ASCENT project", reporting results from multicycle SESMR/regeneration tests performed at University of L'Aquila on CSCM developed by other work package 4 partners;
- Addendum B "Validation of SESMR models", underlining the contribution from data and results collected in the course of this thesis work to SESMR mathematical modelling, another duty of University of L'Aquila in the work package 4.

Chapter 2

Materials and methods

This chapter details the techniques employed to produce information and data collected in this thesis. Four main subject areas are developed:

- *Materials synthesis;*
- *Characterization methods;*
- *Procedures of experimental study in microreactor scale;*
- *Procedures for industrial applicability study.*

2.1 Materials synthesis

As far as CaO-based sorbent are concerned, several synthesis methods are described in scientific literature, including hydration/calcination [169], coprecipitation [170], mixed precipitation [171], mechanical mixing [172], sol-gel process [173], assisted self-combustion [150]. With regard to Ni addition, available methods include wet impregnation [150], incipient wetness impregnation [149], hydration/calcination [142,151], sol-gel process [174].

Wet mixing and wet impregnation, as described in Di Giuliano et al. [133], are the methods employed to synthesize materials studied in this thesis; in the framework of the ASCENT process, these methods are considered particularly suitable for a potential industrial scale-up, as they require only thermal treatments under air at atmospheric pressure and the use of water as the unique solvent in wet steps. From here on, their names are shortened as WM and WI, respectively.

WM is the starting point shared by all kind of materials. It is a modification of the method described by Zamboni et al. [175], which is in turn a modification of a method previously published by Li et al. [5]. Its goal is the production of a nominally solo-mayenite support or CaO-mayenite sorbents, depending on the molar Ca/Al ratio of the masses of respective precursor salts: 6/7 corresponds to nominal composition of solo-mayenite, while

values higher than 6/7 lead to the formation of CaO-mayenite sorbents. A proper tuning of this parameter allows to regulate sorbents' nominal free CaO fraction.

WI is the second part of the procedure and is applied on WM products with the aim of adding the reforming catalytic active phase on them. It is a modification of the method described by D'Orazio et al. [176] and by Micheli [177]. Its application on solo-mayenite produces a Ni-mayenite catalyst for SMR, whereas on CaO-mayenite yields Ni-CaO-mayenite CSCM. The ratio of Ni precursor mass to that of solid to be impregnated controls the desired Ni fraction in the final product.

2.1.1 Wet mixing

Employed precursor salts are $Ca(CH_3COO)_2 \cdot xH_2O$ (ACROS ORGANICS, purity = 99 %, x experimentally determined by TGA) for calcium and $Al(NO_3)_3 \cdot 9H_2O$ (SIGMA-ALDRICH, purity > 98 %) for aluminium.

WM steps are:

1. Calcination of $Ca(CH_3COO)_2 \cdot xH_2O$ to obtain CaO, by a 3 °C min^{-1} heating ramp up to 750 °C and a 4 h dwell at 750 °C;
2. Solubilization of $Al(NO_3)_3 \cdot 9H_2O$ in stirred distilled water and addition of CaO powder in this solution. The initial volume of the whole mixing is 10 ml per gram of desired product, to be halved by stirring and heating at 70 °C;
3. Drying of resulting slurry for 12 h at 120 °C;
4. Calcination of dried solid by a 3 °C min^{-1} heating ramp up to 750 °C and a 4 h dwell at 750 °C;
5. Hydration of calcined solid, reduced in granules of millimetre order, by manual crushing in a mortar (1 ml of distilled water per gram of solid);
6. Drying of hydrated solid for 12 h at 120 °C;
7. Calcination of dried solid by a 3 °C min^{-1} heating up to 900 °C and a 1.5 h dwell at 900 °C.

2.1.2 Wet impregnation

Ni precursor salts are $Ni(NO_3)_2 \cdot 6H_2O$ (SIGMA-ALDRICH, purity > 97 %) or $Ni(CH_3COO)_2 \cdot 4H_2O$ (ALFA AESAR, purity 98 %); from here on they are shortened by the notations Ni(N) and Ni(Ac), respectively.

WI steps are:

1. Solubilization of Ni(N) or Ni(Ac) in stirred distilled water and then addition in this solution of granular WM product (particle dimension in the order of the millimetre). The initial volume of this mixing is 10 ml per gram of desired product, to be halved by stirring and heating at 70 °C;
2. Drying of resulting slurry for 12 h at 120 °C;
3. Calcination of dried solid by a 3 °C min^{-1} heating ramp up to 900 °C and a 4 h dwell at 900 °C.

2.1.3 Nomenclature and list of materials

Table 2.1 lists all materials synthesized in the course of this thesis, with their nominal compositions. From here on, the following nomenclature applies for their identification:

- WM products are named as *CaOx*, where *x* is the nominal weight percentage of free CaO associated to mayenite (e.g. CaO0 is nominally solo-mayenite, CaO30 is nominally composed by 30 wt% of free CaO and 70 wt% of mayenite);
- WI products are named as *CaOxNi(Y)z*, where: *CaOx* is the starting parent material resulted from WM; *Y* specifies the precursor salt from which Ni arises, "N" for Ni(N) or "Ac" for Ni(Ac); *z* quantifies the nominal weight percentage of metallic Ni in the final reduced product.

Table 2.1: List of synthesized materials

Name	Nominal phases	Function	Nominal free CaO* [wt%]	Nominal Ni [wt%]
CaO0	mayenite	inert	0	0
CaO0Ni(N)3	Ni-mayneite	SMR catalyst	0	3
CaO0Ni(N)4.5	Ni-mayneite	SMR catalyst	0	4.5
CaO0Ni(N)6	Ni-mayneite	SMR catalyst	0	6
CaO0Ni(N)10	Ni-mayneite	SMR catalyst	0	10
CaO0Ni(Ac)3	Ni-mayneite	SMR catalyst	0	3
CaO0Ni(Ac)4.5	Ni-mayneite	SMR catalyst	0	4.5
CaO0Ni(Ac)6	Ni-mayneite	SMR catalyst	0	6
CaO0Ni(Ac)10	Ni-mayneite	SMR catalyst	0	10
CaO15	CaO-mayenite	CO_2 sorbent	15	0
CaO15Ni(N)3	Ni-CaO-mayenite	CSCM	15	3
CaO15Ni(N)10	Ni-CaO-mayenite	CSCM	14	10
CaO15Ni(Ac)3	Ni-CaO-mayenite	CSCM	15	3
CaO15Ni(Ac)10	Ni-CaO-mayenite	CSCM	14	10
CaO30	CaO-mayenite	CO_2 sorbent	30	0
CaO30Ni(N)3	Ni-CaO-mayenite	CSCM	29	3
CaO30Ni(N)10	Ni-CaO-mayenite	CSCM	27	10
CaO30Ni(Ac)3	Ni-CaO-mayenite	CSCM	29	3
CaO45	CaO-mayenite	CO_2 sorbent	45	0
CaO45Ni(N)3	Ni-CaO-mayenite	CSCM	44	3
CaO45Ni(Ac)3	Ni-CaO-mayenite	CSCM	44	3
CaO54	CaO-mayenite	CO_2 sorbent	54	0
CaO54Ni(N)3	Ni-CaO-mayenite	CSCM	52	3
CaO54Ni(N)10	Ni-CaO-mayenite	CSCM	49	10
CaO54Ni(Ac)3	Ni-CaO-mayenite	CSCM	52	3
CaO54Ni(Ac)10	Ni-CaO-mayenite	CSCM	49	10

*for the CSCM named *CaOxNi(Y)z* : $Nominal\ free\ CaO\ = x \times (1 - z/100)$

2.2 Characterization methods

Characterization of synthesized materials consists in the application of:

- ICP-AES (Inductively Coupled Plasma - Atomic Emission Spectroscopy) for calcium, aluminium and Ni elemental composition;
- XRD (X-Ray Diffraction) for crystalline phase investigation;

- BET (Brunauer-Emmett-Teller) multipoint method for surface area quantification [178];
- BJH (Barrett-Joyner-Halenda) method for mesopores assessment [179];
- SEM (Scanning Electron Microscopy) and TEM (Transmission Electron Microscopy) both combined with EDS (Energy Dispersive X-ray Spectrometry) for morphological and topographic observations;
- TPR (Temperature Programmed Reduction) to study samples' reducibility;
- TGA (Thermo-Gravimetric Analysis) for CO_2 sorption properties.

2.2.1 Atomic emission spectroscopy

Samples elemental mass percentages of Ca, Al and Ni are detected by a VARIAN 720-ES ICP-AES. Solid samples are decomposed in a concentrated strong acid, then diluted in deionized water, so to be ready for nebulization operated by the device.

2.2.2 X-ray diffraction

XRD spectra are recorded by an X-ray diffractometer BRUCKNER AXS D8 ADVANCED, using CuKα_1 radiation to detect crystalline phases, with a Bragg-Brentano geometry.

Powdery samples (particle diameter < 100 μm) are horizontally distributed on the central zone of a quartz disc-shaped sample holder, so to form a thin layer, then flattened by the downwards pressure of a second disc-shaped sample holder. This preparation method is completely dry, so to hold back potential CaO conversion to $Ca(OH)_2$.

XRD spectra are recorded in a Bragg angle (2θ) range from 20 ° to 70 °, with a 0.0158 ° scanning step and a sampling time of 1 s per step. Phase identification is performed in the proprietary software environment EVA, by comparison with PDF (Powder Diffraction Files) listed in Table 2.2, from the database of the ICDD (International Centre of Diffraction Data), formerly known as JCPDS (Joint Committee on Powder Diffraction Standards).

Table 2.2: PDF (Powder Diffraction Files) employed for crystalline phase identification in XRD, with 2θ *chosen for* L *calculations by Scherrer equation (Equation 2.1)*

Number	Name	Formula	Lattice system	Bravais lattice	2θ for L [°]
00-009-0413	Mayenite	$Ca_{12}Al_{14}O_{33}$	Cubic	Body-centred	33 ÷ 34
00-037-1497	Lime	CaO	Cubic	Face-centred	32 ÷ 33
00-005-0586	Calcite	$CaCO_3$	Rhombohedral	Primitive	29 ÷ 30
00-044-1481	Portlandite	$Ca(OH)_2$	Hexagonal	Primitive	/
01-070-0134	Calcium aluminium oxide	$CaAl_2O_4$	Monocline	Primitive	/
00-038-1429	Calcium aluminium oxide	$Ca_3Al_2O_6$	Cubic	Primitive	/
00-023-1037	Grossite	$CaAl_4O_7$	Monoclinic	Base-centred	/
00-047-1049	Bunsenite	NiO	Cubic	Face-centred	43 ÷ 44
03-065-2865	Nickel	Ni	Cubic	Face-centred	44 ÷ 45
00-010-0339	Nickel aluminium oxide	$NiAl_2O_4$	Cubic	Face-centred	/

Acquired spectra are also used for the estimation of average crystallite sizes (L) of main detected phases, by Scherrer equation [180,181] (Equation 2.1).

$$L = \frac{K\,\lambda}{\beta\,\cos(2\theta/2)} \qquad \textit{Equation 2.1}$$

Constants K and λ (wavelength of CuKα_1 radiation) are set equal to 0.9 and 0.15406 nm, respectively. FWHM (Full Width at Half Maximum, β, in radian) and Bragg angle (2θ, in radian) at ray's maximum are measured on diffraction rays such that minimum or any overlapping occurs with other ones. The estimation of these quantities is operated by the manual tool "Area" in the software environment EVA. For each detected crystalline phase, the referred ray for L calculation has the same 2θ position in all analysed samples, chosen so to ensure the lowest overlap with rays of other phases (Table 2.2); in the case of Ni and NiO, a partial overlap with a secondary peak of $Ca_{12}Al_{14}O_{33}$ at 44 °, lowers the reliability of corresponding L estimates, especially for nominal Ni fractions lower than 4.5 wt%.

2.2.3 Surface area and porosity analysis

A MICROMERITICS ASAP 2420 surface area and porosity analyser records N_2 adsorption and desorption isotherms at -196 °C, performing calculations after BET and BJH methods by ASAP 2420 software v2.09. Samples consist of 100-200 mg of powder (particle diameter in the range from 100 µm to 125 µm), previously degassed in high vacuum, with a 10 °C min^{-1} heating ramp until 250 °C and a dwell at this temperature for 8 h at least.

Considered measures are BET surface area (S_{BET}), BJH cumulative pore volumes (V_{BJH}), BJH pore volume distributions with respect to pore sizes, and BJH averaged cylindrical pore diameter ($D_{av,BJH}$).

N_2 desorption data are recommended for BJH mesoporosity assessment (V_{BJH} and $D_{av,BJH}$), as they are representative of a reversible liquid-vapor transition in the case of capillary condensed molecules typical of mesopores [182–185].

2.2.4 Scanning electron microscopy

SEM micrographs are recoded by a PHILIPS XL30CP device. Operative conditions are: high tension at 20 kV, detector in BSE (Back Scattering Electron) Z-contrast mode, and vacuum in control-pressure mode.

Samples in the form of powder are observed on their external surface. Moreover, powders are embedded in Buehler Epoxycure bi-component epoxy resin and polished with diamond suspensions, for internal cross-sectional area observations. In both sample forms, a gold thin layer is deposed on the surface by sputtering.

For elemental analyses by in-situ EDS, the SEM PHILIPS XL30CP is equipped with an OXFORD ENERGY 250 INCAx-act LN2-free detector. For powder samples, EDS spectra are acquired on spots or zones of external surfaces: peak intensities of detected

elements allow qualitative speculations about elemental distribution, in terms of molar ratios. For embedded samples, EDS maps are acquired on internal cross-sectional areas, providing elemental topography. Because of gold deposition by sputtering, elemental Au is detected by EDS even though originally absent in materials.

2.2.5 Transmission electron microscopy

TEM micrographs are acquired by a JEOL 2100 LaB_6 (lanthanum hexaboride filament) operating at 200 kV, with a punctual resolution equal to 0.2 nm in parallel mode and 2-3 nm in STEM (Scanning Transmission Electron Microscopy) mode, equipped with a SDD detector (30 mm^2) for elemental analysis by in-situ EDS.

About 10 mg of powdery samples are firstly ultrasonicated for 5 min in 50 ml of ethanol, so to obtain a suspension, 3 or 4 drops of which impregnate the sample-holder (a polymeric membrane sustained by a copper grid). After ethanol natural evaporation, sonicated particles result dispersed on the membrane.

Because of the sample-sample older, elemental C and Cu easily appears in STEM-EDS elemental analyses as contaminant agents, unless one can isolate a portion to be analysed which clearly hangs in a membrane void hole.

2.2.6 Temperature programmed reduction

A MICROMERITICS AUTOCHEM II 2920 chemisorption analyser performs TPR.

The sample, 100 mg of a powder with particle diameter in the range from 100 µm to 125 µm, is placed between two quartz wool flocks in a fused quartz Flow-Thru sample tube (9 mm internal diameter), so to form a packed bed. This reaction cell is placed inside a furnace controlled by an internal thermocouple.

Before the actual TPR, a TPD (Temperature Programmed Desorption) is operated, so to clean adsorbed gases and decompose contingent $CaCO_3$ or $Ca(OH)_2$ in the sample, due to room atmosphere exposure. TPD steps are a 15 °C min^{-1} heating ramp up to 750 °C, a 30 min dwell at 750 °C and a cooling down to room temperature, all under an Ar stream of 50 Nml min^{-1}. After that, actual TPR starts, with a 15 °C min^{-1} heating ramp up to 1000 °C and a 30 min dwell at 1000 °C, under a 50 Nml min^{-1} reductive stream (10 vol% of H_2 in Ar).

Downstream the reaction cell, a TCD (Thermal Conductibility Detector) measures H_2 consumption, then recorded together with process temperature as a function of time and stored by AUTOCHEM II software v4.02.

2.2.7 Thermogravimetric analysis

A LINSEIS STA PT1000 device, equipped with alumina crucibles, performs TGA to quantify the maximum CO_2 sorption capacity of CaO-mayenite sorbents and CSCM.

Firstly, the sample (30-40 mg, particle diameter in the range from 38 µm to 100 µm) undergoes a preliminary cleaning treatment, counting a 10 °C min^{-1} heating ramp up to 800 °C, a 30 min dwell at 800 °C and a cooling down to 650 °C, all under 142 Nml min^{-1}

of N_2, with the same purpose of TPD described in §2.2.6. Afterwards, the sample stays for 7 h at 650 °C under 167 Nml min^{-1} of a gaseous stream containing 15 vol% of CO_2 in N_2. This duration is assumed to be sufficient to convert all the available CaO in $CaCO_3$ (Reaction 1.5). The same test is carried out on empty crucibles, to record disturbances and apparent mass changes related to flow and temperature variations; the so obtained blank is subtracted from the homologue sample CO_2 capture curves with respect to time, so to correct them.

The corrected mass increase measured during these 7 h (Δm), with respect to sample mass at the end of cleaning treatment (m_0), allows to calculate the experimental maximum CO_2 sorption capacity (Γ_{CO2}), expressed as grams of captured CO_2 per 100 g of calcined tested material (Equation 2.2).

$$\Gamma_{CO_2} = \frac{\Delta m}{m_0} 100 \qquad \textit{Equation 2.2}$$

Furthermore, multicycle CO_2 capture/regeneration tests are performed for a selected group of materials by a LINSEIS L81 device for TGA. Sample preparation and preliminary cleaning are the same described just above, except the sample mass of about 100 mg. Process conditions for CO_2 capture (Reaction 1.5) are also the same, just varying the step duration from 7 h to 30 min. Additionally, the sample undergoes a regeneration (reverse of Reaction 1.5), starting from 650 °C, by the same heating ramp, dwell and cooling used in the preliminary treatment. The alternation between CO_2 capture steps and regenerations is carried out 50 times. For the generic i^{th} cycle, captured CO_2 ($\gamma_{CO2}^{(i)}$) is estimated from the measured mass increase during the 30 min CO_2 capture session ($\Delta m^{(i)}$), with respect to the mass at the end of the preceding regeneration ($m^{(i)}$).

$$\gamma_{CO_2}^{(i)} = \frac{\Delta m^{(i)}}{m_0^{(i)}} 100 \qquad \textit{Equation 2.3}$$

The 50^{th} cycle ends with the CO_2 capture step, in order to obtain a carbonated sample for further evaluations.

2.3 Reforming tests in microreactor

Figure 2.1 schematizes the microreactor scale experimental apparatus for reforming reactivity tests. Atmospheric pressure in the apparatus, net of pressure drops, is a constant condition for all tests.

A cylindrical packed bed quartz reactor (internal diameter 7 mm) contains the powdery sample (particle diameter from 100 µm to 125 µm) supported by quartz wool. Reactor heating is provided by a cylindrical furnace, managed by a MINICOR CORECI ND 51-81 automatic control system, associated with a thermocouple located inside the granular packed bed.

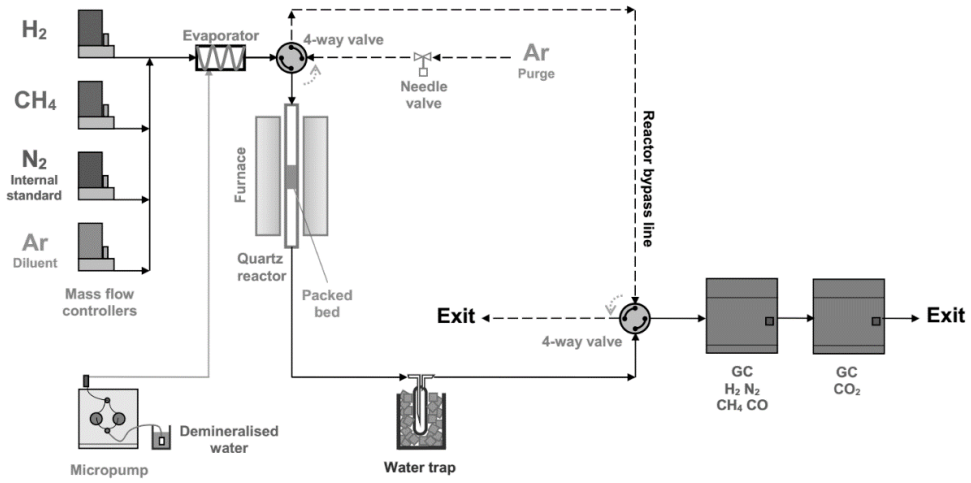

Figure 2.1: Schematic view of microreactor scale packed bed experimental apparatus for reforming reactivity tests

Two feeding lines access the reactor or its bypass by means of a 4-way valve. The purge line feeds Ar, its flowrate fixed by a manual needle valve. The reaction line provides H_2, CH_4, N_2 (internal standard), Ar (diluent) and steam. Mass flow controllers regulate inlet flowrates of permanent gases. A micropump GILSON 350, managed by UniPointLC Software v5.11, controls the volumetric flowrate of liquid demineralised water, directed to an evaporation chamber at 260 °C, where generated steam and other reaction line gases mix together.

Downstream the reactor, an ice-cooled water trap serves as a condenser, separating unreacted water from other gaseous products. A second 4-way valve receives them and the reactor bypass line, sending each stream straight to final exit or towards the analytical system for gas composition. This counts two GC (Gas Chromatographs) in series:

- The first is an AGILENT 7890A, equipped for H_2, N_2, CH_4, CO separation and detection with a molecular sieve capillary column (stationary phase: HP-PLOT molesieve, Ar as carrier) and a TCD; data acquisition and integration of corresponding chromatographic peaks is automatically performed by the proprietary software GC Chemstation Rev.B.04.03;
- The second is a DELSI INSTRUMENT Di200, equipped for CO_2 separation and detection with a metal packed column containing a polymeric matrix (stationary phase: HayeSep® Q, He as carrier) and a TCD; data acquisition and integration of corresponding chromatographic peak is automatically performed by the software Winlab III.

On-line sampling and injections for the two GC are automatized and synchronized, with a frequency of one injection every 5 min.

GC calibrations are periodically updated to provide the mathematical relationship between areas of measured chromatographic peaks and corresponding species concentrations ($c^{GC}_{i,out}$). Products molar flowrates ($F_{i,out}$) are calculated by means of these

concentrations, assuming N_2 as the internal standard (Equation 2.4), i.e. considering its molar flowrate ($F_{N2,in}$) to be unchanged throughout the whole process.

$$F_{i,out} = \frac{{c^{GC}}_{i,out}}{{c^{GC}}_{N_2,out}} F_{N_2,in} \quad ; \quad i = CH_4, H_2, CO, CO_2 \qquad \textit{Equation 2.4}$$

Equation 2.5 and Equation 2.6 define WHSV (Weight Hourly Space Velocity) and Ni-WHSV (Nickel Weight Hourly Space Velocity) as univocal parameters to express reaction conditions, depending on CH_4 inlet molar flowrate ($F_{CH4,in}$), sample mass (m) and its Ni percentage (ω_{Ni}). If the assumed ω_{Ni} is nominal, Equation 2.6 results is called "Nominal Ni-WHSV"; if ω_{Ni} is the one measured by ICP-AES (§2.2.1), Equation 2.6 result is the "Actual NI-WHSV".

$$WHSV = \frac{F_{CH_4,in}}{m} \qquad \textit{Equation 2.5}$$

$$Ni\text{-}WHSV = \frac{F_{CH_4,in}}{m \cdot (\omega_{Ni}/100)} \qquad \textit{Equation 2.6}$$

Performance of SMR catalysts and CSCM are evaluated by CH_4 conversion (χ_{CH4}, Equation 2.7) and products percentage on dry and inert-free basis ($C_{i,out}$, Equation 2.8).

$$\chi_{CH_4} = \frac{F_{CH_4,in} - F_{CH_4,out}}{F_{CH_4,in}} \cdot 100 \qquad \textit{Equation 2.7}$$

$$C_{i,out} = \frac{F_{i,out}}{\sum_j F_{i,out}} \cdot 100 \quad ; \quad i,j = CH_4, H_2, CO, CO_2 \qquad \textit{Equation 2.8}$$

2.3.1 Reforming on Ni-mayenite

The sample mass is 500 mg. Firstly, a pre-reduction is necessary since NiO in the as-synthesized sample must be converted in metallic Ni, the active phase for steam reforming catalysis. Pre-reduction counts a 10 °C min^{-1} heating ramp up to 900 °C and a 1 h dwell at this temperature, under 2.8 Nml min^{-1} of H_2, 2.0 Nml min^{-1} of N_2 and 9.2 Nml min^{-1} of Ar, corresponding to 20 vol% of H_2.

After that, the reactor is cooled under Ar purge, down to the temperature chosen for the reforming, while the reaction inlet mixture flows in the bypass to homogenize steam with gaseous components.

Two different procedures for the regulation of SMR temperature are applied:

- SMR-1: SMR is operated at 850 °C for 1 h, then at 750 °C for 1 h and in the end at 650 °C for 1 h. During the whole process, the inlet molar steam/carbon

ratio is 3 and inlet gas flows are: 2 Nml min^{-1} of CH_4, 2 Nml min^{-1} of N_2 and 10 Nml min^{-1} of Ar.

- SMR-2: after SMR-1, reactor is cooled down to room temperature and then heated up to 650 °C under Ar purge; at 650 °C SMR is started by feeding again the same flows, as in SMR-1.

These two procedures are set to search differences in the catalytic activity of Ni at 650 °C, the temperature of interest for SESMR with CSCM, depending on the way this temperature is approached: in SMR-1 the reforming has been already started before reaching 650 °C, while in SMR-2 it is triggered exactly at 650 °C.

2.3.2 Reforming on 2-material systems

The sample masses are 200 mg of Ni-mayenite catalyst and 300 mg of CaO-mayenite sorbent or CaO0. Two configurations are explored, with respect to the mutual position between the two materials:

- Separate beds: Ni-mayenite catalyst is located upstream of CaO-mayenite, with a thin layer of quartz wool between the two beds;
- Raw mixing: Ni-mayenite catalyst and CaO-mayenite or CaO0 are mixed and placed within the reactor as a unique packed bed.

Pre-reduction step described in §2.3.1 is applied for these tests too. Afterwards, the reactor is cooled down to 650 °C under Ar purge stream, and at this temperature reforming starts by the switch from the Ar purge stream to the same inlet flows used for SMR in §2.3.1 (steam, CH_4, N_2, Ar). Reforming lasts for 3 h.

The purpose is to test the activity of both kinds of materials in SESMR operating conditions (especially by separate beds test) and possible mutual influences between catalyst and sorbent (by comparison of the results from two configurations and from raw mixings containing CaO-mayenite or CaO0).

2.3.3 Reforming on Ni-CaO-mayenite

The sample mass is 500 mg of CSCM. The same pre-reduction and reforming procedure adopted for 2-material (§2.3.2) is carried out for SESMR tests on CSCM.

2.3.4 Carbon balance

For all tests in microreactor scale, a molar balance on elemental C is performed around packed bed reactor. Assumptions in force for these balances follow:

- According to experimental procedures described just above, a unique flow brings C in the reactor, belonging to CH_4 and being constant with respect to time ($F_{CH4,in}$, regulated by CH_4 mass flow controller);

- C leaves the reactor in the form of CO, CO_2 and CH_4, flow rates of which $F_{CO,out}$, $F_{CO2,out}$, $F_{CH4,out}$ are determined as functions of time by GC measurements (Equation 2.4).

Total elemental C moles entering the reactor ($N_{C,in}$) are calculated by numerical integration with respect to time of profiles of $F_{CH4,in}$, based on trapezoidal rule. Analogously, total elemental C moles leaving the reactor ($N_{C,out}$) are computed by $F_{CO,out}$ $F_{CO2,out}$ $F_{CH4,out}$. A uniform integration grid with its spacing equal to GC sampling frequency is adopted. C-balance deviation is expressed in terms of percentage error ΔC (Equation 2.9):

$$\Delta C = \frac{N_{C,in} - N_{C,out}}{N_{C,in}} 100 \qquad \textit{Equation 2.9}$$

2.4 Study for industrial applications

Tests performed in microreactor scale (§2.3) are employed as a screening to select the most promising materials for a study addressed to industrial applications. This study includes:

- SESMR/regeneration multicycle tests;
- Evaluation of material's mechanical properties.

2.4.1 SESMR/regeneration multicycle tests

The core of experimental apparatus for SESMR/regeneration multicycle tests (Figure 2.2) is an AISI 316L stainless-steel packed bed reactor in vertical configuration, ¾" nominal outside diameter. About 7 g of granular sample, with particle diameter in the range between 212 µm and 600 µm, constitute the active packed bed.

The reactor is located inside an electric cylindrical furnace CARBOLITE MTF, having its controlling thermocouple placed in the active packed bed.

Available inlet gases are H_2, CH_4, N_2, CO_2, their flowrate being regulated by BRONKHORST mass flow controllers. Steam is generated upstream the reactor, by feeding liquid distilled water into an evaporation chamber kept at 220 °C, where steam and other inlet gases are mixed and sent to the reactor. Water is pumped by a stainless-steel pressure syringe (capacity of 50 ml) pushed by an electric engine KDS LEGATO 110, which controls the volumetric liquid flowrate.

Downstream the reactor, a glass condenser separates unreacted water from product gases. The condenser uses ethylene glycol as a service cooling liquid (0-1 °C) managed by a JULABO cryostat.

Dried product gases pass through a BRONKHORST mass flow meter, recording overall flowrate, and then access an ABB online analysis system, equipped with an ADVANCE OPTIMA URAS 14 module, measuring CO, CO_2, CH_4 volumetric concentrations by NDIR (Non-Dispersive InfraRed), and an ADVANCE OPTIMA CALDOS 17 module, measuring H_2 volumetric concentration by a TCD.

Since ABB system requires a minimum inlet stream for its optimal performance, but reactor product gases do not reach this threshold value, an additional N_2 dilution stream is added between the condenser and the mass flow meter, in order to reach the minimum flow required by ABB. The mass flow meter for this N_2 dilution line is controlled by an analogic controller DYNAMASS.

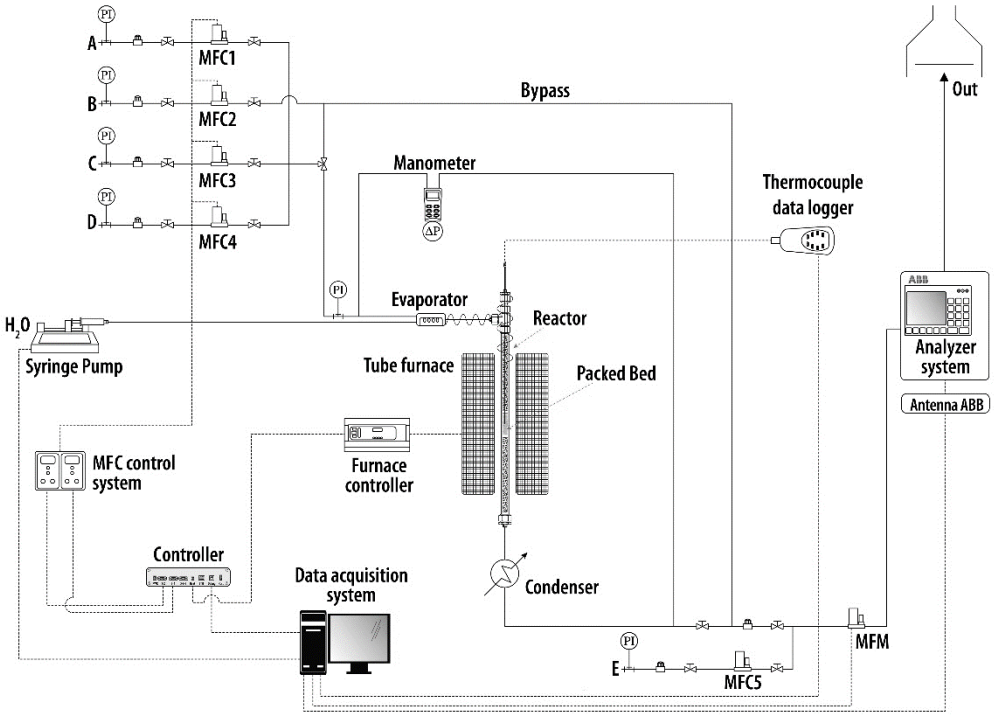

Figure 2.2: Schematic view of bench scale packed bed automated experimental apparatus for SESMR/regeneration multicycle tests (A: H_2, B: CH_4; C: N_2; D: CO_2; E: N_2 dilution)

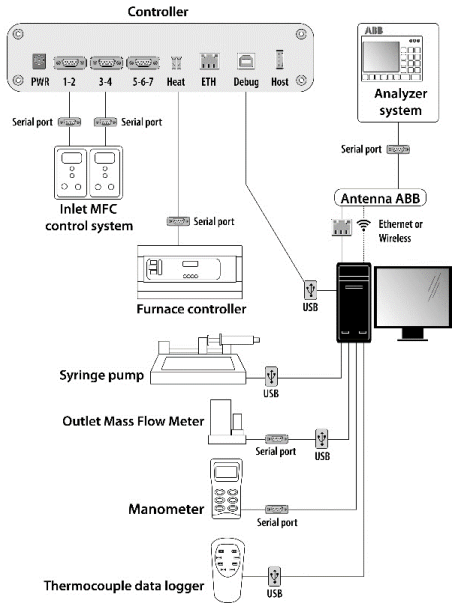

Figure 2.3: Control system of bench scale packed bed automated experimental apparatus for active bed temperature, by CARBOLITE MTF thermocouple;

An automated control system (Figure 2.3), developed and customized by DigiPower s.r.l. for SESMR/regeneration multicycle experiments, manages:

- flowrates of H_2, CH_4, N_2, CO_2 by BRONKHORST mass flow controllers;
- inlet water liquid flowrate by KDS LEGATO 110 engine;
- packed bed temperature by CARBOLITE MTF furnace.

And records:

- overall dry product flowrate (F_{out}), by downstream BRONKHORST mass flow meter;
- H_2, CH_4, CO and CO_2 outlet volumetric percentages by ABB system ($c^{ABB}_{i,out}$);
- Packed bed pressure drops;
- Actual temperature within the packed bed.

Flowrates for each species exiting the reactor ($F_{i,out}$) are calculated by Equation 2.10, then Equation 2.5, Equation 2.6, Equation 2.7 and Equation 2.8 are applied to evaluate the experimental test conditions and materials performances in terms of WHSV, Ni-WHSV, χ_{CH4} and $C_{i,out}$, respectively.

$$F_{i,out} = \frac{c^{ABB}{}_{i,out}}{100} F_{out} \quad ; \quad i = CH_4, H_2, CO, CO_2, N_2 \qquad \textit{Equation 2.10}$$

Steps employed in SESMR/regeneration multicycle test follow:

1. Pre-reduction. For the same reason explained in §2.3.1, NiO must be converted to metallic Ni. Then, a reducing flow (15 Nml min^{-1} of H_2, 135 Nml min^{-1} of N_2) passes through the active packed bed, heated from room temperature to 900 °C by a 10 °C min^{-1} heating ramp, and kept at 900 °C for 30 min.
2. Cooling 1. The reactor is cooled down from 900 °C to 650 °C, while a mild reducing stream flows (7.5 Nml min^{-1} of H_2 and 142.5 Nml min^{-1} of N_2).
3. Steaming. At 650 °C, for 1 min, 0.066 ml min^{-1} of liquid distilled water are fed together with 150 Nml min^{-1} of N_2, in order to ensure the evaporating chamber to be ready for steam production when reforming is started.
4. Reforming. At 650 °C, the inlet stream contains 27 Nml min^{-1} of CH_4 and 100 Nml min^{-1} of N_2, with inlet molar steam/carbon ratio equal to 3. Two different durations are chosen: for the first cycle and those multiple of 5, a long reforming lasts 1 h, so to measure packed bed's breakthrough i.e. sorbent saturation; for other cycles, reforming lasts 10 min, so to avoid breakthrough occurrence. After the reforming, reactor is purged at 650 °C for 1 min by 150 Nml min^{-1} of N_2.
5. Mild regeneration. The active packed bed is heated by a 10 °C min^{-1} ramp, from 650 °C to 850 °C, and kept at 850 °C for a time corresponding to the duration of the preceding reforming, feeding 150 Nml min^{-1} of N_2 during the whole step.

6. Severe regeneration. The active packed bed is heated by a 10 °C min^{-1} ramp, from 650 °C to 925 °C, and kept at 925 °C for a time corresponding to the duration of the preceding reforming, feeding 150 Nml min^{-1} of CO_2. After that, reactor is purged at 925 °C for 1 min by 150 Nml min^{-1} of N_2.
7. Cooling 2. The reactor cools down from the regeneration dwell temperature to 650 °C, while a mild reducing stream flows (7.5 Nml min^{-1} of H_2 and 142.5 Nml min^{-1} of N_2);
8. Cooling-Reduction. The reactor cools down from the regeneration dwell temperature to 850 °C under 150 Nml min^{-1} of N_2; afterwards, a highly reducing stream (100 Nml min^{-1} of H_2 and 100 Nml min^{-1} of N_2) flows through the bed at 850 °C to restore metallic Ni; eventually, the reactors cools down under a mild reducing stream (7.5 Nml min^{-1} of H_2 and 142.5 Nml min^{-1} of N_2) down to 650 °C.

Experiments count 205 SESMR/regeneration cycles, so to tests long-term stability of studied materials. SESMR condition (step 4) are the same for all tests, while several regeneration strategies are considered:

- In tests with mild regeneration, after Pre-reduction and Cooling 1, the cycle $3 \rightarrow 4 \rightarrow 6 \rightarrow 7$ is repeated, so that the active packed-bed is regenerated in pure N_2 at a relatively low temperature;
- In tests with severe regeneration, after Pre-reduction and Cooling 1, the cycle $3 \rightarrow 4 \rightarrow 6 \rightarrow 7$ is repeated, so that the active packed bed is regenerated in pure CO_2 at a higher temperature;
- In tests with severe regeneration and cyclical reduction, after Pre-reduction and Cooling 1, after Pre-reduction and Cooling 1, the cycle $3 \rightarrow 4 \rightarrow 6 \rightarrow 8$ is repeated, so that the active packed bed is regenerated in pure CO_2 at a higher temperature and subsequently reduced.

Whatever the used regeneration strategy, the 205th cycle is just $3 \rightarrow 4$, so to get the carbonated material at the end of each experiment.

In order to obtain an overall picture of SESMR performances from a 205-cycles test, averaged χ_{CH4} and $C_{i,out}$ are calculated for the 3rd minute of each Reforming step, and for the 57th minute of each long Reforming step.

2.4.2 Mechanical properties evaluation

Particle mechanical resistance of materials for SESMR, for their applicability in fluidized beds (§1.5.4), is evaluated by a procedure and a device (Figure 2.4) based on ASTM D5757-11 (Standard Test Method for Determination of Attrition and Abrasion of Powdered Catalysts by Air Jets), so to constitute a jet system where interaction between particles, promoted by exchange of gas momentum, are dominant.

The device (Figure 2.4) counts:

- a stainless-steel attrition vertical tube, with a 30 mm inside diameter, having at its base three equidistant nozzles (diameter = 0.381 mm, distance from the centre = 10 mm);
- a stainless-steel settling chamber, flanged on the attrition tube top, counting a 300 mm long cylinder with a 110 mm inside diameter and with conical ends reducing to 30 mm inside diameter; the upper cone is approximately 100 mm long and the lower cone is approximately 230 mm long;
- a fines collector, made up of a 250 ml filtering flask and a 13 mm diameter metal tubing bent to an angle of 125 °, connecting the top of the flask to the top of the settling chamber;

About 50 g of a powdery sample (m_s), with selected particle diameter between 106 µm and 212 µm, are placed on the bottom of the attrition tube; 10 Nml min^{-1} of N_2 are blown upwards through the nozzles and therefore through the solid particles, so to cause attrition; the cross-section expansion of the settling chamber allows only fine particles to be entrained and collected in the terminal flask. Recovered fines mass in this flask is measured after 1 h ($m_{fines}(1\ h)$) and after 5 h ($m_{fines}(5\ h)$), as well as residual mass (m_r) in the attrition tube at the end of the 5 h test.

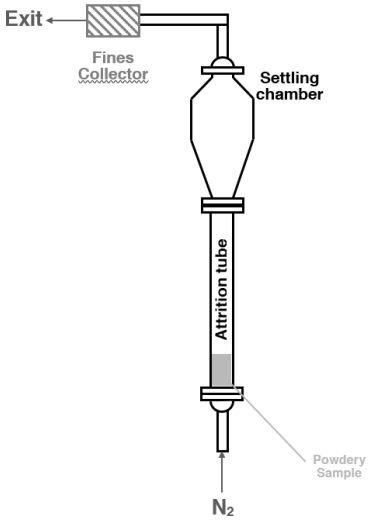

Figure 2.4: Experimental apparatus for attrition tests

The Air Jet Index (AJI) is then calculated as the percent attrition loss after a given time (Equation 2.11, Equation 2.12):

$$AJI(1\ h) = \frac{m_{fines}(1\ h)}{m_s} \cdot 100 \qquad \textit{Equation 2.11}$$

$$AJI(5\ h) = \frac{m_{fines}(5\ h)}{m_s} \cdot 100 \qquad \textit{Equation 2.12}$$

To attest the test reliability, the overall sample mass recovery is also calculated (Equation 2.13):

$$Recovery = \frac{m_r + m_{fines}(5\ h)}{m_S} \cdot 100 \qquad \textit{Equation 2.13}$$

2.5 Chemical equilibrium calculation

In the process simulation environment CHEMCAD® 6.5, a Gibbs Free Energy Reactor UnitOp, in isothermal mode, is used for calculations of equilibrium compositions corresponding to experimental conditions described in §2.3 for reforming microreactor tests and §2.4.1 for SESMR/regeneration multicycles, including CH_4, H_2O, CO, CO_2, H_2, Ar, N_2, CaO, $CaCO_3$ in the component list.

Chapter 3

As-synthesized materials

CaO-mayenite sorbents for CO_2 capture, Ni-mayenite catalysts for SMR and Ni-CaO-mayenite CSCM for SESMR are purposely synthesized at laboratory scale (10^0-10^1 g of final product) and characterized by means of methods described in §2.1 and §2.2, respectively.

Characterization results allow to investigate the influence on material properties of parameters varied among the set of syntheses:

- *Free CaO fraction;*
- *Ni salt precursors;*
- *Ni fraction.*

3.1 Elemental composition

A first overview about syntheses comes from elemental Ca, Al and Ni quantification by ICP-AES, compared for each material with corresponding nominal fractions in Table 3.1. Since ICP-AES is performed on as-synthesized materials, nominal compositions are calculated for this state, i.e. assuming nominal Ni to be in the form of NiO. Indeed, last step of WI (§2.1.2) is a calcination.

Most of experimental ICP-AES values agree with nominal compositions, with some exceptions. CaO45 has less Ca than expected, as well as CSCM deriving from its WI, which also have a Ni fraction lower than nominal; similar observations can be extended to CaO0Ni(N)6. CaO30Ni(N)10 bears similar defects, because of an Al content higher than nominal. CaO15 and its CSCM, CaO15Ni(N)10 excepted, have a common slight Ca deficiency.

No clear relation emerges between these discrepancies and investigated parameters (free CaO fraction, Ni precursor, Ni fraction), therefore they can be ascribed to experimental variability in individual syntheses.

Table 3.1: Nominal elemental contents and ICP-AES experimental results for as-synthesized materials

	Nominal content				ICP-AES results			
Material	**Al [wt%]**	**Ca [wt%]**	**Ni [wt%]**	**Ca/Al [wt/wt]**	**Al [wt%]**	**Ca [wt%]**	**Ni [wt%]**	**Ca/Al [wt/wt]**
CaO0	27.2	34.7	0	1.3	28.1	36.0		1.3
CaO0Ni(N)3	26.2	33.4	3.0	1.3	28.7	37.3	2.9	1.3
CaO0Ni(N)4.5	25.7	32.7	4.4	1.3	27.3	32.9	4.1	1.2
CaO0Ni(N)6	25.2	32.1	5.9	1.3	21.3	19.6	3.8	0.9
CaO0Ni(N)10	23.9	30.4	9.7	1.3	24.3	31.7	11.7	1.3
CaO0Ni(Ac)3	26.2	33.4	3.0	1.3	27.9	37.0	3.1	1.3
CaO0Ni(Ac)4.5	25.7	32.7	4.4	1.3	27.3	36.0	4.5	1.3
CaO0Ni(Ac)6	25.2	32.1	5.9	1.3	26.8	36.0	6.1	1.3
CaO0Ni(Ac)10	23.9	30.4	9.7	1.3	25.8	33.9	10.1	1.3
CaO15	23.2	40.2	0.0	1.7	22.0	34.0		1.5
CaO15Ni(N)3	22.3	38.7	3.0	1.7	22.3	32.0	2.6	1.4
CaO15Ni(N)10	20.3	35.2	9.7	1.7	18.2	37.3	13.2	2.0
CaO15Ni(Ac)3	22.3	38.7	3.0	1.7	26.2	37.0	2.9	1.4
CaO15Ni(Ac)10	20.3	35.2	9.7	1.7	23.9	33.0	9.9	1.4
CaO30	19.1	45.7	0.0	2.4	18.5	44.0		2.4
CaO30Ni(N)3	18.3	44.0	3.0	2.4	17.6	44.0	2.6	2.5
CaO30Ni(N)10	16.7	40.1	9.7	2.4	22.9	41.0	6.0	1.8
CaO30Ni(Ac)3	18.3	44.0	3.0	2.4	18.9	41.0	2.7	2.2
CaO45	15.0	51.2	0.0	3.4	16.4	45.0		2.7
CaO45Ni(N)3	14.4	49.3	3.0	3.4	11.8	33.6	1.5	2.8
CaO45Ni(Ac)3	14.4	49.3	3.0	3.4	11.1	30.0	1.8	2.7
CaO54	12.5	54.5	0.0	4.4	12.6	55.0		4.4
CaO54Ni(N)3	12.1	52.5	3.0	4.4	10.3	47.0	2.4	4.6
CaO54Ni(N)10	11.0	47.8	9.7	4.4	11.0	48.0	9.3	4.4
CaO54Ni(Ac)3	12.1	52.5	3.0	4.4	10.1	47.0	2.5	4.7
CaO54Ni(Ac)10	11.0	47.8	9.7	4.4	11.5	48.0	9.8	4.2

3.2 Crystalline phases

X-ray diffractograms in Figure 3.1, Figure 3.2 and Figure 3.3 show crystalline phases detected in as-synthesized materials: in all cases, desired phases appear ($Ca_{12}Al_{14}O_{33}$, CaO, NiO) and rays intensities are qualitatively in agreement with expected nominal compositions.

As far as WM products are concerned, inherent imperfections emerge. CaO0, meant to be uniquely $Ca_{12}Al_{14}O_{33}$, also contains CaO and $CaAl_2O_4$ traces (Figure 3.1); the latter is a stable calcium aluminate, in equilibrium with $Ca_{12}Al_{14}O_{33}$ for Ca/Al molar ratios in the range from 1/2 to 6/7 (Figure 1.13) [127]. CaO15 and CaO30, meant to contain CaO and $Ca_{12}Al_{14}O_{33}$, show the presence of $CaAl_2O_4$ too, whereas CaO45 and CaO54 do not (Figure 3.2 and Figure 3.3).

One can hypothesize a partial reluctance of calcium species in reacting with aluminium compounds to form $Ca_{12}Al_{14}O_{33}$, so that the actual reactive Ca/Al molar ratio lowers to a value between 1/2 and 6/7, leading to an equilibrium solid separation of $Ca_{12}Al_{14}O_{33}$ and $CaAl_2O_4$ phases (Figure 1.13). The absence of $CaAl_2O_4$ in CaO45 and CaO54 corroborates this hypothesis, since the higher quantity of CaO in the reactive environment increases the probability for aluminium to commit calcium, enough to form only $Ca_{12}Al_{14}O_{33}$. Consequently, Ni-mayenite SMR catalysts (Figure 3.1) and CSCM deriving from CaO15

and CaO30 have some $CaAl_2O_4$, while CSCM descending from CaO45 and CaO54 are $CaAl_2O_4$-free under XRD analyses (Figure 3.2 and Figure 3.3). A cross-correlation between these evidences and ICP-AES results makes one infer that the limit Ca/Al mass elemental ratio for the emergence of $CaAl_2O_4$ lays between 2.5 (CaO30Ni(N)3 in Table 3.1, higher experimental value with $CaAl_2O_4$ XRD detection) and 2.7 (CaO45 or CaO45Ni(Ac)3 in Table 3.1, lower experimental value without $CaAl_2O_4$ XRD detection), i.e. 1.7 and 1.8 in moles.

Anyway, the presence of various calcium aluminates can occur in procedures designed for mayenite synthesis [186]; in addition, in this case $CaAl_2O_4$ formation could be considered as a minor defect of the synthesis, as it is a stable phase [127] and it is also documented as a support for Ni-based catalysts [187,188]. The synthesis of pure mayenite, not a primary purpose of this thesis, is documented in literature as a difficult task, achieved for instance by the modified glycine/nitrate procedure [189]. The increase of thermal treatment temperatures, depending on the synthesis method, is another parameter which can favourably affect the formation of mayenite, even though this brings about a negative influence on specific surface area, e.g. in the study about hydrothermal synthesis or the ceramic route described in [190].

With regard to WI, XRD spectra of Ni-mayenite SMR catalysts (Figure 3.1) and CSCM (Figure 3.2 and Figure 3.3) prove that this method is effective in the addition of Ni, except in the final product. Furthermore, emergence of Ni-containing crystalline phases in XRD patterns (Figure 3.1, Figure 3.2 and Figure 3.3) is in agreement with elements detection by ICP-AES results, even though solid products show some limited variability of the desired Ni fraction with respect to the mass ratio chosen for the precursor salts, (Table 3.1). Considering that the last step in the procedure is a calcination, NiO is the only new detectable crystalline phase formed because of WI, for both Ni-mayenite and CaO-Ni-mayenite materials, the higher its nominal fraction the more intense NiO main ray (Bragg angle at about 43 °). No other Ni-containing phases are detected by XRD (Figure 3.1, Figure 3.2 and Figure 3.3).

Generally, contingent $Ca(OH)_2$ and $CaCO_3$ phases can be ascribed to the exposure to normal ambient conditions (Figure 3.2 and Figure 3.3).

Table 3.2 reports average crystallite sizes estimated by Scherrer equation (Equation 2.1). For each considered phase, dimensions are quite uniform. A tendency of CaO and NiO crystallite sizes to enlarge can be observed with increasing CaO fraction (i.e. decreasing mayenite fraction), confirming the mayenite dispersion effect.

This data, together with observation on XRD spectra, assess a good repeatability of the synthesis method as far as formation and properties of crystalline phases are concerned.

Table 3.2: Average crystallite size (L) estimation by Scherrer equation (Equation 2.1) for as-synthesized materials main phases

Material	$Ca_{12}Al_{14}O_{33}$ [nm]	CaO [nm]	NiO [nm]
CaO0	37.0	23.8	
CaO0Ni(N)3	35.0	28.4	15.9
CaO0Ni(N)4.5	34.4	28.0	15.8
CaO0Ni(N)6	33.3	24.0	17.9
CaO0Ni(N)10	32.9	26.6	13.8
CaO0Ni(Ac)3	35.1	27.5	17.9
CaO0Ni(Ac)4.5	34.0	28.3	16.5
CaO0Ni(Ac)6	32.9	30.0	16.7
CaO0Ni(Ac)10	32.3	31.8	17.4
CaO15	26.9	26.2	
CaO15Ni(N)3	38.6	26.8	18.9
CaO15Ni(N)10	34.5	29.2	15.7
CaO15Ni(Ac)3	37.7	27.4	19.5
CaO15Ni(Ac)10	34.7	28.8	17.7
CaO30	33.2	29.7	
CaO30Ni(N)3	33.4	29.6	18.2
CaO30Ni(N)10	30.8	32.2	19.4
CaO30Ni(Ac)3	33.2	29.5	21.1
CaO45	30.6	33.1	
CaO45Ni(N)3	33.8	29.1	16.9
CaO45Ni(Ac)3	32.0	27.2	20.1
CaO54	31.4	36.4	
CaO54Ni(N)3	34.4	38.3	21.1
CaO54Ni(N)10	36.2	40.7	22.1
CaO54Ni(Ac)3	33.2	37.4	21.1
CaO54Ni(Ac)10	30.8	34.6	18.8

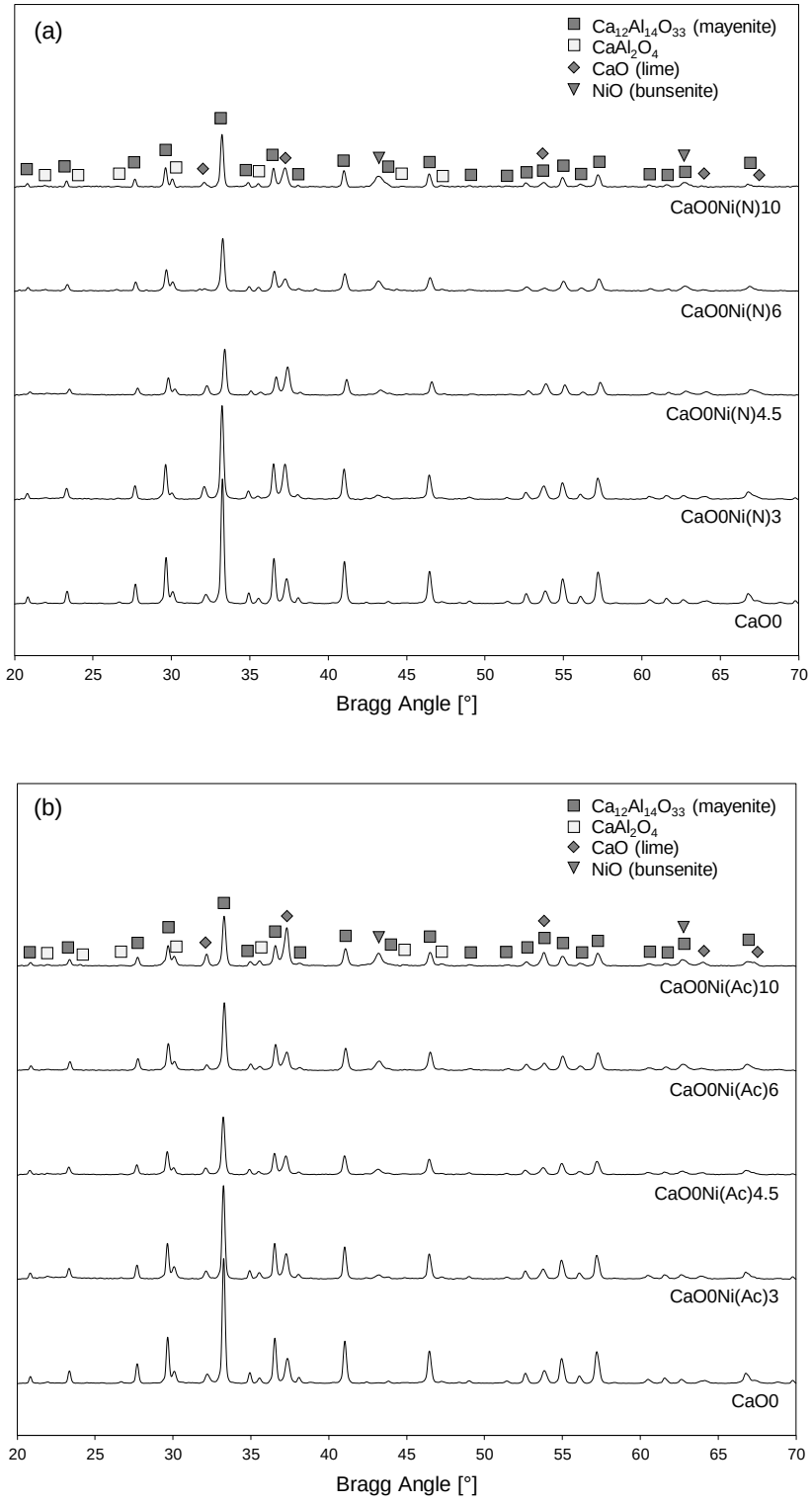

Figure 3.1: X-ray diffractograms for Ni-mayenite SMR catalyst, impregnated with Ni(N) (a) and Ni(Ac) (b), compared with corresponding parent material

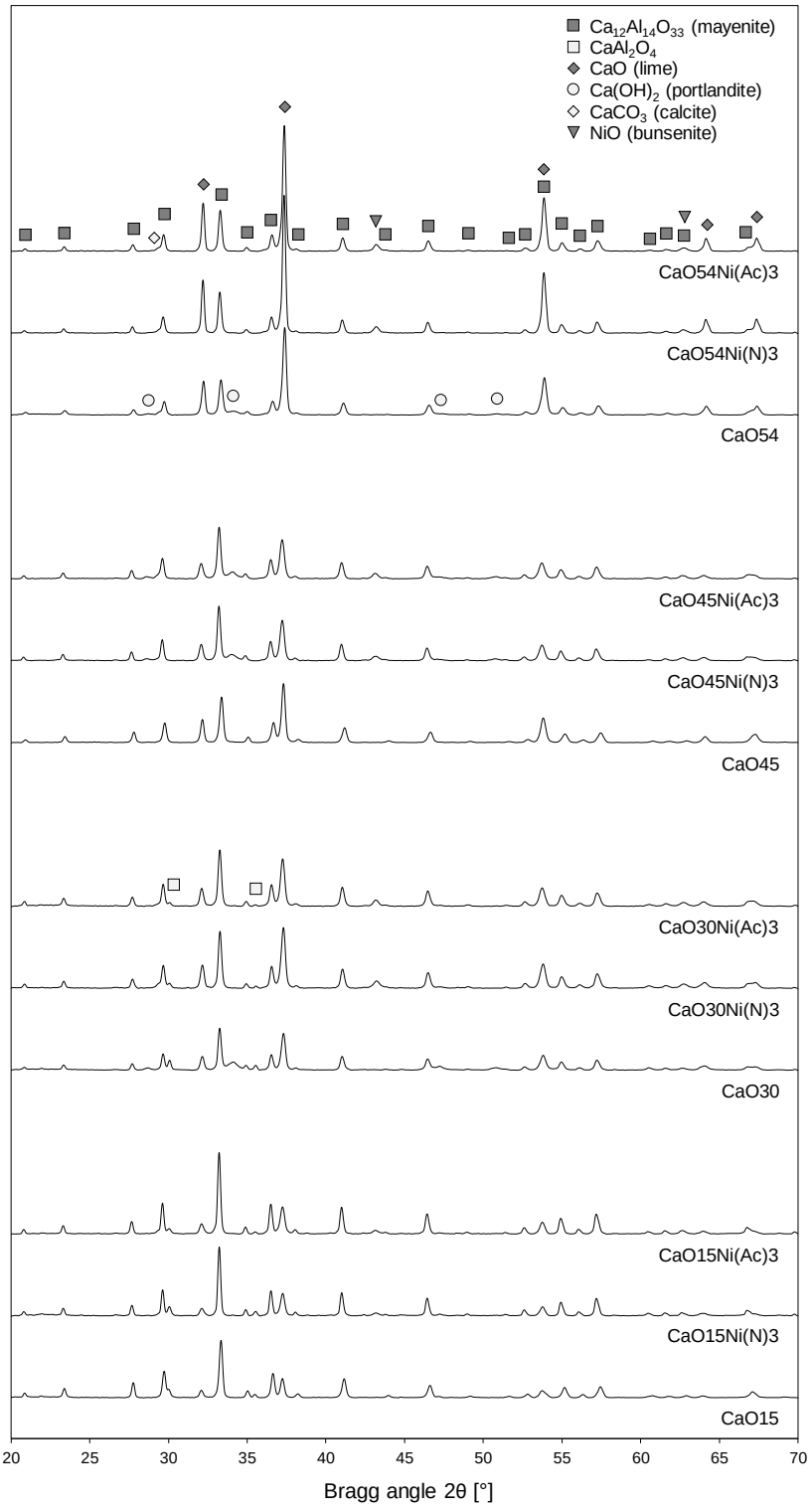

Figure 3.2: X-ray diffractograms for CSCM with nominal 3 wt% of Ni, compared with corresponding parent sorbents

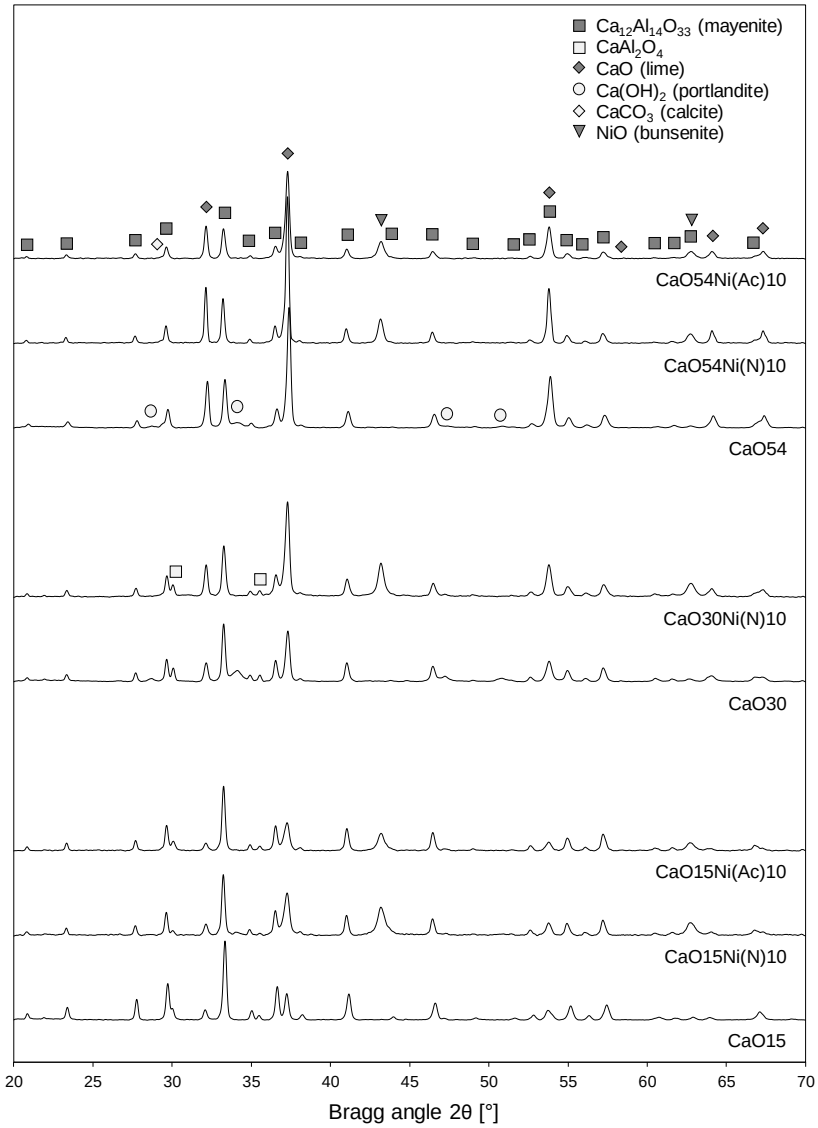

Figure 3.3: X-ray diffractograms for CSCM with nominal 10 wt% of Ni, compared with corresponding parent sorbents

3.3 Morphology and topography

In the following, morphologic and topographic evidences found by SEM and TEM micrographs are reported.

3.3.1 SEM

SEM micrographs, coupled with EDS elemental analyses, allow to get a deeper insight in morphology and elemental topography of synthesized materials.

Figure 3.4a and Figure 3.4b show external porous texture of CaO0 powder, with some cubic shapes. In-situ EDS on the same sample detects elemental Ca and Al with different

peak intensity ratios in different spots (Figure 3.5a), in accordance with XRD results (Figure 3.1) finding both $Ca_{12}Al_{14}O_{33}$ and $CaAl_2O_4$. After WI with Ni(N) (Figure 3.4c) and Ni(Ac) (Figure 3.4d), the microscopic cubic structure disappears, leaving its place to more irregular microgranular surfaces, without significant differences related to Ni salt precursor. In-situ EDS on CaO0Ni(N)3 and CaO0Ni(Ac)3 powders confirms what already evidenced in CaO0 about elemental Ca and Al, moreover detecting elemental Ni (Figure 3.5b and Figure 3.5c). The same analysis on Ni-mayenite embedded samples highlights additional details about Ni deposition: elemental Ni is mainly located in external shells, surrounding the calcium aluminate support, without substantial differences between WI by Ni(N) (Figure 3.6a) and by Ni(Ac) (Figure 3.6b), respectively.

Moving the attention to CaO-mayenite sorbents and CSCM, examples for the two extreme CaO fractions explored in this thesis are in Figure 3.7 and Figure 3.8: comments and remarks about these two families of samples can be extended to all synthesized CaO-sorbents and CSCM.

CaO-mayenite sorbents have a similar morphology, exposing a microgranular external surface (examples in Figure 3.7a, Figure 3.7b, Figure 3.8a, Figure 3.8b). In-situ EDS on powder external surfaces always locate both elemental Ca and Al, with different peak intensity ratios in different zones: in CaO15, similarly to CaO0, the ratio happens to be unbalanced towards elemental Al in some zones (Figure 3.9a), in accordance with XRD detecting $Ca_{12}Al_{14}O_{33}$ and $CaAl_2O_4$ (Figure 3.2, Figure 3.3); on the other hand, for CaO54 it is unbalanced towards elemental Ca (Figure 3.10a), in agreement with nominal compositions and XRD results detecting CaO more intensely than $Ca_{12}Al_{14}O_{33}$ (Figure 3.2, Figure 3.3).

Whatever the desired final Ni fraction or the Ni precursor, WI does not cause significant alterations of external morphology of CSCM (Figure 3.7c, Figure 3.7d, Figure 3.7e, Figure 3.8c, Figure 3.8d, Figure 3.8e) in comparison with their parent sorbents (Figure 3.7a, Figure 3.7b, Figure 3.8a, Figure 3.8b). On CSCM external surfaces, elemental Ni is detected by EDS, the higher its nominal faction the more intense its peaks, while elemental Ca and Al keep the same features of their corresponding parent sorbents (Figure 3.9b, Figure 3.9c, Figure 3.9d, Figure 3.9e, Figure 3.10b, Figure 3.10c, Figure 3.10d, Figure 3.10e). EDS on embedded CSCM locates elemental Ni mainly in external shells enveloping particles, or in veins adherent to their internal voids, without significant distinctions between Ni(N) and Ni(Ac) deriving products (Figure 3.11, Figure 3.12). In the case of CaO54Ni(N)10 (Figure 3.12c) and CaO30Ni(N)10 (shown in Di Giuliano et al. [133]) elemental Ni appears as better dispersed than in other materials, even though far from uniform.

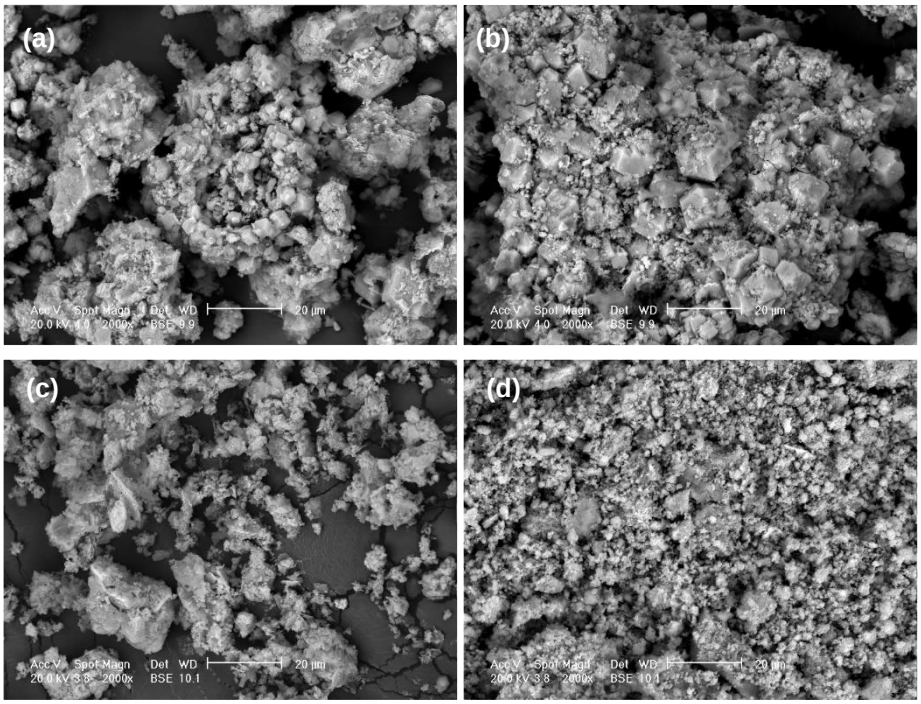

Figure 3.4: SEM micrographs at 2000x magnification of CaO0 (a) (b), CaO0Ni(N)3 (c) and CaO0Ni(Ac)3 (d) powder samples

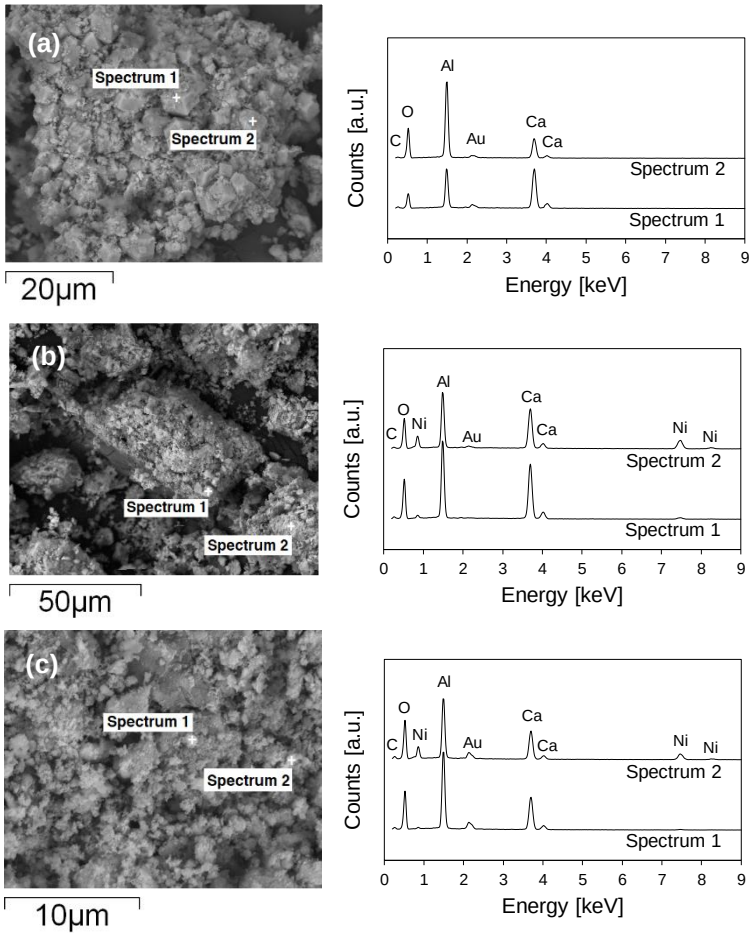

Figure 3.5: SEM-EDS on external surfaces of CaO0 (a), CaO0Ni(N)3 (b), CaO0Ni(Ac)3 (c)

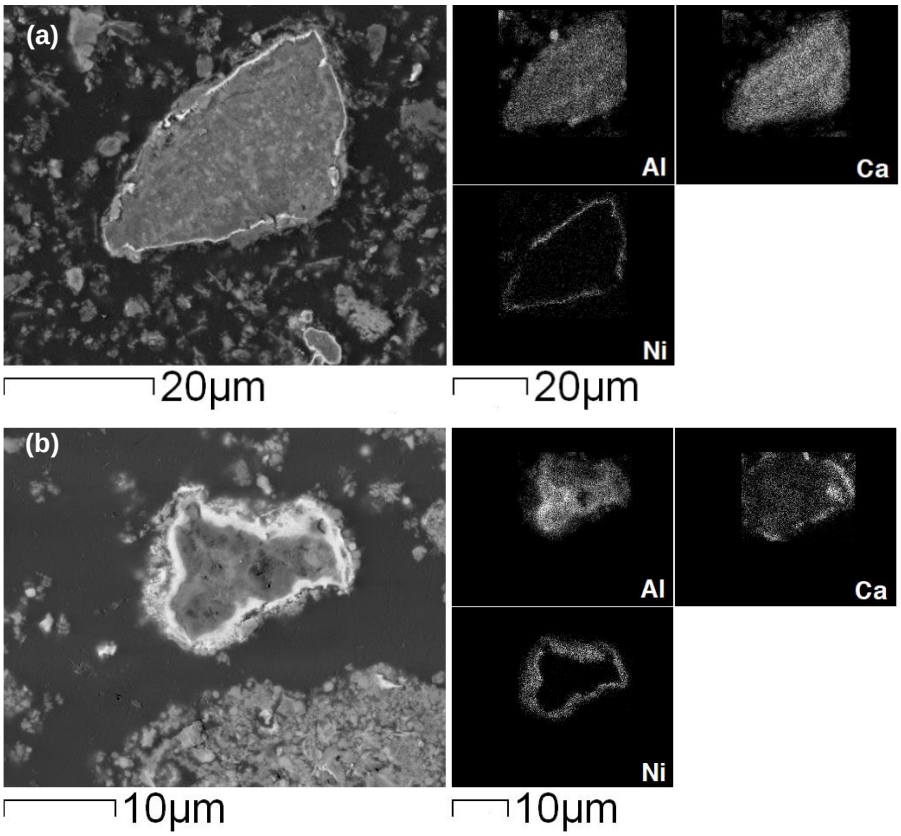

Figure 3.6: SEM-EDS elemental maps for embedded CaO0Ni(N)3 (a) and CaO0Ni(Ac)3 (b)

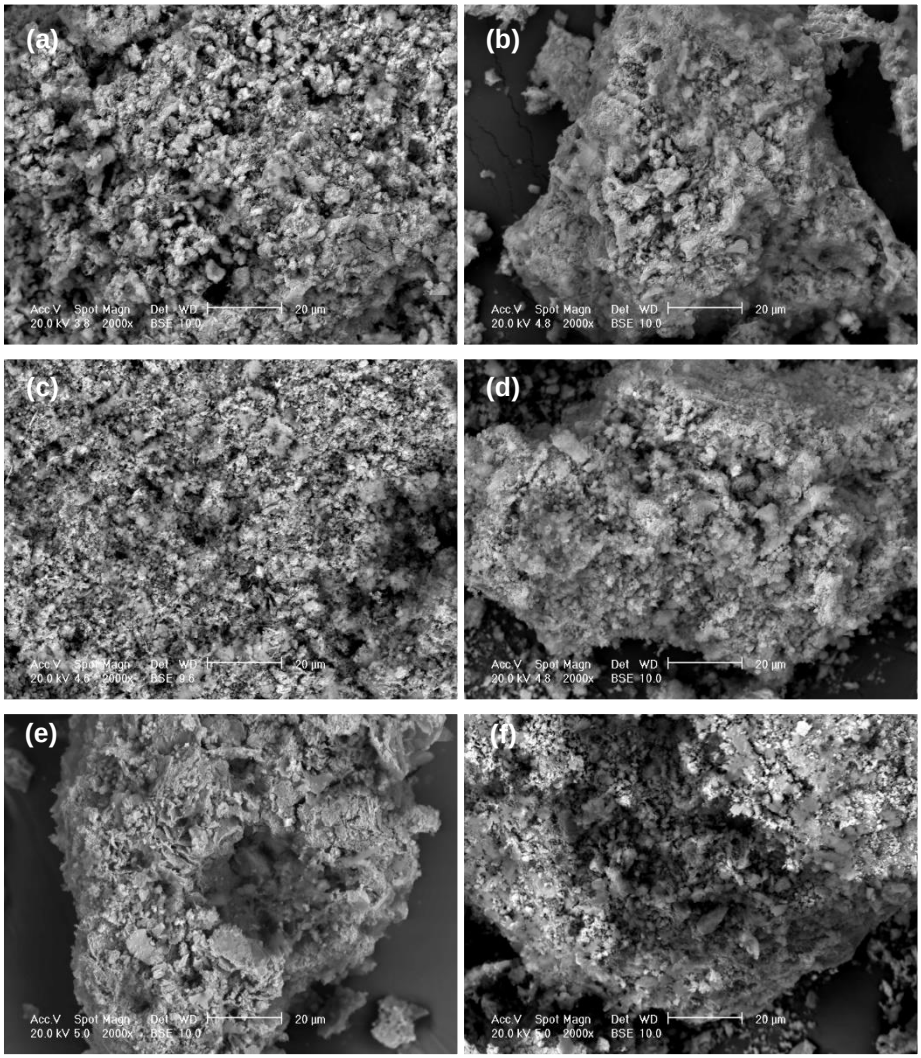

Figure 3.7: SEM micrographs at 2000x magnification of CaO15 (a) (b), CaO15Ni(N)3 (c), CaO15Ni(Ac)3 (d), CaO15Ni(N)10 (e), CaO15Ni(Ac)10 (f) powder samples

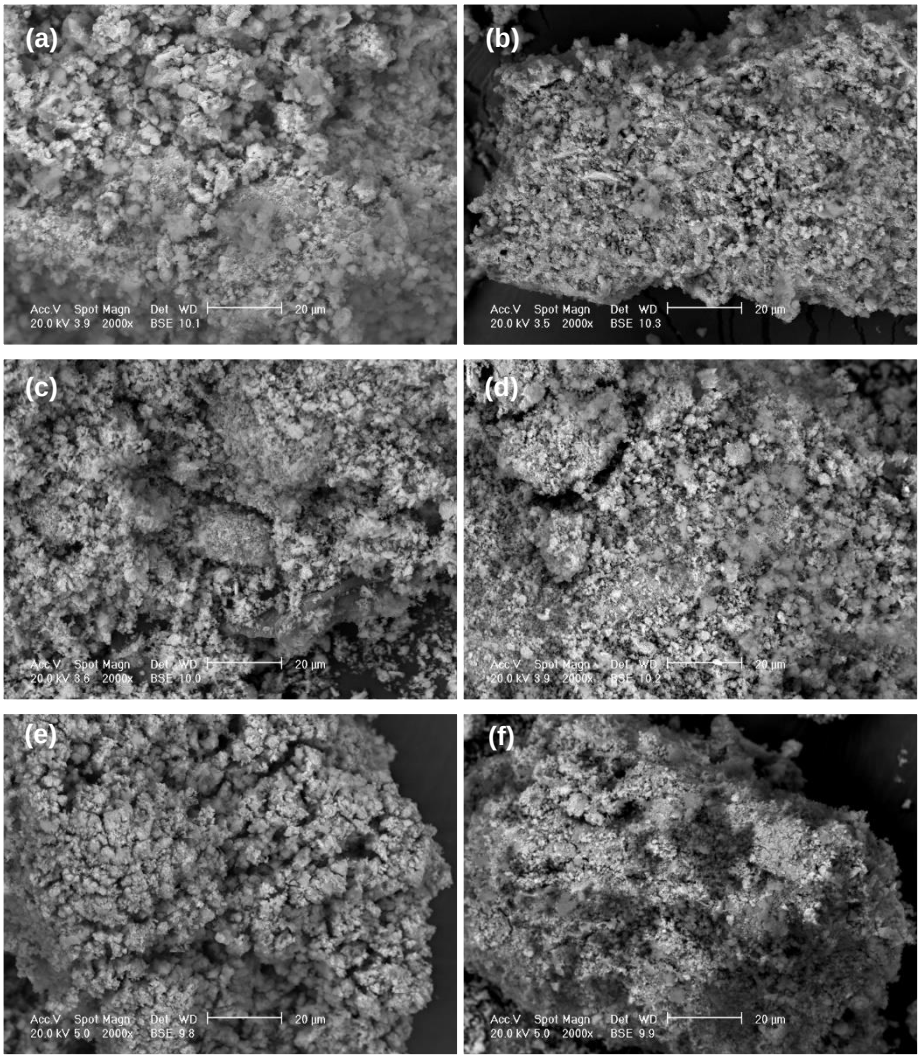

Figure 3.8: SEM micrographs at 2000x magnification of CaO54 (a) (b), CaO54Ni(N)3 (c), CaO54Ni(Ac)3 (d), CaO54Ni(N)10 (e), CaO54Ni(Ac)10 (f) powder samples

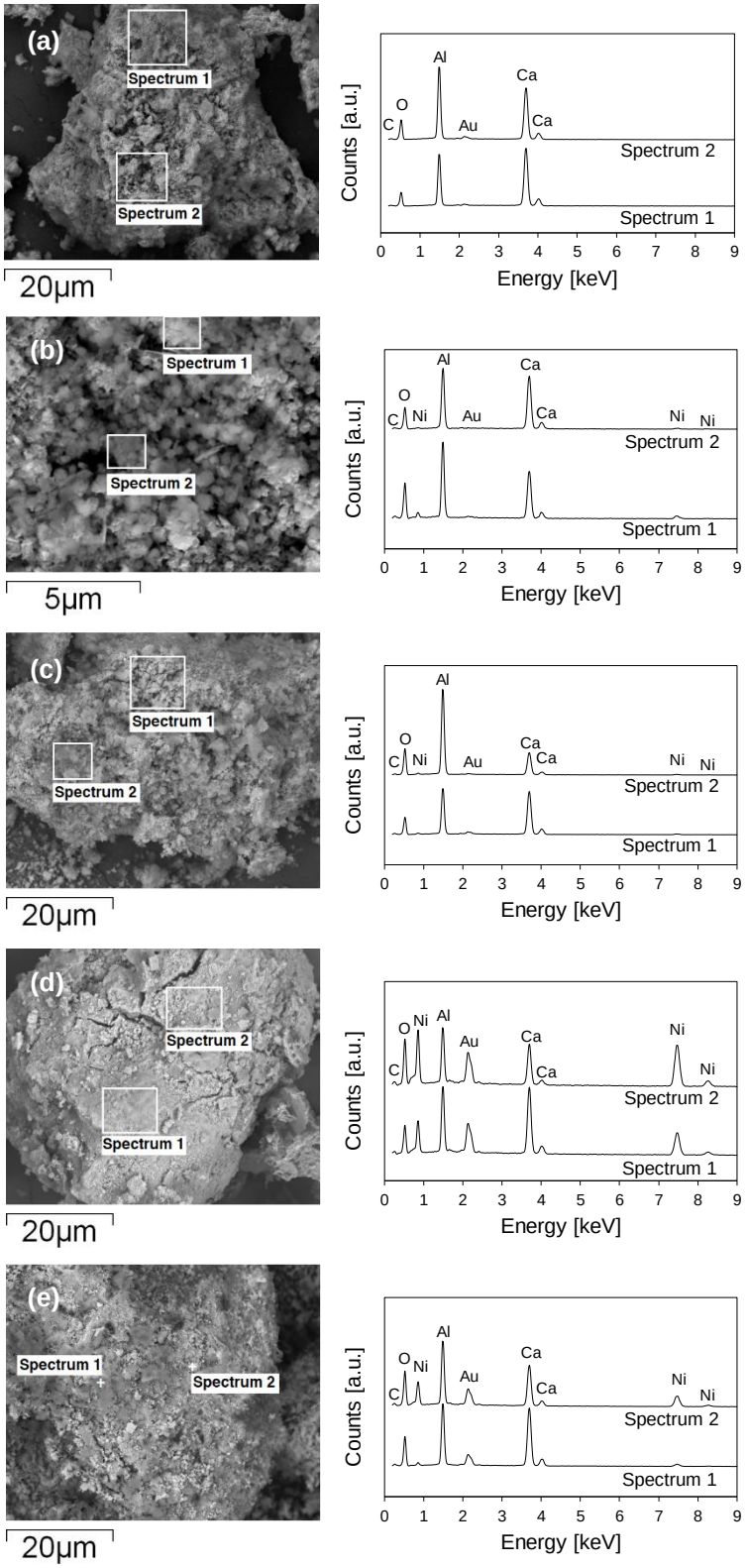

Figure 3.9: SEM-EDS on external surfaces of CaO15 (a), CaO15Ni(N)3 (b), CaO15Ni(Ac)3 (c), CaO15Ni(N)10 (d), CaO15Ni(Ac)10 (e)

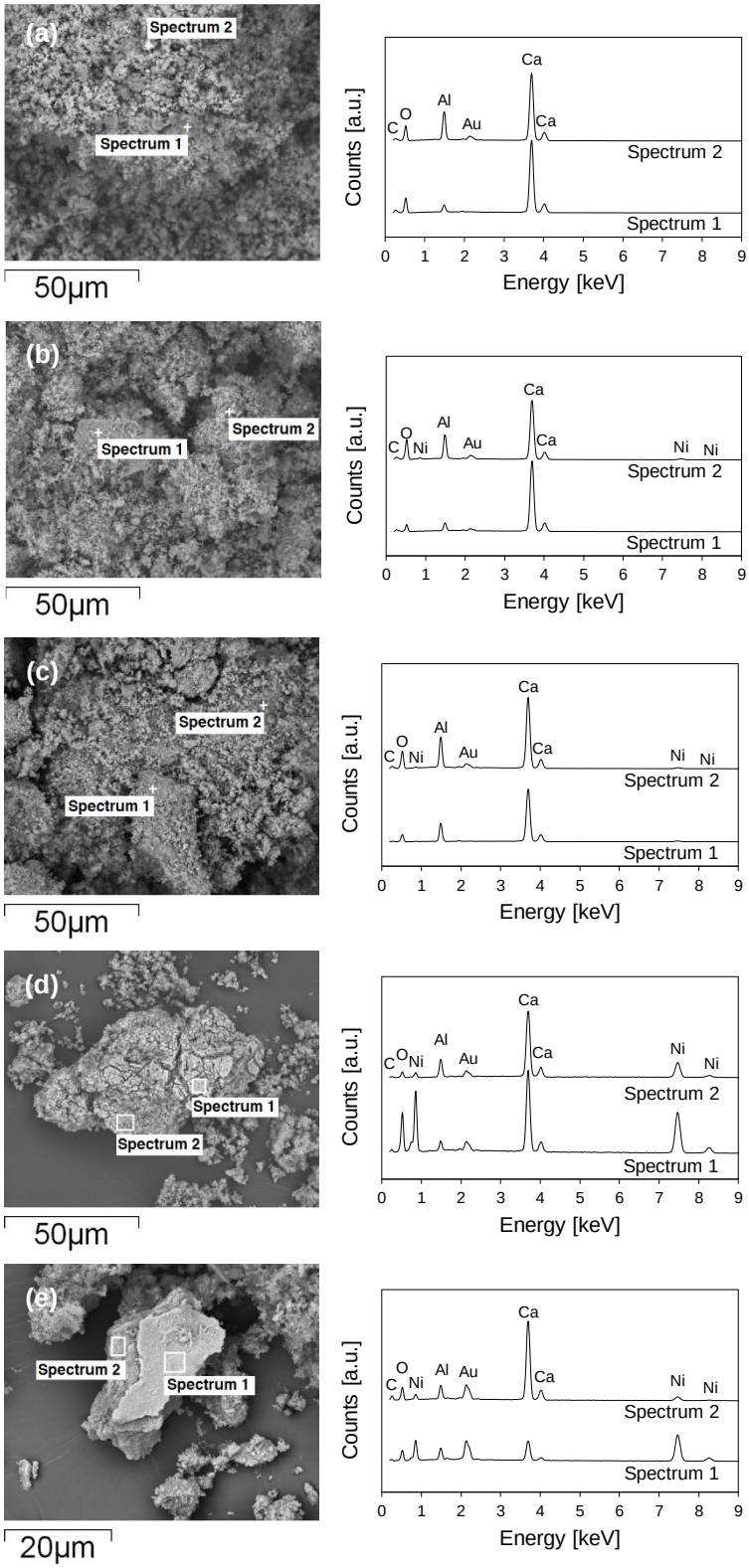

Figure 3.10: SEM-EDS on external surfaces of CaO54 (a), CaO54Ni(N)3 (b), CaO54Ni(Ac)3 (c), CaO54Ni(N)10 (d), CaO54Ni(Ac)10 (e)

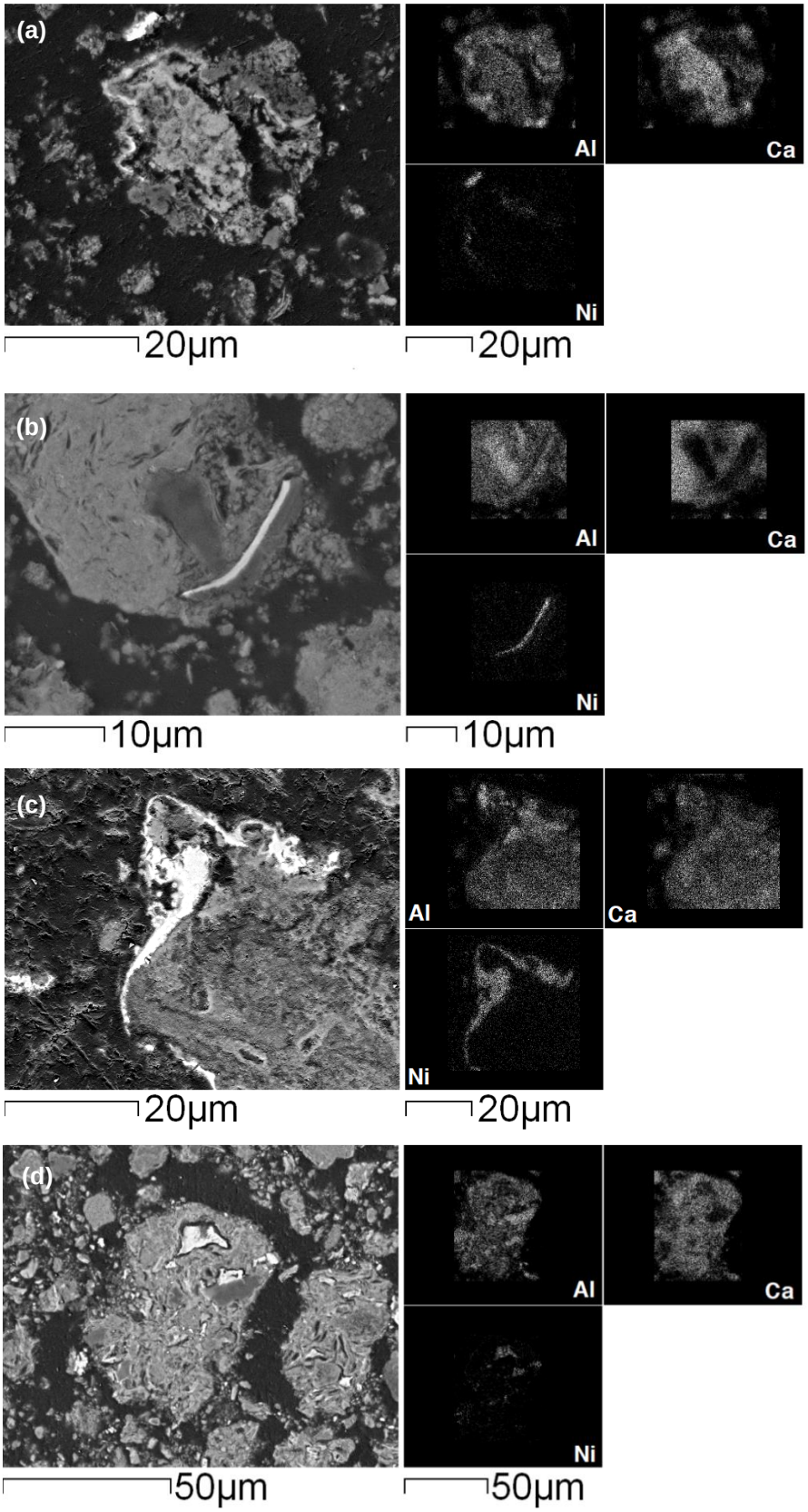

Figure 3.11: SEM-EDS map for embedded CaO15Ni(N)3 (a), CaO15Ni(Ac)3 (b), CaO15Ni(N)10 (c), CaO15Ni(Ac)10 (d)

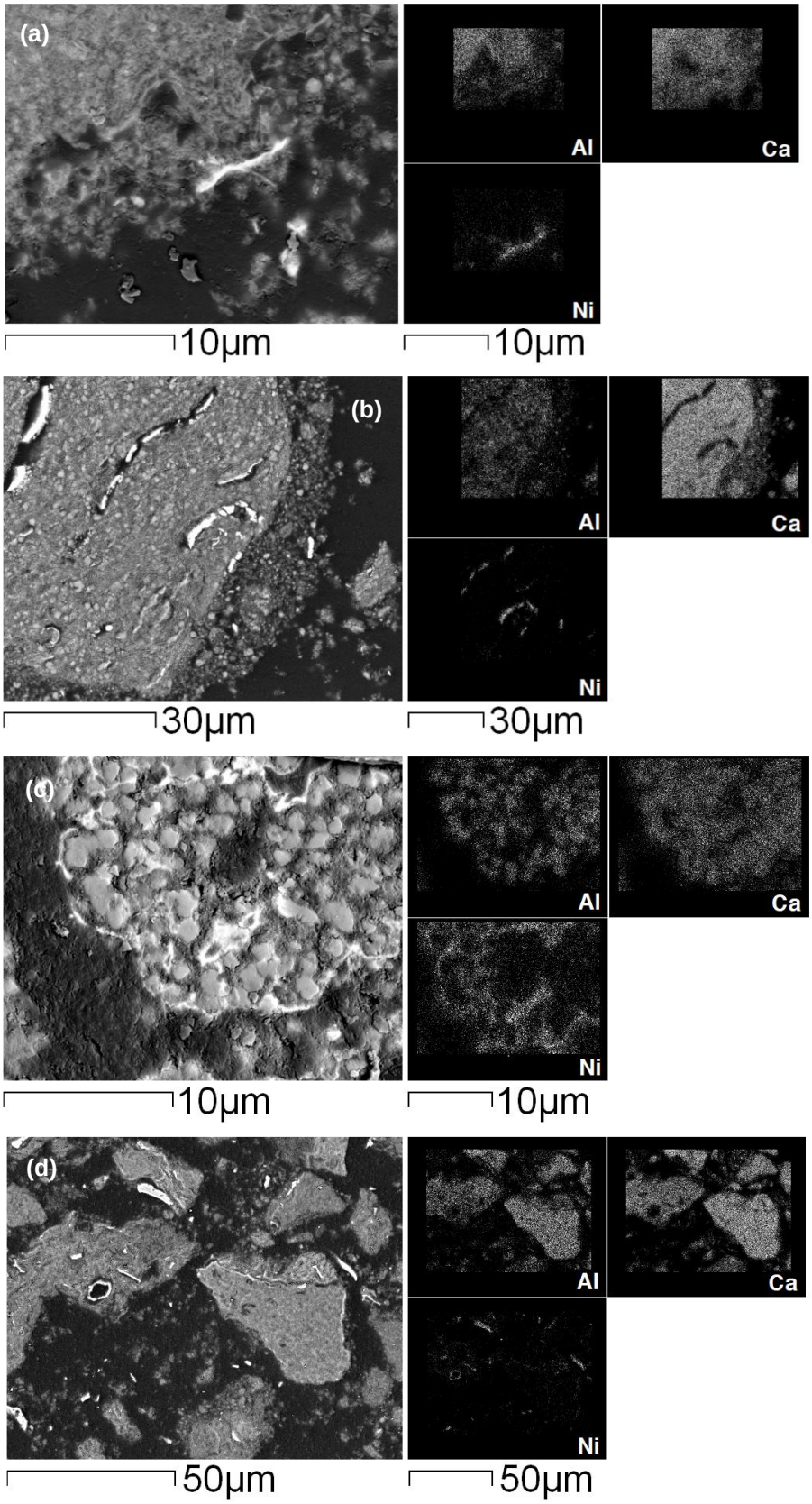

Figure 3.12: SEM-EDS map for embedded CaO54Ni(N)3 (a), CaO54Ni(Ac)3 (b), Cao54Ni(N)10 (c), CaO54Ni(Ac)10 (d)

3.3.2 TEM

TEM micrographs of Ni-mayenite SMR catalysts with 10 wt% of Ni are reported in Figure 3.13. Dark spheroidal particles are NiO, dispersed on a mayenite matrix, as confirmed by cross-correlating XRD spectra (Figure 3.1) and STEM-EDS elemental analysis, detecting Ni preponderance in spheroids (zone 2 in Figure 3.16a, Table 3.3) and Ca/Al ratio close to $Ca_{12}Al_{14}O_{33}$ one in the surrounding matrix (zone 1 in Figure 3.16a, Table 3.3). Magnifications Figure 3.13b and Figure 3.13d show that NiO spheroids dimensions are comparable to *L* estimates (Table 3.2). Moreover, a difference between Ni(N) and Ni(Ac) derivation stands out, as NiO particles in CaO0Ni(N)10 (Figure 3.13b) are surrounded by a shell of different nature, while in CaO0Ni(Ac)10 they are not (Figure 3.13d). An additional feature encountered only in CaO0Ni(Ac)10 is the detection of whirl-like structures (Figure 3.14), compatible with carbon black formations (see Figure 3.14c or Figure 1B in [191]) and therefore the most likely ascribable to the decomposition of acetate species, the only organic compound within the synthesized mass.

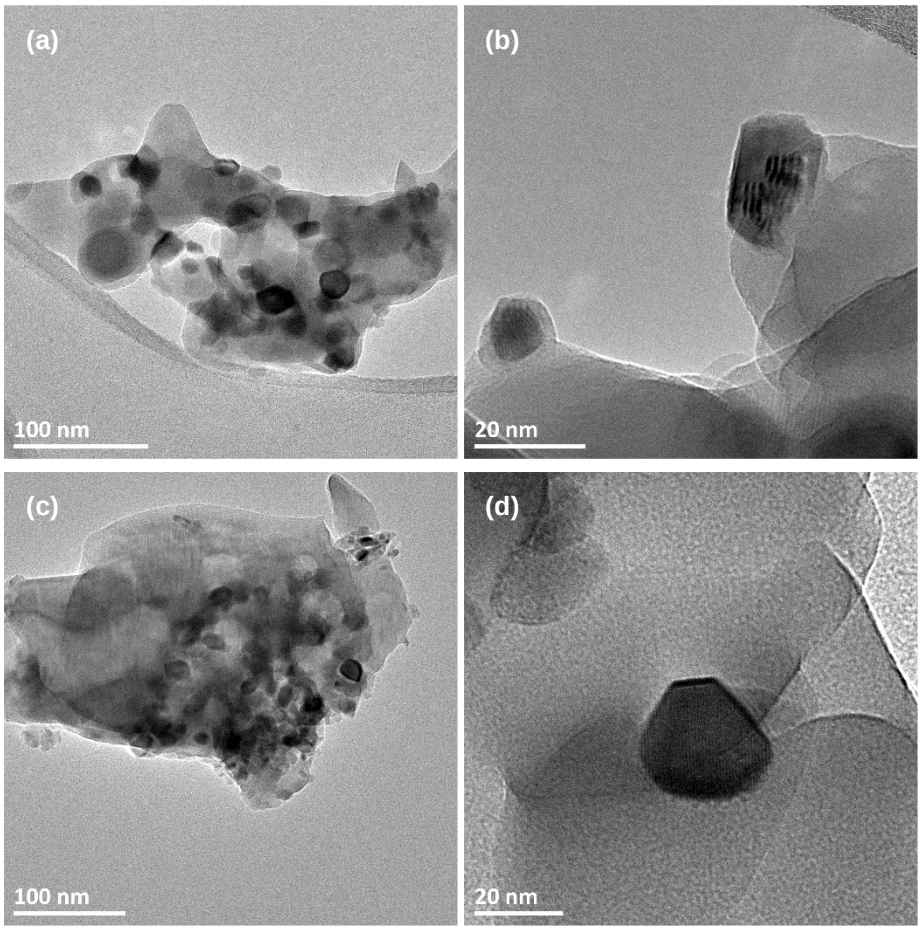

Figure 3.13: TEM micrographs of as-synthesized CaO0Ni(N)10 (a, b) and CaO0Ni(Ac)10 (c, d)

Figure 3.15 show some TEM micrographs from CaO54Ni(N)10, revealing the same qualitative nanometric structure, with spheroidal NiO particles dispersed on a matrix made of calcium and aluminium compounds. In this case too, NiO dimensions (Figure 3.15b) are compatible *L* estimate in Table 3.2. STEM-EDS analyses on CaO54Ni(N)10 (Figure 3.15)

reveal zones with different distributions of elemental Ca and Al, some of them with a Ca excess (zone 9 in Figure 3.16b, Table 3.3) and others closer to mayenite Ca/Al ratio (zone 11 in Figure 3.16c, Table 3.3), in accordance with desired nominal composition and crystalline phases detected by XRD (Figure 3.3).

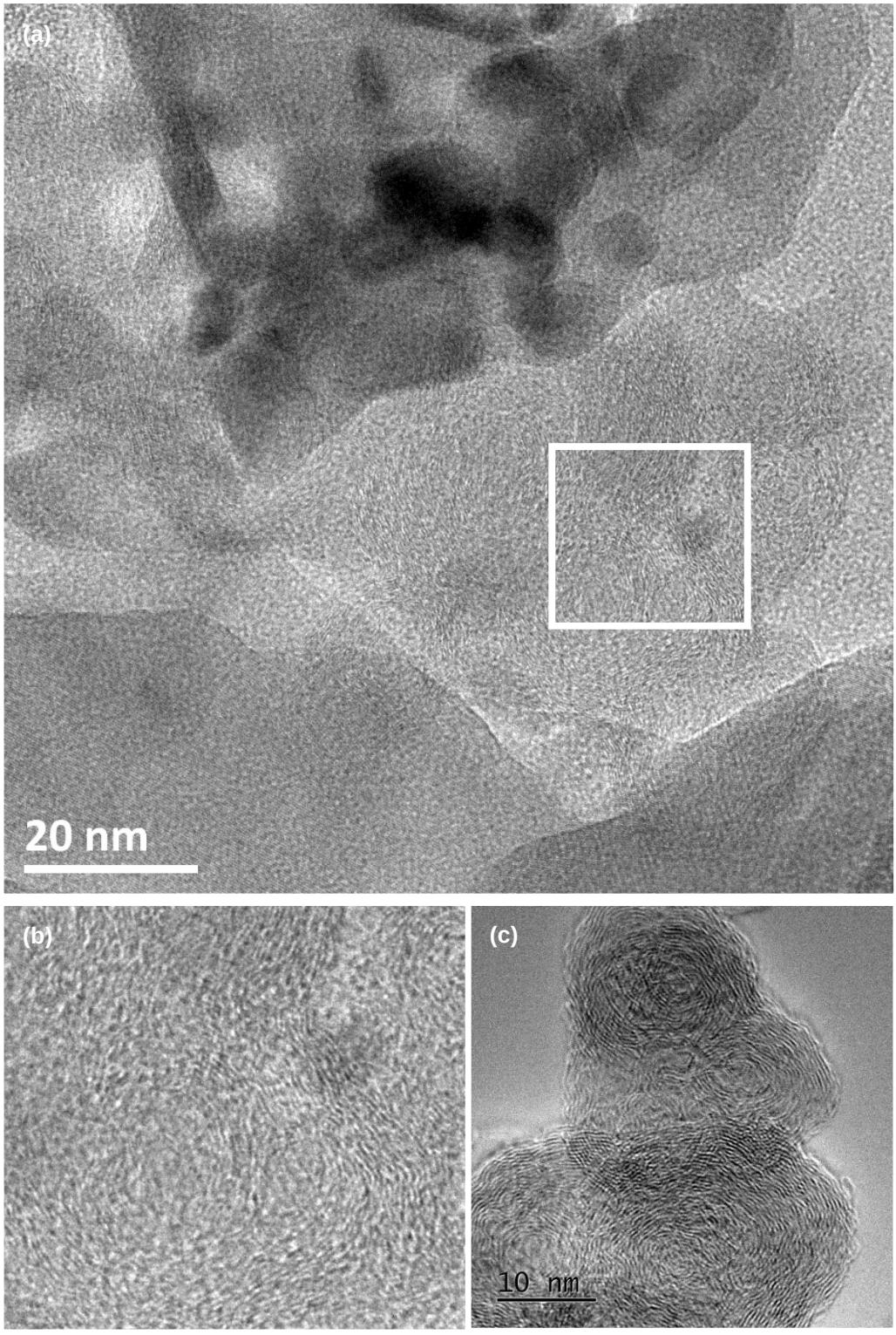

Figure 3.14: TEM micrograph of as-synthesized CaO0Ni(Ac)10 (a) with graphical magnification of the zone within the white box (b), and comparison with a HRTEM micrograph of carbon black [192] *(c)*

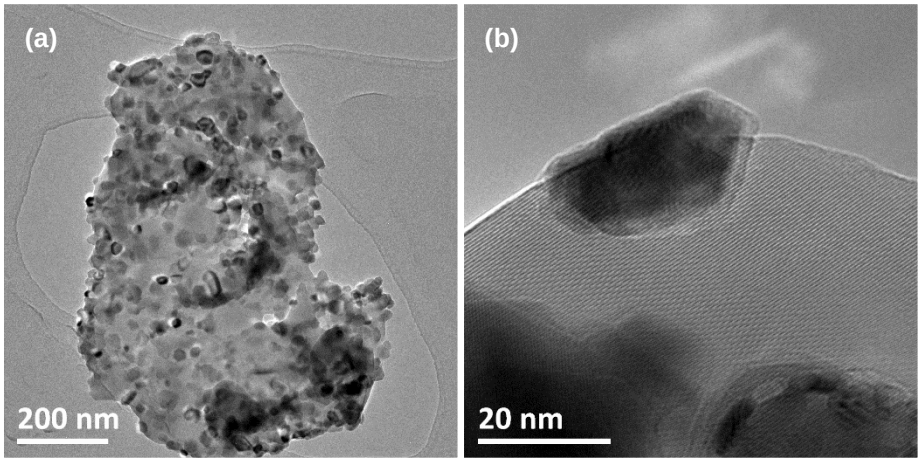

Figure 3.15: TEM micrographs of as-synthesized CaO54Ni(N)10 (a) (b)

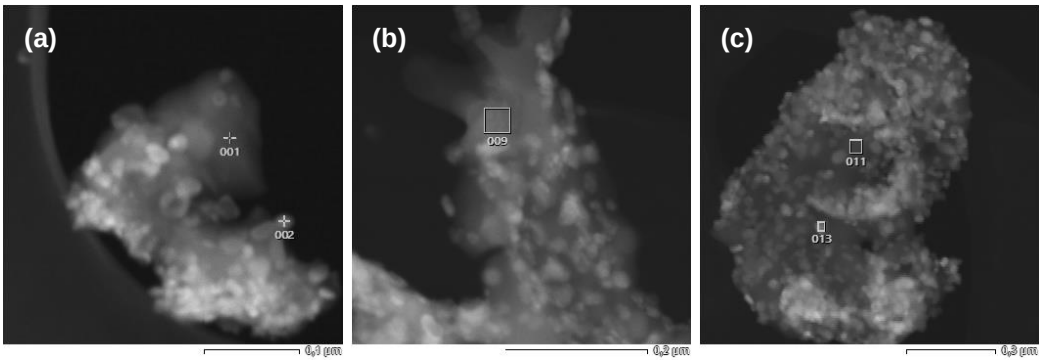

Figure 3.16: STEM-EDS analyses on as-synthesized CaO0Ni(N)10 (a) and CaO54Ni(N)10 (b) (c)

Table 3.3: Relative elemental percentage detected in STEM-EDS spot analysis; "Zone" refers to Figure 3.16

		Mass relative fractions				Atom relative fraction			
Material	**Zone**	**Al [wt%]**	**Ca [wt%]**	**Ni [wt%]**	**Ca/Al [wt/wt]**	**Al [mol%]**	**Ca [mol%]**	**Ni [mol%]**	**Ca/Al [mol/mol]**
CaO0Ni(N)10	1	44.7	52.2	3.1	1.2	55.0	43.3	1.7	0.8
CaO0Ni(N)10	2	10.4	8.5	81.1	0.8	19.5	10.8	69.8	0.5
CaO54Ni(N)10	9	31.6	67.9	0.5	2.1	40.8	58.9	0.3	1.4
CaO54Ni(N)10	11	43.9	55.3	0.7	1.2	53.9	45.7	0.4	0.8
CaO54Ni(N)10	13	23.3	35.9	40.8	1.5	35.2	36.5	28.3	1.0

3.4 Textural properties

The classification of pores dimension adopted in the following discussion comes from IUPAC (International Union of Pure and Applied Chemistry) recommendations [193]:

- Macropores: pores with widths exceeding about 50 nm;
- Mesopores: pores with widths between 2 nm and 50 nm;
- Micropores: pores not exceeding about 2 nm.

3.4.1 Shape of N_2 adsorption and desorption isotherms

Isotherms are plotted in the form of adsorbed N_2 quantity per unit of degassed solid mass, as a function of equilibrium relative pressure (P/P_0), i.e. the ratio between experimental pressure (P) and N_2 vapour pressure at the operating temperature (P_0). Isotherm shapes, together with those of possible hysteresis loops, are observed in the light of respective IUPAC classifications (2015) [182], allowing considerations about pores dimension and shape.

Experimental N_2 adsorption and desorption isotherms have the same shape for all synthesized materials (Table 2.1): a borderline case between Type II and Type IV(a) from IUPAC classification of physisorption isotherms (2015) [182]. Features of these two archetypes follow:

- Type II isotherm belongs to non-porous or macroporous adsorbents and is reversible, i.e. no hysteresis loops emerge, as adsorption and desorption branches coincide. It is originated by unrestricted monolayer-multilayer gas adsorption, up to high P/P_0. In the low P/P_0 region, a knee on the adsorption isotherm, called Point B, corresponds to the completion of monolayer adsorption: the less distinguishable Point B, the more significant the overlap between monolayer and multilayer phenomena. The thickness of multilayer adsorbate does not suffer limitation as pressure increases, so isotherms approach a vertical asymptote for P/P_0 close to 1 [182];
- Type IV isotherm arises from mesoporous materials. At low P/P_0, monolayer-multilayer adsorption occurs, giving the same initial path of Type II. At higher P/P_0, adsorptive gas undergoes capillary condensation, i.e. the formation of a liquid-like phase which fills the residual space left by previously adsorbed multilayers. This kind of condensation occurs at P lower than P_0, so that pores get filled and isotherms become flat, or at least show an inflexion point, at P/P_0 values minor than 1 [182]. Particularly, Type IV(a) exhibits an hysteresis loop, caused by pores exceeding a critical dimension for a certain adsorptive/temperature system, about 4 nm for operative conditions in this work (N_2/-196 °C) [182,183,185].

An example representing all experimental N_2 isotherms is in Figure 3.17: comments and evidences can be extended to all synthesized materials.

In the low P/P_0 region (Figure 3.17b), Point B is located on a very smoothed knee of adsorption curve, indicating an overlap between monolayer and multilayer adsorptions. A linear region follows Point B in the P/P_0 range from 0.05 to 0.30 (Figure 3.17a), making the application of BET method reliable [182]. This feature is common to Types II and IV(a).

As P/P_0 increases, a hysteresis loop appears between adsorption and desorption branches (Figure 3.17a) as in Type IV(a), corroborating the hypothesis of mesoporosity presence. One can consider this loop as a Type H2(b), according to IUPAC hysteresis classification (2015) [182]: it is associated with Type IV(a) isotherms and related to complex porous structures, not uniformly defined in size and shape [182,193].

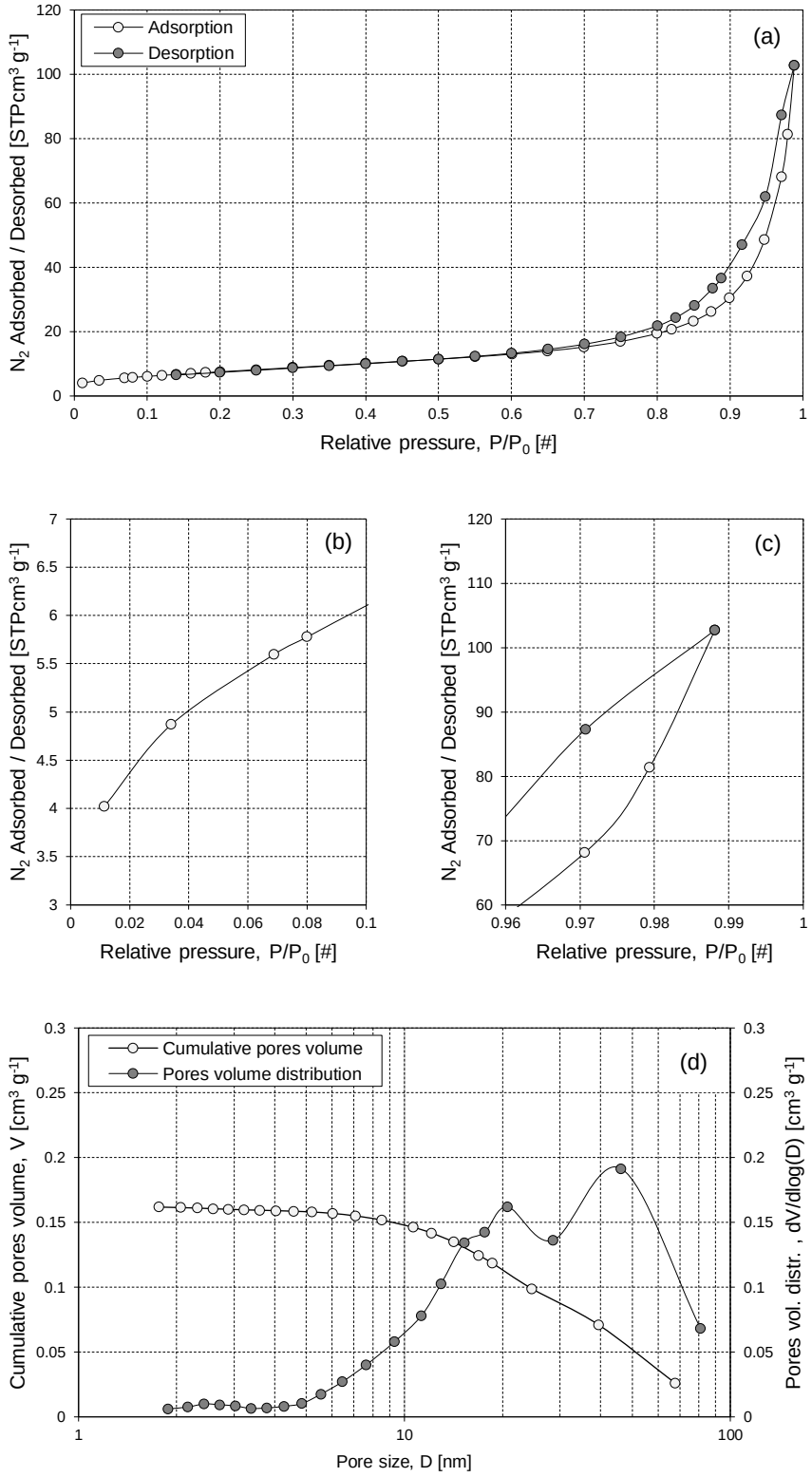

Figure 3.17: N_2 adsorption/desorption data for CaO0Ni(N)3: isotherms (a) and their magnifications in low (b) and high (c) relative pressure regions; BJH porosity assessment (d)

These structures can be oversimplified as a set of ink-bottle shaped pores with a large distribution of neck sizes, at the bottom of the blockage which hinders desorption from void zones with larger diameters, causing hysteresis phenomenon [182,193]. Consequently, average pore size calculation by BJH method ($D_{av,BJH}$) acquires a merely indicative value, since it assumes a cylindrical geometry.

At P/P_0 close to 1 (Figure 3.17c), hysteresis does not end up as a flat line, contrary to Type IV(a). Instead, adsorption curve has a nearly vertical final segment, similarly to a Type II behaviour, therefore revealing some macroporosity. This lowers the reliability of total pore volume evaluation by BJH method, further reducing the significance of average pore size calculation ($D_{av,BJH}$) [182].

Pores volume distribution with respect to pore size (Figure 3.17d) confirms deductions collected just above, since the majority of pores volume is contained in the mesopores range, with a tail crossing 50 nm, the mesopores/macropores border value.

Overall, Figure 3.17 suggests materials to have a hybrid mesoporous-macroporous internal void system, organized in irregular pores far from an open-ended cylindrical geometry. Morphologies observed in §3.3 agree with this last comment.

3.4.2 BET and BJH results

Table 3.4 reports experimental measures of BET surface area (S_{BET}), BJH cumulative pores volume calculated from desorption branch (V_{BJH}), and consequent estimation of averaged pore diameter ($D_{av,BJH}$). In the light of previous observations on N_2 adsorption and desorption isotherms, BET results are reliable, while BJH ones could be affected by macroporosity and network effects.

For WM products, a differentiation occurs between CaO0 and CaO-mayenite sorbents (Table 3.4), the former approximately doubling S_{BET} of the latter, and presenting a higher V_{BJH}. Among CaO-mayenite sorbents, S_{BET} values are close to each other, while V_{BJH} decreases as CaO fraction increases; CaO45 is out of this trend, probably because of singularity in its synthesis hypothesized above by ICP-AES results (Table 3.1).

As far as Ni-mayenite SMR catalysts are concerned, nominal Ni faction and its precursor salt affect pores properties (Figure 3.18):

- In the case of WI by Ni(N), S_{BET} is always increased with respect to parent material CaO0, with a slight negative trend as the nominal Ni fraction increases (Figure 3.18a); V_{BJH} of CaO0Ni(N)3, CaO0Ni(N)4.5 and CaO0Ni(N)6 is higher than that of CaO0, however the contrary happens for CaO0Ni(N)10, revealing a negative influence of Ni fraction increase (Figure 3.18b);
- For WI by Ni(Ac), same trends as in the previous point can be inferred, however they are quantitatively more evident. In fact, S_{BET} decreases more markedly as nominal Ni fraction increases, with values significantly lower than that of CaO0, for 6 wt% and 10 wt% of Ni (Figure 3.18a); V_{BJH} behaves analogously (Figure 3.18b);
- Being the nominal Ni fraction equal, Ni-mayenite samples impregnated with Ni(N) show higher S_{BET} and V_{BJH} than those with Ni(Ac), respectively.

Table 3.4: Measured BET surface areas (S_{BET}), BJH cumulative volumes (V_{BJH}) and averaged pore diameters ($D_{av,BJH}$) for as synthesized materials

Material	S_{BET} [$m^2\ g^{-1}$]	$V_{BJH,des}$ [$cm^3\ g^{-1}$]	$D_{av,BJH}$ [nm]
CaO0	23.19	0.121	19
CaO0Ni(N)3	28.23	0.162	20
CaO0Ni(N)4.5	28.15	0.160	22
CaO0Ni(N)6	26.05	0.160	20
CaO0Ni(N)10	24.69	0.100	14
CaO0Ni(Ac)3	25.67	0.140	18
CaO0Ni(Ac)4.5	22.20	0.123	22
CaO0Ni(Ac)6	17.27	0.083	22
CaO0Ni(Ac)10	13.05	0.062	17
CaO15	14.06	0.079	22
CaO15Ni(N)3	20.85	0.098	17
CaO15Ni(N)10	12.44	0.043	11
CaO15Ni(Ac)3	23.37	0.120	20
CaO15Ni(Ac)10	13.52	0.061	18
CaO30	12.79	0.074	20
CaO30Ni(N)3	9.22	0.039	10
CaO30Ni(N)10	5.78	0.023	13
CaO30Ni(Ac)3	10.11	0.040	12
CaO45	12.96	0.096	26
CaO45Ni(N)3	11.41	0.055	17
CaO45Ni(Ac)3	10.58	0.081	30
CaO54	13.69	0.058	14
CaO54Ni(N)3	12.71	0.054	14
CaO54Ni(N)10	8.79	0.042	16
CaO54Ni(Ac)3	14.91	0.061	13
CaO54Ni(Ac)10	7.08	0.029	30

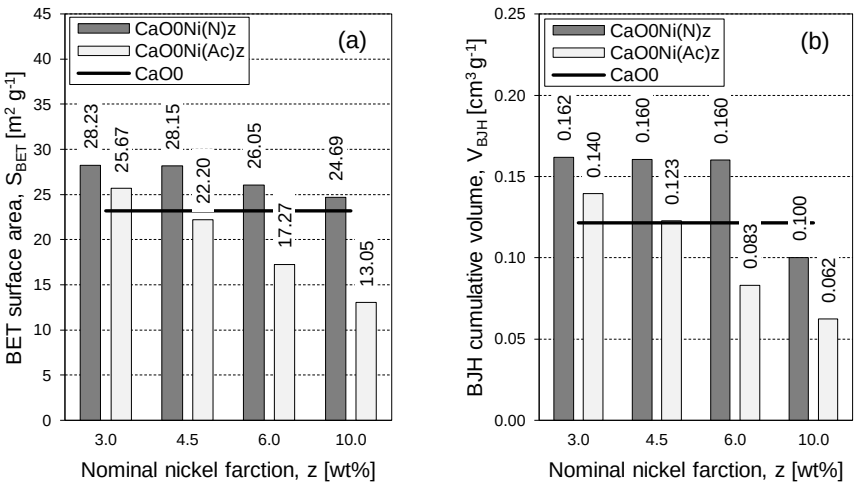

Figure 3.18: BET surface areas (S_{BET}) (a) and BJH cumulative volumes (V_{BJH}) (b) for Ni-mayenite SMR catalysts, with corresponding CaO0 values as a reference

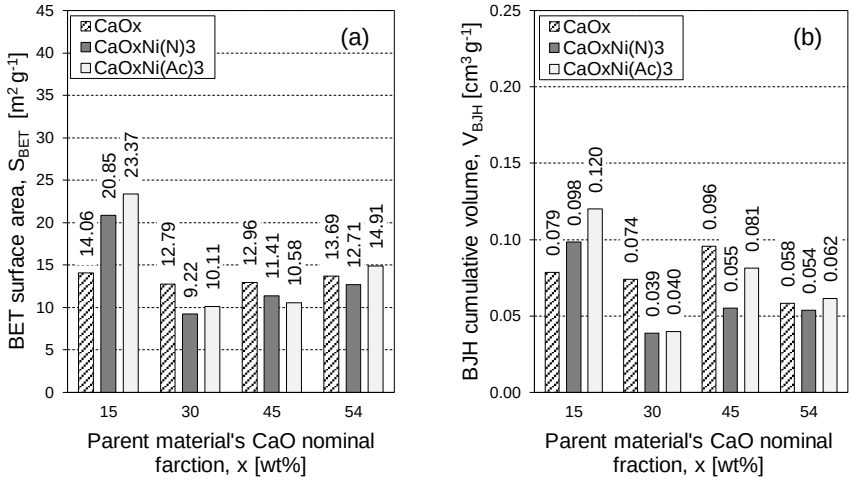

Figure 3.19: BET surface areas (S_{BET}) (a) and BJH cumulative volumes (V_{BJH}) (b) for CSCM nominally containing 3 wt% of Ni and their parent CaO-mayenite sorbents

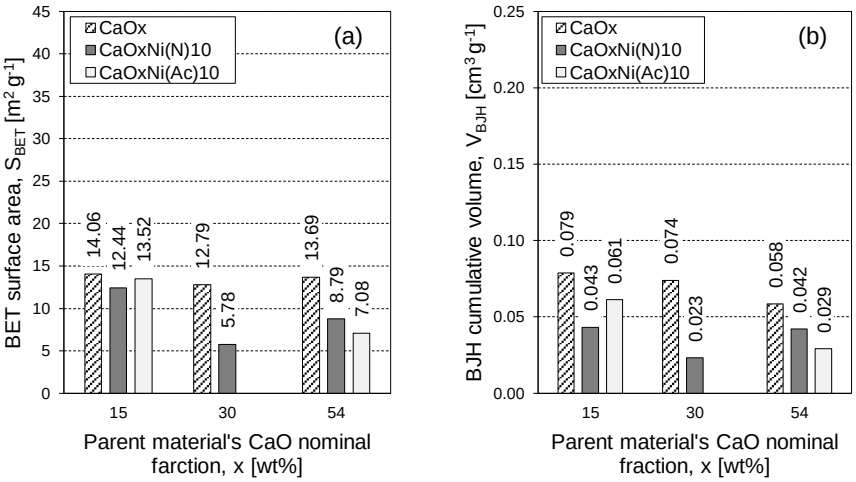

Figure 3.20: BET surface areas (S_{BET}) (a) and BJH cumulative volumes (V_{BJH}) (b) for CSCM nominally containing 10 wt% of Ni and their parent CaO-mayenite sorbents

For CSCM, the effect of free CaO fraction in the respective parent sorbents must be considered together with those from Ni fraction and its origin. Materials coming from WI of CaO15 have a different behaviour from those arising from CaO30, CaO45 and CaO54, the former being closer to Ni-mayenite trends than the others:

- After WI to obtain 3 wt% of Ni (Figure 3.19), S_{BET} and V_{BJH} of CaO15Ni(N)3 and CaO15Ni(Ac)3 significantly increase with respect to CaO15, while for other CSCM a slight decrease occurs from values shown by corresponding parent sorbents, except for CaO54Ni(Ac)3. WI by Ni(Ac) gives higher S_{BET} and V_{BJH} than those by Ni(N), respectively, except for Ca45Ni(N)3 and CaO45Ni(Ac)3;

- After WI to obtain 10 wt% of Ni (Figure 3.20), all CSCM have a decrease of S_{BET} and V_{BJH} in comparison to the respective values of their parent sorbents, more limited for CaO15 than for others, especially as far as S_{BET} is concerned; for CaO30Ni(N)10, this reduction is the most significant, probably because of singularity in its synthesis hypothesized by ICP-AES results (Table 3.1).

3.5 Reducibility properties

TPR data interpretation follows this principle: peaks of hydrogen consumption depict a chart for the interaction energies between the reducible species and their surrounding environment, the stronger the interactions the higher the reduction temperature [194]. The nature of the support, its affinity with reducible species and materials synthesis methods have a noteworthy influence [150,195,196]. Table 3.5, obtained by a cross-correlation of TPR literature data, shows a classification of different reduction peaks for NiO on Ca/Al-based materials.

3.5.1 Crystalline phases after TPR

XRD analyses on Ni-mayenite SMR catalysts (Figure 3.21) and CSCM (Figure 3.22) after TPR confirm the occurrence of NiO reduction to metallic Ni. Crystalline phases already present in as-synthesized materials are kept. $Ca(OH)_2$, occasionally found in samples after TPR (Figure 3.22), can be ascribed to CaO reactions with environmental moisture. Moreover, small traces of $Ca_3Al_2O_6$ (left shoulder on mayenite peak at 33 °) and $CaAl_4O_7$ (peak at $2\theta = 25$ °) are sometimes detected. According to calcium aluminates phase diagram (Figure 1.13), $Ca_3Al_2O_6$ is in equilibrium with mayenite for Ca/Al molar ratios higher than 6/7 and lower than 3, while $CaAl_4O_7$ equilibrates $CaAl_2O_4$ for Ca/Al molar ratios higher than 1/4 and lower than 1/2 [127]. TPR procedure nominally reaches 1000 °C, therefore acts as an additional thermal treatment on as-synthesized samples, with the potentiality to provoke new solid state reactions; in fact, the formation of these new calcium aluminates could be related to $Ca_{12}Al_{14}O_{33}$ instability in dry conditions at 1050 C, temperature close to those of the TPR dwell [127], also considering that in the used TPR device (§2.2.6) control thermocouple is not within the active packed bed.

In Ni-mayneite catalysts (Figure 3.21), $Ca_3Al_2O_6$ and $CaAl_4O_6$ are both formed during TPR: being equal the nominal Ni fraction, their XRD rays are more intense in Ni(Ac) deriving materials. In both Ni(N) and Ni(Ac) families, Ni rays intensity increases as Ni nominal fraction increases.

In CSCM after TPR (Figure 3.22), $Ca_3Al_2O_6$ is barely distinguishable only for samples with nominal 10 wt% of Ni, while $CaAl_4O_7$ is formed in traces only within samples already containing $CaAl_2O_4$ before TPR.

Table 3.6 summarizes average crystallite size estimates by Scherrer equation (Equation 2.1) for samples after TPR. With $Ca_{12}Al_{14}O_{33}$ and CaO phases, values are systematically higher, with the only exception of CaO54Ni(N)10, than those of the same material in as-synthesized state (Table 3.2), showing the occurrence of slight sintering phenomena

because of TPR heating procedure. Values estimated for Ni phase crystallites, quite homogeneous among all samples, can be used as a reference to evaluate sintering occurrence in materials tested for SMR and SESMR in the following chapters.

Table 3.5: Nature of TPR peaks in Ni-based catalysts on Ca/Al supports

Range [°C]	**Classification**	**Nature**	**Temp. [°C]**	**Support**	**Ni [wt%]**	**TPR conditions**	**Ref.**
< 350		Pure NiO	331			7 °C min^{-1} 10 vol% H_2	[197]
350-500	Weakly bonded NiO species	Segregated NiO	400	Ca(5 wt%)-γAl_2O_3	8	Not reported	[163]
		Free NiO	415	Ca(3 wt%)-γAl_2O_3	10	10 °C min^{-1} 5 vol% H_2	[164]
		Free NiO	420 500	CaO-$Ca_{12}Al_{14}O_{33}$	5	15 °C min^{-1} 10 vol% H_2	[150]
		Free NiO	440	Ca(7 wt%)-γAl_2O_3	10	10 °C min^{-1} 5 vol% H_2	[164]
		NiO in weak interaction with CaO	456	CaO	15	10 °C min^{-1} 10 vol% H_2	[174]
		Free NiO	~480	CaO-$Ca_5Al_6O_{14}$	15	10 °C min^{-1} 10 vol% H_2	[174]
		Isolated surface NiO units	400 450	$CaAl_2O_4$	11.8	7 °C min^{-1} 10 vol% H_2	[197]
500-650	Strongly bonded NiO species	Bulk phase fixed NiO	522	Ca(3 wt%)-γAl_2O_3 Ca(7 wt%)-γAl_2O_3	10	10 °C min^{-1} 5 vol% H_2	[164]
		NiO in interaction with CaO	550	CaO	5	15 °C min^{-1} 10 vol% H_2	[150]
		Bulk phase fixed NiO	553	γAl_2O_3	10	10 °C min^{-1} 5 vol% H_2	[164]
		NiO bidimensional monolayer	575	$CaAl_2O_4$	11.8	7 °C min^{-1} 10 vol% H_2	[197]
		NiO in interaction with CaO	~600	CaO-$Ca_5Al_6O_{14}$	15	10 °C min^{-1} 10 vol% H_2	[174]
		NiO in strong interaction with CaO	635	CaO	15	10 °C min^{-1} 10 vol% H_2	[174]
		NiO in interaction with $Ca_5Al_6O_{14}$	~650	CaO-$Ca_5Al_6O_{14}$	15	10 °C min^{-1} 10 vol% H_2	[174]
650-750	Nickel integrated with support components	Amorphous Ni-Ca-Al	700	$CaAl_2O_4$	11.8	7 °C min^{-1} 10 vol% H_2	[197]
		Integrated nickel	730	CaO-$Ca_5Al_6O_{14}$	15	10 °C min^{-1} 10 vol% H_2	[174]
		Ni-Al oxide (no free NiO)	750	CaO-$Ca_{12}Al_{14}O_{33}$	5	15 °C min^{-1} 10 vol% H_2	[150]
>800 [198]	$NiAl_2O_4$ spinel	$NiAl_2O_4$ spinel	820	γAl_2O_3	15	10 °C min^{-1} 10 vol% H_2	[174]
		$NiAl_2O_4$ spinel	850	$NiAl_2O_4$	15	7 °C min^{-1} 5 vol% H_2	[199]
		$NiAl_2O_4$ spinel	870 910	γAl_2O_3	8	Not reported	[163]
		$NiAl_2O_4$ spinel	870 930	αAl_2O_3	18	20 °C min^{-1} 15 vol% H_2	[200]

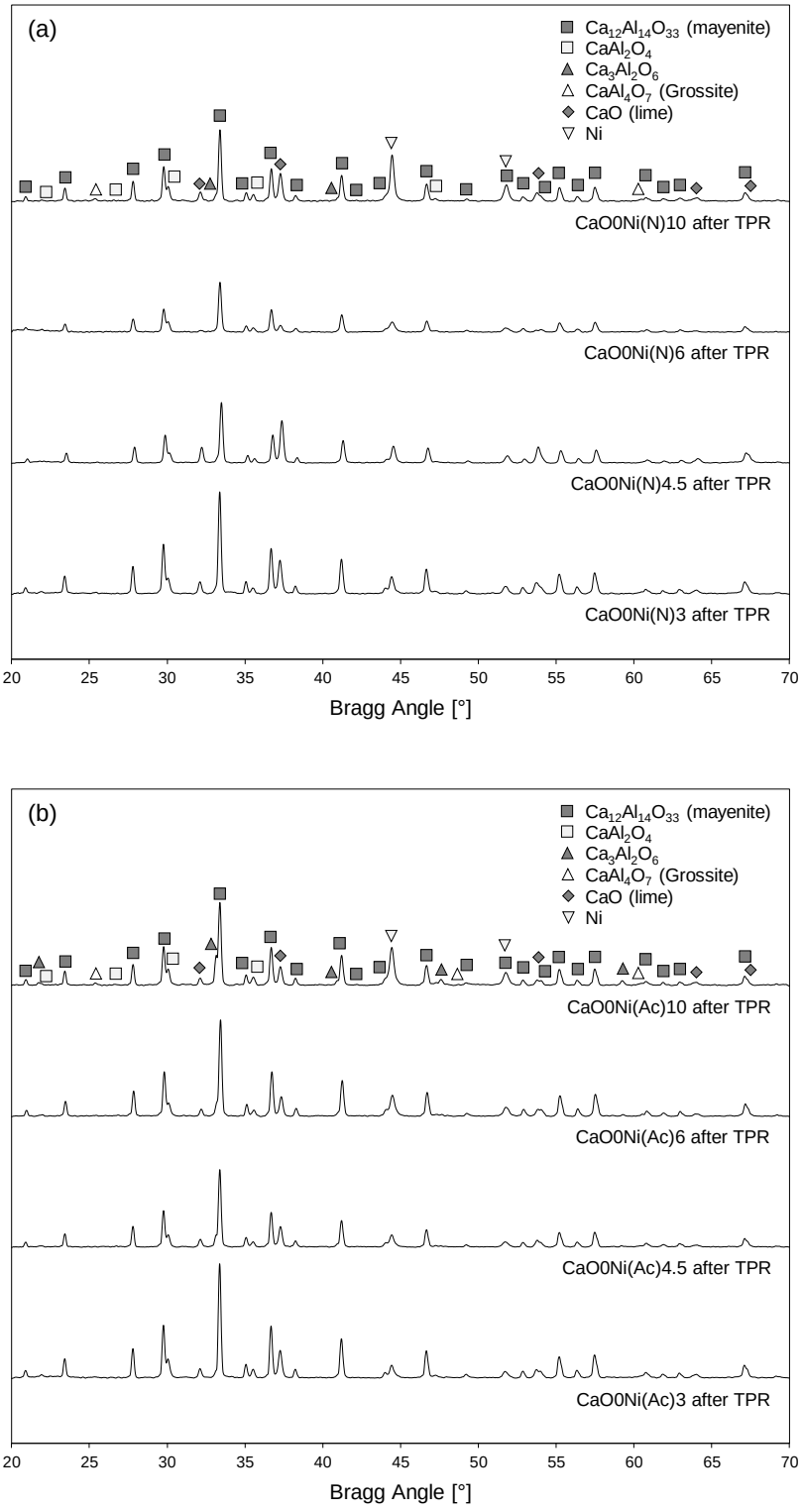

Figure 3.21: X-ray diffractograms for Ni-mayenite SMR catalyst, impregnated with Ni(N) (a) and Ni(Ac) (b), after TPR

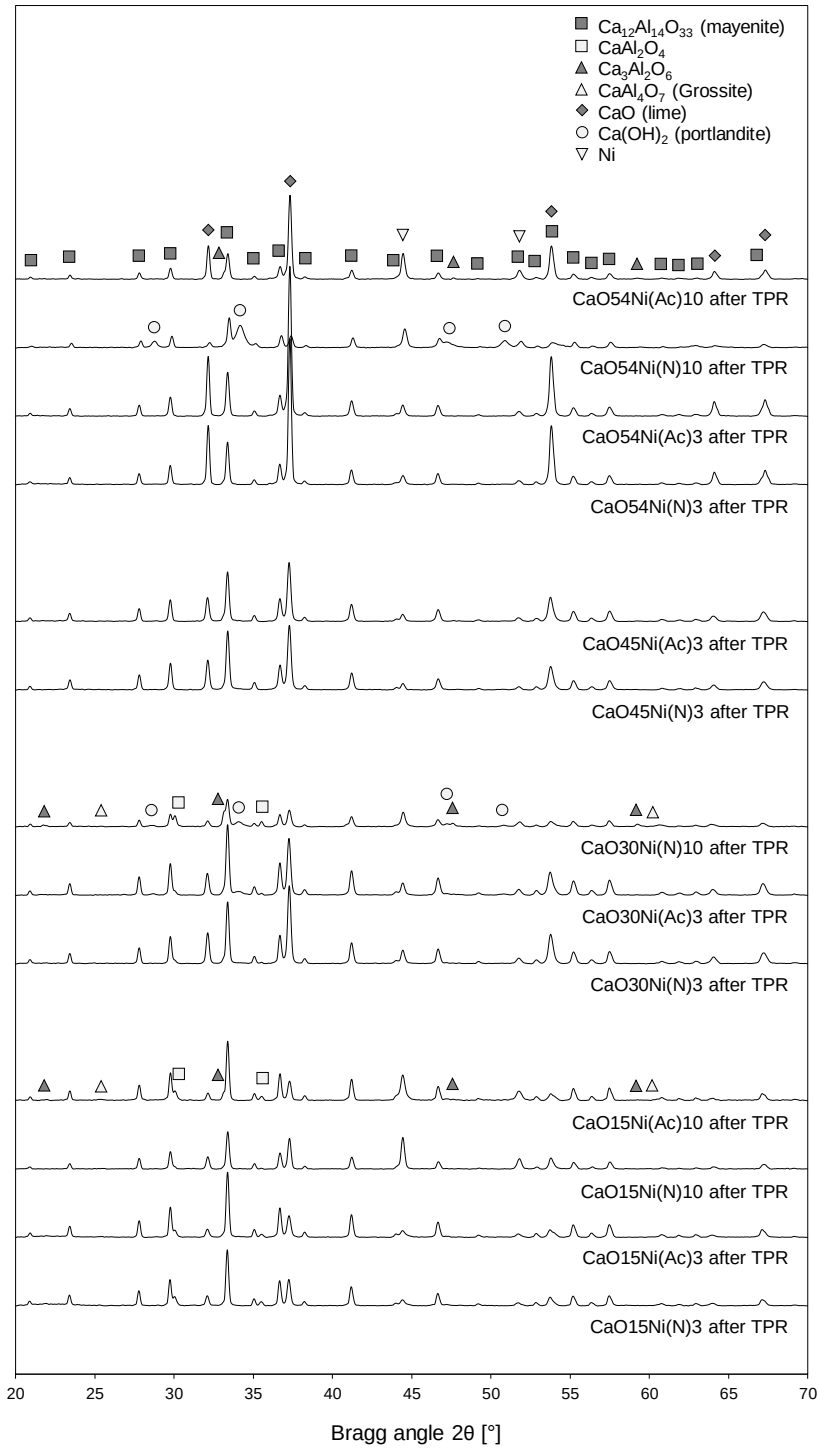

Figure 3.22: X-ray diffractograms for Ni-CaO-mayenite CSCM, impregnated with Ni(N) (a) and Ni(Ac) (b), after TPR

Table 3.6: Average crystallite size (L) estimation by Scherrer equation (Equation 2.1) for main phases of materials after TPR

Material	$Ca_{12}Al_{14}O_{33}$ [nm]	CaO [nm]	Ni [nm]
CaO0Ni(N)3	37.4	34.2	29.0
CaO0Ni(N)4.5	38.1	34.6	27.1
CaO0Ni(N)6	37.7	24.9	20.2
CaO0Ni(N)10	40.1	32.8	29.6
CaO0Ni(Ac)3	39.5	35.3	22.9
CaO0Ni(Ac)4.5	40.5	34.0	25.8
CaO0Ni(Ac)6	39.5	36.4	24.3
CaO0Ni(Ac)10	37.9	33.3	25.9
CaO15Ni(N)3	39.7	34.7	25.3
CaO15Ni(N)10	37.5	35.6	33.3
CaO15Ni(Ac)3	39.1	32.9	25.3
CaO15Ni(Ac)10	39.5	35.2	26.1
CaO30Ni(N)3	37.7	36.3	31.3
CaO30Ni(N)10	34.9	32.0	29.6
CaO30Ni(Ac)3	37.2	35.3	30.5
CaO45Ni(N)3	36.1	35.2	30.9
CaO45Ni(Ac)3	35.9	35.0	29.4
CaO54Ni(N)3	37.7	40.7	28.5
CaO54Ni(N)10	32.9	30.9	27.6
CaO54Ni(Ac)3	36.2	40.3	31.1
CaO54Ni(Ac)10	33.9	39.0	31.2

3.5.2 TPR profiles

TPR hydrogen consumption profiles for Ni-mayenite SMR catalysts are reported in Figure 3.23, showing several kinds of reduction peaks.

Ni(N) derived catalysts (Figure 3.23a) exhibit their main peak at temperatures higher than 800 °C, then related to $NiAl_2O_4$ spinel phase reduction by H_2 to metallic Ni, Al_2O_3 and water [61], the intensity of which grows with nominal Ni content. A left shoulder in the range 650-750 °C indicates the presence of Ni in strong interaction with the support structure. Peaks in the range 450-550 °C, representing NiO in moderate interaction with the support, are more and more relevant as Ni nominal fraction increases. Minor peaks from free NiO appear in the region below 400 °C.

Ni(Ac) derived catalysts (Figure 3.23b) present a different behaviour, having their main reduction peak in the range 650-685 °C, the higher the Ni fraction the more intense the peak, with a right shoulder at 775-785 °C. These temperatures correspond to Ni somehow in strong interaction with the support structure, but not in the form of $NiAl_2O_4$ spinel, to which only the smaller peaks at 910-915 °C can be related. Secondary peaks appear, ascribable to NiO in moderate (485-510 °C) and weak (400 °C or less) interactions with the support, similarly to Ni(N) derived catalysts.

TPR profiles of CSCM are in Figure 3.24, showing influence on reducibility properties from nominal fractions of free CaO and Ni.

As far as WI by Ni(N) is concerned to obtain 3 wt% of Ni (Figure 3.24a), 30 wt% of free CaO represents a boundary line for reducibility properties. In fact, the most intense peaks of CaO30Ni(N)3, CaO45Ni(N)3 and CaO54Ni(N)3 are remarkably shifted towards lower temperature (500-650 °C, NiO species in strong interaction with CaO or calcium

aluminates) when compared to the main peak of CaO0Ni(N)3. On the other hand, CaO15Ni(N)3 keeps the same reduction trend of CaO0Ni(N)3, even though it is slightly shifted towards higher temperatures, then showing the main reduction phenomena in correspondence to $NiAl_2O_4$ conversion region (835 °C and 950 °C). Similar considerations stand for CSCM containing 3 wt% of Ni from Ni(Ac) (Figure 3.24c).

In the case of WI by Ni(N) to obtain 10 wt% of Ni (Figure 3.24b), the main reduction phenomena shift towards lower temperatures with respect to CaO0Ni(N)10, therefore evidencing weaker Ni-support interactions. The main peak of CaO15Ni(N)10 falls into the zone of strongly bonded NiO (575 °C), with shoulders corresponding to weakly bonded NiO (415 °C) and amorphous Ni-Ca-Al (695 °C); just a secondary peak at 825 °C shows $NiAl_2O_4$ reduction. For CaO30Ni(N)10, reduction arises just for NiO in weak (495 °C) and stronger interactions (625 °C), with a shoulder related to amorphous Ni-Ca-Al (705 °C). A similar situation appears for CaO54Ni(N)10.

For WI to obtain 10 wt% of Ni from Ni(Ac) (Figure 3.24d), CaO15Ni(Ac)10 keeps the same reduction profile as that of CaO0Ni(Ac)10, while CaO54Ni(Ac)10 concentrates approximatively all the reduction between 400 °C and 800 °C, with two peaks at 555 °C and 630 °C due to NiO in strong interaction with CaO, and two small shoulders beyond 800 °C related to $NiAl_2O_4$.

It is worth stressing here that, in the above discussion of TPR results, high temperature peaks are attributed to $NiAl_2O_4$, even if this phase is not detected by XRD analyses on as-synthesized materials (§3.2, Figure 3.21, Figure 3.22). Nevertheless, the formation of this spinel as a surface species, hardly detectable by XRD although causing TPR high temperature peaks, is reported in literature as a factual data [61,163,174,197,201].

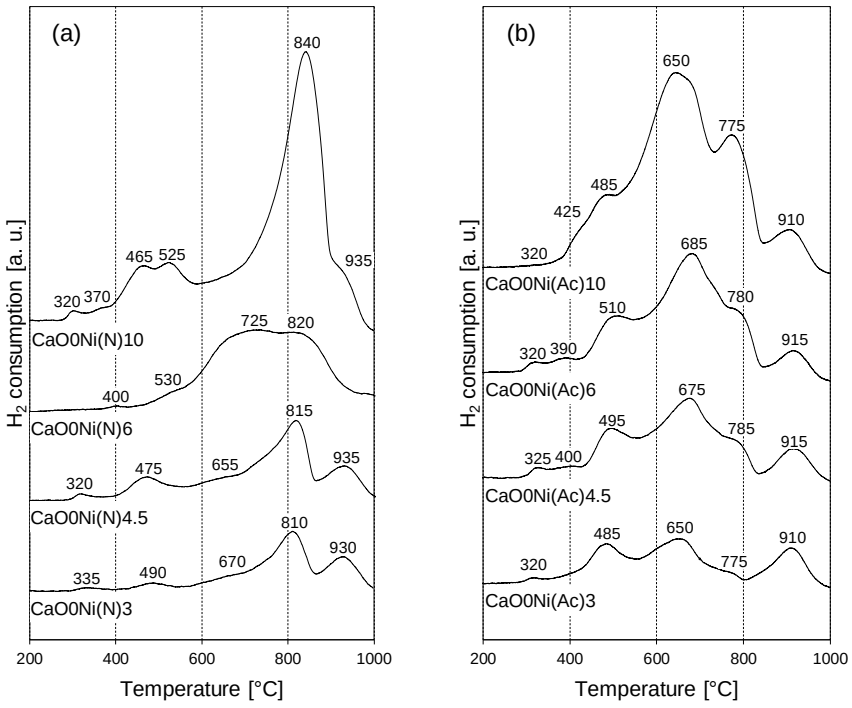

Figure 3.23: TPR profiles of Ni-mayenite SMR catalysts; numbers on curves represent temperature in °C at the maximum of the corresponding reduction peak

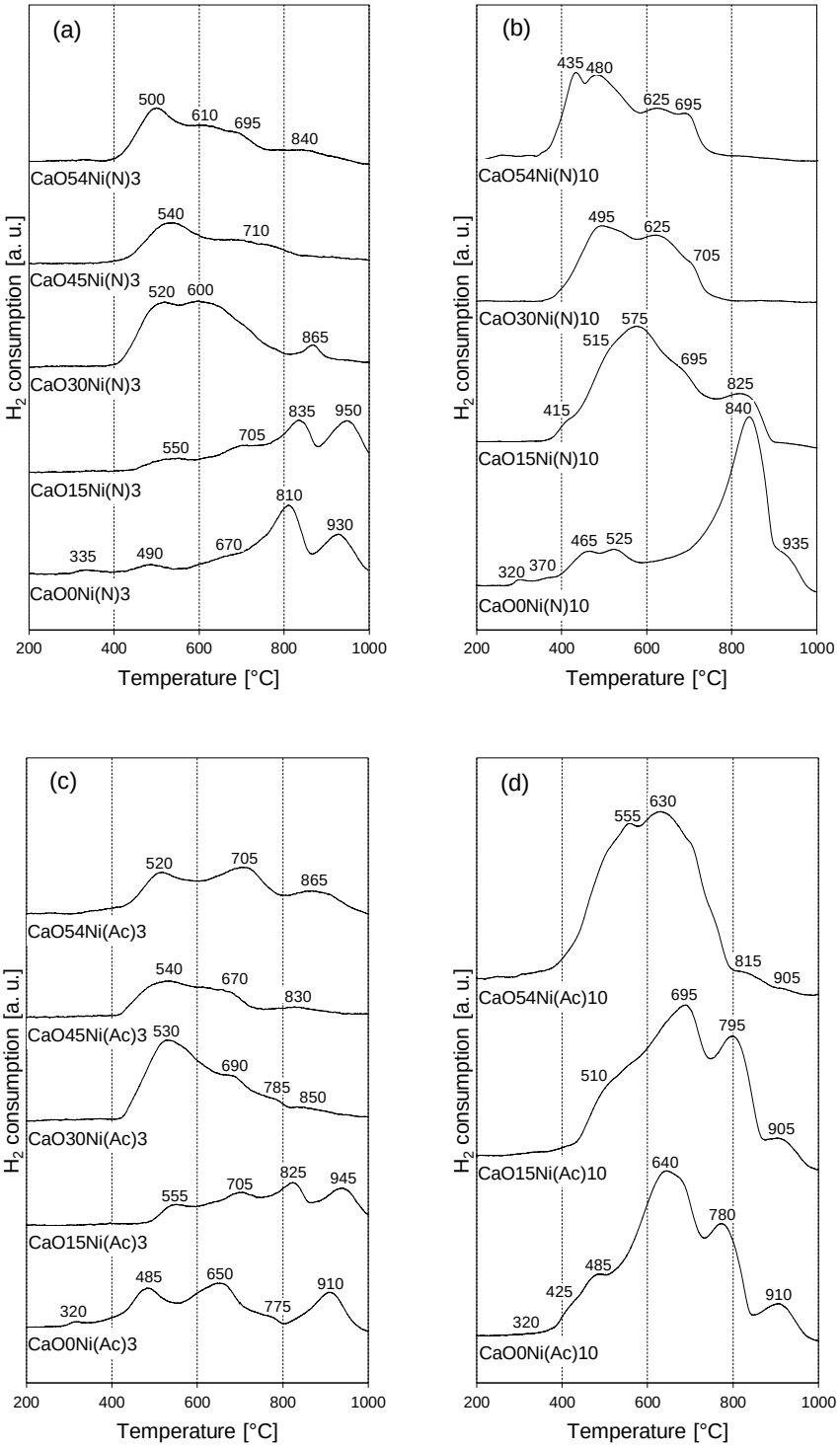

Figure 3.24: TPR profiles of materials impregnated with 3 wt% and 10 wt% of Ni from Ni acetate, 3 wt% and 10 wt% of Ni from Ni nitrate; numbers on curves represent temperature in °C at the maximum of the corresponding reduction peak

3.6 Carbon capture properties

For all synthesized CaO-mayenite sorbents and CSCM, the experimental maximum CO_2 sorption capacity (Γ_{CO2}) is determined by TGA as described in §2.2.7 (Equation 2.3). Table 3.7 summarizes experimental results and compare them with nominal sorption capacity, calculated on the basis of nominal compositions of materials in their as-synthesized state, i.e. based on the ratio between $Al(NO_3)_3 \cdot 9H_2O$ and CaO (obtained from $Ca(CH_3COO)_2 \cdot xH_2O$) utilized in wet mixing procedure, and on the ratio between masses of parent material and Ni salt precursors, Ni(N) or Ni(Ac), in wet impregnation procedure.

Table 3.7: TGA experimental results: maximum CO_2 sorption capacity (Γ_{CO2}) of CaO-mayenite sorbents and CSCM, compared to nominal sorption capacities of calcinated materials

Material	Γ_{CO2} [g_{CO2} 100 $g_{caclined\ material}^{-1}$]	**Nominal sorption capacity** [g_{CO2} 100 $g_{caclined\ material}^{-1}$]	**Efficiency [%]**
CaO15	8.6	11.8	73
CaO15Ni(N)3	9.7	11.3	86
CaO15Ni(N)10	10.3	10.3	100
CaO15Ni(Ac)3	10.2	11.3	90
CaO15Ni(Ac)10	7.1	10.3	69
CaO30	25.8	23.5	110
CaO30Ni(N)3	23.0	22.7	101
CaO30Ni(N)10	14.7	20.6	71
CaO30Ni(Ac)3	16.2	22.7	71
CaO45	24.7	35.3	70
CaO45Ni(N)3	26.3	34.0	77
CaO45Ni(Ac)3	23.8	34.0	70
CaO54	35.6	42.4	84
CaO54Ni(N)3	36.7	40.8	90
CaO54Ni(N)10	22.1	37.1	60
CaO54Ni(Ac)3	35.3	40.8	86
CaO54Ni(Ac)10	30.1	37.1	81

All materials show a relatively high sorption capacity; anyway, the situation depicted, in terms of CO_2 capture efficiencies, is rather diversified with no clear influences related to CaO or Ni contents, or Ni precursor salt. Efficiency values in Table 3.7 different from unity should not surprise: they are referred to nominal desired compositions, calculated by precursors masses under the hypothesis that only desired phases would form ($Ca_{12}Al_{14}O_{33}$, CaO, NiO), while in the real situation phases other than those counted in the nominal composition appear (Figure 3.2, Figure 3.3); in addition, ICP-AES analyses (Table 3.1) suggest the occurrence of syntheses singularities. For instance, in the case of CaO30, the 110 % efficiency could be explained by the presence of $CaAl_2O_4$ found by XRD (Figure 3.2) combined with an elemental Ca/Al mass ratio equal to the nominal one; this means a quantity of Ca engaged with Al lower than expected, or in other words a higher quantity of available free CaO. In the opposite direction, CaO45 family shows efficiencies between 70-77 % (Table 3.7), explainable by an elemental Ca/Al ratio lower than nominal one (Table 3.1) with the absence of undesired crystalline phases (Figure 3.2).

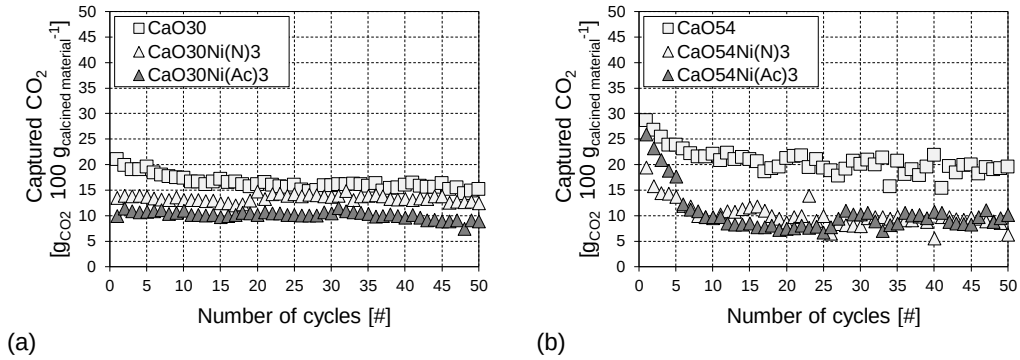

Figure 3.25: Experimental results of TGA multicycle CO_2 capture/regeneration tests

Two groups of materials underwent multicycle CO_2 capture/regeneration tests in TGA, by the procedure described in §2.2.7: CaO30, CaO30Ni(N)3, CaO30Ni(Ac)3 (Figure 3.25a) and CaO54, CaO54Ni(N)3, CaO54Ni(Ac)3 (Figure 3.25b).

Results from the two groups show a stabilization of the sorption function, roughly after the 15th cycle; however, the drop of $\gamma_{CO2}^{(i)}$ during the first 15 cycles is more important for CaO54 and its derived CSCM, while the CaO30 group suffer a very limited lowering of the same property. This confirms the positive role of mayenite as a stabilizer against CaO sintering, both in CaO-mayenite and CSCM. The effect of WI is always detrimental for sorption capacity, but more relevant in the case of CaO54 and its derived materials.

3.7 Conclusions

WM and WI methods were generally proved to be appropriate to produce Ni-mayenite SMR catalysts, CaO-mayenite CO_2 sorbents and CSCM for SESMR, as shown by the following results:

- With the exclusion of some contingent singularities, ICP-AES (§3.1) results acceptably match with desired nominal elemental compositions for all kinds of materials.
- XRD (§3.2) detects the desired phases as main components in CaO-mayenite sorbents ($Ca_{12}Al_{14}O_{33}$, CaO) and CSCM ($Ca_{12}Al_{14}O_{33}$, CaO, NiO). Average crystallite sizes of each main phase are included in a narrow specific range among materials families, assessing WI an WM crystallographic repeatability;
- From a morphological point of view (§3.3), all materials except CaO0 have in common a microgranular external structure showing porosity in the form of irregular holes and slits, with Ni located mainly in external shells and internal veins in impregnated materials;
- Texture (§3.4) is an additional common characteristic among materials synthesized by WM and WI, all presenting features ascribable to mesoporous-macroporous materials with irregular pores.

The nominal free CaO fraction in WM and WI products provides the following influence on materials properties:

- In XRD patterns (§3.2), traces of $CaAl_2O_4$, appear in materials with 30 wt% of free CaO or less. This can be explained by WM difficulties in involving Ca species in reactions with Al ones, which are resolved only when the Ca/Al molar ratio exceeds 1.8. WI does not determine relevant changes on this aspect. CaO emergence in Ni-mayenite catalysts is an additional implication of this occurrence. Anyway, $CaAl_2O_4$ formation is considered a minor defect of the synthesis, since it is a stable calcium aluminate as well as $Ca_{12}Al_{14}O_{33}$ [127], and used as a support for Ni-based materials [197].
- Regarding S_{BET} (§3.4), the presence of an intended nominal free CaO excess (15 wt% or more in the parent sorbent) decreases this property in comparison to CaO0. Moreover, WI of CaO0 and CaO15 have quite similar outcomes with a significant increase of surface area in the case of 3 wt% of Ni; on the other hand, for nominal free CaO content of 30 wt% or more, WI generally results in a decrease of the same property;
- According to TPR (§3.5), materials from WI of CaO15 behave more similarly to Ni-mayenite catalysts than to other CSCM, especially in the case of 3 wt% of Ni. As a matter of facts, their actual ICP-AES values are close to each other.
- Multicyclic CO_2 capture/regeneration tests in TGA evidence the important role of mayenite as a stabilizer of CaO in both CaO-mayenite sorbents and CSCM, the more effective the higher its mass ratio with respect to CaO.

Variation of Ni precursor salt and its fraction in WI mainly affects textural and reducibility properties:

- In Ni-mayenite catalysts, textural properties (S_{BET} and V_{BJH}) decrease as the final Ni fraction increases, more dramatically in the case of WI by Ni(Ac);
- In CSCM, impregnation effects on textural properties are combined with the starting nominal free CaO fraction of the parent sorbent, without a clear differentiation between Ni(N) and Ni(Ac). Impregnation with 10 wt% of Ni suppresses surface area and pore volume more than 3 wt%, having respective parent sorbents values as a reference;
- As demonstrated by TPR, Ni species in Ni-mayenite deriving from Ni(N) have more intense interaction than in Ni(Ac) ones; in both families, as Ni fraction increases, the specific kind of the main interaction remains unchanged;
- In CSCM, the influence of free CaO fraction on reducibility of Ni species is predominant on potential effects from variation of WI parameters: only materials derived from CaO15 keep some memory of Ni(Ac) and Ni(N) effects, as evidenced in the preceding point.

Chapter 4

Reactivity tests

This chapter reports all results from reforming tests in microreactor scale (§2.3) on Ni-mayenite catalysts, 2-material systems in separate beds and raw mixing configurations, Ni-CaO-mayenite CSCM. Evaluated parameters are:

- *Ni precursor salt and its fraction, for Ni-mayenite;*
- *Ni and free CaO fractions, together with spatial relative configurations, for 2-material systems;*
- *Ni precursor salt, Ni and free CaO fractions, for CSCM.*

4.1 Results of chemical equilibrium calculation

According to specifications in §**Errore. L'origine riferimento non è stata trovata.**, equilibrium compositions and CH_4 conversion are calculated by CHEMCAD 6.5® at experimental conditions explored in microreactor tests (§2.3). Results are summarized in Table 4.1 and assumed as reference values for the evaluation of experimental results.

Table 4.1: Results from equilibrium simulations by CHEMCAD 6.5® according to specifications in §0, for microreactor tests conditions (SESMR simulation with CaO/CH_4 inlet molar ratio = 52)

Reaction	**Temperature [°C]**	$C_{i,out}$ **[vol% dry, dil.-free]**				χ_{CH4} **[%]**
		H_2	**CH_4**	**CO**	**CO_2**	
SMR	850	76.8	0.0	16.0	7.2	100.0
SMR	750	77.1	0.1	14.1	8.7	99.8
SMR	650	77.0	0.8	11.5	10.7	96.7
SESMR	650	97.7	0.0	1.5	0.8	100.0

4.2 Preliminary tests

Some preliminary tests are carried out, by the experimental procedure developed for CSCM (§2.3.3), on the empty quartz reactor (Figure 4.1a), CaO0 (Figure 4.1b) and CaO54

since it is the sorbent with higher free CaO fraction (Figure 4.1c). The aim is to verify the absence of intrinsic reactivity caused by species other than Ni at operative conditions of interest for SESMR.

For one hour, in all examined cases, the reactivity is null, except for the first acquired point in tests on CaO0 (Figure 4.1b) and CaO54 (Figure 4.1c), showing feeble attempts of CH_4 conversion, more relevant in the former material. Anyway, this cannot be considered as a main index for SESMR occurrence, therefore one can state the test rig and parent materials before WI as such do not show reactivity towards reforming reactions.

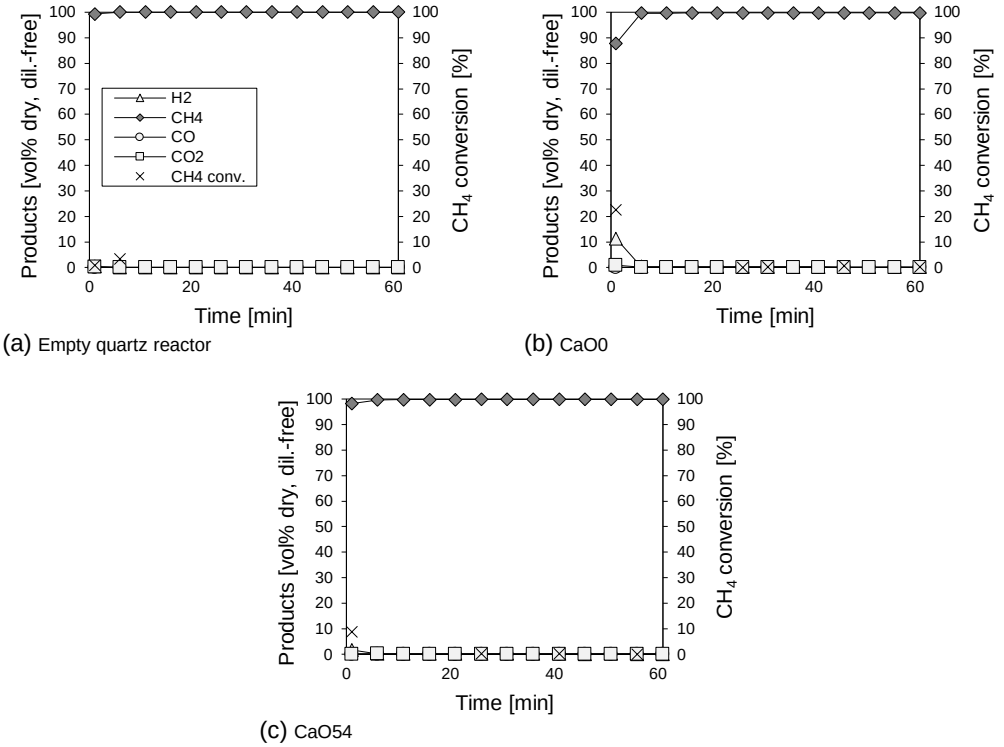

Figure 4.1: Preliminary reforming tests, according to procedure described in §2.3.3, on empty quartz reactor (a), CaO0 (b) and CaO54 (c); legend in (a) is valid for all diagrams

4.3 Ni-mayenite reactivity

Tests based on SMR-1 and SMR-2 procedures (§2.3.1) are carried out on Ni-mayenite SMR catalysts derived from both Ni(N) and Ni(Ac), scoring a total working time between 6 h and 7 h for each tested material. Afterwards, results of post-test characterization are cross-correlated with SMR reactive performances.

4.3.1 Results of reforming tests

Table 4.2 summarizes SMR catalytic activity tests on Ni-mayenite materials, evidencing a general acceptable quality of experimental measurements, attested by reported ΔC (Equation 2.9): they should be 0 for SMR under the hypothesis of no solid carbon deposition on active packed-bed particles, but their actual measured values are in the order

of $\pm 10^0$ %, which can be attributed to intrinsic experimental error, to the differences between relative compositions of SMR product and standard calibration gases, as well as carbon potential deposition in the case of negative ΔC. From the reactive point of view, very different χ_{CH4} are detected, depending on the Ni precursor salt.

Table 4.2: Experimental χ_{CH4} and ΔC from reforming activity tests on Ni-mayenite materials, according to SMR-1 and SMR-2 procedures (§2.3.1); WHSV = 0.24 Nl h^{-1} g_{cat}^{-1}; χ_{CH4} reported as a unique number results from the average of experimental measurements, χ_{CH4} as a range indicates the extreme values of a clearly increasing (↑) or decreasing (↓) trend

Material	Ni-WHSV		SMR-1				SMR-2	
	Nominal	Actual	χ_{CH4} 850 °C	χ_{CH4} 750 °C	χ_{CH4} 650 °C	ΔC	χ_{CH4} 650 °C	ΔC
	[$Nl_{CH4,in}$ h^{-1} g_{Ni}^{-1}]	[$Nl_{CH4,in}$ h^{-1} g_{Ni}^{-1}]	[%]	[%]	[%]	[%]	[%]	[%]
CaO0Ni(N)10	2.4	2.1	100.0	100.0	97.8	-3.3	96.4	-5.6
CaO0Ni(N)6	4.0	6.3	100.0	99.6	96.7	-5.2	96.5	-7.2
CaO0Ni(N)4.5	5.3	5.8	100.0	100.0	97.3	-0.5	97.1	-7.3
CaO0Ni(N)3	8.0	8.3	100.0	99.5	96.7	+2.7	96.2	-5.5
CaO0Ni(Ac)10	2.4	2.4	81.7 ↑ 90.3	33.3 ↑ 37.3	5.9	-1.3	10.2 ↓ 4.4	+1.3
CaO0Ni(Ac)6	4.0	3.9	94.2	45.9	7.1	-3.6	19.5 ↓ 5.4	-0.1
CaO0Ni(Ac)4.5	5.3	5.3	83.1 ↑ 92.3	39.1 ↑ 42.3	6.2	-2.6	14.7 ↓ 2.8	-0.8
CaO0Ni(Ac)3	8.0	7.7	59.1 ↑ 92.6	40.1 ↑ 45.0	7.4	-1.5	19.5 ↓ 4.3	+0.0

Figure 4.2 reports SMR results for Ni-mayenite catalysts from Ni(N). Their performances always stabilize around values very close to SMR equilibrium (Table 4.1 as a reference), whatever the nominal Ni fraction in the range from 3 wt% to 10 wt%. As far as SMR-1 is concerned, χ_{CH4} is complete at 850 °C (i.e. no CH_4 detectable downstream), almost complete at 750 °C, and with a further decrease of some percentage points at 650 °C. During the transition between 750 °C and 650 °C, $C_{H2,out}$ is temporary higher than its expected equilibrium value (Table 4.1 as a reference), especially for CaO0Ni(N)3 and CaO0Ni(N)4.5; this can be ascribed to a sorption enhancing effect due to residual CaO found in as-synthesized materials (Figure 3.1a). For each material, χ_{CH4} in SMR-1 at 650 °C is slightly higher than in SMR-2. This can be related to the two different SMR triggering environments at 650 °C in the two cases: already developed H_2 in SMR-1 and only reactants (CH_4 and $H_2O_{(v)}$) diluted in Ar in SMR-2, the former being more reductive than the latter [133]. Another hypothesis is a fatigue underwent by catalysts, due to the transition between SMR-1 and SMR-2.

The situation radically changes for Ni-mayenite SMR catalysts from Ni(Ac) (Figure 4.3). They generally show a dramatic decrease of SMR catalytic activity in comparison with materials from Ni(N) (Table 4.2), very far from SMR equilibrium achievement (Table 4.1 as a reference). In SMR-1 experiments, for all Ni(Ac) catalysts except CaO0Ni(Ac)6, a kind of systematic self-activation occurs at 850 °C and 750 °C, as can be seen by χ_{CH4} increasing trends (Figure 4.3a, Figure 4.3c, Figure 4.3e, Figure 4.3g, Table 4.2); this could be related to the conversion of carbonaceous deposits documented in Figure 3.14. The influence of temperature is considerable: χ_{CH4} reaches values higher than 90 % at 850 °C, passes through a range between 33 % and 46 % at 750 °C, and eventually gets to less than 8 % at 650 °C. It is worth to stress here that all tested materials undergo the same

pre-reduction process (§2.3.1) and that, before the end of its final dwell at 900 °C, H_2 consumption always ends to zero for all reported experiments, confirming the occurrence of the maximum Ni reduction achievable at operating conditions. As far as SMR-2 is concerned, all Ni-mayenite catalysts from Ni(Ac) exhibit the same pattern: an initial attempt of reaction, with an exponential decrease towards χ_{CH4} lower than those obtained by SMR-1 procedure at 650 °C.

4.3.2 Post-test characterization

After reforming tests documented in §4.3.1, Ni-mayenite materials are examined by XRD (Figure 4.4). For both Ni(N) (Figure 4.4a) and Ni(Ac) (Figure 4.4b) derived materials, Ni is located only in its reduced metallic state, formed by the pre-reduction operated at the beginning of each test (§2.3.1). No NiO is detected in post-test samples (Figure 4.4), so no bulk re-oxidation of catalytic phase occurred. Formation of $CaCO_3$ in Ni-mayenite from Ni(N) results from Figure 4.4a, in agreement with observed occurrence of sorption enhancing during the cooling phase between 750 °C and 650 °C. No other relevant variations are detected by a comparison with materials in their as-synthesized state (Figure 3.1).

Table 4.3 reports results of *L* estimates by Scherrer equation (Equation 2.1) for Ni-mayenite materials after SMR catalytic reforming tests. For $Ca_{12}Al_{14}O_{33}$, post-test *L* are systematically higher than in as-synthesized state (Table 3.2), evidencing the occurrence of a slight sintering, similarly to TPR (Table 3.6). The same consideration is valid for unconverted residual CaO in Ni(Ac) catalysts, whereas detected *L* of $CaCO_3$ are 29.8 nm in CaO0Ni(N)3 and 34.3 nm in CaO0Ni(N)4.5, slightly higher than dimensions of corresponding originating CaO crystallites (Table 3.2). Metallic Ni diameters are quite similar to those obtained after TPR, so the catalytic active phase does not undergo severe sintering within the reaction environment.

TEM micrographs of CaO0Ni(N)10 and CaO0Ni(Ac)10 after reforming tests are in Figure 4.5. Dark spheroidal particles are metallic Ni, as inferred by cross-correlating STEM-EDS elemental analyses detecting elemental Ni (Figure 4.6a and Figure 4.6c, where they correspond to brighter zones) and XRD spectra locating metallic Ni as the only Ni-containing phase (Figure 4.4). The main difference is in the developing of proto-filamentous, carbonaceous structures nearby these Ni particles in CaO0Ni(N)10 after SMR (Figure 4.5b), but not in CaO0Ni(Ac)10 (Figure 4.5d). The presence of elemental carbon in CaO0Ni(N)10 is confirmed by STEM-EDS (Figure 4.6b). Basing on experimental reforming results (Table 4.2), CaO0Ni(N)10 fully develops SMR (Figure 4.2a, Figure 4.2b) while CaO0Ni(Ac)10 is very less reactive (Figure 4.3a, Figure 4.3b), so these structures could be a signal of a higher Ni affinity towards solid carbon-containing species in the case of Ni(N) derived catalysts, in comparison with the Ni(Ac) ones.

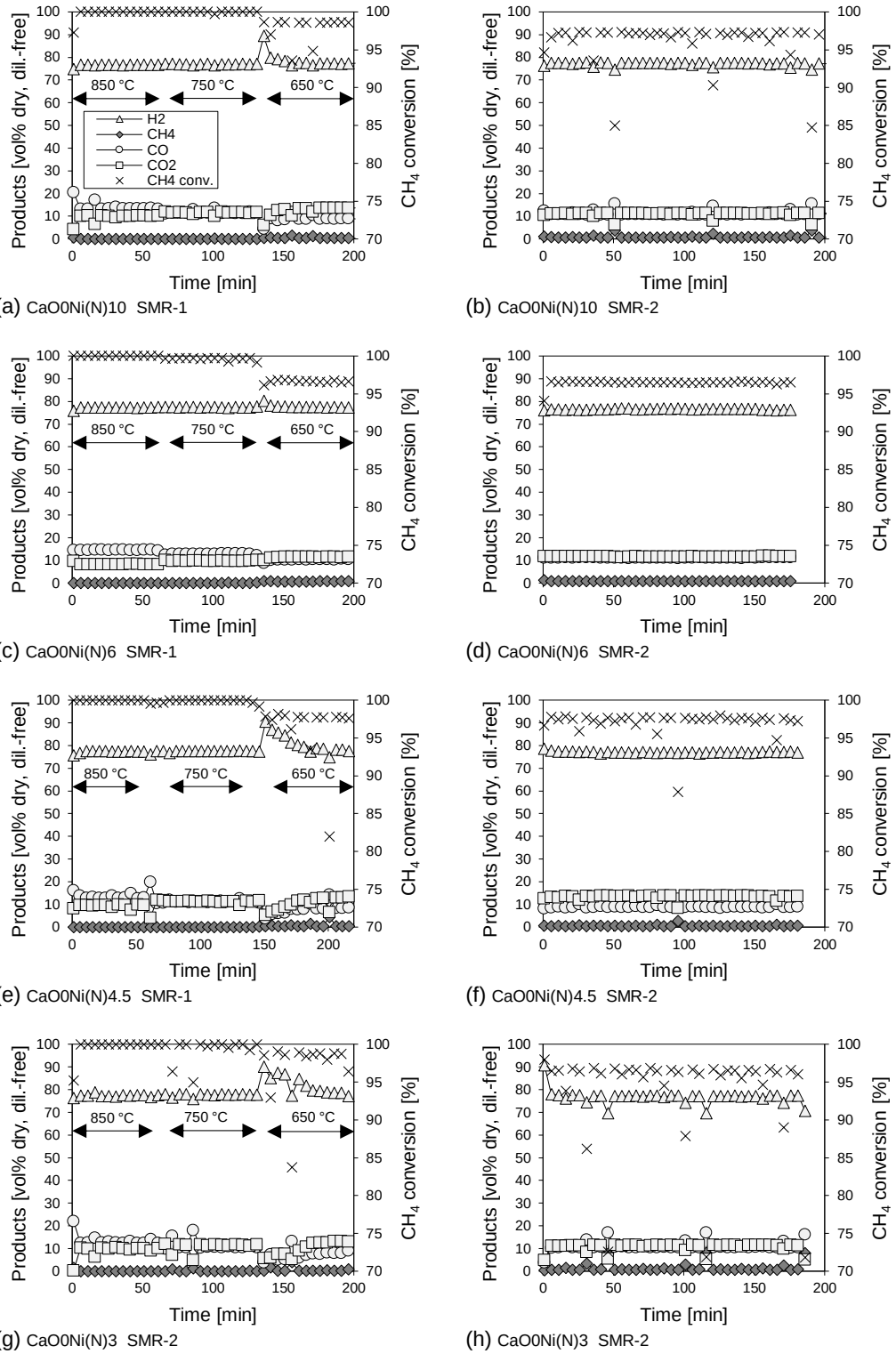

Figure 4.2: Results from reforming tests on CaO0Ni(N)10 (a, b), CaO0Ni(N)6 (c, d), CaO0Ni(N)4.5 (e, f), CaO0Ni(N)3 (g, h); first column descends from SMR-1 procedure, second column from SMR-2 procedures (§2.3.1); legend in (a) is valid for all diagrams

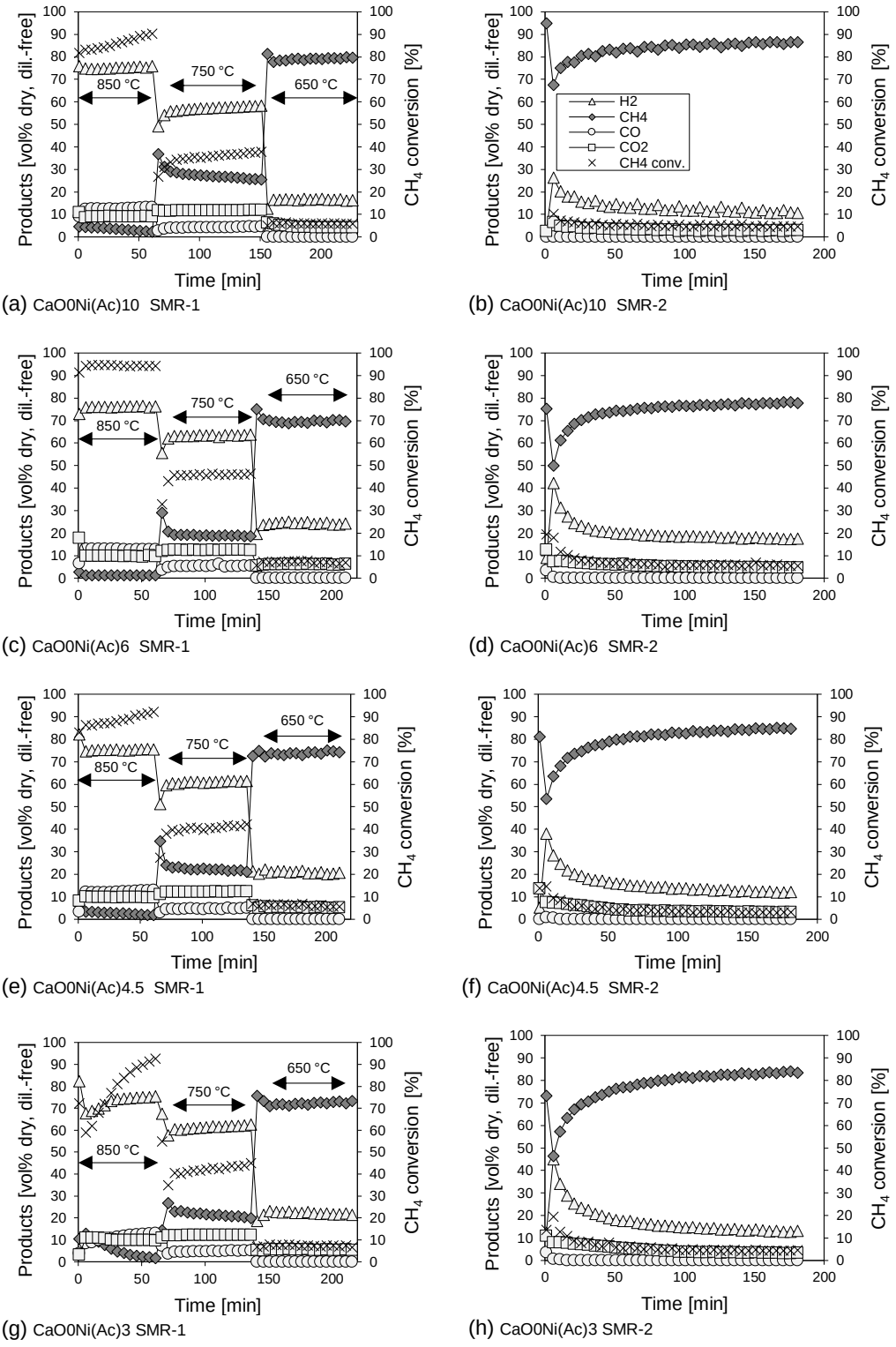

Figure 4.3: Results from reforming tests on CaO0Ni(Ac)10 (a, b), CaO0Ni(Ac)6 (c, d), CaO0Ni(Ac)4.5 (e, f), CaO0Ni(Ac)3 (g, h); first column descends from SMR-1 procedure, second column from SMR-2 procedures (§2.3.1); legend in (b) is valid for all diagrams

Table 4.3: Average crystallite size (L) estimation by Scherrer equation (Equation 2.1) for main phases of Ni-mayenite SMR catalysts after reforming tests by SMR-1 and SMR-2 procedures (§2.3.1)

Material	$Ca_{12}Al_{14}O_{33}$ [nm]	CaO [nm]	$CaCO_3$ [nm]	Ni [nm]
CaO0Ni(N)3	36.7	/	29.8	27.3
CaO0Ni(N)4.5	36.7	/	34.3	29.6
CaO0Ni(N)6	36.9	/	/	24.5
CaO0Ni(N)10	38.4	/	/	28.5
CaO0Ni(Ac)3	38.8	35.0	/	24.9
CaO0Ni(Ac)4.5	39.3	36.6	/	23.8
CaO0Ni(Ac)6	39.1	38.3	/	25.2
CaO0Ni(Ac)10	38.2	34.4	/	25.5

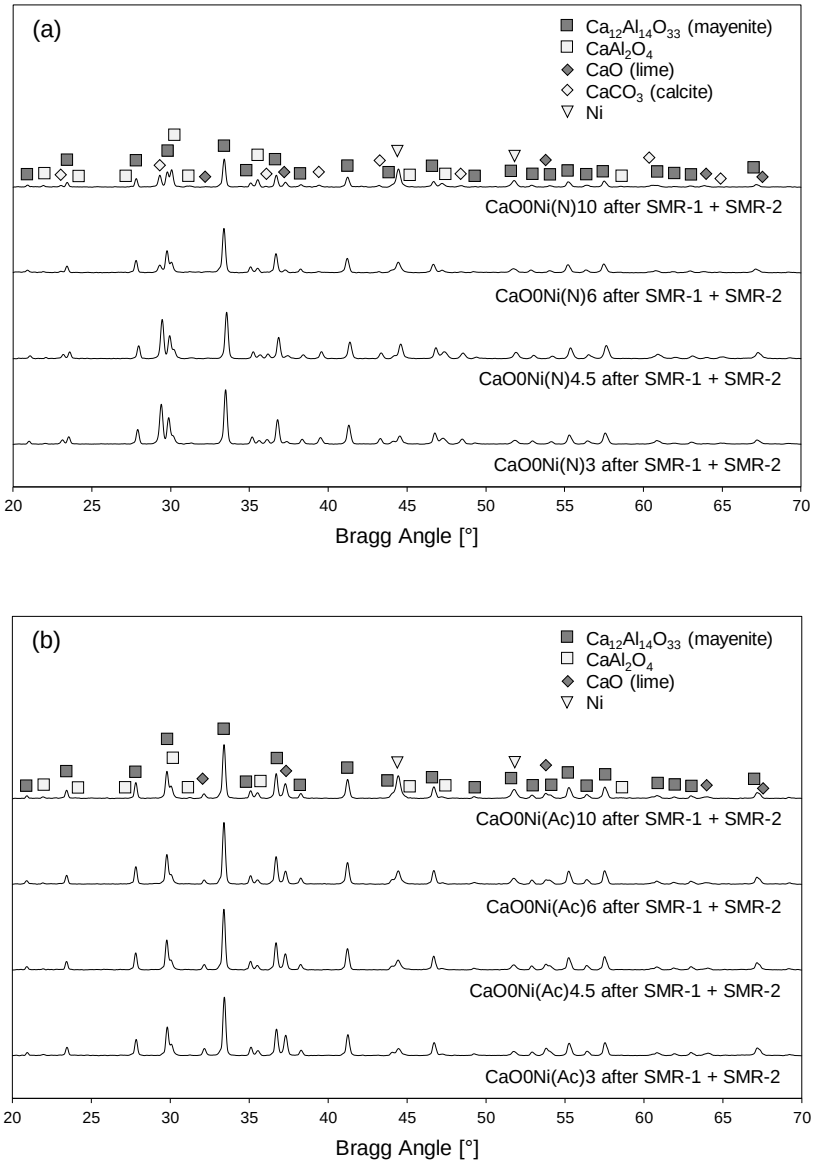

Figure 4.4: X-ray diffractograms for Ni-mayenite SMR catalysts impregnated with Ni(N) (a) and Ni(Ac) (b), after reforming tests by SMR-1 and SMR-2 procedures (§2.3.1)

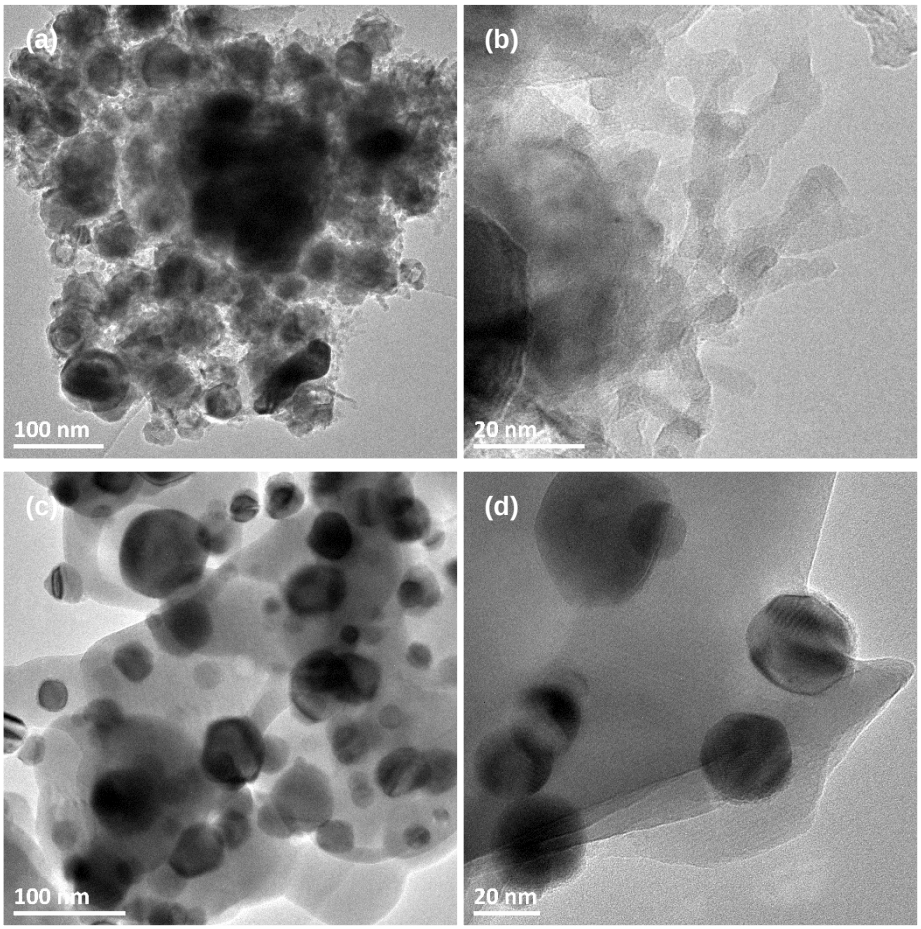

Figure 4.5: TEM micrographs of CaO0Ni(N)10 (a) (b) and CaO0Ni(Ac)10 (c) (d) after reforming tests by SMR-1 and SMR-2 procedures (§2.3.1)

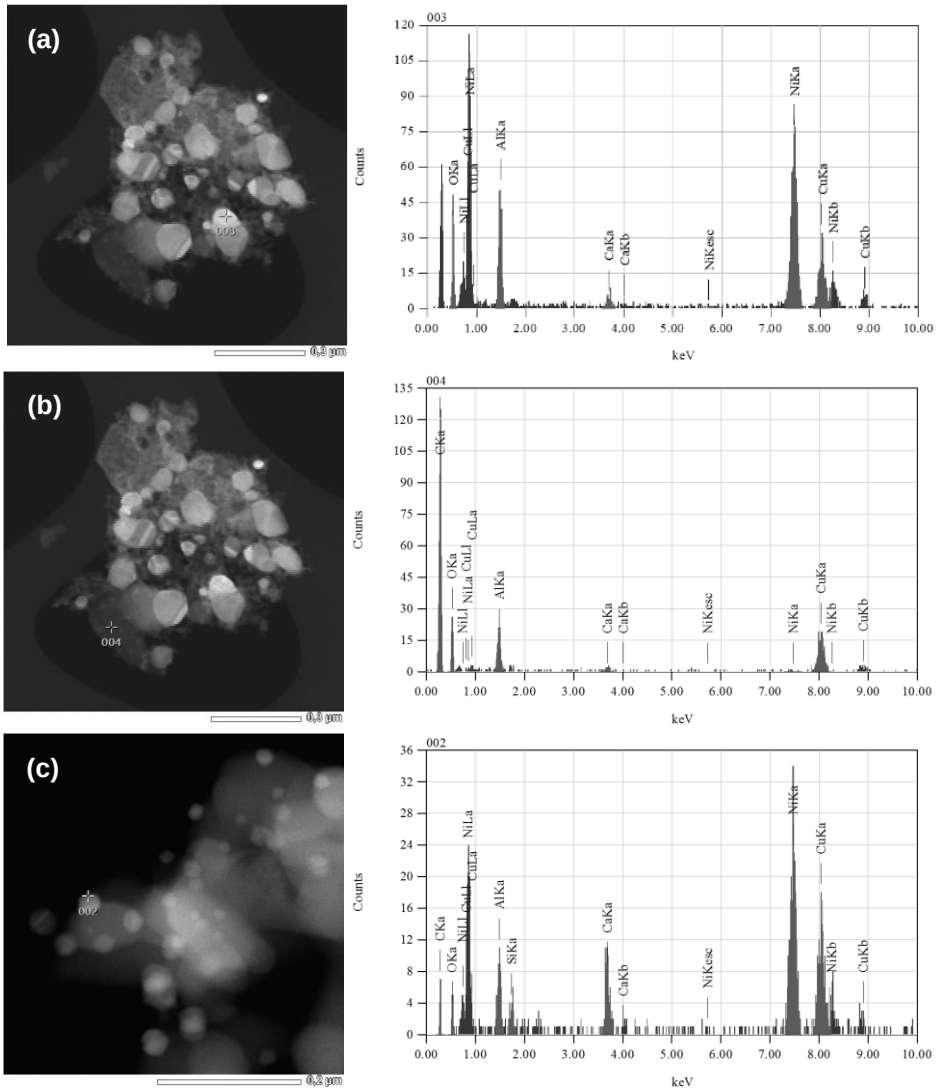

Figure 4.6: STEM-EDS analyses on CaO0Ni(N)10 (a) (b) and CaO0Ni(Ac)10 (c) after reforming tests by SMR-1 and SMR-2 procedures (§2.3.1)

4.4 Reactivity of 2-material systems

Tests on 2-material systems are carried out by the method reported in §2.3.2, choosing appropriate combinations of materials, in both separate beds and raw mixing configurations.

Only Ni-mayenite catalysts deriving from Ni(N) are used in these tests, while the homologous Ni(Ac) series is completely excluded, because of their very scarce catalytic activity exhibited towards SMR at 650 °C, the temperature of interest for SESMR (§4.3.1).

4.4.1 Results of separate beds tests

Table 4.4 lists all 2-material systems undergoing reforming tests in separate beds configuration, also summarizing main experimental results in the form of χ_{CH4} and ΔC before and after breakthrough completion time (t^*), empirically located among sampling test times (t) by means of $C_{H2,out}$ and $C_{CO2,out}$ stabilization, related to sorbent saturation.

Table 4.4: Experimental χ_{CH4} and ΔC from reforming activity tests on 2-material systems in separate beds configuration, according to §2.3.2 procedure; WHSV = 0.60 Nl h^{-1} g_{cat}^{-1}; χ_{CH4} results from the average of experimental measurements acquired in the considered time range

Catalyst		Sorbent	Ni-WHSV Nominal [$Nl_{CH4,i}$ h^{-1} g_{Ni}^{-1}]	Ni-WHSV Actual [$Nl_{CH4,in}$ h^{-1} g_{Ni}^{-1}]	t^* [min]	χ_{CH4} $t \le t^*$ [%]	χ_{CH4} $t > t^*$ [%]	ΔC $t \le t^*$ [%]	ΔC $t > t^*$ [%]
CaO0Ni(N)10	→	CaO54	6.0	5.1	56	95.8	95.8	+44.5	-3.6
CaO0Ni(N)10	→	CaO45	6.0	5.1	51	95.9	96.0	+38.0	-7.6
CaO0Ni(N)10	→	CaO30	6.0	5.1	51	95.9	96.1	+28.9	-8.6
CaO0Ni(N)10	→	CaO15	6.0	5.1	36	95.5	95.5	+33.3	-6.0
CaO0Ni(N)3	→	CaO54	20.0	20.7	76	94.9	94.9	+35.1	-5.1

Basically, in this configuration, all tested materials fully proved their functionality, as shown in Figure 4.7 and Figure 4.8.

Although WHSV are higher than those adopted in §4.3.1, both CaO0Ni(N)10 (Figure 4.7) and CaO0Ni(N)3 (Figure 4.8) stably sustain SMR reaction, with high χ_{CH4}, initial $C_{H2,out}$ roughly at 90 vol% dry, dilution-free, and post-breakthrough product concentrations approaching SMR equilibrium values at the operating conditions (compare Table 4.1 values for SMR at 650 °C to Figure 4.7).

CaO-mayenite sorbents capture CO_2 at 650 °C (Reaction 1.5) and in presence of steam, as evidenced by profiles of products concentrations before t^*: $C_{H2,out}$ is higher than its SMR equilibrium concentration, while $C_{CO,out}$ and $C_{CO2,out}$ are lower (compare with Table 4.1 values). Carbon balances performed between the beginning of each test and t^* gives largely positive ΔC (Table 4.4), therefore corroborating the hypothesis of CO_2 capture by CaO carbonation (Reaction 1.5). Negative values of ΔC after t^* (Table 4.4) are similar to those detected for SMR tests on Ni-mayenite (Table 4.2), and the same possible explanations given in §4.3.1 could be applied to this case. In the series of CaO0Ni(N)10 coupling all available sorbents, t^* decreases as sorbent CaO fraction decreases, as expected. The relevant similarity between breakthrough profiles and t^* from tests with CaO45 and CaO30

could be related to the actual lack of CaO in the former sorbent with respect to its nominal faction, measured by ICP-AES (Table 3.1).

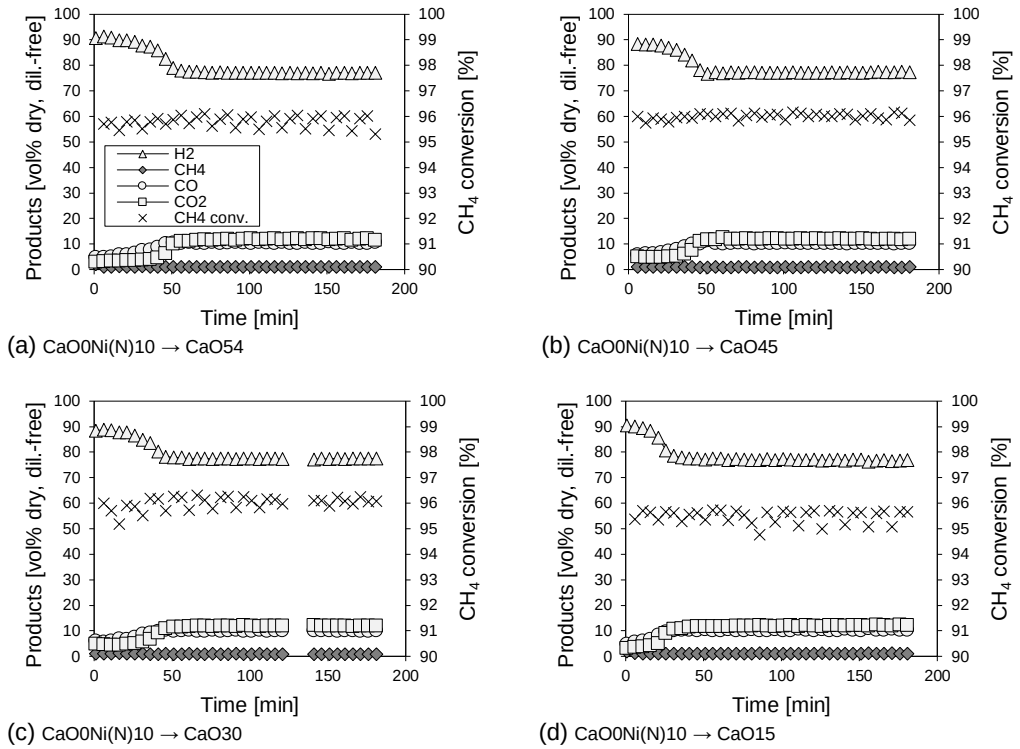

Figure 4.7: Results from reforming tests on 2-material systems in separate beds configuration counting CaO0Ni(N)10 as a catalyst, followed by CaO54 (a), CaO45 (b), CaO30 (c), CaO15 (d) as sorbents; legend in (a) is valid for all diagrams

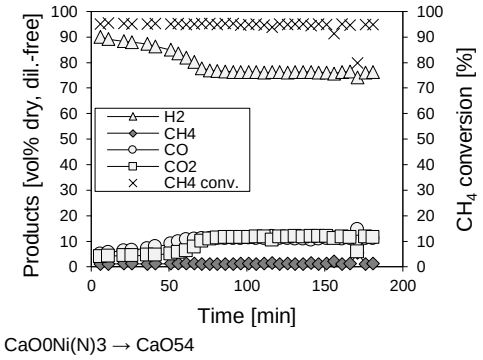

Figure 4.8: Results from reforming tests on 2-material system in separate beds configuration counting CaO0Ni(N)3 as a catalyst followed by CaO54 as a sorbent

4.4.2 Separate beds: post-test characterization

After tests described in §4.4.1, catalyst and sorbent beds were separately recovered from the reactor, for post-test characterization.

XRD of post-test Ni-mayenite catalysts (Figure 4.9a), compared with their as-synthesized state (Figure 3.1a), show the appearance of metallic Ni and $CaCO_3$ in place of NiO and CaO, respectively. Metallic Ni is formed during the pre-reduction step (§2.3.2)

and preserved during the reforming step in each test, as NiO is not detected. $CaCO_3$ derives from the carbonation (Reaction 1.5) of residual CaO detected in as-synthesized state (Figure 3.1a), similarly to what already noted in §4.3.2 for post-test Ni-mayenite catalysts derived from Ni(N). With regard to CaO-mayenite sorbents (Figure 4.9b), the occurrence of carbonation (Reaction 1.5) is attested by $CaCO_3$ detection together with traces of unreacted CaO.

Table 4.5: Average crystallite size (L) estimation by Scherrer equation (Equation 2.1) for Ni-mayenite SMR catalysts impregnated with Ni(N), after tests on 2-material systems in separate beds configuration

Material	**Other bed**	**$Ca_{12}Al_{14}O_{33}$ [nm]**	**$CaCO_3$ [nm]**	**Ni [nm]**
CaO0Ni(N)10	(→ CaO54)	36.9	29.2	28.1
CaO0Ni(N)10	(→ CaO45)	37.0	29.5	28.5
CaO0Ni(N)10	(→ CaO30)	37.2	28.6	28.5
CaO0Ni(N)10	(→ CaO15)	36.5	31.6	28.0
CaO0Ni(N)3	(→ CaO54)	31.0	26.0	26.4

Table 4.6: Average crystallite size (L) estimation by Scherrer equation (Equation 2.1) for CaO-mayenite sorbents, after tests on 2-material systems in separate beds configuration

Material	**Other bed**	**$Ca_{12}Al_{14}O_{33}$ [nm]**	**$CaCO_3$ [nm]**
CaO54	(CaO0Ni(N)10 →)	35.8	32.0
CaO45	(CaO0Ni(N)10 →)	32.9	29.9
CaO30	(CaO0Ni(N)10 →)	35.4	31.1
CaO15	(CaO0Ni(N)10 →)	34.9	28.5
CaO54	(CaO0Ni(N)3 →)	32.3	31.1

Table 4.7: Measured BET surface areas (S_{BET}), BJH cumulative volumes (V_{BJH}) and averaged pore diameters ($D_{av,BJH}$) for CaO-mayenite sorbents after tests in separate beds configuration; ΔS_{BET}, ΔV_{BJH} and $\Delta D_{av,BJH}$ are the percentage variations with respect to corresponding values in as-synthesized state

Material	**Other bed**	**S_{BET} [$m^2\ g^{-1}$]**	**ΔS_{BET} [%]**	**V_{BJH} [$cm^3\ g^{-1}$]**	**ΔV_{BJH} [%]**	**$D_{av,BJH}$ [nm]**	**$\Delta D_{av,BJH}$ [%]**
CaO54	(CaO0Ni(N)10 →)	2.75	-80	0.014	-76	20	+43
CaO45	(CaO0Ni(N)10 →)	5.26	-59	0.030	-69	17	-34
CaO30	(CaO0Ni(N)10 →)	6.50	-49	0.041	-45	17	-15
CaO15	(CaO0Ni(N)10 →)	4.96	-65	0.036	-54	32	-45
CaO54	(CaO0Ni(N)3 →)	2.48	-82	0.010	-83	17	-21

Table 4.5 resumes the evaluations of *L* (Equation 2.1) for main crystalline phases of Ni-mayenite catalysts after tests in separate beds configuration, as well as Table 4.6 makes for respective post-test CaO-mayenite sorbents. Except for CaO0Ni(N)3, *L* of $Ca_{12}Al_{14}O_{33}$ is always slightly higher in post-tests samples than in as-synthesized state (Table 3.2), pointing to the occurrence of mild sintering phenomena. Concerning metallic Ni in post-test catalysts (Table 4.5), its *L* is not so far from values obtained after TPR (Table 3.6) or after SMR catalytic tests (Table 4.3), then confirming the absence of severe sintering of Ni-mayenite at the operating conditions chosen for SESMR test. $CaCO_3$ crystallite size ranges between 26.0 nm and 31.6 nm for post-test Ni-mayenite catalysts (Table 4.5) and between 28.5 nm and 32.0 nm for post-test CaO-mayenite (Table 4.6), a shift towards

slightly higher values one could relate to the lower content of mayenite, turning into a weaker action against sintering; in fact, CaO54 has the two higher measured *L* (Table 4.6)

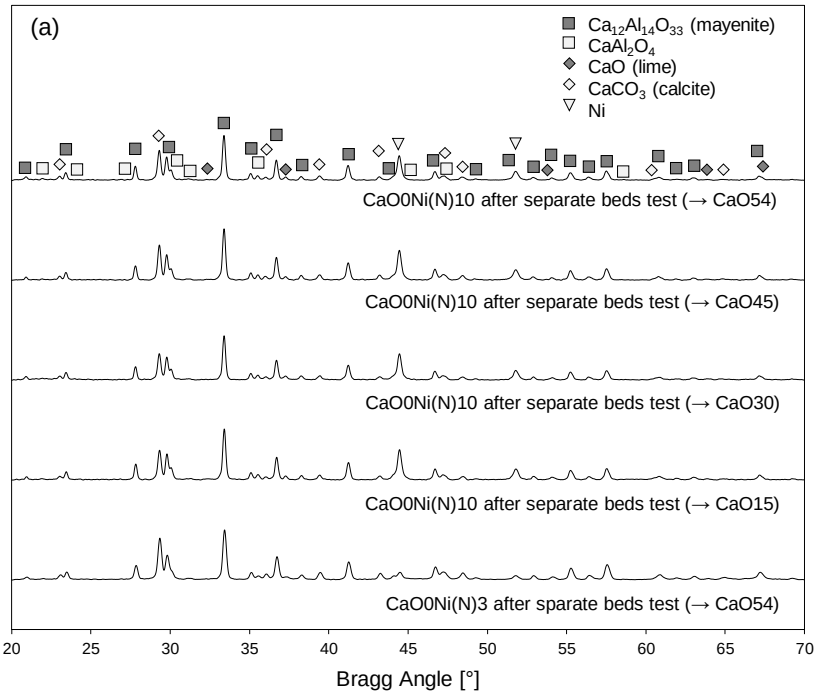

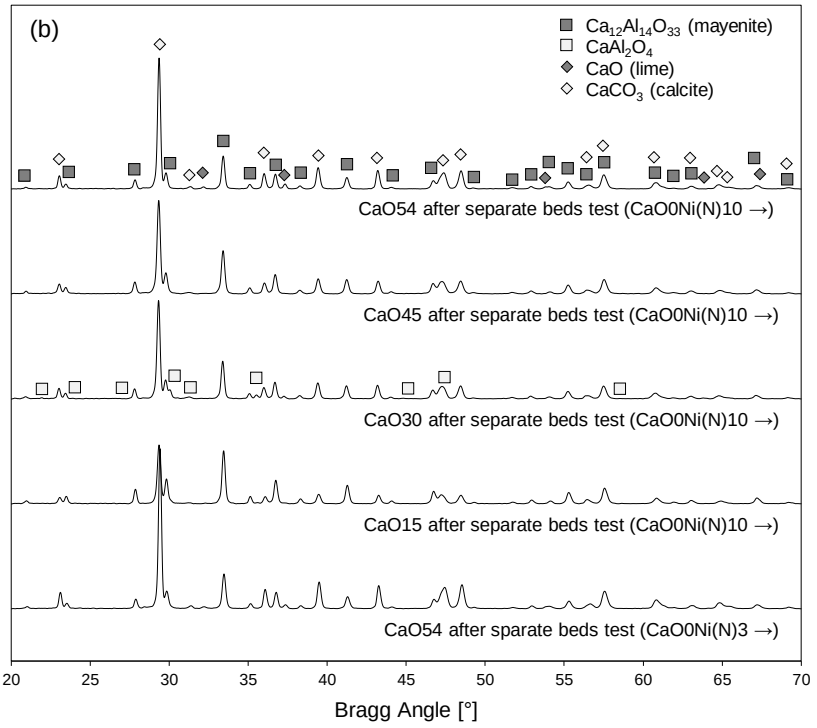

Figure 4.9: X-ray diffractograms for Ni-mayenite SMR catalysts impregnated with Ni(N) (a) and CaO-mayenite sorbents (b), after tests on 2-material systems in separate beds configuration; the material in the other bed during the tests is indicated within round brackets

Table 4.7 reports textural properties measurements for CaO-mayneite sorbents after tests in separate beds configuration. Because of experimental procedure and events, sorbents are in their carbonated state, as corroborated by XRD analyses (Figure 4.9b). Because of the difference between CaO and $CaCO_3$ molar volumes, 16.8 $cm^3\ mol^{-1}$ and 36.9 $cm^3\ mol^{-1}$, respectively [202], carbonated sorbents present markedly smaller values of S_{BET} and V_{BJH} in comparison to their corresponding as-synthesized state (Table 3.4), with variations in the order of magnitude of -10^1 % having as-synthesized state as a reference.

4.4.3 Results of raw mixing tests

For the sake of clarity, all tests on Ni-mayenite + CaO-mayenite couples in raw mixing configuration are divided in two groups:

- Group-1 (Table 4.8): all available CaO-mayenite materials are coupled with CaO0Ni(N)10, in order to test their sorption function; CaO0Ni(N)10 is chosen as it is the catalyst with the highest Ni fraction, so to guarantee the SMR catalytic activity within the mixed packed-bed;
- Group-2 (Table 4.9): several Ni-mayenite materials from Ni(N) are coupled with CaO54, in order to test the influence of sorbent proximity to each catalyst; CaO54 is chosen since it is the available synthesized sorbent with the highest free CaO fraction.

Table 4.8: Experimental χ_{CH4} and ΔC from reforming activity tests on 2-material systems in raw mixing configuration (Group-1) according to §2.3.2 procedure; WHSV = 0.60 Nl h^{-1} g_{cat}^{-1}; χ_{CH4} as a unique number results from the average of experimental measurements, ranged χ_{CH4} indicates the extreme values of a clearly decreasing trend (↓)

Raw mixing		**Ni-WHSV**		t^*	χ_{CH4}		ΔC	
		Nominal	**Actual**		$t \le t^*$	$t > t^*$	$t \le t^*$	$t > t^*$
		[$Nl_{CH4,i}$ h^{-1} g_{Ni}^{-1}]	**[$Nl_{CH4,in}$ h^{-1} g_{Ni}^{-1}]**	**[min]**	**[%]**	**[%]**	**[%]**	**[%]**
CaO0Ni(N)10	+ CaO54	6.0	5.1	56	96.2 ↓ 94.2	94.3	+46.3	-3.4
CaO0Ni(N)10	+ CaO45	6.0	5.1	46	96.5 ↓ 95.5	95.5	+40.2	-7.4
CaO0Ni(N)10	+ CaO30	6.0	5.1	36	97.2 ↓ 93.5	94.7	+48.5	-6.6
CaO0Ni(N)10	+ CaO15	6.0	5.1	31	95.7 ↓ 94.7	94.7	+37.6	-5.3

Results from Group-1 are represented in Figure 4.10. All sorbents coupled with CaO0Ni(N)10 prove their functionality in raw mixing configuration, giving place to a sorption enhancing (initial $C_{H2,out}$ roughly at 92-95 vol% dry, dilution-free), the duration of which decreases as sorbent free CaO fraction lowers, as can be observed by $C_{H2,out}$ and $C_{CO2,ou}$ profiles (Figure 4.10) and t^* values (Table 4.8). CO_2 sorption occurrence (Reaction 1.5) is corroborated by fully positive values of ΔC before t^*, whereas for slightly negative values of ΔC after t^*, explanations given in §4.3.1 can be assumed (Table 4.8). The trends of χ_{CH4} with respect to time in Figure 4.10 have non-random shapes, even though they are developed within narrow numerical ranges (Table 4.8). In fact, they trace the trend of corresponding $C_{H2,out}$, suggesting χ_{CH4} to be influenced by CO_2 sorption phenomena in raw mixing configuration.

Table 4.9: Experimental χ_{CH4} and ΔC from reforming activity tests on 2-material systems in raw mixing configuration (Group-2) according to §2.3.2 procedure; WHSV = 0.60 Nl h^{-1} g_{cat}^{-1}; χ_{CH4} as a unique number results from the average of experimental measurements, ranged χ_{CH4} indicates the extreme values of a clearly decreasing trend (↓)

Raw mixing			Ni-WHSV Nominal [$Nl_{CH4,i}$ h^{-1} g_{Ni}^{-1}]	Ni-WHSV Actual [$Nl_{CH4,in}$ h^{-1} g_{Ni}^{-1}]	t^* [min]	χ_{CH4} $t \le t^*$ [%]	χ_{CH4} $t > t^*$ [%]	ΔC $t \le t^*$ [%]	ΔC $t > t^*$ [%]
CaO0Ni(N)10	+	CaO54	6.0	5.1	56	96.2 ↓ 94.2	94.3	+46.3	-3.4
CaO0Ni(N)4.5	+	CaO54	13.3	14.6	71	94.2 ↓ 44.7	44.7 ↓ 38.5	+34.0	-4.7
CaO0Ni(N)3	+	CaO54	20.0	20.7	26	94.3 ↓ 25.1	25.1 ↓ 3.3	+23.3	-6.2

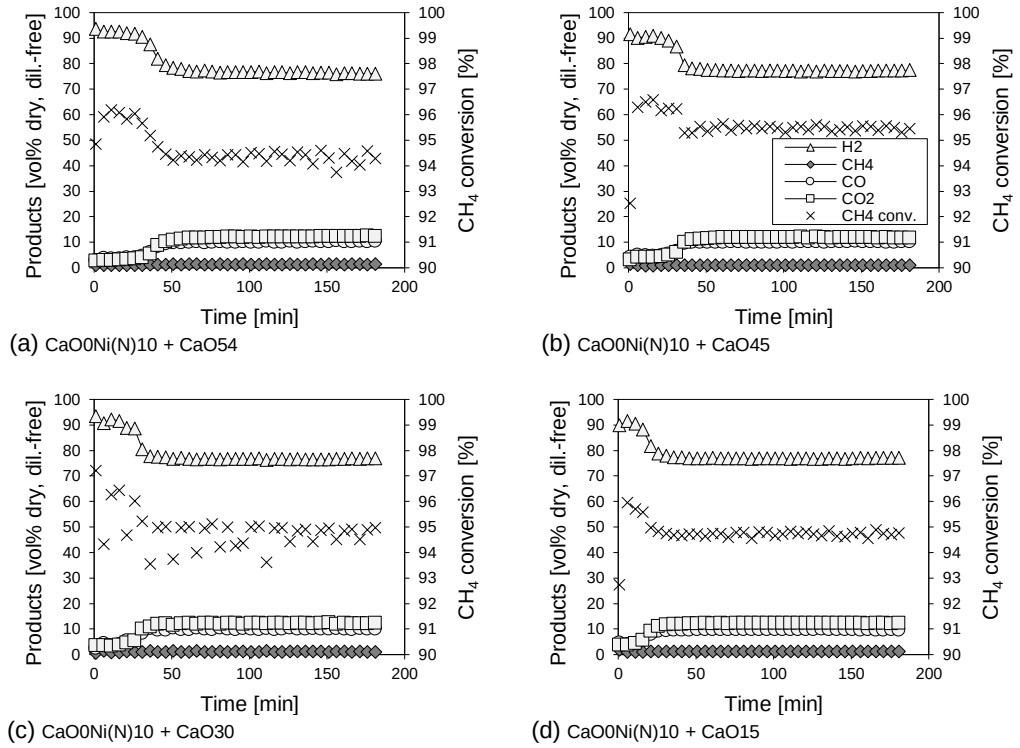

Figure 4.10: Results from reforming tests on 2-material systems in raw mixing configuration counting CaO0Ni(N)10 as a catalyst, and CaO54 (a), CaO45 (b), CaO30 (c), CaO15 (d) as sorbents; legend in (b) is valid for all diagrams

Figure 4.10a and Figure 4.11 show results belonging to Group-2. The main feature is a progressive catalyst deactivation in the case of CaO0Ni(N)4.5 and CaO0Ni(N)3 coupled with CaO54 (Figure 4.11): the higher the Ni-WHSV the more important the deactivation, i.e. the larger the overall drop of χ_{CH4} (see also Table 4.9). On the other hand, no deactivation is detected in the raw mixing couple CaO0Ni(N)10 + CaO54 (Figure 4.10a, Table 4.9), confirming the positive influence from Ni-WHSV decrease on catalytic activity in raw mixing configuration. In spite of the deactivation of CaO0Ni(N)3 + CaO54 and CaO0Ni(N)4.5 + CaO54, the shape of $C_{H2,out}$ and $C_{CO2,out}$ suggests the occurrence of CO_2 capture (Reaction 1.5), in some extent (Figure 4.11), in accordance with corresponding positive ΔC before t^*, while hypothesis formulated in §4.3.1 are valid for negative ΔC after t^* (Table 4.9).

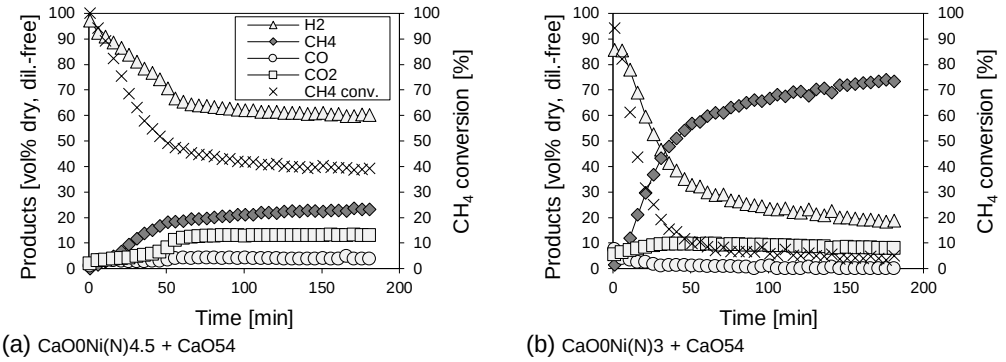

Figure 4.11: Results from reforming tests on 2-material systems in raw mixing configuration counting CaO54 as a sorbent, and CaO0Ni(N)4.5 (a), CaO0Ni(N)3 (b) as catalysts; legend in (a) is valid for all diagrams

4.4.4 Raw mixing: post-test characterization

All post-test raw mixed materials studied in §4.4.3 are characterized for further evaluations on observed reactive phenomena.

XRD (Figure 4.12) reveals the formation of metallic Ni in place of the NiO introduced in raw mixings by fresh Ni-mayenite catalysts (Figure 3.1a). NiO reduction is caused by pre-reduction (§2.3.2), and Ni is kept in its metallic form during the reforming step, whatever the reactivity expressed by the catalyst within the packed-bed. For all tested raw mixings, except CaO0Ni(N)3 + CaO54, $CaCO_3$ strongly appears (Figure 4.12, ray at about $2\theta = 29$ °) at the expense of the CaO brought by both mixed materials in as-synthesized state (Figure 3.1a, Figure 3.2 and Figure 3.3). On the contrary, post-test CaO0Ni(N)3 + CaO54 shows a faint ray for $CaCO_3$ at about $2\theta = 29$ ° and a relevant presence of CaO (Figure 4.12, ray at about $2\theta = 37$ °). In fact, CaO0Ni(N)3 + CaO54 is the raw mixing with the weakest reactivity, showing a rapid and dramatic decrease of χ_{CH4} during its reforming tests (Figure 4.11b), and the lowest ΔC before t^* among all tests listed in Table 4.8 and Table 4.9. Crystalline calcium aluminates detected in post-test raw mixings (Figure 4.12) are the very same contained in as-synthesized Ni-mayenite and CaO-mayenite materials (Figure 3.1a, Figure 3.2 and Figure 3.3).

Table 4.10: Average crystallite size (L) estimation by Scherrer equation (Equation 2.1) for samples after tests on 2-material systems in raw mixing configuration

Raw mixing			**$Ca_{12}Al_{14}O_{33}$ [nm]**	**CaO [nm]**	**$CaCO_3$ [nm]**	**Ni [nm]**
CaO0Ni(N)10	+	CaO54	35.6	/	30.4	29.8
CaO0Ni(N)10	+	CaO45	34.4	/	28.7	28.1
CaO0Ni(N)10	+	CaO30	35.4	/	30.2	27.7
CaO0Ni(N)10	+	CaO15	35.8	/	30.1	28.1
CaO0Ni(N)4.5	+	CaO54	36.7	37.4	31.7	26.9
CaO0Ni(N)3	+	CaO54	36.7	37.1	/	23.2

Table 4.10 summarized L estimates by Scherrer equation (Equation 2.1) applied to XRD data of post-test raw mixings. L of $Ca_{12}Al_{14}O_{33}$, CaO, $CaCO_3$ represents an average extended on the two materials of each raw mixing, as they are contained in both Ni-mayenite and CaO-mayenite. Metallic Ni is the only phase which can be clearly traced

back to Ni-mayenite catalysts; for CaO0Ni(N)3 and CaO0Ni(N)4.5, its *L* estimation has a reduced reliability, as the overall Ni fraction in the raw mixing is lowered by the dilution with CaO54, resulting in a weak main XRD ray for metallic Ni (Figure 4.12, ray at about $2\theta = 44\,°$), besides affected by overlapping with a secondary $Ca_{12}Al_{14}O_{33}$ ray. Nevertheless, Ni *L* in post-test raw mixings are close to relative sizes in Ni-mayenite after TPR (Table 3.6), evidencing the absence of severe sintering in the catalytic active phase.

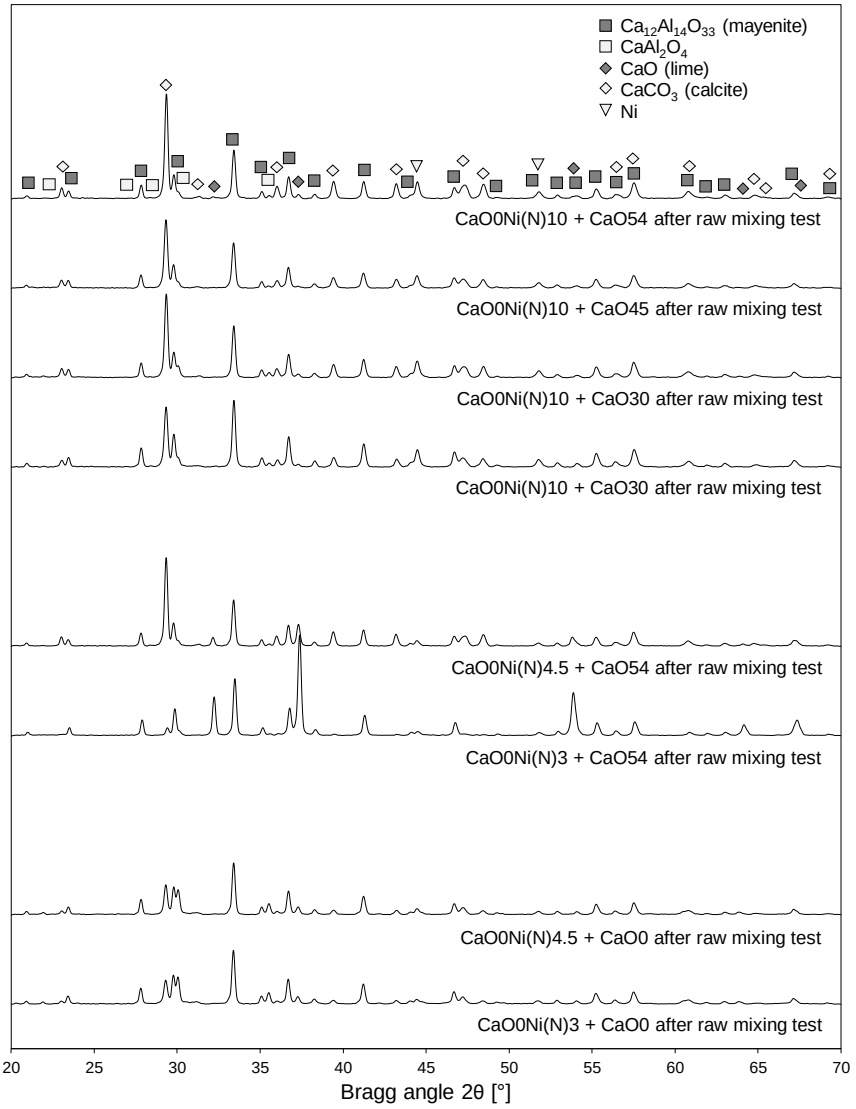

Figure 4.12: X-ray diffractograms for Ni-mayenite SMR catalysts impregnated with Ni(N) and CaO-mayenite sorbents, after SESMR tests raw mixing configuration

4.4.5 Comparison of spatial configurations

Focusing on 2-material experiments using CaO0Ni(N)10 as a catalyst, with both separate beds (Figure 4.7) and raw mixing configurations (Figure 4.10), SMR is always stably sustained close to its thermodynamic equilibrium (Table 4.1 as a reference) after sorbent breakthrough.

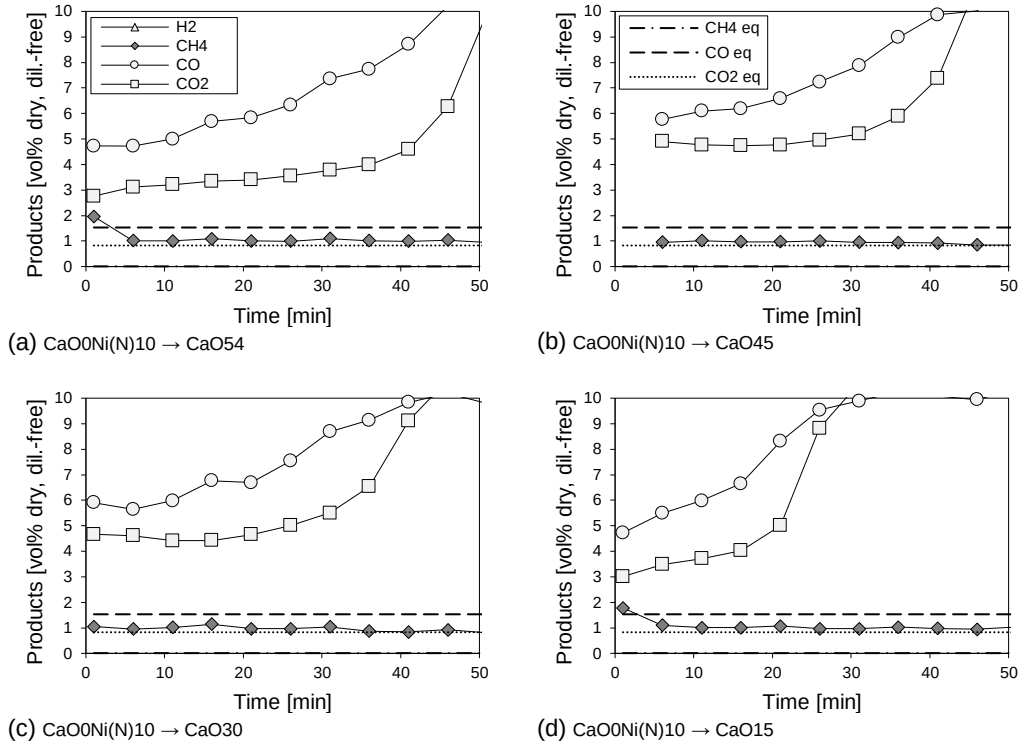

Figure 4.13: Magnification of results in Figure 4.7, from reforming tests on 2-material systems in separate beds configuration counting CaO0Ni10 as a catalyst, followed by CaO54 (a), CaO45 (b), CaO30 (c), CaO15 (d) as sorbents; equilibrium concentrations ("eq") for SESMR at 650 °C, 1 atm come from Table 4.1; legend in (a) and (b) is valid for all diagrams

However, being equal the sorbent coupled with CaO0Ni(N)10, reactive phenomena before the breakthrough have slight but relevant differences due to the adopted spatial configuration:

- Magnifications of initial outlet concentrations as a function of time (Figure 4.13, Figure 4.14) show that $C_{CO,out}$ is lower in raw mixing tests (Figure 4.14) than in separate beds ones (Figure 4.13), being equal time and tested materials; remarkably, $C_{CO,out}$ profile in the case of separate system suggests the occurrence of some positive effect from the CaO-mayenite sorption (Reaction 1.5) towards WGS (Reaction 1.2), an effect already documented for other CaO-based sorbents [48]. Considering the roles of CO and CO_2 in SESMR main reactions, an explanation is that CO_2 sorption (Reaction 1.5) pushes more intensely WGS equilibrium (Reaction 1.2) towards products in raw mixings than in separate beds. A corroboration comes from a comparison between Figure 4.15a and Figure 4.15b: $C_{H2,out}$ before breakthrough is higher in raw mixing tests (92 - 95 vol% dry, diluent-free) than in the separate beds experiments (90 vol% dry, diluent-free) and the breakthrough takes place earlier and more abruptly, being equal the CaO-sorbent and therefore CaO quantity within the reactor;
- As already pointed up in §4.4.3, χ_{CH4} in raw mixing configuration is influenced by concomitant carbonation (Reaction 1.5), since it has trends tracing those of corresponding $C_{H2,out}$ (Figure 4.10); on the other hand, χ_{CH4} in separate beds

configuration has not peculiar trends, being quite stable during each test (Figure 4.7), as confirmed by the strong similarity between its averaged values before and after *t** (Table 4.4).

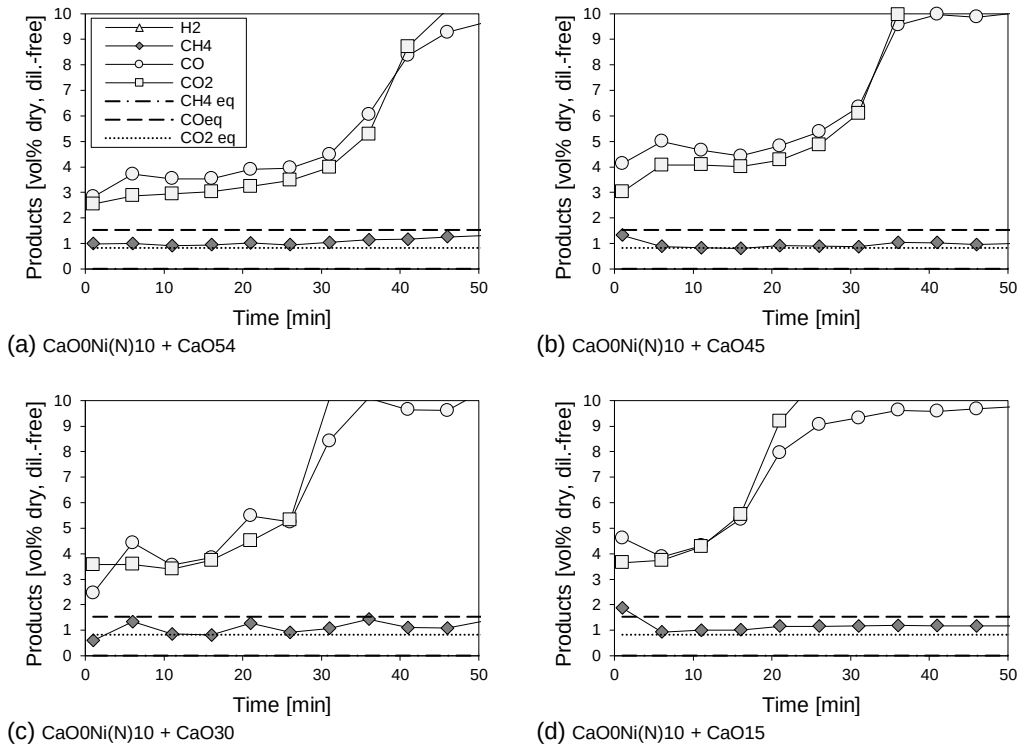

Figure 4.14: Magnification of results in Figure 4.10, from reforming tests on 2-material systems in raw mixing configuration counting CaO0Ni10 as a catalyst, and CaO54 (a), CaO45 (b), CaO30 (c), CaO15 (d) as sorbents; equilibrium values ("eq") for SESMR at 650 °C, 1 atm come from Table 4.1; legend in (a) is valid for all diagrams

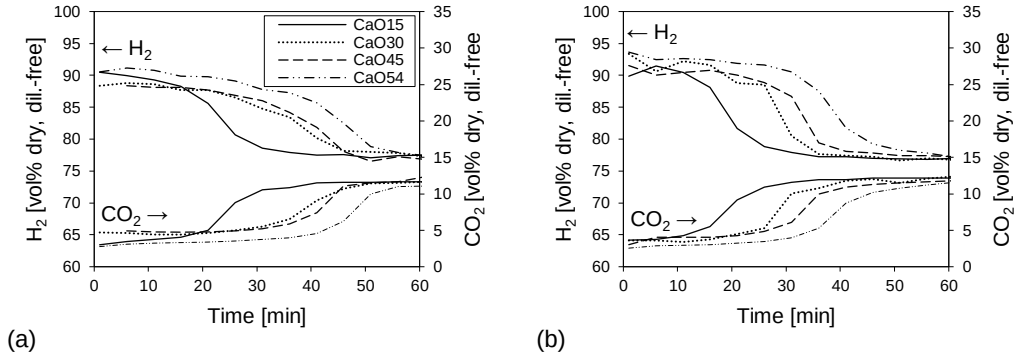

Figure 4.15: $C_{H2,out}$ *and* $C_{CO,out}$ *breakthrough curves from reforming tests with separate beds (a) and raw mixing (b) configurations, having CaO0Ni(N)10 as a catalyst*

Moving the attention to 2-material experiments using CaO0Ni(N)3 as a catalyst and CaO54 as a sorbent, despite the same Ni-WHSV, the mere change of spatial configuration gives place to very different outcomes. In the separate beds case (Figure 4.8), CaO0Ni(N)3 stably catalyses SMR, with high χ_{CH4} during the whole test (Table 4.4), and CaO54 captures the produced CO_2, as confirmed by post-test XRD analysis (Figure 4.9b). On the contrary,

in the raw mixing case (Figure 4.11b), χ_{CH4} rapidly falls below 10 %, very far from levels guaranteed by the same quantity of CaO0Ni(N)3 in the separate beds test.

In the transition from separate beds to raw mixing the following changes are relevant:

- the dilution of the catalysts within the packed-bed;
- the introduction of a relevant quantity of CaO within the packed-bed carrying out SMR; in fact, CaO is the only alien phase brought by CaO54, as it contains CaO and $Ca_{12}Al_{14}O_{33}$, based on its XRD (Figure 3.2), however $Ca_{12}Al_{14}O_{33}$ is already in CaO0Ni(N)3 (Figure 3.1a).

Table 4.11: Experimental χ_{CH4} and ΔC from reforming activity tests on 2-material systems in raw mixing configuration counting Ni-mayenite and CaO0, according to §2.3.2 procedure; WHSV = 0.60 Nl h^{-1} g_{cat}^{-1}; χ_{CH4} as a unique number results from the average of experimental measurements

Raw mixing			**Ni-WHSV**		χ_{CH4}	ΔC
			Nominal	**Actual**		
			[$Nl_{CH4,i}$ h^{-1} g_{Ni}^{-1}]	**[$Nl_{CH4,in}$ h^{-1} g_{Ni}^{-1}]**	**[%]**	**[%]**
CaO0Ni(N)4.5	+	CaO0	13.3	14.6	95.2	-3.7
CaO0Ni(N)3	+	CaO0	20.0	20.7	94.4	-2.4

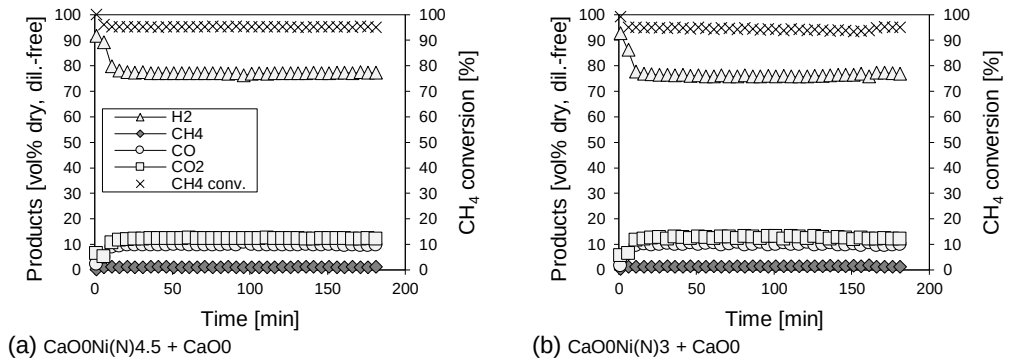

Figure 4.16: Results from reforming tests on 2-material systems in raw mixing configuration counting CaO0 as a solid diluent, and CaO0Ni(N)4.5 (a), CaO0Ni(N)3 (b), as catalysts; legend in (a) is valid for all diagrams

In order to figure out how these two features influence the activity of Ni-mayenite in a raw mixing, two further tests in this configuration are performed on CaO0Ni(N)4.5 and CaO0Ni(N)3 mixed with CaO0 instead of CaO54, according to the procedure in §2.3.2, so to dramatically reduce CaO quantity within the packed-bed and keep the same dilution of catalysts particles. Results (Table 4.11 and Figure 4.16) indicate that bed dilution itself does not affect Ni-mayenite activity. CaO0Ni(N)4.5 + CaO0 and CaO0Ni(N)3 + CaO0 give stable performances, with high χ_{CH4} (Table 4.11) and product concentrations close to SMR thermodynamic equilibrium (Table 4.1 as a reference), except for the first 10 min, characterized by some sorption enhancing (Figure 4.16), due to the carbonation (Reaction 1.5) of residual CaO in fresh Ni-mayenite catalysts and CaO0 (see $CaCO_3$ detection by XRD in Figure 4.12). The situation depicted by tests with CaO0 is quite different from the one coming from corresponding tests with CaO54 (last two rows in Table 4.9, Figure 4.11), in which the two very same catalysts undergo deactivation, more severe the higher is the Ni-WHSV. Considering that Ni-mayenite catalyst dilution is equal in all raw mixing tests,

as they all follow procedure §2.3.2, the quantity of CaO within the packed-bed is the only feature left to explain the lack of catalytic activity underwent by CaO0Ni(N)4.5 and CaO0Ni(N)3 in raw mixing with CaO54. On the other hand, no deactivation occurred for the raw mixing CaO0Ni(N)10 + CaO54 (first row in Table 4.8, Figure 4.10a), so that it could be more correct to consider the ratio Ni/CaO as the actual factor affecting Ni-mayenite catalytic properties in raw mixing configuration.

4.5 Reactivity of Ni-CaO-mayenite CSCM

Tests on all synthesized Ni-CaO-mayenite CSCM are carried out according to the procedure described in §2.3.3; afterwards, post-test CSCM are characterized to get a deeper insight in the occurred processes.

4.5.1 Results of reforming tests

Table 4.12 summarizes results from reforming activity tests on all available CSCM, showing relevant mutual influences among Ni origin, Ni fraction and CaO fraction.

Table 4.12: Experimental χ_{CH4} and ΔC from reforming activity tests on Ni-CaO-mayenite CSCM, according to procedure in §2.3.3; WHSV = 0.24 Nl h^{-1} g_{CSCM}^{-1}; χ_{CH4} as a unique number results from the average of experimental measurements, ranged χ_{CH4} indicates the extreme values of a clearly increasing (↑) or decreasing (↓) trend

CSCM	Ni-WHSV		t^*	χ_{CH4}			ΔC		
	Nominal	Actual		$t \le t^*$	$t > t^*$	Overall	$t \le t^*$	$t > t^*$	Overall
	[$Nl_{CH4,i}$ h^{-1} g_{Ni}^{-1}]	[$Nl_{CH4,in}$ h^{-1} g_{Ni}^{-1}]	[min]	[%]	[%]	[%]	[%]	[%]	[%]
CaO54Ni(N)10	2.4	2.6	76	94.5	95.5	/	+30.4	-0.7	/
CaO54Ni(N)3	8.0	10.0	/	/	/	39.5 ↓ 10.2	/	/	+0.8
CaO45Ni(N)3	8.0	16.0	/	/	/	0.9	/	/	+6.2
CaO30Ni(N)10	2.4	4.0	46	69.7 ↑ 95.1	95.3	/	+25.8	-6.1	/
CaO30Ni(N)3	8.0	9.2	/	/	/	48.8 ↓ 10.5	/	/	+0.8
CaO15Ni(N)10	2.4	1.8	31	96.4	95.9	/	+34.8	-6.4	/
CaO15Ni(N)3	8.0	9.2	31	96.1	94.9	/	+24.3	-13.4	/
CaO54Ni(Ac)10	2.4	2.4	/	/	/	0.6	/	/	+6.3
CaO54Ni(Ac)3	8.0	9.6	/	/	/	0.0	/	/	-0.5
CaO45Ni(Ac)3	8.0	13.3	/	/	/	0.0	/	/	+5.3
CaO30Ni(Ac)3	8.0	8.9	/	/	/	1.0	/	/	-8.9
CaO15Ni(Ac)10	2.4	2.4	/	/	/	93.3 ↓ 0.7	/	/	+6.1
CaO15Ni(Ac)3	8.0	8.2	/	/	/	99.9 ↓ 0.1	/	/	-1.4

Figure 4.17 show results from reforming tests on CSCM impregnated with Ni(N), allowing several comments:

- In CSCM descending from WI of CaO54 and CaO30, Ni fraction plays a relevant role on reactive performances, as nominal 3 wt% of Ni is not sufficient to stably catalyse SESMR (Figure 4.17b, Figure 4.17e), while 10 wt% is (Figure 4.17a, Figure 4.17d). In fact, for CaO54Ni(N)3 and CaO30Ni(N)3, χ_{CH4} suffers a rapid decrease down to about 10 % (Table 4.12), so that it is quite difficult to infer whether some sorption enhancing occurs or not. On the other

hand, for CaO54Ni(N)10 and CaO30Ni(N)10, SMR is stably sustained throughout the whole test duration, with χ_{CH4} beyond 94 %, allowing the sorption enhancing effect in the first part, as confirmed by positive ΔC before t^* (Table 4.12), with initial $C_{H2,out}$ equal to about 90 vol% dry, diluent free;

- A different behaviour appears for CSCM originated from CaO15. SESMR fully occurs for both CaO15Ni(N)10 (Figure 4.17f) and CaO15Ni(N)3 (Figure 4.17g) as verified by ΔC before t^*, and their performances are quite similar as far as χ_{CH4}, t^* and product concentrations are concerned (Table 4.12). In these cases too, initial $C_{H2,out}$ is about 90 % vol% dry, diluent free;
- CaO45Ni(N)3 does not work at all, the most likely because of its actual Ni fraction (measured by ICP-AES, Table 3.1) and therefore because of the high actual NI-WHSV in the experiment.

All this considered, one can infer that for CSCM derived from Ni(N), there is a threshold between 15 wt% and 30 wt% for the CaO content in the parent sorbent, above which CaO has a detrimental role on Ni catalytic activity towards SMR at 650 °C and 1 atm, for Ni-WHSV higher than 9.2 Nl h^{-1} g_{Ni}^{-1}.

Figure 4.18 reports results from reforming tests on all synthesized CSCM derived from Ni(Ac). As evidenced by χ_{CH4} in Table 4.12, the reactivity is almost or entirely zero for CaO54Ni(Ac)10 (Figure 4.18a), CaO54Ni(Ac)3 (Figure 4.18b), CaO45Ni(Ac)3 (Figure 4.18c), CaO30Ni(Ac)3 (Figure 4.18d), whereas some attempts of CH_4 conversion occur only at the beginning of tests on CaO15Ni(Ac)10 and CaO15Ni(Ac)3. Consequently, even with the very reduced reactivity of CSCM based on Ni(Ac), the detrimental role of CaO on Ni activity is confirmed.

4.5.2 Post-test characterization

All CSCM tested in §4.5.1 are characterized after reported experiments.

Figure 4.19 shows XRD analyses on post-test CSCM from Ni(N). CaO54Ni(N)10, CaO30Ni(N)10, CaO15Ni(N)10 and CaO15Ni(N)3 after reforming tests show the emergence of $CaCO_3$ with a concomitant relevant decrease of CaO rays intensity, in comparison to the same CSCM in as-synthesized state (Figure 3.2, Figure 3.3), so corroborating the occurrence of carbonation (Reaction 1.5) and therefore of SESMR. $CaCO_3$ appears less intensely in CaO54Ni(N)3 and CaO30Ni(N)3, while CaO rays persist more strongly, in accordance with observed reforming experimental results revealing a scarce but not negligible reactivity (Figure 4.17b, Figure 4.17e), sufficient to produce enough CO_2 to trigger a partial CaO carbonation (Reaction 1.5). XRD of post-test CaO45Ni(N)3 agrees with corresponding reforming results (Figure 4.17c): no reactivity at all, then no $CaCO_3$ formation. On the other hand, it is interesting to observe some traces of NiO in post-test CaO45Ni(N)3, together with the metallic Ni produced during the pre-reduction step (see procedure in §2.3.3), most likely a consequence of a 3 h exposure to SESMR reactants (CH_4 and $H_2O_{(v)}$) in the total absence of any reactivity; for all other materials in Figure 4.19, only Ni in its metallic state is detected.

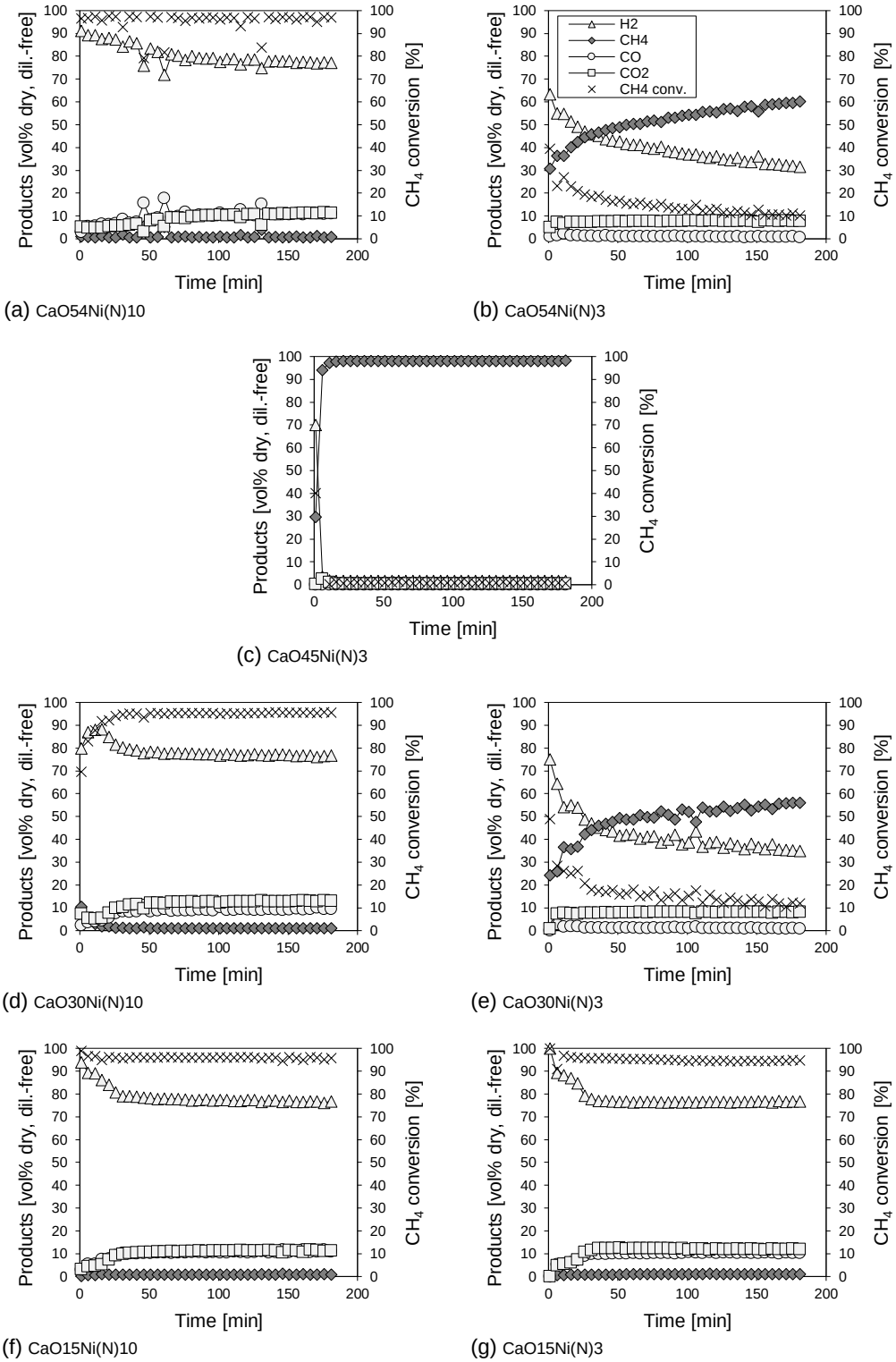

Figure 4.17: Results from reforming tests on CSCM from Ni(N): CaO54Ni(N)10 (a), CaO54Ni(N)3 (b), CaO45Ni(N)3 (c), CaO30Ni(N)10 (d), CaO30Ni(N)3 (e), CaO15Ni(N)10 (f), CaO15Ni(N)3 (g); legend in (b) is valid for all diagrams

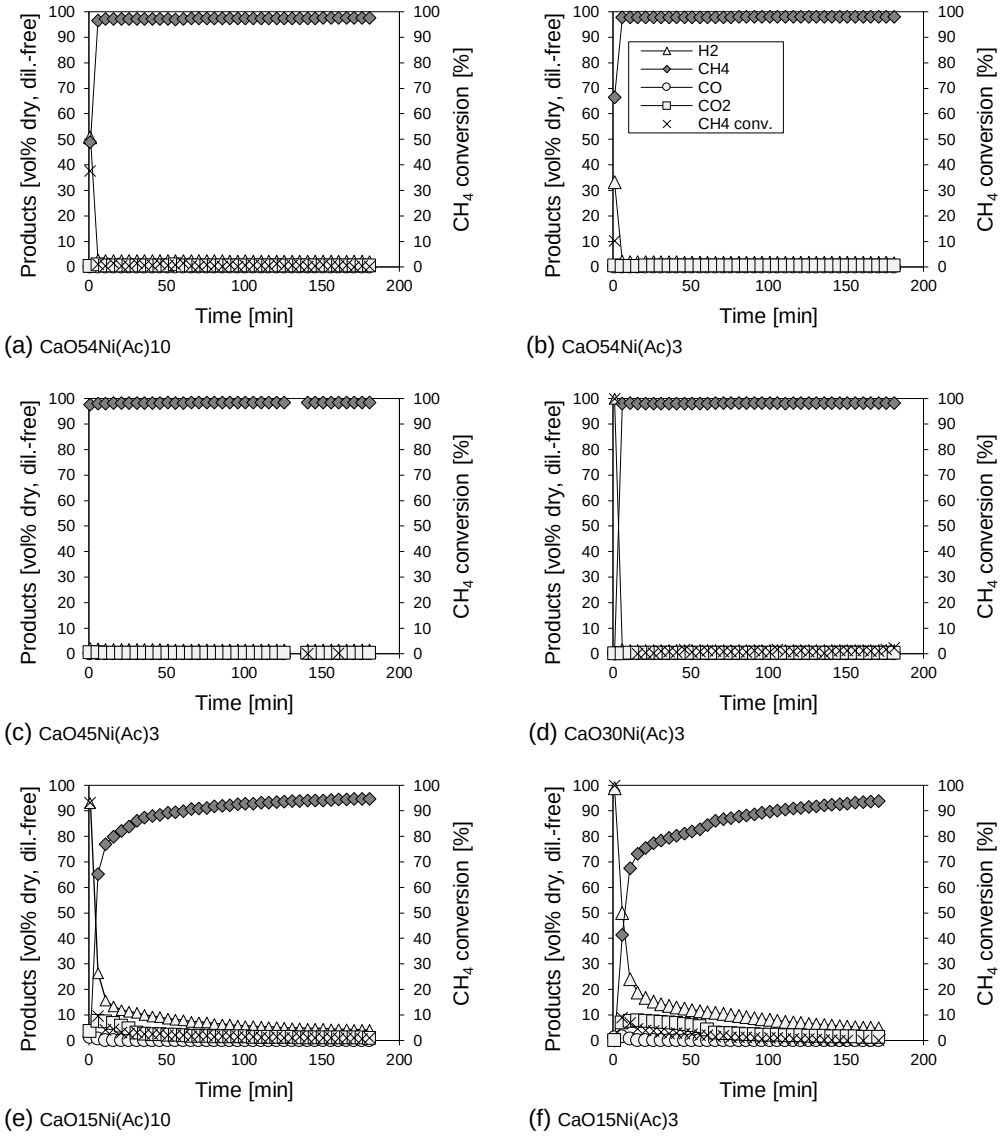

Figure 4.18: Results from reforming tests on CSCM from Ni(Ac): CaO54Ni(Ac)10 (a), CaO54Ni(Ac)3 (b), CaO45Ni(Ac)3 (c), CaO30Ni(Ac)3 (d), CaO15Ni(Ac)10 (e), CaO15Ni(Ac)3 (f); legend in (b) is valid for all diagrams

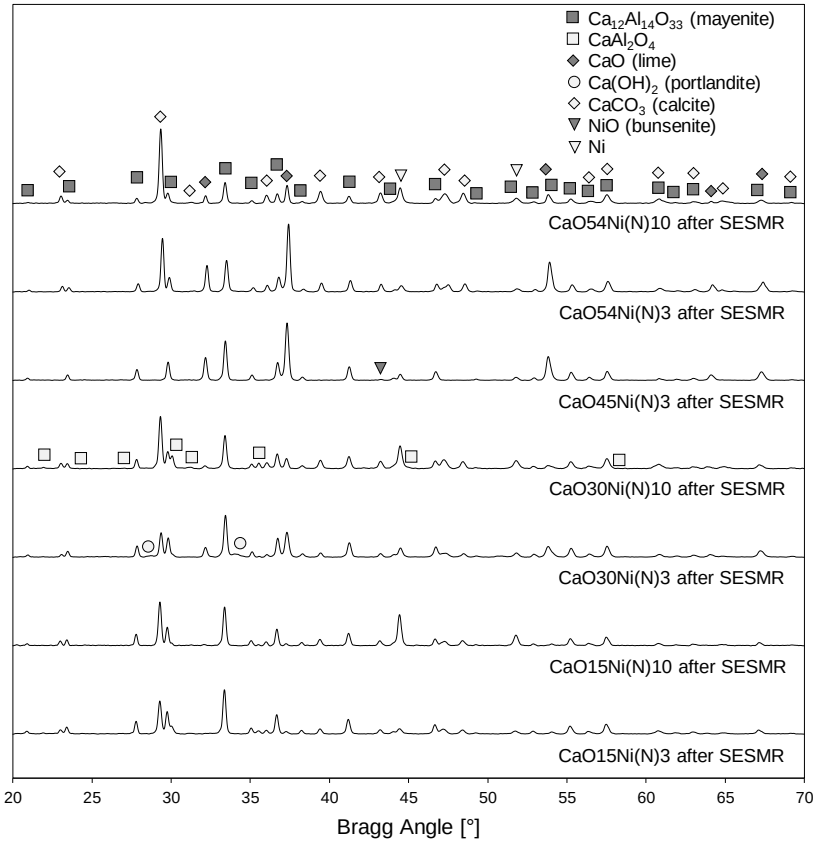

Figure 4.19: X-ray diffractograms for Ni-CaO-mayenite CSCM impregnated with Ni(N) after reforming tests

Figure 4.20 reports XRD spectra of post-test CSCM derived from Ni(Ac), in which the unique phase variation in comparison to their as-synthesized state (Figure 3.2, Figure 3.3) is the emergence of metallic Ni, as a consequence of pre-reduction (§2.3.3). No $CaCO_3$ is detected, in accordance with the absence of sufficient reforming reactivity (Figure 4.18, Table 4.12). Moreover, traces of NiO appear in Ni(Ac) post-test CSCM deriving from WI on sorbents with 30 wt% of free CaO or more, most likely because of reduced Ni exposure to SESMR reactants (CH_4 and $H_2O_{(v)}$) for 3 h, (Figure 4.18a, Figure 4.18b, Figure 4.18c, Figure 4.18d). On the other hand, NiO crystals are not detected in CaO15Ni(Ac)3 and CaO15Ni(Ac)10 (Figure 4.20), bearing out the hypothesis of re-oxidation due to reactants if completely unconverted; in fact, unlike other Ni(Ac) CSCM, these two materials expressed some reactivity, no matter how scarce it was, producing H_2 (Figure 4.18e, Figure 4.18f).

Table 4.13 summarizes *L* calculations by Scherrer equation (Equation 2.1) on main crystalline phases contained in post-test CSCM. A relevant tendency appears for CaO45Ni(N)3, CaO54Ni(Ac)3, CaO45Ni(Ac)3, CaO30Ni(Ac)3, i.e. CSCM with null reactivity and nominal 3 wt% of Ni: they all have metallic Ni *L* higher than corresponding values in post-TPR samples (Table 3.6), sensibly out of the range of values encountered so far, revealing the occurrence of sintering. For all other CSCM the opposite happens.

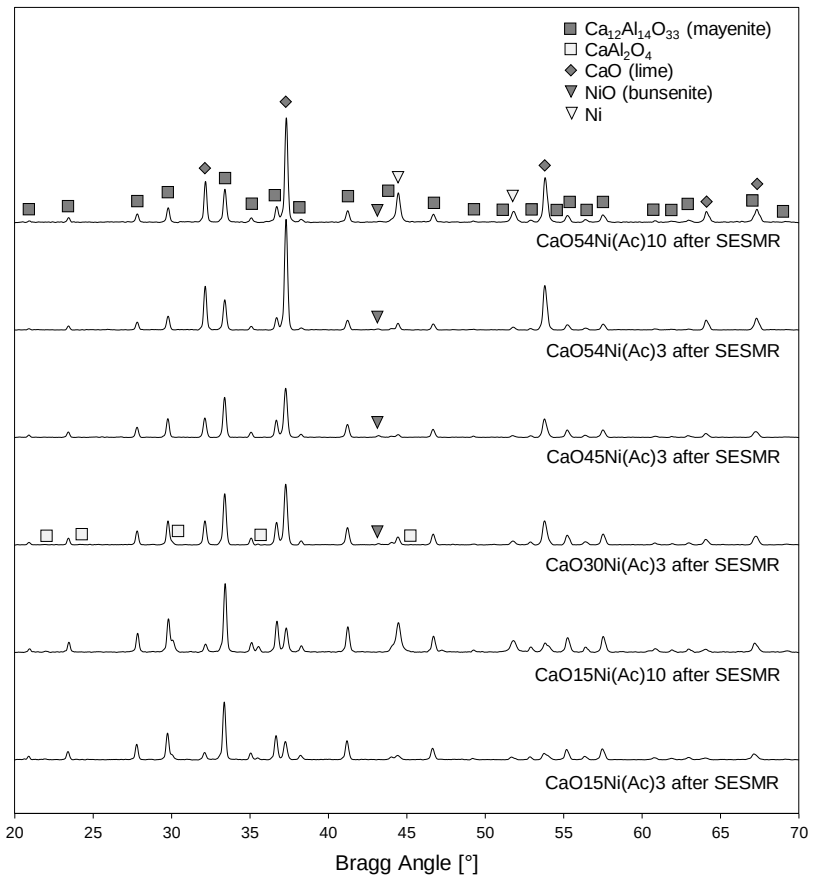

Figure 4.20: X-ray diffractograms for Ni-CaO-mayenite CSCM impregnated with Ni(Ac) after SESMR tests

Table 4.13: Average crystallite size (L) estimation by Scherrer equation (Equation 2.1) for main phases of Ni-CaO-mayenite CSCM after reforming tests

Material	**$Ca_{12}Al_{14}O_{33}$ [nm]**	**CaO [nm]**	**$CaCO_3$ [nm]**	**Ni [nm]**
CaO54Ni(N)10	35.8	40.3	28.4	27.6
CaO54Ni(N)3	35.5	38.1	33.4	25.9
CaO45Ni(N)3	36.1	36.1	/	32.6
CaO30Ni(N)10	34.6	31.0	29.5	28.3
CaO30Ni(N)3	35.0	32.7	33.2	28.2
CaO15Ni(N)10	37.0	36.1	32.8	32.1
CaO15Ni(N)3	36.4	34.7	31.4	24.1
CaO54Ni(Ac)10	36.4	39.6	/	29.7
CaO54Ni(Ac)3	35.6	38.8	/	36.7
CaO45Ni(Ac)3	36.5	35.3	/	32.1
CaO30Ni(Ac)3	36.4	35.9	/	32.1
CaO15Ni(Ac)10	37.7	34.6	/	25.1
CaO15Ni(Ac)3	38.2	34.4	/	22.9

Table 4.14 lists measures of textural properties of post-test CSCM. For CaO54Ni(N)10, CaO30Ni(N)10, CaO15Ni(N)10, CaO15Ni(N)3, i.e. the materials with high reactivity towards SESMR and SMR (Table 4.12, Figure 4.17), a relevant drop in S_{BET} and V_{BJH} is

detected, due to the higher molar volume of developed $CaCO_3$ (36.9 cm^3 mol^{-1} [202]) in comparison with that of CaO (16.8 cm^3 mol^{-1} [202]).

Table 4.14: Measured BET surface areas (S_{BET}), BJH cumulative volumes (V_{BJH}) and averaged pore diameters ($D_{av,BJH}$) for CSCM after reforming tests; ΔS_{BET}, ΔV_{BJH} and $\Delta D_{av,BJH}$ are the percentage variations with respect to corresponding values in as-synthesized state

Material	S_{BET} [m^2 g^{-1}]	ΔS_{BET} [%]	V_{BJH} [cm^3 g^{-1}]	ΔV_{BJH} [%]	$D_{av,BJH}$ [nm]	$\Delta D_{av,BJH}$ [%]
CaO54Ni(N)10	2.29	-74	0.014	-67	25	-36
CaO54Ni(N)3	10.57	-17	0.046	-15	16	-14
CaO45Ni(N)3	10.85	-5	0.042	-24	13	-23
CaO30Ni(N)10	3.34	-42	0.012	-48	11	-15
CaO30Ni(N)3	11.00	+20	0.048	+23	13	+30
CaO15Ni(N)10	6.98	-44	0.031	-28	16	+45
CaO15Ni(N)3	16.82	-19	0.072	-26	15	+12
CaO54Ni(Ac)10	7.90	+11	0.030	+3	15	-50
CaO15Ni(Ac)10	10.69	-21	0.054	-11	22	+22

Some post-test CSCM proved to undergo carbonation (Reaction 1.5) by preceding characterization, are observed by SEM (Figure 4.21). CaO54Ni(N)10 (Figure 4.21a), exhibiting a high SESMR reactivity (Figure 4.17a), in its post-test state is externally more clogged than in its as-synthesized one (Figure 3.8e). CaO54Ni(N)3, showing a lower reactivity, is not so clogged in its post-test state (Figure 4.21b), keeping an external aspect not so far from its as-synthesized one (Figure 3.8c). All this considered, this evident morphological modification in post-test CaO54Ni(N)10 is definitively related to CaO conversion in $CaCO_3$, in agreement with its dramatic S_{BET} and V_{BJH} reductions (see ΔS_{BET} and ΔV_{BJH} in Table 4.14). In the case of CaO15Ni(N)10 and CaO15Ni(N)3, the as-synthesized microgranular external structure is partially kept after SESMR (Figure 4.21c and Figure 4.21d), even though these CSCM and CaO54Ni(N)10 have very close catalytic activities (Table 4.12); this effect could be related to the higher calcium aluminates content ($Ca_{12}Al_{14}O_{33}$ and $CaAl_2O_4$), acting as an inert porous binder. In-situ EDS on post-test external surfaces (Figure 4.22) locates elemental Ni mainly in zones keeping their original microgranular morphology, the lower the nominal CaO content the neater the separation on Ni towards more porous zones. EDS on embedded post-test CaO54Ni(N)10 (Figure 4.23a), CaO15Ni(N)10 (Figure 4.23b) and CaO15Ni(N)3 (Figure 4.23c) do not evidence significant variations in the radial texture, as the elemental Ni is distributed similarly to their as-synthesized state (Figure 3.12c, Figure 3.11b and Figure 3.11a, respectively).

Post-test CaO54Ni(N)10 is observed by TEM (Figure 4.24), showing a nanometric morphology not so far from its as-synthesized state (Figure 3.15). Similarly to post-test CaO0Ni(N)10 or CaO0Ni(Ac)10 (Figure 4.5, Figure 4.6), by cross correlating STEM-EDS (Figure 4.25a) and XRD analyses (Figure 4.19), one can infer that dark spheroidal particles (Figure 4.24a, magnified in Figure 4.24b) are metallic Ni, of which dimensions are close to corresponding *L* estimate in Table 4.13. Moreover, STEM-EDS in Figure 4.25b reveals the detection of $CaCO_3$, as only elemental Ca, C and O are detected in an apical zone hanging in a hole of the membrane, so undoubtedly without interferences from the sample-holder (§2.2.5)

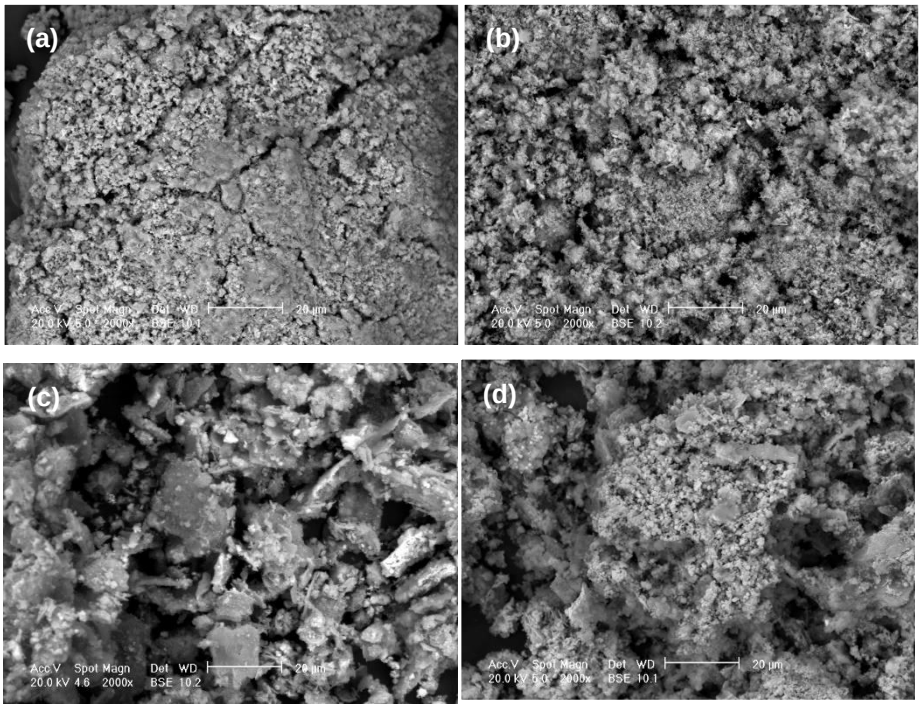

Figure 4.21: SEM micrographs at 2000x magnification of post-test CaO54Ni(N)10 (a), post-test CaO54Ni(N)3 (b), post-test CaO15Ni(N)10 (c), post-test CaO15Ni(N)3 (d) powder samples

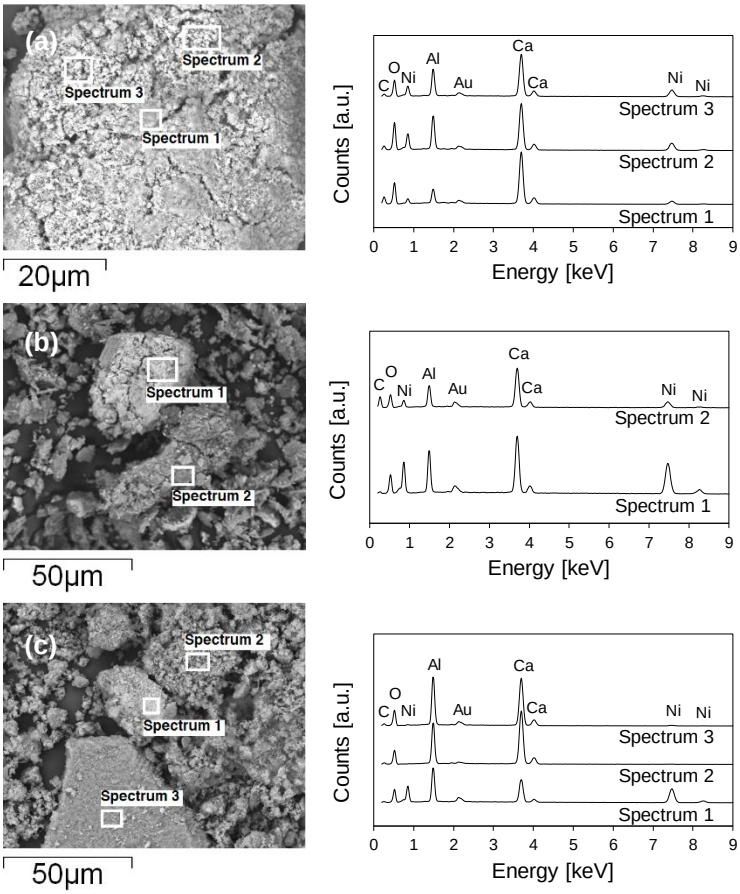

Figure 4.22: SEM-EDS on external surfaces of post-test CaO54Ni(N)10 (a), CaO15Ni(N)10 (b), CaO15Ni(N)10 (c)

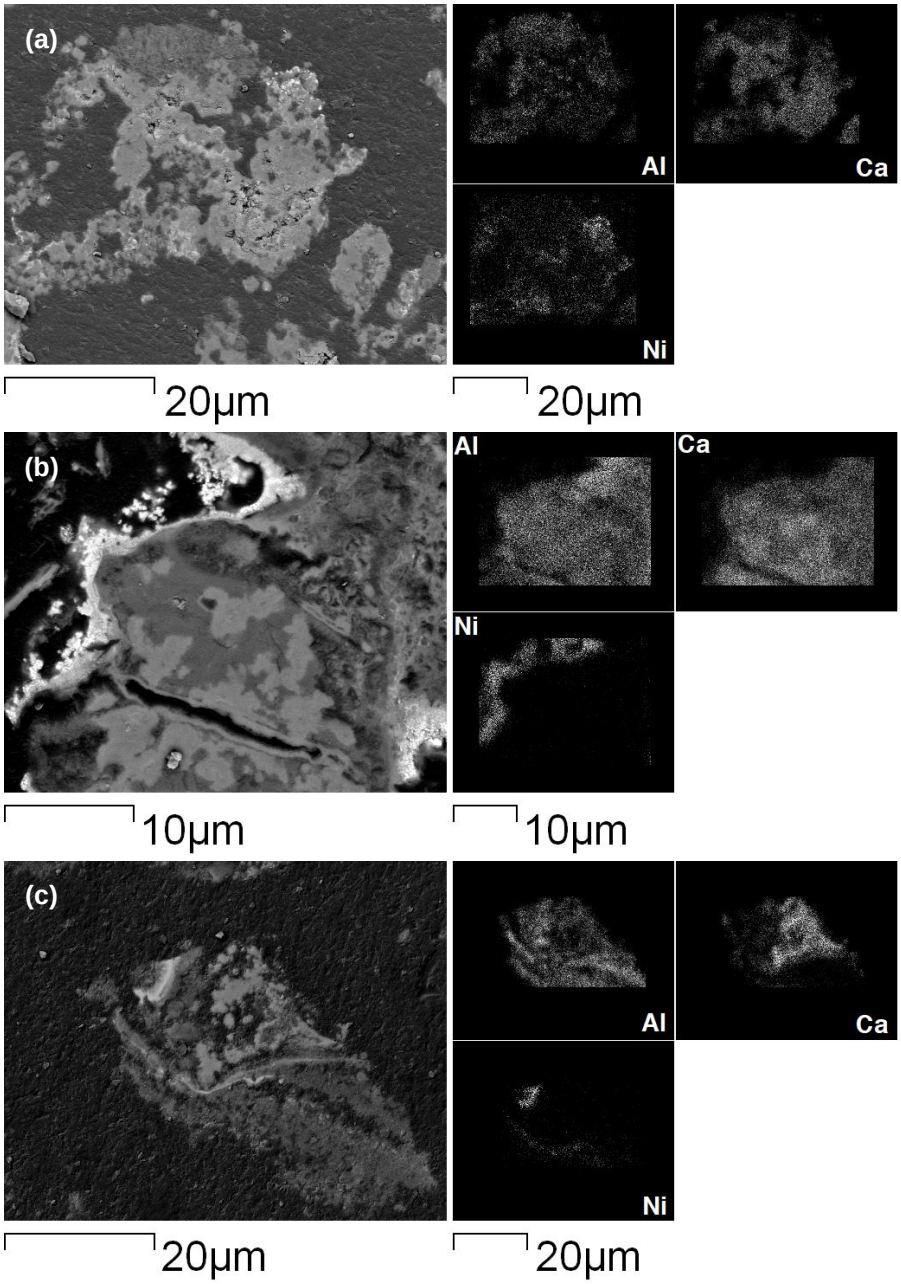

Figure 4.23: SEM-EDS map for embedded post-test CaO54Ni(N)10 (a), CaO15(Ni)10 (b) and CaO15Ni(N)3 (c)

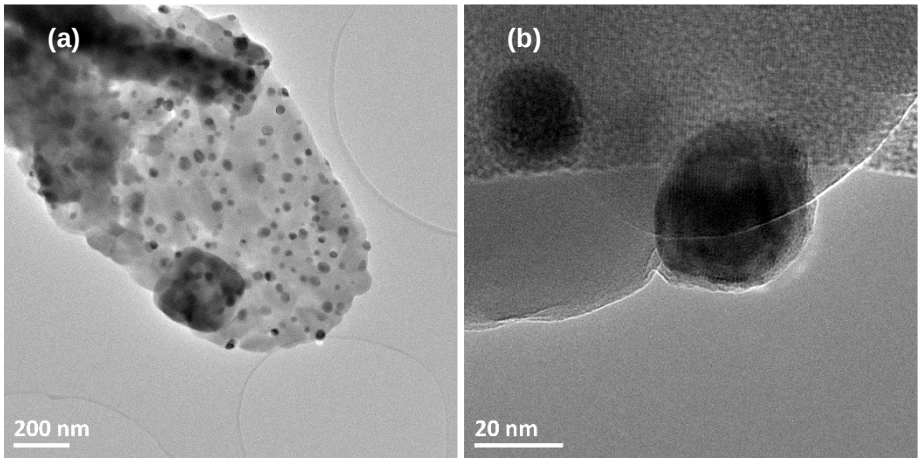

Figure 4.24: TEM micrographs of post-test CaO54Ni(N)10 (a) (b)

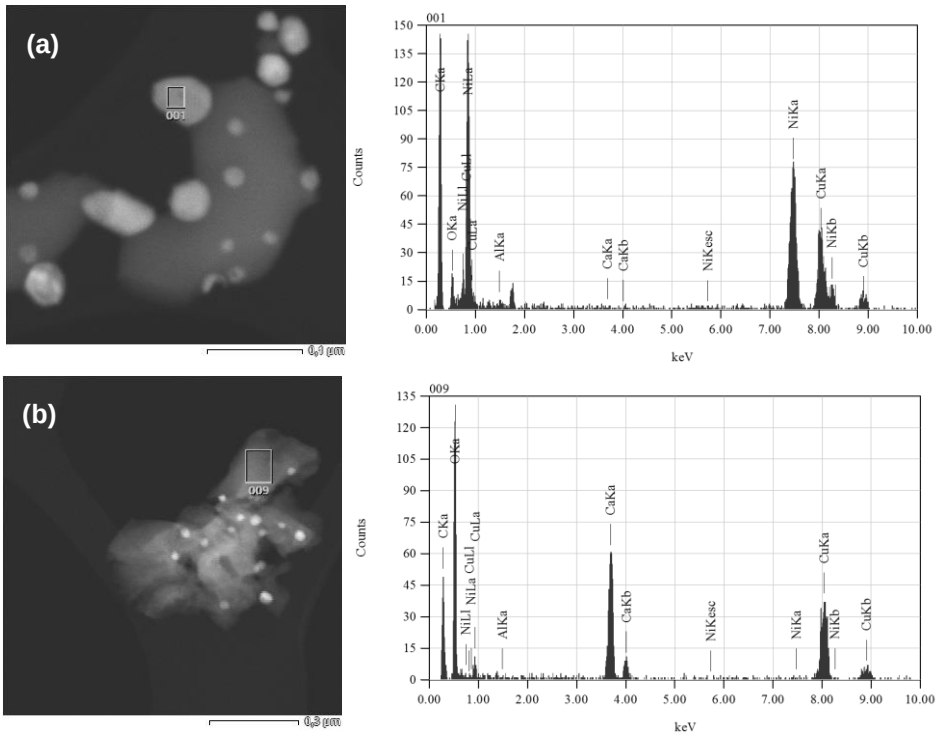

Figure 4.25: STEM-EDS analyses on post-test CaO54Ni(N)10 (a) (b)

4.6 Conclusions

As far as Ni-mayenite SMR catalysts are concerned, the main feature is a clear distinction between Ni(N) and Ni(Ac) derivation:

- WI by Ni(N) determines a high SMR reactivity at WHSV equal to 0.24 $Nl_{CH4,in}\ h^{-1}\ g_{cat}^{-1}$, whatever the nominal Ni fraction between 3 wt% and 10 wt% and the tested temperature;
- Ni(Ac) derived catalysts have quite worse performances than Ni(N) ones at the very same operating conditions, especially unsatisfactory at 650 °C, the temperature of interest for SESMR.

A comparison between characterization results from Ni-mayenite materials in post-test and as-synthesized states does not give significant signals of Ni(Ac) catalysts deterioration. The only relevant differences between Ni(N) and Ni(Ac) catalysts arise from post-test TEM images, suggesting a higher affinity towards carbonaceous species in the first case.

Tests on 2-material systems, counting Ni-mayenite from Ni(N) and CaO-mayenite or CaO0, provide the following indications about CaO:

- Results from separate beds configuration evidence CaO-mayente sorbents ability to perform CO_2 capture (Reaction 1.5) at chosen SESMR process conditions, including steam presence;
- The direct contact between Ni-mayneite catalysts and CaO54 sorbent, realized during raw mixing tests, highlights opposite effects due to CaO. On the one hand, for low Ni-WHSV (5.1 $Nl_{CH4,in}\ h^{-1}\ g_{Ni}^{-1}$), CaO carbonation (Reaction 1.5) has a direct positive effect on CH_4 conversion, allowing to carry out SESMR; on the other hand, for high Ni-WHSV (14.6 $Nl_{CH4,in}\ h^{-1}\ g_{Ni}^{-1}$ or 20.7 $Nl_{CH4,in}\ h^{-1}\ g_{Ni}^{-1}$) a progressive decrease of CH_4 conversion occurs because of CaO presence within the bed, the higher the Ni-WHSV the more dramatic the decrease. Catalyst dilution effects are excluded at the same Ni-WHSV by means of results from raw mixings reforming tests with CaO0 in the place of CaO54.

All these features reverberate on CSCM materials tested for SESMR. In fact:

- Catalytic activity of Ni(Ac) derived CSCM is almost zero if their parent sorbents have 30 wt% of free CaO or more, and quite scarce in the case of derivation from CaO15, empirically confirming all at once negative influences on SESMR/SMR catalysis from WI by Ni(Ac) and CaO content increase;
- Those deriving from Ni(N) generally exhibit a higher catalytic activity than their homologue from Ni(Ac). SESMR and SMR are completely developed and sustained by Ni(N) derived CSCM with nominal 10 wt% of Ni, i.e. nominal Ni-WHSV equal to 2.4 $Nl_{CH4,in}\ h^{-1}\ g_{Ni}^{-1}$, whatever the examined nominal CaO excess. When Ni fraction lowers to 3 wt%, so that nominal Ni-WHSV rises to 8.0 $Nl_{CH4,in}\ h^{-1}\ g_{Ni}^{-1}$, only the Ni(N) derived CSCM originated from CaO15 performs like samples with 10 wt% of Ni, while those

from CaO-mayenite with 30 wt% of free CaO or more have a reduced activity, confirming the detrimental role of CaO.

As a consequence of these experimental observations, criteria for the choice of the most promising CSCM are:

- Use of Ni(N) for WI, because of their general better attitude towards reforming than Ni(Ac) derived materials;
- Use of CaO15 as a base for WI, as it limits CaO negative effects on catalysis;
- Choice of Ni content equal to 10 wt%, since it has always guaranteed catalytic activity in micro-reactor scale tests, whatever the CaO content of the CSCM.

All this considered, among all materials synthesized by WM and WI, CaO15Ni(N)10 is the CSCM to be examined for industrial applicability.

Chapter 5

Study for industrial applicability

This chapter presents experimental results concerning the industrial applicability to SESMR of the most promising material developed so far in this thesis. Investigated aspects are:

- *Multicyclic stability for SESMR/regeneration process, examining also different regeneration conditions;*
- *Mechanical resistance to attrition, for the use in fluidized beds.*

5.1 SESMR/regeneration multicycle stability

The screening by microreactor scale tests, presented in the previous chapter, made CaO15Ni(N)10 rise above the others materials synthesized by WM and WI as the best candidate for the industrial applicability study (§4.6). Results from multicycle SESMR/regeneration tests, carried out according to the procedures and conditions described in §2.4.1, and post-test characterizations are presented in the following.

5.1.1 Results of multicycle SESMR/regeneration tests

CaO15Ni(N)10 underwent two multicycle SESMR/regeneration tests:

- Test 1, with mild regeneration conditions, that is to say using N_2 at 850 °C as regenerating gas; having §2.4.1 as a reference, the SESMR/regeneration cycle $3 \rightarrow 4 \rightarrow 5 \rightarrow 7$ loop was performed 204 times, stopping the 205^{th} cycle at the step 4, so to get the CSCM in its carbonated state; the overall duration of the test was 16 days no stop;
- Test 2, applying a severe regeneration strategy with pure CO_2 at 925 °C: for the first 140 SESMR/regeneration cycles, the $3 \rightarrow 4 \rightarrow 6 \rightarrow 7$ loop (§2.4.1 as

a reference) was performed; because of a severe loss in catalytic activity, and aiming to restore the CSCM performance, the process loop was changed for the remaining 64 cycles, by the addition of a strong reduction step (30 min, 50 vol% of H_2 in N_2 at 850 °C) after the regeneration dwell, resulting in the new loop 3 → 4 → 6 → 8 (§2.4.1 as a reference); the 205th cycle was stopped at the step 4, so to get the CSCM in its carbonated state; the overall duration of the test was 19 days no stop.

5.1.1.1. Test 1: mild regeneration

The overall performance throughout SESMR/mild-regeneration cycles is represented in Figure 5.1, by means of averaged χ_{CH4} , $C_{H2,out}$ and $C_{CO2,out}$ from SESMR steps, before and after breakthrough (§2.4.1). An excellent stability of CaO15Ni(N)10 emerges, as:

- $C_{H2,out}$ is constantly around 90 vol% dry, dilution-free in the pre-breakthrough period, while in the post-breakthrough has just a nearly imperceptible decline from 77.0 vol% dry, dilution-free to 76.5 vol% dry, dilution-free, therefore very close to SMR thermodynamic equilibrium at SESMR operating conditions (see Table 4.1);
- Similarly, $C_{CO2,out}$ is constantly in the range 3.5-4.0 vol% dry, dilution-free before breakthrough, and between 10.5-12.0 vol% dry, dilution-free in the post-breakthrough;
- χ_{CH4} is constantly higher than 95 % in both pre- and post-breakthrough.

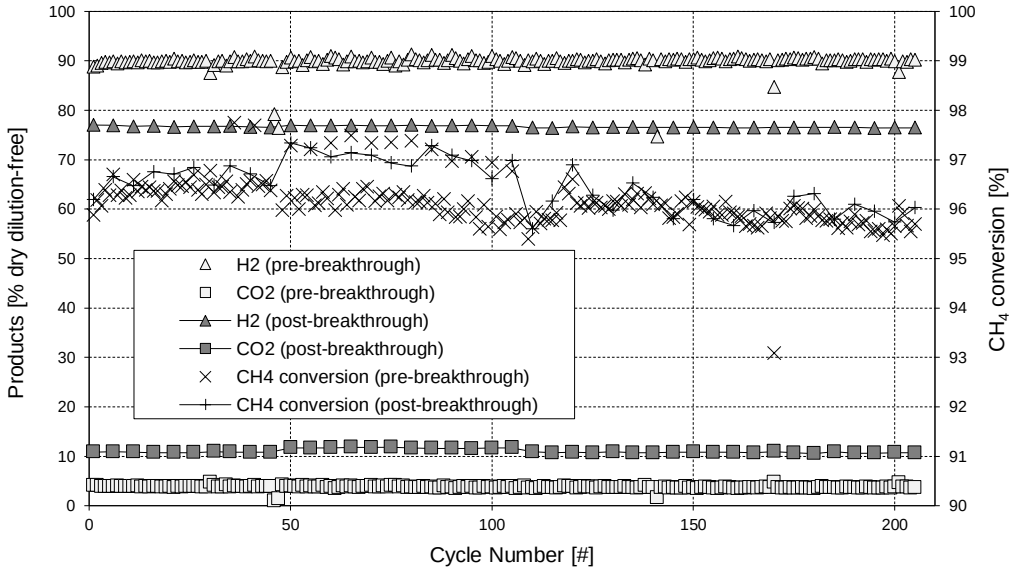

Figure 5.1: Overall experimental results of multicycle SESMR/regeneration tests with mild regeneration conditions (N_2 at 850 °C as a regeneration medium); having §2.4.1 as a reference, the SESMR/regeneration loop 3 → 4 → 5 → 7 was performed 204 times, stopping the cycle 205 at the step 4

Pre-breakthrough values of $C_{H2,out}$ and $C_{CO2,out}$ from Figure 5.1 depict a SESMR performance below the maximum allowed by equilibrium calculations (see Table 4.1),

however, the CO_2 capture function is very stable, as can be seen by the high similarity between breakthrough curves at the beginning and at the end of the multicycle test with mild regeneration (Figure 5.2).

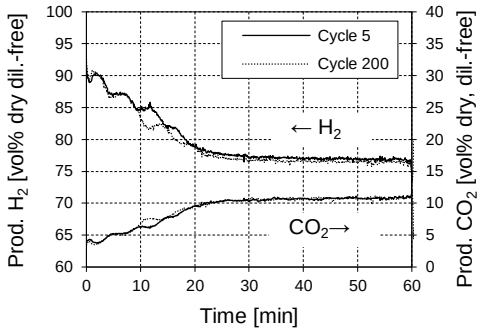

Figure 5.2: $C_{H2,out}$ *and* $C_{CO2,out}$ *breakthrough curves for cycles 5 and 200 from multicycle SESMR/regeneration tests with mild regeneration conditions (*N_2 *at 850 °C as a regeneration medium)*

5.1.1.2. Test 2: severe regeneration

A further step towards the industrial applicability is the transition to severe regeneration conditions, as in Test 2. Overall results are summarized in Figure 5.3, in terms of averaged χ_{CH4} , $C_{H2,out}$ and $C_{CO2,out}$ from SESMR steps (§2.4.1):

- The performance of the first 5 cycles is comparable with values constantly obtained in Test 1 (§5.1.1.1);
- An abrupt decline occurs in the following 10 cycles, coming to a first stabilization until cycle 50 of χ_{CH4} (63-67 %), $C_{H2,out}$ (77-81 vol% dry, dilution-free in pre-breakthrough, 69-71 vol% dry, dilution-free in the post-breakthrough) and $C_{CO2,out}$ (5.5-6.5 vol% dry, dilution-free in pre-breakthrough, 11.2-11.8 vol% dry, dilution-free in post-breakthrough);
- In the cycles between 50 and 140, a dramatic decrease of CSCM performances is detected, as χ_{CH4} approaches 20 % and values of $C_{H2,out}$ and $C_{CO2,out}$ are not distinguishable anymore a at the end of this test portion;
- Because of the behaviour described above, a drastic reduction step is added after the severe regeneration step, so to try to restore catalytic activity, under the hypothesis that performance worsening could be related to negative effects on Ni by regeneration conditions. A partial recovery due to the cyclical strong reduction appears, as in cycles after the 141st pre-breakthrough $C_{H2,out}$ and χ_{CH4} have a slight increase and the sorption enhancing effect is partially reactivated as differences between pre- and post-breakthrough $C_{H2,out}$ and $C_{CO2,out}$ are measured; nevertheless, in the long run a deactivation tendency emerges again until the end of the tests.

The progressive worsening of CaO15Ni(N)10 during the first 140 SESMR/severe-regeneration cycles is also evident by the decline of breakthrough curves

(Figure 5.4a), as well as the partial but not decisive recovery achieved by the addition, from the 141st cycle, of the strong reduction after each regeneration (Figure 5.4b).

The partial catalytic reactivation in the second part of Test 2, obtained by means of the additional strong reduction, suggests that Ni re-oxidation by CO_2 could be a concomitant cause of the poor CSCM performance, as suggested in §1.5.4. As a matter of fact, during the regeneration by CO_2, especially in the heating ramp from 650 °C to 925 °C, some traces of CO are systematically detected in the stream leaving the reactor, probably the result of CO_2 scavenging deposited solid carbon or oxidizing superficial Ni.

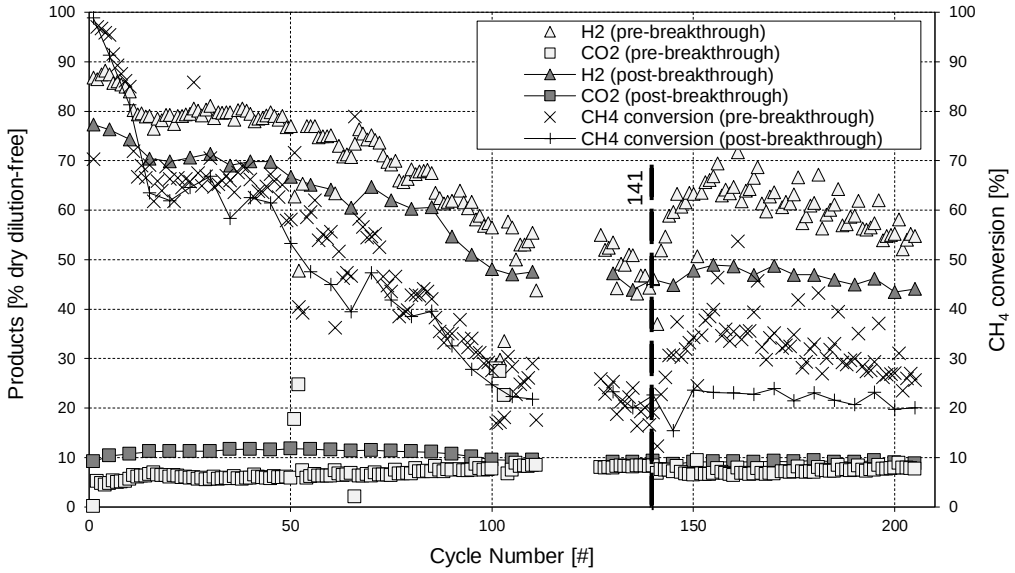

Figure 5.3: Overall experimental results of multicycle SESMR/regeneration tests with severe regeneration conditions (CO_2 at 925 °C as a regeneration medium); having §2.4.1 as a reference, the SESMR/regeneration loop 3 → 4 → 6 → 7 was performed for the first 140 cycles, the loop 3 → 4 → 6 → 8 from the loop 141 to the 204, stopping the 205 at the step 4; cycles from 112 to 126 are missing because of recording failure

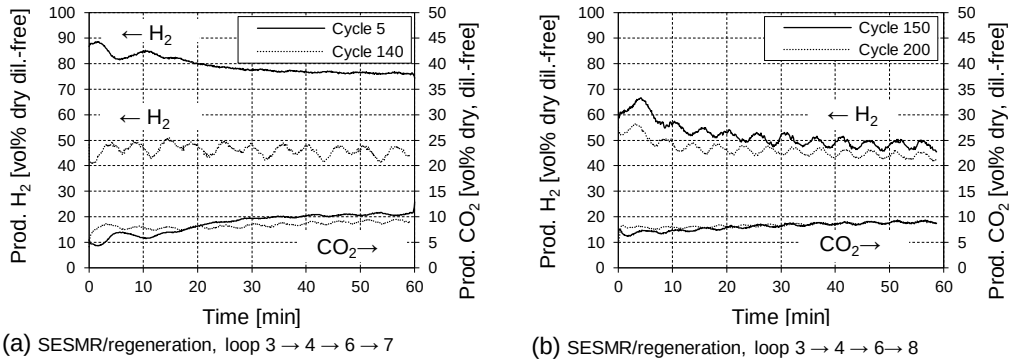

Figure 5.4: $C_{H2,out}$ and $C_{CO2,out}$ breakthrough curves from multicycle SESMR/regeneration tests with severe regeneration conditions (CO_2 at 925 °C as a regeneration medium); having §2.4.1 as a reference for the SESMR/regeneration loop 3 → 4 → 6 → 7 (cycles 1-140 (a) and the loop 3 → 4 → 6 → 8 (cycles 141-204 (b))

5.1.2 Post-test characterization

It is worth to repeat here, before the examination of post-test characterization results, that in both Test 1 and Test 2, the last loop was interrupted after the SESMR step, so that

post-test CaO15Ni(N)10 samples were not regenerated, in the case of Test 1, or regenerated and reduced, in the case of Test 2.

Figure 5.5 shows XRD analyses on CaO15Ni(N)10 after SESMR/regeneration multicycle Test 1 and Test 2. In comparison with the as-synthesized state (Figure 3.3), Ni appears in place of NiO, because of pre-reduction step (§2.4.1) and metallic Ni preservation throughout the 205 cycles of both tests, so that the Ni re-oxidation hypothesized in §1.5.4 cannot be a bulk phenomenon in a single SESMR step. $CaCO_3$ also appears, because of CO_2 capture by CaO (Reaction 1.5), more intensely in post-Test 1 sample than in post-Test 2, in accordance with their different reactive performances (Figure 5.1 and Figure 5.3, respectively). An interesting feature is the low intensity of CaO peaks (e.g. at 2θ = 37.5 °) in CaO15Ni(N)10 after Test 2, qualitatively not counterbalancing feeble $CaCO_3$ rays, having the as-synthesized materials as a reference (Figure 3.3): this could be explained by the development during Test 2 of amorphous CaO, not detectable by XRD. The development of $Ca(OH)_2$ can be explained by exposure to residual steam during reactor shut-down procedures, or to atmospheric moisture. Other crystalline phases are the same of as-synthesized state (Figure 3.3).

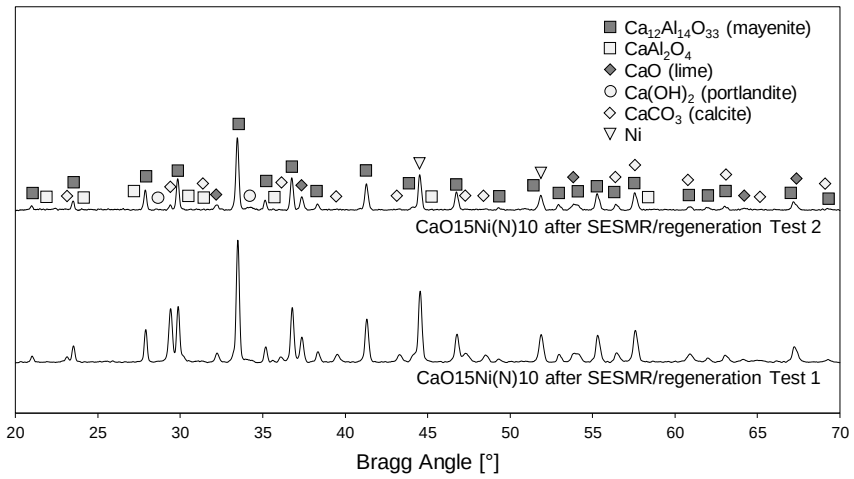

Figure 5.5: X-ray diffractograms for CaO15Ni(N)10 after SESMR/regeneration multicycle tests

Table 5.1 summarizes results of *L* estimates by Scherrer equation for CaO15Ni(N)10 after SESMR/regeneration multicycle Test 1 and Test 2: $Ca_{12}Al_{14}O_{33}$ has slightly higher *L* than the as-synthesized material (Table 3.2), as well as residual CaO, suggesting sintering phenomena; similar comments are valid for metallic Ni, having CaO15Ni(N)10 after TPR (Table 3.6) or after SESMR test in microreactor (Table 4.13) as a reference. $CaCO_3$ *L* is reported only for post-Test 1 sample, as rays are too weak in the post-Test 2: this value is sensibly lower than the one measured on CaO15Ni(N)10 after microreactor SESMR test (Table 4.13). *L* values of samples after Test 1 and Test 2 are quite similar, so the cause of their different reactive SESMR/regeneration performances does not lie in severe crystallite modifications.

Textural properties of CaO15Ni(N)10 after Test 1 and Test 2 are summarized in Table 5.2. The post-Test 2 sample, which underwent the severe regeneration for 205 times, has a

more dramatic decrease in S_{BET} and V_{BJH} than the one regenerated in mild conditions (Test 1), especially of S_{BET}, as indicated by the values of theoretical $D_{av,BJH}$ and by the comparison to as-synthesized CaO15Ni(N)10 (see ΔS_{BET} and ΔV_{BJH} in Table 5.2). The two different behaviours of post-test samples cannot uniquely be ascribed to the development of $CaCO_3$: both samples come from the 205th reforming step, without any further regeneration, so that they are in a partially carbonated state (Figure 5.5); anyway, the difference between CaO and $CaCO_3$ molar volumes does not explain the more evident textural collapse in post-Test 2 sample, as its reactive performance and post-test XRD suggest a lower carbonation (Reaction 1.5) degree than post-Tests 1 sample. All this considered, one can infer that regeneration under more severe conditions (in presence of CO2 at 925 °C) strongly and intimately reduced CaO15Ni(N)10 textural properties, an occurrence which can contribute to explain worse reactivity of this material in the multicycle SESMR/severe-regeneration test.

Table 5.1: Average crystallite size (L) estimation by Scherrer equation (Equation 2.1) for main phases of CaO15Ni(N)10 after SESMR/regeneration multicycle tests

Material	**$Ca_{12}Al_{14}O_{33}$ [nm]**	**CaO [nm]**	**$CaCO_3$ [nm]**	**Ni [nm]**
CaO15Ni(N)10 after Test 1	38.1	31.0	25.8	34.8
CaO15Ni(N)10 after Test 2	37.0	30.9	/	35.3

Table 5.2: Measured BET surface areas (S_{BET}), BJH cumulative volumes (V_{BJH}) and averaged pore diameters ($D_{av,BJH}$) for CaO15Ni(N)10 after SESMR/regeneration multicycle tests; ΔS_{BET}, ΔV_{BJH} and $\Delta D_{av,BJH}$ are the percentage variations with respect to corresponding values in as-synthesized state

Material	**S_{BET} [$m^2\ g^{-1}$]**	**ΔS_{BET} [%]**	**V_{BJH} [$cm^3\ g^{-1}$]**	**ΔV_{BJH} [%]**	**$D_{av,BJH}$ [nm]**	**$\Delta D_{av,BJH}$ [%]**
CaO15Ni(N)10 post Test 1	8.50	-31	0.024	-44	9	-18
CaO15Ni(N)10 post Test 2	3.04	-75	0.012	-73	14	+27

SEM micrographs taken from external surface of CaO15Ni(N)10 after SESMR/regeneration Test 1 are in Figure 5.6. Two morphologies are coupled in the same particle (Figure 5.6d): a porous one (Figure 5.6c), inheritance of the as-synthesized material (Figure 3.7e), and a new, more compact structure (Figure 5.6b). Similar considerations are valid for CaO15Ni(N)10 after Test 2, but SEM micrographs on external surface (Figure 5.7a and Figure 5.7b) evidence an additional relevant feature in this case: the formation of microscopic spheroidal aggregates with high elemental Ni content (brighter spots in Figure 5.7c and Figure 5.7d), confirmed also by in-situ EDS (Figure 5.8b), which are unprecedented in this thesis and therefore related to the severe regeneration strategy in CO_2 at 925 °C.

Figure 5.9 shows the SESM-EDS map of cross-sectional surface taken from embedded post-Test 1 CaO15Ni(N)10: main characteristics found by the same analysis in the as-synthesized state (Figure 3.11c) are kept, with a slightly inhomogeneous distribution of elemental Ca and Al in accordance with the desired presence of a CaO excess, and the distribution of elemental Ni in external shells. However, in post-Test 1 sample, this Ni containing shell appears more dotted, indicating Ni reaggregation phenomena occurred during the 205 SESMR/mild-regeneration cycles. This new morphology of zones rich in

elemental Ni is even more noticeable in SEM-EDS cross-sectional maps of CaO15Ni(N)10 after Test 2 (Figure 5.10), so confirming the severe regeneration as an enhancing factor of Ni migration and reorganization. This occurrence could be a concomitant cause of CaO15(N)10 worst reactive performance in multicycle SESMR/regeneration Test 2.

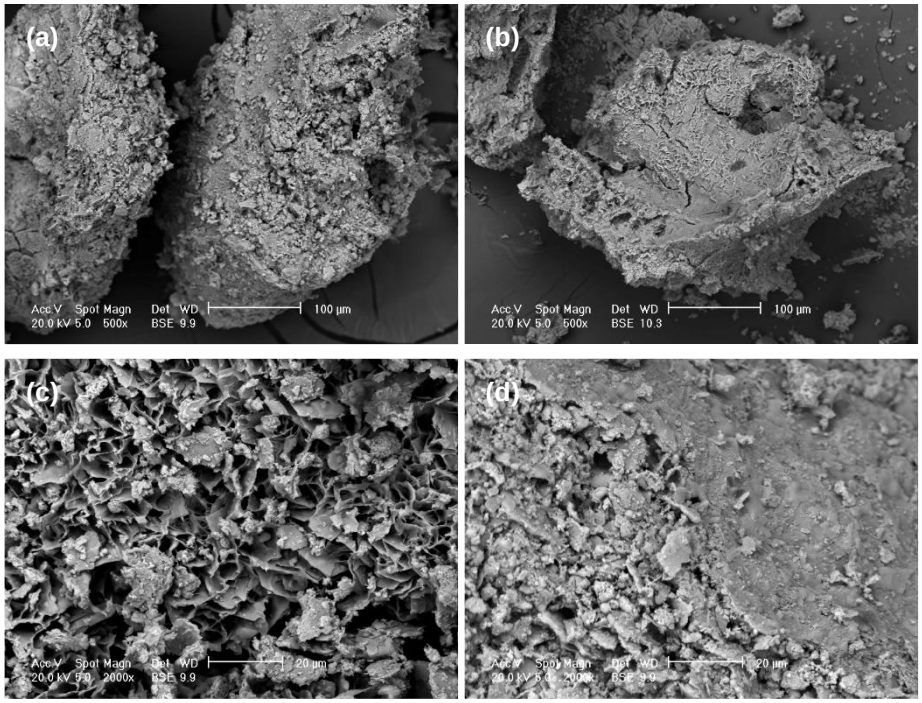

Figure 5.6: SEM micrographs of CaO15Ni(N)10 after SESMR/regeneration multicycle Test 1 at different magnifications: 500x (a) and (b), 2000x (c) and (d)

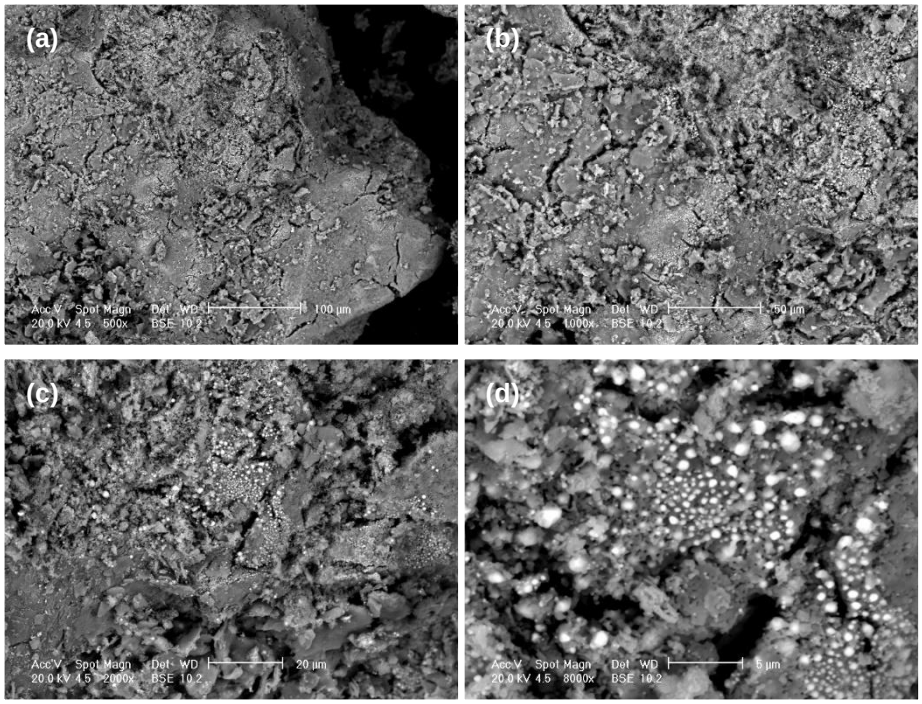

Figure 5.7: SEM micrographs of CaO15Ni(N)10 after SESMR/regeneration multicycle Test 2 at different magnifications of the same particle: 500x (a), 1000x (b), 2000x (c) and 8000x (d)

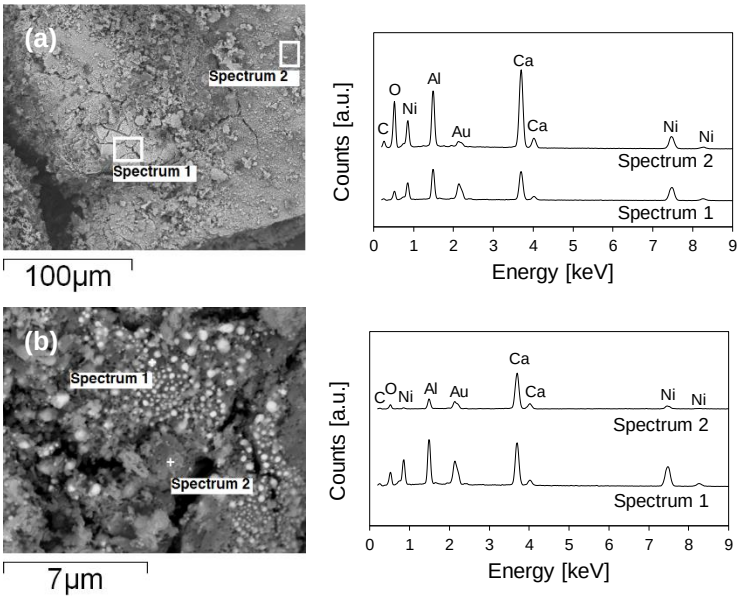

Figure 5.8: SEM-EDS on external surfaces of CaO15Ni(N)10 after SESMR/regeneration multicycle Test 1 (a) and Test 2 (b)

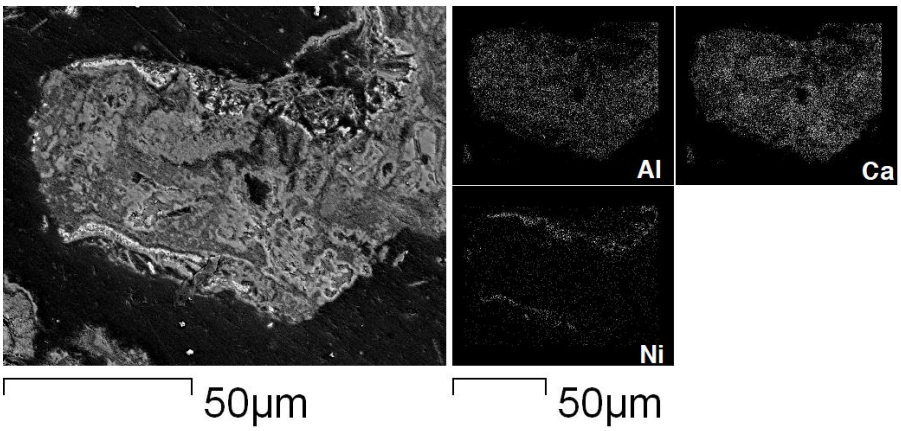

Figure 5.9: SEM-EDS map for embedded CaO15Ni(N)10 after SESMR/regeneration multicycle Test 1

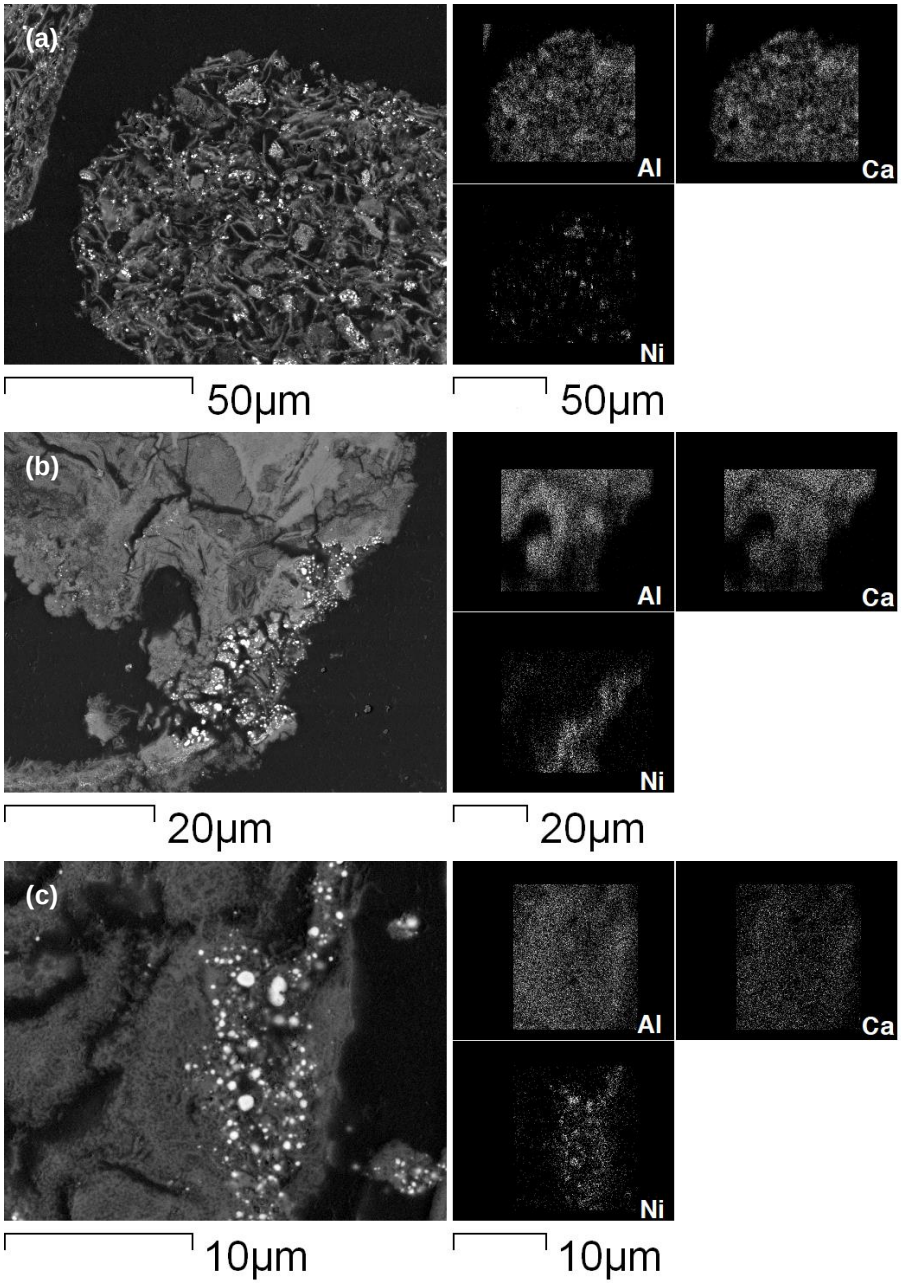

Figure 5.10: SEM-EDS map for embedded CaO15Ni(N)10 after SESMR/regeneration multicycle Test 2

TEM micrographs of CaO15Ni(N)10 after multicycle SESMR/regeneration Test 1 and Test 2 are in Figure 5.11 and Figure 5.13, respectively. In both cases, Ni particles (dark spheroids) dispersed on elemental Ca-Al-O containing support (lighter plates), both identified by STEM-EDS (Figure 5.12), have a broad distribution of size dimension, with bigger particles roughly in the order of magnitude of 10^2 nm (Figure 5.11a and Figure 5.13a), higher than *L* estimated by the XRD study (Table 5.1). These Ni particles are covered by a crystalline shell of a different nature (Figure 5.11b and Figure 5.13b), probably a subtle layer of NiO due to exposure to atmosphere. For the post-Test 2 sample, also a porous morphology is detected (Figure 5.13c and Figure 5.13d), elementally made of Ca, O and C, therefore identifiable as $CaCO_3$ (detected by EDS, not shown).

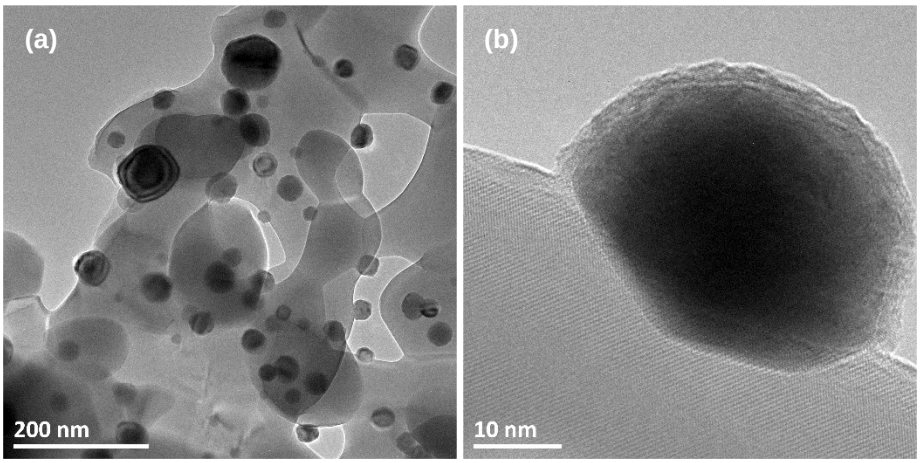

Figure 5.11: TEM micrographs of CaO15Ni(N)10 after SESMR/regeneration multicycle Test 1

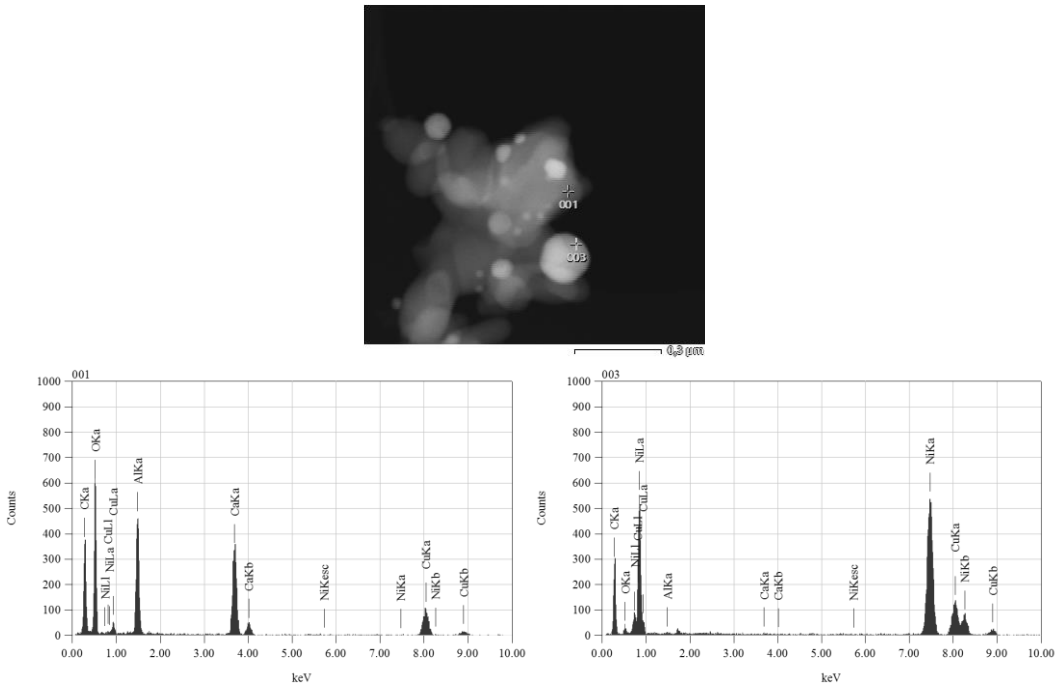

Figure 5.12: STEM-EDS analyses on CaO15Ni(N)10 after SESMR/regeneration multicycle Test 1

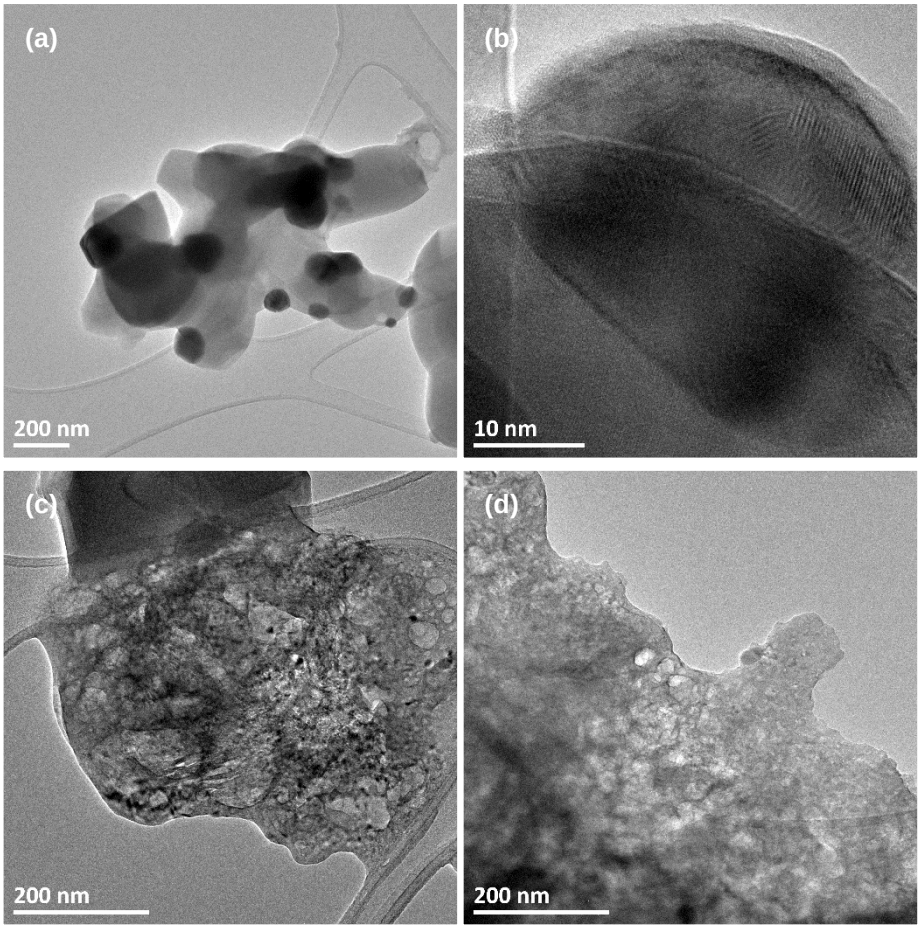

Figure 5.13: TEM micrographs of CaO15Ni(N)10 after SESMR/regeneration multicycle Test 2

5.2 Mechanical properties evaluation

Mechanical resistance to attrition is evaluated by the AJI measurements (Equation 2.11, Equation 2.12) for several materials, according to the procedure described in §2.4.2, so to have references for comparative evaluations.

Chosen reference materials for attrition tests at room temperature are olivine ($(Mg,Fe)_2SiO_4$) and dolomite in carbonated and calcined state; they are well known materials for applications in fluidized bed gasification; particularly, olivine exhibits a high mechanical strength [203].

Table 5.3: Results of attrition tests, according to procedure in §2.4.2; AJI(1 h) calculated by Equation 2.11, AJI(5 h) by Equation 2.12 and Recovery by Equation 2.13

Material	AJI(1 h) [%]	AJI(5 h) [%]	Recovery [%]
Olivine	1.4	5.4	97.4
Carbonated dolomite	4.1	17.6	97.8
Calcined dolomite	7.0	20.1	97.3
CaO15Ni(N)10 (industrial synthesis)	6.6	21.2	98.6

The CaO15Ni(N)10 sample for the attrition tests comes from a batch synthesis (~ 1 kg) performed at industrial level by Marion Technologies [204], a partner of University of L'Aquila within the work package 4 of ASCENT European research project [95]. The industrial scale synthesis has adapted to its scale the WM (§2.1.1) and WI (§2.1.2) methods, adding at their end a grinding step, with resulting average particle diameter of 15 μm, and a granulation step, reaching particle diameters up to 300 μm. The main reason for using this granulation technique is to allow the material densification in the form of quite spherical granules, thus promoting mechanical stability for use in fluidized bed reactors. It consists of wetting the solid fine particles, so to create coalescence and lead to the formation of bigger granules by adding a solution binder, while mixing the solid powder in a bowl with an impeller of appropriated shape; eventually, granules undergo a calcination to remove the residual binder.

AJI of reference materials and CaO15Ni(N)10 are summarized in Table 5.3: all the tests are reliable, as they show high material recovery (Equation 2.13); CaO15Ni(N)10 has AJI(1 h) and AJI(5 h) very close to those of calcined dolomite, significantly lower than olivine ones.

5.3 Conclusions

The automated packed-bed test rig, purposely developed to carry out multicycle SESMR/regeneration tests, successfully accomplished its mission, managing experiments with respective durations of 16 days and 19 days, with high frequency data sampling, a relevant number of process steps alternations per day, and the limited necessity of operators' intervention.

Moving the attention to experimental results from these tests, having CaO15Ni(N)10 as active packed-bed, a crucial influence on SESMR performances came from the two used regeneration strategy:

- Mild regeneration (pure N_2 at 850 °C) allowed a very stable and satisfactory H_2 production by SESMR for 205 cycles, therefore attesting a basic ability of CaO15Ni(N)10 to operate the process studied in this thesis;
- Severe regeneration (pure CO_2 at 925 °C) brought about a very deactivation in 140 cycles; the addition of a strong reduction step (50 vol% of H_2 in N_2, 850 °C) after each severe regeneration, caused only a partial restoration of catalytic activity in the following 65 cycles. These results proved a limitation of CaO15Ni(N)10 to operate in severe regeneration conditions.

The two post-test materials have different textural and morphologic-topographic properties:

- The severely regenerated CaO15Ni(N)10 suffered a more dramatic collapse of its texture in comparison to the mildly regenerated one, as evidenced by BET and BJH results, only ascribable to the different regeneration procedure.

- Ni underwent a severe rearrangement at microscopic scale in the hardly regenerated CaO15Ni(N)10, unprecedented in all other tests presented in this thesis.

These two features are considered as concomitant causes of CSCM worse performance in the multicycle SESMR/hard-regeneration test.

An industrially synthesized version of CaO15Ni(N)10, was tested according to ASTM D5757, as well as some reference materials for fluidized beds applications. It resulted very close to a calcined dolomite in terms of attrition resistance, but inferior to olivine. In other words, mechanical resistance to attrition of CaO15Ni(N)10 is acceptable, but could be improved.

General conclusions

Climate change is a fact, correlated by the clear majority of the international scientific community to anthropogenic GHG emissions. Among possible strategies for the containment of these emissions, the use of H_2 as a fuel for fuel cells is a promising path, as well as the coupling of carbon capture and storage technologies with traditional fossil-fuel systems.

SESMR has the potential to combine these two paths, since it consists of an intensification of the traditional H_2 production process via SMR, by means of in-situ CO_2 capture. Among several goals, the European research project ASCENT, to which this thesis is a contribution, aims to give a solid proof-of-concept of SESMR.

Ni and CaO were respectively chosen as active phases for SMR catalysis and CO_2 capture, then associated with mayenite ($Ca_{12}Al_{14}O_{33}$) as a support, so to obtain:

- Ni-mayenite SMR catalysts;
- CaO-mayenite CO_2 sorbents;
- Ni-CaO-mayenite CSCM for SESMR.

The effects of different Ni precursor salts (Ni(N) or Ni(Ac)), Ni fractions (nominally within the range 3-10 wt%) and free CaO fractions (nominally within 0-54 wt%) were investigated, by ICP-AES, XRD, BET/BJH, SEM-EDS, TEM, STEM-EDS, TPR, TGA and by reactivity tests.

WM method successfully produced CaO-mayenite sorbents and mayenite support (CaO0). WI method was effective in in the addition of Ni (from both N(N) and Ni(Ac)) on WM products, so to get Ni-mayenite SMR catalysts or Ni-CaO-mayenite CSCM. In fact, XRD always detected the desired crystalline phases.

SEM micrographs proved that synthesized materials share a common microgranular external morphology. With regard to impregnated samples, SEM-EDS showed elemental Ni to be mainly in external shells around material particles, or in lodes within pores. N_2 adsorption/desorption isotherms allowed to infer a common texture for all synthesised materials: a set of meso- and macroporous internal voids of irregular shape, in good accordance with SEM micrographs taken from cross sectional surfaces of embedded samples.

Characterization of as-synthesized Ni-mayenite catalysts showed that:

- S_{BET} and V_{BJH} decreased as the final Ni fraction increased, more dramatically in the case of WI by Ni(Ac) compared to Ni(N);
- Catalysts derived from Ni(N) had more intense Ni-support interactions than Ni(Ac) derived ones, since for the former TPR main peaks were measured at higher temperatures than for the latter.

Regarding as-synthesized CaO-mayenite sorbents:

- A nominal elemental Ca/Al molar ratio higher than 1.8 avoided the formation of crystalline calcium aluminates other than mayenite by WM method;
- Whatever the intended nominal CaO excess, S_{BET} decreased in comparison to CaO0;

Concerning as-synthesized CSCM:

- a threshold limit linked to CaO excess was found about textural and reducibility properties, between CSCM derived from CaO15 and those obtained from CaO30, CaO45, CaO54: the first exhibited a behaviour close to Ni-mayenite materials, with higher S_{BET} or V_{BJH} than the remaining CSCM, and stronger Ni-support interactions (especially for Ni(N) derived ones);
- With 10 wt% of Ni, WI reduced S_{BET} and V_{BJH} more than in the case of 3 wt% of Ni, having respective parent sorbents values as a reference, without a clear differentiation between Ni(N) and Ni(Ac).

Multicyclic CO_2 capture/regeneration tests were performed in TGA, on two selected groups of parent sorbent and respective CSCM: CaO30, CaO30Ni(N)3, CaO30Ni(Ac)3 and CaO54, CaO54Ni(N)3, CaO54Ni(Ac)3. Tests confirmed the important action of mayenite in the containment of CaO sintering, for both CaO-mayenite sorbents and CSCM, the more effective the higher is its mass ratio with respect to CaO.

Since main differences among synthesized materials were located in textural and reducibility properties, future work could involve the use of analytical techniques other than those described in this thesis.

Several reactivity tests were carried out at atmospheric pressure in a purposely assembled microreactor scale packed-bed test rig (0.5 mg):

- SMR tests on Ni-mayente catalysts showed that the derivation from Ni(N) determines remarkably higher reactivity than Ni(Ac), at all tested temperatures and especially at 650 °C, the temperature of interest for SESMR;
- SESMR tests on 2-material systems in separate beds configuration showed the ability of all synthesized CaO-mayenite sorbents to capture CO_2 at the chosen SESMR experimental conditions (650 °C, 1 atm, molar steam/carbon = 3);
- SESMR tests on 2-material systems in raw mixing configuration confirmed the detrimental effect of CaO on Ni reforming activity, occasionally suggested in the literature;
- SESMR tests on CSCM summed up all features guessed by foregoing microreactor scale tests. In fact, Ni(Ac) derived CSCM were definitely less

active than Ni(N) ones, while CaO excess in the parent sorbent equal to 30 wt% or more caused in the corresponding CSCM a reduced activity of Ni, in comparison to CSCM derived from CaO15, restored only in the case of Ni(N) derivation by increasing Ni fraction from 3 wt% to 10 wt%.

It is worth noticing here that the same threshold limit for CaO excess found with regard to reducibility and textural properties, somehow applies also about catalytic activity in microreactor scale tests: CSCM derived from CaO15 showed a reactivity close to Ni-mayenite materials at the conditions chosen for SESMR, higher than other CSCM and more important in the case of derivation from Ni(N). Some CSCM, even though exhibited high sorption capacities in TGA CO_2 capture tests, had low reactivity or did not work at all for SESMR, therefore proving that, for Ni-CaO-mayenite materials synthesized by WM and WI, the catalytic aspects of the process must be favoured in order to perform SESMR.

All trends highlighted by microreactor scale tests served as criteria to choose CaO15Ni(N)10 as the best CSCM to be studied for industrial applicability. This study consisted of multicycle SESMR/regeneration experiments, and attrition tests according to ASTM D5757.

Multicycle tests were performed in an automated bench scale packed-bed (10 g) tests rig, specially designed and realized during this thesis work, to manage cyclical processes alternating several operating conditions for a relevant number of times:

- A first test counted 205 SESMR/regeneration cycles with a mild regeneration procedure (pure N_2, 850 °C), in which CaO15Ni(N)10 had a satisfactory and stable performance (roughly 90 vol% dry, dilution-free of H_2 in pre-breakthrough for all cycles), without significant drop in catalytic activity and sorption enhancing duration;
- A second test counted 205 SESMR/regeneration cycles with severe regeneration conditions (pure CO_2, 925 °C), closer to those of a hypothetical industrial process, which caused a decline of CaO15Ni(N)10 reactive performance, related by post-test characterization to a collapse of CSCM texture and a rearrangement of Ni species in coarse microscopic granules.

It is worth noticing here that complementary tests performed by the candidate in the ASCENT project, on materials synthesized by other partner, showed that when an industrial catalyst is mechanically mixed and granulated together with a CaO-mayenite sorbent to get a CSCM, more satisfactory performances were obtained in multicycle test with severe regeneration condition. This points to the need of further studies to strengthen the Ni catalytic activity in CSCM synthesized by wet mixing and wet impregnation.

Moving the attention to attrition resistance, an industrially synthesized version of CaO15Ni(N)10 underwent the experimental procedure of ASTM D5757, as well as some reference materials. CaO15Ni(N)10 mechanical features resulted very close to those of calcined dolomite, but lower than those of olivine, well known for its hardness. This indicates an acceptable, but at the same time improvable resistance to attrition, as far as the utilization in fluidized beds is concerned. Incidentally, the fact that CaO15Ni(N)10 had

been synthesized industrially for this test, proved the scalability of WM and WI at commercial level thanks to their intrinsic simplicity.

As an overall consideration, in this thesis efforts were focused on the empirical understanding of mutual influences between Ni and CaO, and between reforming catalysis and CO_2 sorption in SESMR, by means of reactivity tests and with the support of several characterization techniques. These efforts brought to the formulation of a CSCM able to face without noticeable aftermath 205 SESMR/mild-regeneration cycles, therefore proving its basic effectiveness. On the other hand, in the light of worse performances under relevant conditions relevant for industrial applicability, further efforts are needed to improve this intrinsic effectiveness. Future studies could be about the effects of severe regeneration under CO_2 at very high temperatures, or the optimization of synthesis methods so to improve CSCM attrition resistance, without affecting catalytic and CO_2 sorption functionalities.

Addendum A

Other materials in the ASCENT project

A.1 Introduction

In the framework of ASCENT research project, other partners produced materials for SESMR by alternative synthetic routes. Some of them had resulted as worthy for an evaluation of their industrial applicability, so that they were tested at University of L'Aquila for multicycle SESMR/regeneration.

Tested materials were industrially produced by Marion Technologies (France) on the basis of a formulation elaborated by IFE (Institutt For Energiteknikk, Norway) in cooperation with CSIC-ICB (Consejo Superior de Investigaciones Cientificas – Instituto de Carboquimíca, Spain).

This formulation counts:

- The synthesis of a CaO-mayenite sorbent by a hydrothermal method, with nominal 30 wt% of free CaO, from here on named CaO30-IFE;
- The use of a commercial Ni-based reforming catalyst (roughly 15 wt% of Ni), from here on named Ni-comm;
- The grinding in fine particles (< 75 μm) of the materials in the two preceding points, and their combined granulation (§5.2) in a proportion CaO30-IFE : Ni-comm equal to 6 : 4, to form a mechanically CSCM, from here on named CaO30Ni-IFE.

A.2 Materials and methods

The employed automated packed-bed test rig and the method for data elaboration are the same described in §2.4.1. Steps employed in these SESMR/regeneration multicycle test follow:

1. Pre-reduction. In order to reduce NiO to metallic Ni, 200 Nml min^{-1}, 50 vol% of H_2 in N_2 flow through the active packed bed, heated from room temperature to 850 °C by a 5 °C min^{-1} heating ramp, and kept at 900 °C for 30 min.
2. Cooling 1. The reactor is cooled at 5 °C min^{-1}, down from 8500 °C to 650 °C, while a mild reducing stream flows (7.5 Nml min^{-1} of H_2 and 142.5 Nml min^{-1} of N_2).
3. Steaming. At 650 °C, for 4 min, 0.240 ml min^{-1} of liquid distilled water are fed together with 150 Nml min^{-1} of N_2, in order to ensure the evaporating chamber to be ready for steam production when reforming is started.
4. Reforming. At 650 °C, the inlet stream contains 75 Nml min^{-1} of CH_4, with inlet molar steam/carbon ratio equal to 4 or 3. Two different durations are chosen: long reforming steps last 40 min, so to measure packed-bed's breakthrough i.e. sorbent saturation; for other cycles, reforming lasts 20 min, so to avoid breakthrough occurrence. After the reforming, reactor is purged at 650 °C for 2 min by 150 Nml min^{-1} of N_2.
5. Severe regeneration. The active packed-bed is heated by a 10 °C min^{-1} ramp, from 650 °C to 925 °C, and kept at 925 °C for 15 min, feeding 150 Nml min^{-1} of CO_2. After that, reactor is purged at 925 °C for 1 min by 150 Nml min^{-1} of N_2.
6. Cooling-Reduction. The reactor cools down from 925 °C min^{-1} to 850 °C, under 150 Nml min^{-1} of N_2, at 5 °C min^{-1}; afterwards, a highly reducing stream (100 Nml min^{-1} of H_2 and 100 Nml min^{-1} of N_2) flows through the bed at 850 °C to restore metallic Ni; eventually, the reactors cools down under a mild reducing stream (7.5 Nml min^{-1} of H_2 and 142.5 Nml min^{-1} of N_2) down to 650 °C.

Tests were carried out on:

- the 2-material system in raw mixing configuration, made of CaO30-IFE (9 g, particle diameter in the range 212-300 µm) and Ni-comm (3 g, particle diameter in the range 212-300 µm): after Pre-reduction and Cooling 1, the loop 3 → 4 → 5 → 6 was repeated 208 times;
- CaO30Ni-IFE (12.0 g, particle diameter in the range 212-300 µm): after Pre-reduction and Cooling 1, the loop 3 → 4 → 5 → 6 was repeated 200 times.

A.3 Experimental results

Results from the multicycle SESMR/regeneration test on the raw mixing CaO30-IFE + Ni-comm and on CaO30Ni-IFE are shown in Figure A.1 and Figure A.2, respectively.

The raw mixing, tested with inlet molar steam/carbon ratio of 4, have a very stable performance in terms of $C_{H2,out}$ and $C_{CO2,out}$ respectively within the range 93-95 vol% dry, dilution-free and 2.0-3.0 vol% dry, dilution-free in the pre-breakthrough period, and very close to SMR equilibrium values in the post-breakthrough; χ_{CH4} suffers a slight decline

from values at about 97 % in the 15 first cycles, stabilized between 92 % and 93 % after the 60th cycle.

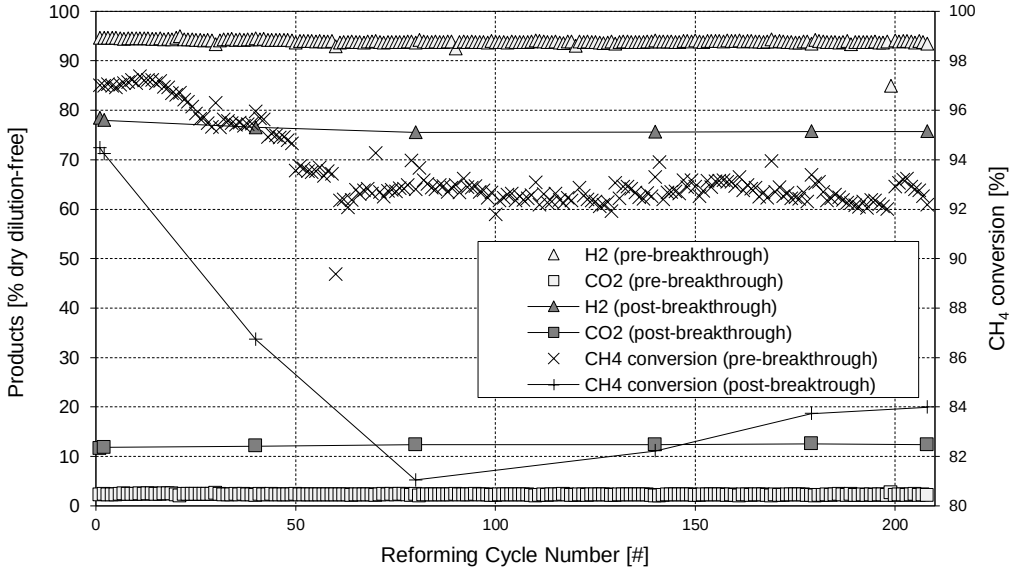

Figure A.1: Overall experimental results of multicycle SESMR/regeneration test on the 2-material system in raw mixing configuration CaO30-IFE + Ni-comm; long reforming steps performed at cycles 1, 2, 40, 80, 140, 179, 208; all cycles with inlet steam/carbon molar ratio = 4

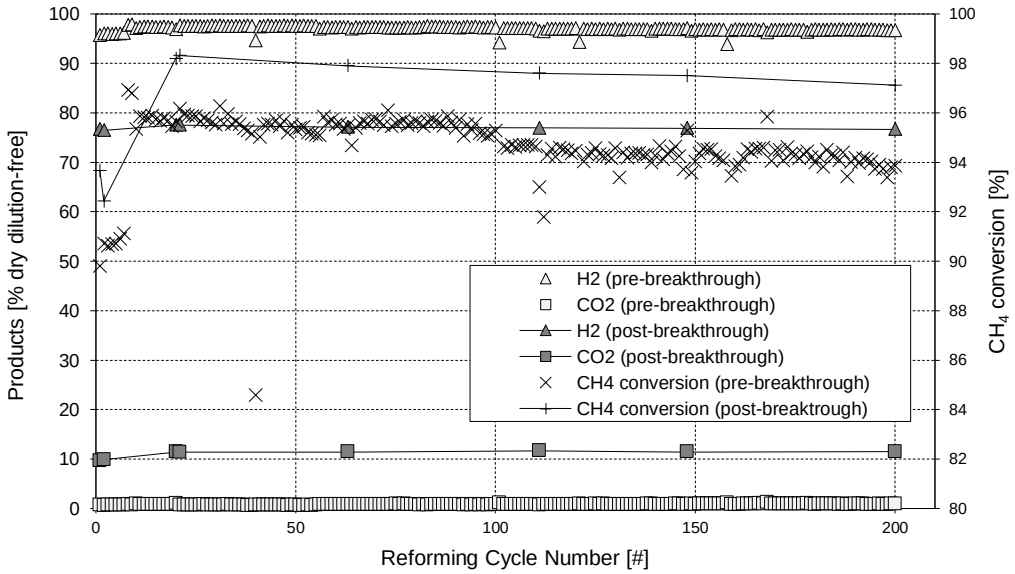

Figure A.2: Overall experimental results of multicycle SESMR/regeneration test on Ca30Ni-IFE CSCM; long reforming steps performed at cycles 1, 2, 20, 21, 63, 111, 148, 200; first 7 cycles with inlet steam/carbon molar ratio = 3, all the rest with inlet steam/carbon molar ratio = 4

The CSCM, tested for the first 7 cycles with inlet molar steam/carbon ratio of 3 and then of 4, gave even better results than the 2-material system, when the same evaluation parameters are taken into account. For cycles with molar steam/carbon ratio 4, pre-breakthrough $C_{H2,out}$ and $C_{CO2,out}$ are respectively 96-98 vol% dry, dilution-free and

0.5-1.0 vol% dry, dilution-free, whereas χ_{CH4} slowly declines from about 96 % to about 94 %; homologue post-breakthrough parameters are closer to SESMR thermodynamic equilibrium than the 2-material system. The influence of the inlet molar steam/carbon ratio is evidenced by the different performances in the first 7 cycles, exhibiting pre-breakthrough $C_{H2,out}$ and χ_{CH4} lower than subsequent cycles with steam/carbon 4.

Figure A.3 shows breakthrough curves from the 2-material system (Figure A.3a) and the CSCM (Figure A.3b): the longer pre-breakthrough duration in the former case is primarily caused by the sensibly higher CaO quantity available in its tested packed-bed, if compared to the latter case. Anyway, in both cases an anticipation of the breakthrough is detected, ascribable to the decrease of CaO sorption capacity.

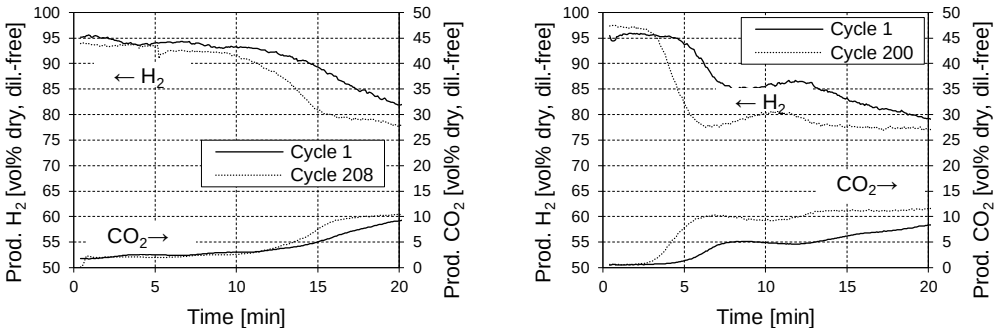

(a) SESMR/regeneration, CaO30-IFE + Ni-comm (b) SESMR/regeneration, CaO30Ni-IFE

Figure A.3: $C_{H2,out}$ *and* $C_{CO2,out}$ *breakthrough curves from multicycle SESMR/regeneration tests on the -2-material system in raw mixing configuration CaO30-IFE + Ni-comm (a) and the CSCM CaO30Ni-IFE (b)*

Addendum B

Validation of SESMR models

B.1 Introduction

In the framework of ASCENT project work package 4, the commitment of University of L'Aquila has been addressed also to mathematical modelling of SESMR.

A Particle Grain Model (PGM) was previously developed by Stendardo and Foscolo [205] to simulate the CO_2 capture behaviour of a CaO-based sorbents, with an inert binder, e.g. dolomite or CaO-mayenite developed in this thesis (Reaction 1.5).

As a first step for SESMR modelling, Aloisi et al. [101] adapted this PGM to a Ni-CaO-inert binder CSCM carrying out SESMR, by the addition of SMR (Reaction 1.1) and WGS (Reaction 1.2) kinetic laws by Numaguchi and Kikuchi [206], also implementing their new PGM in a MATLAB® code and validating it by the comparison of simulation results with literature data of CO_2 sorption.

This thesis work contributed to further modelling steps: Aloisi et al. [102] verified the flexibility of the PGM [101], re-validating it against experimental data of multicycle CO_2 capture/regeneration TGA tests in §3.6; moreover, they integrated the PGM [101] in an Axial Dispersion Plug Flow Reactor (ADPFR) dynamic model and implemented the result in a MATLAB® code, so to validate it by the comparison of simulations with experimental data of SMR and SESMR tests in microreactor scale presented in §4.3 and §4.5.

Basic hypotheses, together with mathematical elaboration and details of PGM and ADPFR dynamic model are fully reported in [101,102]. Main validation results, achieved by the exploiting of experimental results presented in this thesis, follow.

B.2 Validation of PGM

In Aloisi et al. [102], as far as CO_2 capture function is concerned, the PGM model is validated by means of TGA data from multicycle CO_2 capture/regeneration tests on the two families CaO30, CaO30Ni(N)3, CaO30Ni(Ac)3 (Figure 3.25a) and CaO54, CaO54Ni(N)3,

CaO54Ni(Ac)3 (Figure 3.25b). This validation was successful, as proved by Figure B.1 showing a good ability of the PGM in fitting the characteristic knee-shaped CO_2 capture curve of CaO-based sorbents.

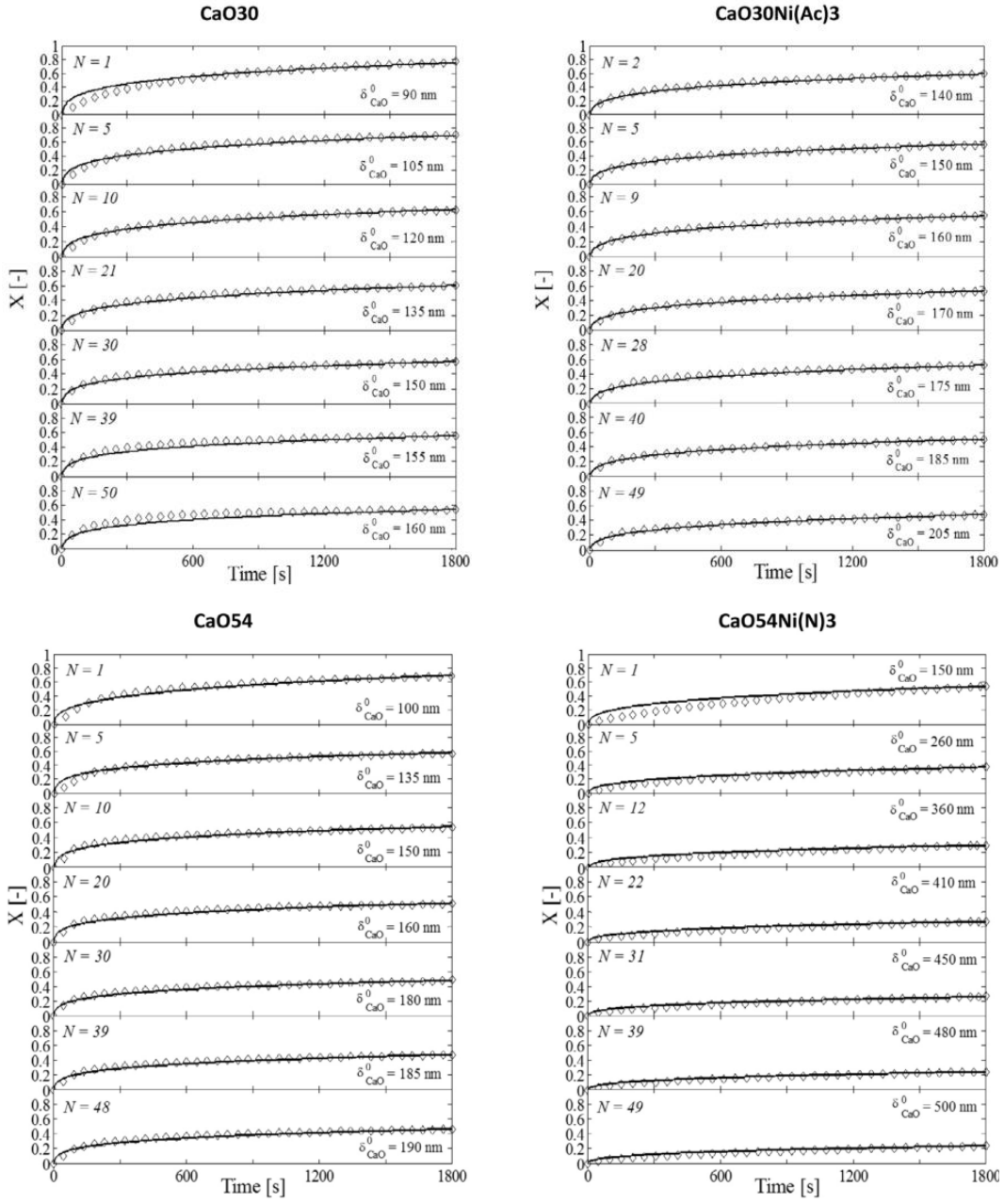

Figure B.1: Experimental data (diamond dots) and PGM numerical simulations (solid lines) of CaO conversion, (X), as a function of time, for multicycle CO_2 capture/regeneration tests in TGA (§3.6); for each simulated cycle (N), the initial average diameter of calcined sorbent grains (δ_{CaO}^0) is pointed out; data and picture from [101]

The main feature arisen from this validation process follows:

- For each material, in order to faithfully fit the progressive decrease of CO_2 capture performances with cycle number increase, only one parameter must be varied in the PGM: the average initial diameter of CaO grains (δ_{CaO}^0), the

higher its value the lower the final amount of CO_2 capture, therefore mimicking sintering phenomena;

- For each family, a unique set of parameters related to the diffusional resistance, caused by $CaCO_3$ layer developing on CaO grains, must be adjusted once and kept constant during the cycle progression; thus, the model well represents the fact that CSCM and the respective parent sorbent have a common originating matrix of which structure is practically unchanged by WI (§3.3.1).

B.3 Validation of ADPFR dynamic model

In Aloisi et al. [102], an ADPFR dynamic model for SESMR is presented and validated by a comparison with SESMR data from microreactor scale tests in §4.5.1. This model results from an integration of the previously developed PGM [101] with mole balances on gaseous species surrounding packed-bed particles and inside their internal pore, assuming an ADPFR configuration.

As shown in Figure B.2, the agreement with corresponding data points (already shown in Figure 4.17d and Figure 4.17b) is quite good and indicates that model assumptions allow to describe simultaneous CO_2 sorption (Reaction 1.5), SMR (Reaction 1.1) and WGS (Reaction 1.2) reactions in the microreactor containing a packed-bed of CSCM particles. A faithful simulation of $C_{H2,out}$ and $C_{CH4,out}$ is obtained, while the kinetic model tends to underestimate $C_{CO2,out}$ and overestimate $C_{CH4,out}$ present in the outlet gas; however, the presence of the breakthrough region and the overall concentration of both carbon oxides is predicted quite well.

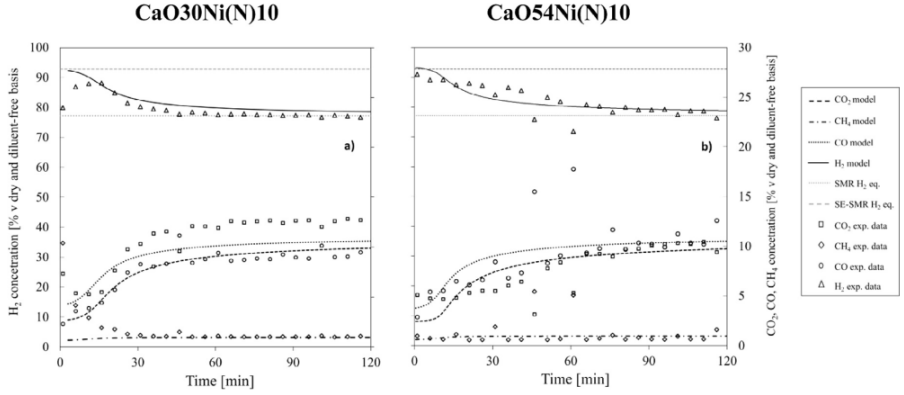

Figure B.2: $C_{H2,out}$ *(LHS vertical axis) and* $C_{CO2,out}$, $C_{CO,out}$, $C_{CH4,out}$ *(RHS vertical axis) as functions of time: measured values and ADPFR dynamic model simulations, for SESMR tests in microreactor scale on CaO30Ni(N)10 (a) and CaO54Ni(N)10 (b); data and picture from* [101]

B.3 ADPFR for SESMR/regeneration cycles

The same ADPFR model [102] has been used to simulate some reforming steps from the multicycle SESMR/regeneration Test 1 carried out on CaO15Ni(N)10 (§5.1.1.1).

As already verified in §B.1, the only parameter to be varied so to fit experimental data as the cycle number increase, is $\delta_{CaO}{}^{0}$ (Figure B.3); all other model parameters, once set to

fit the first SESMR breakthrough, can be kept constant to simulate SESMR of subsequent cycles.

Furthermore, the progression of $\delta_{CaO}{}^{0}$ throughout the 205 cycles of Test 1 is contained in a very small range (90-115 nm, Figure B.4), in accordance with the high experimental stability in SESMR/regeneration cycles (Figure 5.1).

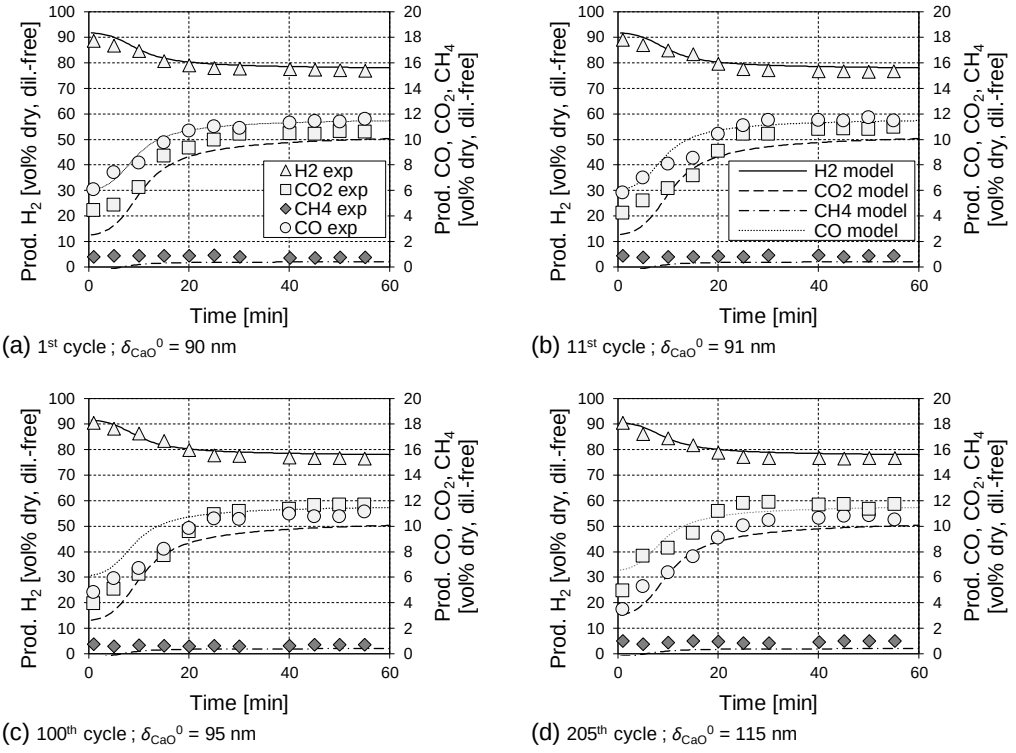

Figure B.3: $C_{H2,out}$ *(LHS vertical axis) and* $C_{CO2,out}$, $C_{CO,out}$, $C_{CH4,out}$ *(RHS vertical axis) as functions of time: measured SESMR breakthrough values and ADPFR dynamic model simulations, for multicycle SESMR/regeneration Test 1 in bench scale automated test rig on CaO15Ni(N)10, cycles 1 (a), 11 (b), 100 (c), 205 (d); legends in (a) and (b) are valid for all pictures; data and picture from* [101]

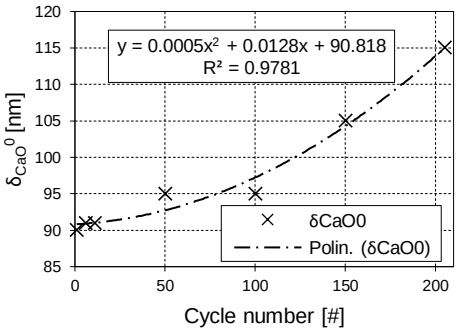

Figure B.4: Polynomial regression of $\delta_{CaO}{}^{0}$ *used to fit SESMR breakthrough experimental data of multicycle SESMR/regeneration*

References

[1] A. Gettelman, R.B. Rood, Climate Change and Global Warming, in: 2016: pp. 23–35. doi:10.1007/978-3-662-48959-8_3.

[2] R.K. Pachauri, M.R. Allen, V.R. Barros, J. Broome, W. Cramer, R. Christ, et al., Climate Change 2014: Synthesis Report. Contribution of Working Groups I, II and III to the Fifth Assessment Report of the Intergovernmental Panel on Climate Change, Epic. Switzerland, IPCC, 151 P., Pp. 151, ISBN 978-92-9169-143-2. (2014).

[3] B.D. Santer, K.E. Taylor, T.M.L. Wigley, T.C. Johns, P.D. Jones, D.J. Karoly, et al., A search for human influences on the thermal structure of the atmosphere, Nature. 382 (1996) 39–46. doi:10.1038/382039a0.

[4] N. Oreskes, The scientific consensus on climate change, Science (80-.). 306 (2013). http://science.sciencemag.org/content/306/5702/1686.full (accessed September 9, 2017).

[5] Z. Li, N. Cai, Y. Huang, Effect of Preparation Temperature on Cyclic CO2 Capture and Multiple Carbonation - Calcination Cycles for a New Ca-Based CO2 Sorbent, Ind. Eng. Chem. Res. (2006) 1911–1917. doi:10.1021/ie051211l.

[6] J.F.B. Mitchell, The "Greenhouse" effect and climate change, Rev. Geophys. 27 (1989) 115–139. doi:10.1029/RG027i001p00115.

[7] M. MacCracken, F. M. Luther, Projecting the Climatic Effects of Increasing Carbon Dioxide, Washington, D.C., 1985. file:///C:/Users/Andrea Di Giuliano/Downloads/Projecting SOA-5885458.pdf.

[8] F. Pachauri, Rajendra K Meyer, Leo Van Ypersele, Jean-Pascal Brinkman, Sander Van Kesteren, Line Leprince-Ringuet, Noëmie Van Boxmeer, Climate Change 2013 - The Physical Science Basis, 2014. doi:10.1017/CBO9781107415324.

[9] EC, Climate Action - Causes of climate change, (2016). https://ec.europa.eu/clima/change/causes_en (accessed September 13, 2017).

[10] T.J. Blasing, Recent Greenhouse Gas Concentrations., Carbon Dioxide Inf. Anal. Center, Oak Ridge Natl. Lab. (2009) 1–5. doi:10.3334/CDIAC/atg.032.

[11] CDIAC, Carbon Dioxide Information Analysis Center (CDIAC), (n.d.). http://cdiac.ornl.gov/ (accessed September 14, 2017).

[12] CRU, Data, (n.d.). https://crudata.uea.ac.uk/cru/data/temperature/#datdow.

[13] NOOA, Global climate change indicators, (n.d.). https://www.ncdc.noaa.gov/monitoring-references/faq/indicators.php.

[14] IPCC, Summary for Policymakers, (n.d.). https://www.ipcc.ch/pdf/assessment-report/ar5/syr/AR5_SYR_FINAL_SPM.pdf (accessed September 10, 2017).

[15] S. Levitus, J.I. Antonov, T.P. Boyer, R.A. Locarnini, H.E. Garcia, A. V. Mishonov, Global ocean heat content 1955-2008 in light of recently revealed instrumentation problems, Geophys. Res. Lett. 36 (2009) n/a-n/a. doi:10.1029/2008GL037155.

[16] C.L. Sabine, The Oceanic Sink for Anthropogenic CO2, Science (80-.). 305 (2004)

367–371. doi:10.1126/science.1097403.
[17] R. Kwok, D.A. Rothrock, Decline in Arctic sea ice thickness from submarine and ICESat records: 1958-2008, Geophys. Res. Lett. 36 (2009) n/a-n/a. doi:10.1029/2009GL039035.
[18] world glacier monitoring service - under the auspices of: ICSU (WDS), IUGG (IACS), UNEP, UNESCO, WMO, (n.d.). http://wgms.ch/ (accessed September 10, 2017).
[19] NASA, Snow Cover : Global Maps, (2017). https://earthobservatory.nasa.gov/GlobalMaps/view.php?d1=MOD10C1_M_SNOW (accessed September 10, 2017).
[20] J.A. Church, N.J. White, A 20th century acceleration in global sea-level rise, Geophys. Res. Lett. 33 (2006) n/a-n/a. doi:10.1029/2005GL024826.
[21] Attribution of Extreme Weather Events in the Context of Climate Change, National Academies Press, Washington, D.C., 2016. doi:10.17226/21852.
[22] P.A. Stott, N. Christidis, F.E.L. Otto, Y. Sun, J.P. Vanderlinden, G.J. van Oldenborgh, et al., Attribution of extreme weather and climate-related events, Wiley Interdiscip. Rev. Clim. Chang. 7 (2016) 23–41. doi:10.1002/wcc.380.
[23] J. Bongaarts, Slow down population growth: within a decade, women everywhere should have access to quality contraceptive services, Nature. 530 (2016) 409–413. http://go.galegroup.com/ps/anonymous?id=GALE%7CA444595365&sid=googleScholar&v=2.1&it=r&linkaccess=fulltext&issn=00280836&p=AONE&sw=w&authCount=1&isAnonymousEntry=true (accessed September 14, 2017).
[24] D. of E. and S.A. United Nations, World Population Prospects, in: 2015. https://esa.un.org/unpd/wpp/publications/Files/WPP2015_DataBooklet.pdf (accessed September 14, 2017).
[25] IEA, Key World Energy Statistics 2016, Statistics (Ber). (2016) 80. doi:10.1787/9789264039537-en.
[26] G. Buxton, The Montreal protocol on substances that deplete the ozone layer., 1988. doi:10.1163/15718069620847781.
[27] U. Nations, Kyoto Protocol To the United Nations Framework Kyoto Protocol To the United Nations Framework, Rev. Eur. Community Int. Environ. Law. 7 (1998) 214–217. doi:10.1111/1467-9388.00150.
[28] E. Commission, EUROPE 2020. A European strategy for smart, sustainable and inclusive growth, Brussels, 2010. file:///C:/Users/Andrea Di Giuliano/Google Drive/Dottorato ASCENT/Literature/Climate change/Europe2020.pdf.
[29] United Nations, Paris Agreement, 21st Conf. Parties. (2015) 3. doi:FCCC/CP/2015/L.9.
[30] Allianz, Analysis & Trends The sixth Kondratieff – long waves of prosperity, 2010. http://scholar.google.com/scholar?hl=en&btnG=Search&q=intitle:Analysis+&+Trends+The+sixth+Kondratieff+?+long+waves+of+prosperity#0.
[31] J.S. Wallace, C.A. Ward, Hydrogen as a fuel, Int. J. Hydrogen Energy. 8 (1983) 255–268. doi:10.1016/0360-3199(83)90136-2.
[32] T.N. Vezirolu, F. Barbir, Hydrogen: the wonder fuel, Int. J. Hydrogen Energy. 17 (1992) 391–404. doi:10.1016/0360-3199(92)90183-W.
[33] T. da Silva Veras, T.S. Mozer, D. da Costa Rubim Messeder dos Santos, A. da Silva César, Hydrogen: Trends, production and characterization of the main process worldwide, Int. J. Hydrogen Energy. 42 (2017) 2018–2033. doi:10.1016/j.ijhydene.2016.08.219.
[34] L. Zhou, Progress and problems in hydrogen storage methods, Renew. Sustain. Energy Rev. 9 (2005) 395–408. doi:10.1016/j.rser.2004.05.005.
[35] F. Zhang, P. Zhao, M. Niu, J. Maddy, The survey of key technologies in hydrogen energy storage, Int. J. Hydrogen Energy. 41 (2016) 14535–14552.

doi:10.1016/j.ijhydene.2016.05.293.
[36] P. Zakkour, G. Cook, CCS Roadmap for Industry: High-purity CO2 sources, (2010). http://hub.globalccsinstitute.com/sites/default/files/publications/15686/ccs-roadmap-industry-high-purity-co2-sources-sectoral-assessment.pdf (accessed September 18, 2017).
[37] M. Broda, V. Manovic, Q. Imtiaz, A.M. Kierzkowska, E.J. Anthony, C.R. Müller, High-Purity Hydrogen via the Sorption-Enhanced Steam Methane Reforming Reaction over a Synthetic CaO-Based Sorbent and a Ni Catalyst, Environ. Sci. Technol. 47 (2013) 6007–6014. doi:10.1021/es305113p.
[38] D.P. Harrison, Sorption-Enhanced Hydrogen Production: A Review, Ind. Eng. Chem. Res. 47 (2008) 6486–6501. doi:10.1021/ie800298z.
[39] T.K. Mandal, D.H. Gregory, Hydrogen: A future energy vector for sustainable development, Proc. Inst. Mech. Eng. Part C J. Mech. Eng. Sci. 224 (2010) 539–558. doi:10.1243/09544062JMES1774.
[40] J.D. Holladay, J. Hu, D.L. King, Y. Wang, An overview of hydrogen production technologies, Catal. Today. 139 (2009) 244–260. doi:10.1016/j.cattod.2008.08.039.
[41] International Energy Agency, Hydrogen Production and Storage. R&D Priorities and Gaps, Hydrog. Implement. Agreem. 13 (2006) 392–392. doi:10.1016/0360-3199(88)90106-1.
[42] L. Bromberg, D.R. Cohn, A. Rabinovich, C. O'Brie, S. Hochgreb, Plasma Reforming of Methane, Energy & Fuels. 12 (1998) 11–18. doi:10.1021/ef9701091.
[43] Y.F. Wang, Y.S. You, C.H. Tsai, L.C. Wang, Production of hydrogen by plasma-reforming of methanol, Int. J. Hydrogen Energy. 35 (2010) 9637–9640. doi:10.1016/j.ijhydene.2010.06.104.
[44] N. Muradov, Emission-free fuel reformers for mobile and portable fuel cell applications, in: J. Power Sources, Elsevier, 2003: pp. 320–324. doi:10.1016/S0378-7753(03)00078-8.
[45] A. D'Orazio, S. Rapagnà, P. Foscolo, K. Gallucci, Gas conditioning in H 2 rich syngas production by biomass steam gasification: Experimental comparison between three innovative ceramic filter candles, Int. J. (2015). http://www.sciencedirect.com/science/article/pii/S0360319915008502 (accessed September 30, 2016).
[46] S. Rapagnà, K. Gallucci, M. di Marcello, M. Matt, M. Nacken, S. Heidenreich, et al., Gas cleaning, gas conditioning and tar abatement by means of a catalytic filter candle in a biomass fluidized-bed gasifier, Bioresour. Technol. 101 (2010) 7123–7130. doi:10.1016/j.biortech.2010.03.139.
[47] S. Rapagna, N. Jand, P.U. Foscolo, Catalytic gasification of biomass to produce hydrogen rich gas, Int. J. Hydrog. Energyt. J. Hydrog. Energy. 23 (1998) 551–557. doi:10.1016/S0360-3199(97)00108-0.
[48] L. Di Felice, C. Courson, N. Jand, K. Gallucci, P.U. Foscolo, A. Kiennemann, Catalytic biomass gasification: Simultaneous hydrocarbons steam reforming and CO2 capture in a fluidised bed reactor, Chem. Eng. J. 154 (2009) 375–383. doi:10.1016/j.cej.2009.04.054.
[49] A. Steinfeld, Solar thermochemical production of hydrogen - A review, Sol. Energy. 78 (2005) 603–615. doi:10.1016/j.solener.2003.12.012.
[50] L.R. Snowdon, Natural gas composition in a geological environment and the implications for the processes of generation and preservation, Org. Geochem. 32 (2001) 913–931. doi:10.1016/S0146-6380(01)00051-1.
[51] S. Faramawy, T. Zaki, A.A.E. Sakr, Natural gas origin, composition, and processing: A review, J. Nat. Gas Sci. Eng. 34 (2016) 34–54. doi:10.1016/j.jngse.2016.06.030.
[52] R. Kothari, D. Buddhi, R.L. Sawhney, Comparison of environmental and economic

aspects of various hydrogen production methods, Renew. Sustain. Energy Rev. 12 (2008) 553–563. doi:10.1016/j.rser.2006.07.012.

[53] K. Liu, C. Song, V. Subramani, Hydrogen and syngas production and purification technologies, John Wiley & Sons, Inc. Publications, 2010. doi:10.1002/9780470561256.fmatter.

[54] R. Chaubey, S. Sahu, O.O. James, S. Maity, A review on development of industrial processes and emerging techniques for production of hydrogen from renewable and sustainable sources, Renew. Sustain. Energy Rev. 23 (2013) 443–462. doi:10.1016/j.rser.2013.02.019.

[55] L. Barelli, G. Bidini, F. Gallorini, S. Servili, Hydrogen production through sorption-enhanced steam methane reforming and membrane technology: A review, Energy. 33 (2008) 554–570. doi:10.1016/j.energy.2007.10.018.

[56] E. Simsek, A.K. Avci, Z.I. Önsan, Investigation of catalyst performance and microstructured reactor configuration for syngas production by methane steam reforming, Catal. Today. 178 (2011) 157–163. doi:10.1016/j.cattod.2011.08.021.

[57] U. Izquierdo, V.L. Barrio, J.F. Cambra, J. Requies, M.B. Güemez, P.L. Arias, et al., Hydrogen production from methane and natural gas steam reforming in conventional and microreactor reaction systems, Int. J. Hydrogen Energy. 37 (2012) 7026–7033. doi:10.1016/j.ijhydene.2011.11.048.

[58] A. Boyano, A.M. Blanco-Marigorta, T. Morosuk, G. Tsatsaronis, Exergoenvironmental analysis of a steam methane reforming process for hydrogen production, Energy. 36 (2011) 2202–2214. doi:10.1016/j.energy.2010.05.020.

[59] L. Di Felice, C. Courson, P.U. Foscolo, A. Kiennemann, Iron and nickel doped alkaline-earth catalysts for biomass gasification with simultaneous tar reformation and CO2 capture, Int. J. Hydrogen Energy. 36 (2011) 5296–5310. doi:10.1016/j.ijhydene.2011.02.008.

[60] M.R. Cesário, B.S. Barros, Y. Zimmermann, C. Courson, D.M.A. Melo, A. Kiennemann, CO2 Sorption Enhanced Steam Reforming of Methane Using Ni/CaO · Ca12Al14O33 Catalysts, Adv. Chem. Lett. 1 (2013) 292–299. doi:10.1166/acl.2013.1037.

[61] J.R. Rostrup-Nielsen, Catalytic Steam Reforming, Catal. Sci. Technol. 5 (1984) 1–117. http://www.scopus.com/inward/record.url?eid=2-s2.0-0021158095&partnerID=40&md5=7183995ebfcff200d638d2d56ce6576d.

[62] I. Dybkjaer, Tubular reforming and autothermal reforming of natural gas - an overview of available processes, Fuel Process. Technol. 42 (1995) 85–107. doi:10.1016/0378-3820(94)00099-F.

[63] M. Shokrollahi Yancheshmeh, H.R. Radfarnia, M.C. Iliuta, High temperature CO<inf>2</inf> sorbents and their application for hydrogen production by sorption enhanced steam reforming process, Chem. Eng. J. 283 (2016) 420–444. doi:10.1016/j.cej.2015.06.060.

[64] D.L. Trimm, Coke formation and minimisation during steam reforming reactions, Catal. Today. 37 (1997) 233–238. doi:10.1016/S0920-5861(97)00014-X.

[65] S.M. Hashemnejad, M. Parvari, Deactivation and regeneration of nickel-based catalysts for steam-methane reforming, Chinese J. Catal. 32 (2011) 273–279. doi:10.1016/S1872-2067(10)60175-1.

[66] G. Natta, I. Pasquon, P. Centola, Principi della chimica industriale vol. 2, 1st ed., CLUP, Milan, 1978. http://www.giulionatta.it/pdf/pubblicazioni/00615.pdf (accessed September 19, 2017).

[67] L. Barelli, G. Bidini, F. Gallorini, S. Servili, Hydrogen production through sorption-enhanced steam methane reforming and membrane technology: A review, Energy. 33 (2008) 554–570. doi:10.1016/j.energy.2007.10.018.

[68] A.B. Stambouli, E. Traversa, Solid oxide fuel cells (SOFCs): A review of an

environmentally clean and efficient source of energy, Renew. Sustain. Energy Rev. 6 (2002) 433–455. doi:10.1016/S1364-0321(02)00014-X.

[69] V. Das, S. Padmanaban, K. Venkitusamy, R. Selvamuthukumaran, F. Blaabjerg, P. Siano, Recent advances and challenges of fuel cell based power system architectures and control – A review, Renew. Sustain. Energy Rev. 73 (2017) 10–18. doi:10.1016/j.rser.2017.01.148.

[70] O.Z. Sharaf, M.F. Orhan, An overview of fuel cell technology: Fundamentals and applications, Renew. Sustain. Energy Rev. 32 (2014) 810–853. doi:10.1016/j.rser.2014.01.012.

[71] S. Satyapal, J. Petrovic, C. Read, G. Thomas, G. Ordaz, The U.S. Department of Energy's National Hydrogen Storage Project: Progress towards meeting hydrogen-powered vehicle requirements, Catal. Today. 120 (2007) 246–256. doi:10.1016/j.cattod.2006.09.022.

[72] A. Choudhury, H. Chandra, A. Arora, Application of solid oxide fuel cell technology for power generation - A review, Renew. Sustain. Energy Rev. 20 (2013) 430–442. doi:10.1016/j.rser.2012.11.031.

[73] S.H. Jensen, P.H. Larsen, M. Mogensen, Hydrogen and synthetic fuel production from renewable energy sources, Int. J. Hydrogen Energy. 32 (2007) 3253–3257. doi:10.1016/j.ijhydene.2007.04.042.

[74] Toyota Motor Company, Hydrogen Fuel Cell Car | Toyota Mirai, (n.d.). https://ssl.toyota.com/mirai/fcv.html (accessed September 18, 2017).

[75] 2017 Clarity Fuel Cell – Environmentally-Conscious Vehicles | Honda, (n.d.). https://automobiles.honda.com/clarity-fuel-cell (accessed September 18, 2017).

[76] ix35 Fuel Cell Highlights | Eco Cars - Hyundai Worldwide, (n.d.). https://www.hyundai.com/worldwide/en/eco/ix35-fuelcell/highlights (accessed September 18, 2017).

[77] J. Alazemi, J. Andrews, Automotive hydrogen fuelling stations: An international review, Renew. Sustain. Energy Rev. 48 (2015) 483–499. doi:10.1016/j.rser.2015.03.085.

[78] D.C. Miller, J.T. Litynski, L.A. Brickett, B.D. Morreale, Toward transformational carbon capture systems, AIChE J. 62 (2016) 2–10. doi:10.1002/aic.15066.

[79] C. Marchetti, On geoengineering and the CO2 problem, Clim. Change. 1 (1977) 59–68. doi:10.1007/BF00162777.

[80] E. Blomen, C. Hendriks, F. Neele, Capture technologies: Improvements and promising developments, in: Energy Procedia, Elsevier, 2009: pp. 1505–1512. doi:10.1016/j.egypro.2009.01.197.

[81] D.Y.C. Leung, G. Caramanna, M.M. Maroto-Valer, An overview of current status of carbon dioxide capture and storage technologies, Renew. Sustain. Energy Rev. 39 (2014) 426–443. doi:10.1016/j.rser.2014.07.093.

[82] B. Metz, O. Davidson, H. de Coninck, M. Loos, L.M. (eds.), IPCC special report on carbon dioxide capture and storage, (2005). https://www.osti.gov/scitech/biblio/20740954 (accessed September 23, 2017).

[83] N. MacDowell, N. Florin, A. Buchard, J. Hallett, A. Galindo, G. Jackson, et al., An overview of CO2 capture technologies, Energy Environ. Sci. 3 (2010) 1645. doi:10.1039/c004106h.

[84] A.S. Bhown, B.C. Freeman, Analysis and status of post-combustion carbon dioxide capture technologies, Environ. Sci. Technol. 45 (2011) 8624–8632. doi:10.1021/es104291d.

[85] M.T. Sander, C.L. Mariz, The Fluor Daniel's econamine FG process: Past experience and present day focus, Energy Convers. Manag. 33 (1992) 341–348. doi:10.1016/0196-8904(92)90029-V.

[86] T. Mimura, S. Shimojo, T. Suda, M. Iijima, S. Mitsuoka, Research and development

on energy saving technology for flue gas carbon dioxide recovery and steam system in power plant, Energy Convers. Manag. 36 (1995) 397–400. doi:10.1016/0196-8904(95)00029-D.

[87] M.E. Boot-Handford, J.C. Abanades, E.J. Anthony, M.J. Blunt, S. Brandani, N. Mac Dowell, et al., Carbon capture and storage update, Energy Environ. Sci. 7 (2014) 130–189. doi:10.1039/C3EE42350F.

[88] A. Brunetti, F. Scura, G. Barbieri, E. Drioli, Membrane technologies for CO2 separation, J. Memb. Sci. 359 (2010) 115–125. doi:10.1016/j.memsci.2009.11.040.

[89] A. Samanta, A. Zhao, G.K.H. Shimizu, P. Sarkar, R. Gupta, Post-combustion CO 2 capture using solid sorbents: A review, Ind. Eng. Chem. Res. 51 (2012) 1438–1463. doi:10.1021/ie200686q.

[90] F. Karadas, M. Atilhan, S. Aparicio, Review on the use of ionic liquids (ILs) as alternative fluids for CO 2 capture and natural gas sweetening, Energy and Fuels. 24 (2010) 5817–5828. doi:10.1021/ef1011337.

[91] C. Chen, E.S. Rubin, CO2 control technology effects on IGCC plant performance and cost, Energy Policy. 37 (2009) 915–924. doi:10.1016/j.enpol.2008.09.093.

[92] I.Y. Mohammed, M. Samah, G. Sabina, A. Mohamed, Comparison of SelexolTM and Rectisol® Technologies in an Integrated Gasification Combined Cycle (IGCC) Plant for Clean Energy Production, Int. J. Eng. Res. 3 (2014) 742–744. doi:10.17950/ijer/v3s12/1207.

[93] S. García, M. V. Gil, C.F. Martín, J.J. Pis, F. Rubiera, C. Pevida, Breakthrough adsorption study of a commercial activated carbon for pre-combustion CO2 capture, Chem. Eng. J. 171 (2011) 549–556. doi:10.1016/j.cej.2011.04.027.

[94] J. Forsyth, CACHET Publishable final activity report CACHET Carbon Dioxide Capture and Hydrogen Production from Gaseous Fuels DSP 5.3 Publishable Final Activity Report, (n.d.). http://cordis.europa.eu/documents/documentlibrary/122320081EN6.pdf (accessed September 23, 2017).

[95] ASCENT project, (2014). http://www.ascentproject.eu/ (accessed September 23, 2016).

[96] Bo Feng, H. An, and Eddie Tan, Screening of CO2 Adsorbing Materials for Zero Emission Power Generation Systems, Energy & Fuels. 21 (2007) 426–434. doi:10.1021/ef0604036.

[97] B.R. Stanmore, P. Gilot, Review-calcination and carbonation of limestone during thermal cycling for CO2 sequestration, Fuel Process. Technol. 86 (2005) 1707–1743. doi:10.1016/j.fuproc.2005.01.023.

[98] N. Hu, A.W. Scaroni, Calcination of pulverized limestone particles under furnace injection conditions, Fuel. 75 (1996) 177–186. doi:10.1016/0016-2361(95)00234-0.

[99] G.D. Silcox, J.C. Kramlich, D.W. Pershing, A mathematical model for the flash calcination of dispersed calcium carbonate and calcium hydroxide particles, Ind. Eng. Chem. Res. 28 (1989) 155–160. doi:10.1021/ie00086a005.

[100] B. Dou, C. Wang, Y. Song, H. Chen, B. Jiang, M. Yang, et al., Solid sorbents for in-situ CO 2 removal during sorption-enhanced steam reforming process : A review, Renew. Sustain. Energy Rev. 53 (2016) 536–546. doi:10.1016/j.rser.2015.08.068.

[101] I. Aloisi, N. Jand, S. Stendardo, P.U. Foscolo, Hydrogen by sorption enhanced methane reforming: A grain model to study the behavior of bi-functional sorbent-catalyst particles, Chem. Eng. Sci. 149 (2016) 22–34. doi:10.1016/j.ces.2016.03.042.

[102] I. Aloisi, A. Di Giuliano, A. Di Carlo, P.U. Foscolo, C. Courson, K. Gallucci, Sorption enhanced catalytic Steam Methane Reforming: Experimental data and simulations describing the behaviour of bi-functional particles, Chem. Eng. J. 314

(2017) 570–582. doi:10.1016/j.cej.2016.12.014.
[103] Z. Li, Y. Liu, N. Cai, Understanding the enhancement effect of high-temperature steam on the carbonation reaction of CaO with CO2, Fuel. 127 (2014) 88–93. doi:10.1016/j.fuel.2013.06.040.
[104] J.C. Abanades, D. Alvarez, Conversion Limits in the Reaction of CO2 with Lime, Energy & Fuels. 17 (2003) 308–315. doi:10.1021/EF020152A.
[105] S.K. Bhatia, D.D. Perlmutter, Effect of the product layer on the kinetics of the CO2-lime reaction, AIChE J. 29 (1983) 79–86. doi:10.1002/aic.690290111.
[106] Z. Li, H. Sun, N. Cai, Rate equation theory for the carbonation reaction of CaO with CO 2, in: Energy and Fuels, American Chemical Society, 2012: pp. 4607–4616. doi:10.1021/ef300607z.
[107] J. Blamey, E.J. Anthony, J. Wang, P.S. Fennell, The calcium looping cycle for large-scale CO2 capture, Prog. Energy Combust. Sci. 36 (2010) 260–279. doi:10.1016/j.pecs.2009.10.001.
[108] G.S. Grasa, J.C. Abanades, CO2 Capture Capacity of CaO in Long Series of Carbonation/Calcination Cycles, Ind. Eng. Chem. Res. 45 (2006) 8846–8851. doi:10.1021/IE0606946.
[109] A.I. Lysikov, A.N. Salanov, A.G. Okunev, Change of CO2 carrying capacity of CaO in isothermal recarbonation-decomposition cycles, Ind. Eng. Chem. Res. 46 (2007) 4633–4638. doi:10.1021/ie0702328.
[110] P. Sun, J.R. Grace, C.J. Lim, E.J. Anthony, A discrete-pore-size-distribution-based gas – solid model and its application to the CaO + CO 2 reaction, Chem. Eng. Sci. 63 (2008) 57–70. doi:10.1016/j.ces.2007.08.054.
[111] A. Silaban, M. Narcida, D.P. Harrison, Characteristics Of The Reversible Reaction Between CO2(g) And Calcined Dolomite, Chem. Eng. Commun. 146 (1996) 149–162. doi:10.1080/00986449608936487.
[112] A. Bandi, M. Specht, P. Sichler, N. Nicoloso, In situ Gas Conditioning in Fuel Reforming for Hydrogen Generation, (n.d.). https://www.netl.doe.gov/File Library/Events/2002/gas cleaning at high temperature/7-07paper.pdf (accessed September 26, 2017).
[113] H. Lu, E.P. Reddy, P.G. Smirniotis, Calcium oxide based sorbents for capture of carbon dioxide at high temperatures, Ind. Eng. Chem. Res. 45 (2006) 3944–3949. doi:10.1021/ie051325x.
[114] G. Grasa, B. González, M. Alonso, J.C. Abanades, Comparison of CaO-based synthetic CO2 sorbents under realistic calcination conditions, Energy and Fuels. 21 (2007) 3560–3562. doi:10.1021/ef0701687.
[115] L. Yang, H. Yu, S. Wang, H. Wang, Q. Zhou, Carbon dioxide captured from flue gas by modified Ca-based sorbents in fixed-bed reactor at high temperature, Chinese J. Chem. Eng. 21 (2013) 199–204. doi:10.1016/S1004-9541(13)60459-0.
[116] V. Manovic, E.J. Anthony, Steam Reactivation of Spent CaO Based Sorbent for Multiple CO2 Capture Cycles, Environ. Sci. Technol. 41 (2007) 1420. doi:10.1021/es0621344.
[117] V. Manovic, E.J. Anthony, Thermal activation of CaO-based sorbent and self-reactivation during CO2 capture looping cycles, Environ. Sci. Technol. 42 (2008) 4170–4174. doi:10.1021/es800152s.
[118] J.M. Valverde, A. Perejon, L.A. Perez-Maqueda, Enhancement of fast CO2 capture by a nano-SiO2/CaO composite at Ca-looping conditions, Environ. Sci. Technol. 46 (2012) 6401–6408. doi:10.1021/es3002426.
[119] M.H. Sedghkerdar, N. Mahinpey, Z. Sun, S. Kaliaguine, Novel synthetic sol-gel CaO based pellets using porous mesostructured silica in cyclic CO2 capture process, Fuel. 127 (2014) 101–108. doi:10.1016/j.fuel.2013.08.007.
[120] M. Mohammadi, P. Lahijani, A.R. Mohamed, Refractory dopant-incorporated CaO

from waste eggshell as sustainable sorbent for CO2 capture: Experimental and kinetic studies, Chem. Eng. J. 243 (2014) 455–464. doi:10.1016/j.cej.2014.01.018.

[121] J. Park, K.B. Yi, Effects of preparation method on cyclic stability and CO 2 absorption capacity of synthetic CaO-MgO absorbent for sorption-enhanced hydrogen production, Int. J. Hydrogen Energy. 37 (2012) 95–102. doi:10.1016/j.ijhydene.2011.09.093.

[122] C.T. Yu, W.C. Chen, Preparation, characterization of Ca/Al carbonate pellets with TiO2 binder and CO2 sorption at elevated-temperature conditions, Powder Technol. 239 (2013) 492–498. doi:10.1016/j.powtec.2013.02.035.

[123] X. Zhang, Z. Li, Y. Peng, W. Su, X. Sun, J. Li, Investigation on a novel CaO-Y2O3 sorbent for efficient CO2 mitigation, Chem. Eng. J. 243 (2014) 297–304. doi:10.1016/j.cej.2014.01.017.

[124] D.S. Tsvetkov, A.S. Steparuk, A.Y. Zuev, Defect structure and related properties of mayenite Ca12Al14O33, Solid State Ionics. 276 (2015) 142–148. doi:10.1016/j.ssi.2015.04.003.

[125] H. Boysen, M. Lerch, A. Stys, A. Senyshyn, Structure and oxygen mobility in mayenite (Ca12Al 14O33): A high-temperature neutron powder diffraction study, Acta Crystallogr. Sect. B Struct. Sci. 63 (2007) 675–682. doi:10.1107/S0108768107030005.

[126] J.T.S. Irvine, M. Lacerda, A.R. West, Oxide ion conductivity in Ca12Al14O33, Mater. Res. Bull. 23 (1988) 1033–1038. doi:10.1016/0025-5408(88)90059-1.

[127] J.-P. Eufinger, A. Schmidt, M. Lerch, J. Janek, Novel anion conductors – conductivity, thermodynamic stability and hydration of anion- substituted mayenite-type cage compounds C 12 A 7 :X (X = O, OH, Cl, F, CN, S, N), Phys. Chem. Chem. Phys. 17 (2015) 6844–6857. doi:10.1039/C4CP05442C.

[128] A. Norlund Christensen, Neutron Powder Diffraction Profile Refinement Studies on Ca11.3Al14O32.3 and CaClO(D0.88H0.12).pdf, Acta Chem. Scand. 41 (1987) 110–112. doi:10.3891/acta.chem.scand.41a-0110.

[129] H. Hosono, K. Hayashi, K. Kajihara, P. V. Sushko, A.L. Shluger, Oxygen ion conduction in 12CaO·7Al2O3: O2- conduction mechanism and possibility of O- fast conduction, Solid State Ionics. 180 (2009) 550–555. doi:10.1016/j.ssi.2008.10.015.

[130] C. Li, D. Hirabayashi, K. Suzuki, A crucial role of O2 - and O2 2- on mayenite structure for biomass tar steam reforming over Ni/Ca12Al14O33, Appl. Catal. B Environ. 88 (2009) 351–360. doi:10.1016/j.apcatb.2008.11.004.

[131] C. Li, D. Hirabayashi, K. Suzuki, Development of new nickel based catalyst for biomass tar steam reforming producing H2-rich syngas, Fuel Process. Technol. 90 (2009) 790–796. doi:10.1016/j.fuproc.2009.02.007.

[132] L. Palacios, A. Cabeza, S. Bruque, S. García-Granda, M.A.G. Aranda, Structure and electrons in mayenite electrides, Inorg. Chem. 47 (2008) 2661–2667. doi:10.1021/ic7021193.

[133] A. Di Giuliano, J. Girr, R. Massacesi, K. Gallucci, C. Courson, Sorption enhanced steam methane reforming by Ni–CaO materials supported on mayenite, Int. J. Hydrogen Energy. 42 (2017) 13661–13680. doi:10.1016/j.ijhydene.2016.11.198.

[134] J.A. Satrio, B.H. Shanks, T.D. Wheelock, Development of a novel combined catalyst and sorbent for hydrocarbon reforming, Ind. Eng. Chem. Res. 44 (2005) 3901–3911. doi:10.1021/ie040284m.

[135] B.T. Carvill, J.R. Hufton, M. Anand, S. Sircar, Sorption-enhanced reaction process, AIChE J. 42 (1996) 2765–2772. doi:10.1002/aic.690421008.

[136] G. hua Xiu, P. Li, A.E. Rodrigues, Sorption-enhanced reaction process with reactive regeneration, Chem. Eng. Sci. 57 (2002) 3893–3908. doi:10.1016/S0009-2509(02)00245-2.

[137] C.S. Martavaltzi, E.P. Pampaka, E.S. Korkakaki, A.A. Lemonidou, Hydrogen Production via Steam Reforming of Methane with Simultaneous CO 2, Chem. Eng. J. 33 (2010) 2589–2595. doi:10.1021/ef9014058.

[138] K.F. Tzanetis, C.S. Martavaltzi, A.A. Lemonidou, Comparative exergy analysis of sorption enhanced and conventional methane steam reforming, Int. J. Hydrogen Energy. 37 (2012) 16308–16320. doi:10.1016/j.ijhydene.2012.02.191.

[139] G.A. Olah, A. Goeppert, G.K.S. Prakash, Chemical Recycling of Carbon Dioxide to Methanol and Dimethyl Ether: From Greenhouse Gas to Renewable, Environmentally Carbon Neutral Fuels and Synthetic Hydrocarbons, J. Org. Chem. 74 (2009) 487–498. doi:10.1021/jo801260f.

[140] I. Ganesh, Conversion of carbon dioxide into methanol – a potential liquid fuel: Fundamental challenges and opportunities (a review), Renew. Sustain. Energy Rev. 31 (2014) 221–257. doi:10.1016/j.rser.2013.11.045.

[141] B. Balasubramanian, A.L. Ortiz, S. Kaytakoglu, D.P. Harrison, Hydrogen from methane in a single-step process, Chem. Eng. Sci. 54 (1999) 3543–3552. doi:10.1016/S0009-2509(98)00425-4.

[142] C.S. Martavaltzi, A.A. Lemonidou, Hydrogen production via sorption enhanced reforming of methane: Development of a novel hybrid material-reforming catalyst and CO2 sorbent, Chem. Eng. Sci. 65 (2010) 4134–4140. doi:10.1016/j.ces.2010.04.038.

[143] C.S. Martavaltzi, T.D. Pefkos, A.A. Lemonidou, Operational Window of Sorption Enhanced Steam Reforming of Methane over CaO−Ca 12 Al 14 O 33, Ind. Eng. Chem. Res. 50 (2011) 539–545. doi:10.1021/ie1002284.

[144] E. Ochoa-Fernández, G. Haugen, T. Zhao, M. Rønning, I. Aartun, B. Børresen, et al., Process design simulation of H 2 production by sorption enhanced steam methane reforming: evaluation of potential CO 2 acceptors, Green Chem. 9 (2007) 654–662. doi:10.1039/B614270B.

[145] A.L. García-Lario, M. Aznar, I. Martinez, G.S. Grasa, R. Murillo, Experimental study of the application of a NiO/NiAl2O4 catalyst and a CaO-based synthetic sorbent on the Sorption Enhanced Reforming process, Int. J. Hydrogen Energy. 40 (2015) 219–232. doi:10.1016/j.ijhydene.2014.10.033.

[146] J.-N. Kim, C.H. Ko, K.B. Yi, Sorption enhanced hydrogen production using one-body CaO–Ca12Al14O33–Ni composite as catalytic absorbent, Int. J. Hydrogen Energy. 38 (2013) 6072–6078. doi:10.1016/j.ijhydene.2012.12.022.

[147] K. Johnsen, H.J. Ryu, J.R. Grace, C.J. Lim, Sorption-enhanced steam reforming of methane in a fluidized bed reactor with dolomite as CO 2 -acceptor, Chem. Eng. Sci. 61 (2006) 1195–1202. doi:10.1016/j.ces.2005.08.022.

[148] K.R. Rout, H.A. Jakobsen, A numerical study of pellets having both catalytic- and capture properties for SE-SMR process: Kinetic- and product layer diffusion controlled regimes, Fuel Process. Technol. 106 (2013) 231–246. doi:10.1016/j.fuproc.2012.07.029.

[149] N. Chanburanasiri, A.M. Ribeiro, A.E. Rodrigues, A. Arpornwichanop, N. Laosiripojana, P. Praserthdam, et al., Hydrogen Production via Sorption Enhanced Steam Methane Reforming Process Using Ni/CaO Multifunctional Catalyst, Ind. Eng. Chem. Res. 50 (2011) 13662–13671. doi:10.1021/ie201226j.

[150] M.R. Cesário, B.S. Barros, C. Courson, D.M.A. Melo, A. Kiennemann, Catalytic performances of Ni-CaO-mayenite in CO2 sorption enhanced steam methane reforming, Fuel Process. Technol. 131 (2015) 247–253. doi:10.1016/j.fuproc.2014.11.028.

[151] A.L. García-Lario, G.S. Grasa, R. Murillo, Performance of a combined CaO-based sorbent and catalyst on H2 production, via sorption enhanced methane steam reforming, Chem. Eng. J. 264 (2015) 697–705. doi:10.1016/j.cej.2014.11.116.

[152] Z.S. Li, N.S. Cai, J.B. Yang, Continuous production of hydrogen from sorption-enhanced steam methane reforming in two parallel fixed-bed reactors operated in a cyclic manner, Ind. Eng. Chem. Res. 45 (2006) 8788–8793. doi:10.1021/ie061010x.
[153] W.E. Waldron, J.R. Hufton, S. Sircar, Production of hydrogen by cyclic sorption enhanced reaction process, AIChE J. 47 (2001) 1477–1479. doi:10.1002/aic.690470623.
[154] J. Meyer, J. Mastin, C. Sanz, Sustainable Hydrogen Production from Biogas Using Sorption- Enhanced Reforming, Energy Procedia. 63 (2014) 6800–6814. doi:10.1016/j.egypro.2014.11.714.
[155] A.L. García-lario, M. Aznar, G.S. Grasa, Evaluation of process variables on the performance of Sorption Enhanced Methane Reforming n Murillo, J. Power Sources. 285 (2015) 90–99. doi:10.1016/j.jpowsour.2015.03.075.
[156] A.P. Simpson, A.E. Lutz, Exergy analysis of hydrogen production via steam methane reforming, Int. J. Hydrogen Energy. 32 (2007) 4811–4820. doi:10.1016/j.ijhydene.2007.08.025.
[157] J.R. Rostrup-Nielsen, J. Sehested, J.K. Nørskov, Hydrogen and synthesis gas by steam- and C02 reforming, Adv. Catal. 47 (2002) 65–139. doi:10.1016/S0360-0564(02)47006-X.
[158] J. Meyer, J. Mastin, T.-K. Bjørnebøle, T. Ryberg, N. Eldrup, Techno-economical study of the Zero Emission Gas power concept, Energy Procedia. 4 (2011) 1949–1956. doi:10.1016/j.egypro.2011.02.075.
[159] E. Marceau, M. Che, J. Čejka, A. Zukal, Nickel(II) Nitrate vs. Acetate: Influence of the Precursor on the Structure and Reducibility of Ni/MCM-41 and Ni/Al-MCM-41 Catalysts, ChemCatChem. 2 (2010) 413–422. doi:10.1002/cctc.200900289.
[160] J. Estellé, P. Salagre, Y. Cesteros, M. Serra, F. Medina, J.E. Sueiras, Comparative study of the morphology and surface properties of nickel oxide prepared from different precursors, Solid State Ionics. 156 (2003) 233–243. doi:10.1016/S0167-2738(02)00612-4.
[161] S.B. Ren, J.H. Qiu, C.Y. Wang, B.L. Xu, Y.N. Fan, Y. Chen, Influence of nickel salt precursors on the hydrogenation activity of Ni/gamma-Al2O3 catalyst, Chinese J. Catal. 28 (2007) 651–656. doi:10.1016/S1872-2067(07)60056-4.
[162] G. Wu, C. Zhang, S. Li, Z. Han, T. Wang, X. Ma, et al., Hydrogen production via glycerol steam reforming over Ni/Al 2O3: Influence of nickel precursors, ACS Sustain. Chem. Eng. 1 (2013) 1052–1062. doi:10.1021/sc400123f.
[163] J.A.C. Dias, J.M. Assaf, Influence of calcium content in Ni/CaO/??-Al2O3 catalysts for CO2-reforming of methane, in: Catal. Today, 2003: pp. 59–68. doi:10.1016/S0920-5861(03)00194-9.
[164] C.K.S. Choong, Z. Zhong, L. Huang, Z. Wang, T.P. Ang, A. Borgna, et al., Effect of calcium addition on catalytic ethanol steam reforming of Ni/Al2O3: I. Catalytic stability, electronic properties and coking mechanism, Appl. Catal. A Gen. 407 (2011) 145–154. doi:10.1016/j.apcata.2011.08.037.
[165] P. Forzatti, Catalyst deactivation, Catal. Today. 52 (1999) 165–181. doi:10.1016/S0920-5861(99)00074-7.
[166] M. Broda, A.M. Kierzkowska, D. Baudouin, Q. Imtiaz, C. Copéret, C.R. Müller, Sorbent-enhanced methane reforming over a Ni-Ca-based, bifunctional catalyst sorbent, ACS Catal. 2 (2012) 1635–1646. doi:10.1021/cs300247g.
[167] L. Dietz, S. Piccinin, M. Maestri, Mechanistic insights into CO2 activation via reverse water - Gas shift on metal surfaces, J. Phys. Chem. C. 119 (2015) 4959–4966. doi:10.1021/jp512962c.
[168] J. Werther, J. Reppenhagen, Catalyst Attrition in Fluidized-Bed Systems, React. Kinet. Catal. 45 (1999) 2001–2010. doi:10.1002/aic.690450916.
[169] Z. Li, N. Cai, Y. Huang, H. Han, Synthesis, Experimental Studies, and Analysis of

a New Calcium-Based Carbon Dioxide Absorbent, Energy Fuels. 19 (2005) 1447–1452. doi:10.1021/EF0496799.

[170] H. Chen, C. Zhao, Development of a CaO-based sorbent with improved cyclic stability for CO2 capture in pressurized carbonation, Chem. Eng. J. 171 (2011) 197–205. doi:10.1016/j.cej.2011.03.091.

[171] N. Florin, P. Fennell, Synthetic CaO-based Sorbent for CO2Capture, in: Energy Procedia, Elsevier, 2011: pp. 830–838. doi:10.1016/j.egypro.2011.01.126.

[172] V. Manovic, E.J. Anthony, CaO-Based Pellets Supported by Calcium Aluminate Cements for High-Temperature CO 2 Capture, Environ. Sci. Technol. 43 (2009) 7117–7122. doi:10.1021/es901258w.

[173] M. Broda, A.M. Kierzkowska, C.R. Müller, Influence of the calcination and carbonation conditions on the CO 2 uptake of synthetic Ca-based CO2 sorbents, Environ. Sci. Technol. 46 (2012) 10849–10856. doi:10.1021/es302757e.

[174] P. Xu, Z. Zhou, C. Zhao, Z. Cheng, Ni/CaO-Al2O3 bifunctional catalysts for sorption-enhanced steam methane reforming, AIChE J. 60 (2014) 3547–3556. doi:10.1002/aic.14543.

[175] I. Zamboni, Y. Zimmermann, A. Kiennemann, C. Courson, Improvement of steam reforming of toluene by CO2 capture using Fe/CaO e Ca12Al14O33 bi-functional materials, Int. J. Hydrogen Energy. 40 (2015) 5297–5304. doi:10.1016/j.ijhydene.2015.01.065.

[176] A. D'Orazio, A. Di Carlo, N. Dionisi, A. Dell'Era, F. Orecchini, Toluene steam reforming properties of CaO based synthetic sorbents for biomass gasification process, Int. J. Hydrogen Energy. 38 (2013) 13282–13292. doi:10.1016/j.ijhydene.2013.07.075.

[177] F. Micheli, Risparmio energetico e micro generazione distribuita, Clean Coal Technologies: CO2 capture, University of L'Aquila and Universtiy of Strasbourg, 2014.

[178] S. Brunauer, P.H. Emmett, E. Teller, Adsorption of Gases in Multimolecular Layers, J. Am. Chem. Soc. 60 (1938) 309–319. doi:10.1021/ja01269a023.

[179] E.P. Barrett, L.G. Joyner, P.P. Halenda, The Determination of Pore Volume and Area Distributions in Porous Substances. I. Computations from Nitrogen Isotherms, J. Am. Chem. Soc. 73 (1951) 373–380. doi:10.1021/ja01145a126.

[180] A. Monshi, Modified Scherrer Equation to Estimate More Accurately Nano-Crystallite Size Using XRD, World J. Nano Sci. Eng. 2 (2012) 154–160. doi:10.4236/wjnse.2012.23020.

[181] J.I. Langford, A.J.C. Wilson, Scherrer after sixty years: A survey and some new results in the determination of crystallite size, J. Appl. Crystallogr. 11 (1978) 102–113. doi:10.1107/S0021889878012844.

[182] M. Thommes, K. Kaneko, A. V. Neimark, J.P. Olivier, F. Rodriguez-Reinoso, J. Rouquerol, et al., Physisorption of gases, with special reference to the evaluation of surface area and pore size distribution (IUPAC Technical Report), Pure Appl. Chem. 87 (2015) 1051–1069. doi:10.1515/pac-2014-1117.

[183] M. Thommes, K.A. Cychosz, Physical adsorption characterization of nanoporous materials: progress and challenges, Adsorption. 20 (2014) 233–250. doi:10.1007/s10450-014-9606-z.

[184] P.A. Monson, Understanding adsorption/desorption hysteresis for fluids in mesoporous materials using simple molecular models and classical density functional theory, Microporous Mesoporous Mater. 160 (2012) 47–66. doi:10.1016/j.micromeso.2012.04.043.

[185] J. Landers, G.Y. Gor, A. V. Neimark, Density functional theory methods for characterization of porous materials, Colloids Surfaces A Physicochem. Eng. Asp. 437 (2013) 3–32. doi:10.1016/j.colsurfa.2013.01.007.

[186] M. Ruszak, S. Witkowski, P. Pietrzyk, A. Kotarba, Z. Sojka, THE ROLE OF INTERMEDIATE CALCIUM ALUMINATE PHASES IN SOLID STATE SYNTHESIS OF MAYENITE (Ca 12 Al 14 O 33), Funct. Mater. Lett. 4 (2011) 183–186. doi:10.1142/S1793604711001907.

[187] A.A. Lemonidou, M.A. Goula, I.A. Vasalos, Carbon Dioxide Reforming of Methane over 5 wt.% Nickel Calcium Aluminate Catalysts - Effect of Preparation Method, Catal. Today. 46 (1998) 175–183. doi:10.1016/S0920-5861(98)00339-3.

[188] J.A. Medrano, H.P. Hamers, G. Williams, M. van Sint Annaland, F. Gallucci, NiO/CaAl 2 O 4 as active oxygen carrier for low temperature chemical looping applications, Appl. Energy. 158 (2015) 86–96. doi:10.1016/j.apenergy.2015.08.078.

[189] B. Matović, M. Prekajski, J. Pantić, T. Bräuniger, M. Rosić, D. Zagorac, et al., Synthesis and densification of single-phase mayenite (C12A7), J. Eur. Ceram. Soc. 36 (2016) 4237–4241. doi:10.1016/j.jeurceramsoc.2016.06.014.

[190] C. Li, D. Hirabayashi, K. Suzuki, Synthesis of higher surface area mayenite by hydrothermal method, Mater. Res. Bull. 46 (2011) 1307–1310. doi:10.1016/j.materresbull.2011.03.023.

[191] A.D.. Clague, J.. Donnet, T.. Wang, J.C.. Peng, A comparison of diesel engine soot with carbon black, Carbon N. Y. 37 (1999) 1553–1565. doi:10.1016/S0008-6223(99)00035-4.

[192] TEM imaging with Gatan digital camera - HRTEM - Cardiff University, (n.d.). http://sites.cardiff.ac.uk/hrtem/experimental-results/tem-imaging-with-gatan-digital-camera/ (accessed September 7, 2017).

[193] K.S.W. Sing, D.H. Everett, R.A.W. Haul, L. Moscou, R.A. Pierotti, J. Rouquérol, et al., Reporting physisorption data for gas/solid systems with special reference to the determination of surface area and porosity (Recommendations 1984), Pure Appl. Chem. 57 (1985) 603–619. doi:10.1351/pac198557040603.

[194] N. Salhi, A. Boulahouache, C. Petit, A. Kiennemann, C. Rabia, Steam reforming of methane to syngas over NiAl2O4 spinel catalysts, Int. J. Hydrogen Energy. 36 (2011) 11433–11439. doi:10.1016/j.ijhydene.2010.11.071.

[195] A. Gil, A. Diaz, L.M. Gandia, M. Montes, Influence of the preparation method and the nature of the support on the stability of nickel catalysts, Appl. Catal. A, Gen. 109 (1994) 167–179. doi:10.1016/0926-860X(94)80116-9.

[196] Z. Xu, Y. Li, J. Zhang, L. Chang, R. Zhou, Z. Duan, Bound-state Ni species — a superior form in Ni-based catalyst for CH4/CO2 reforming, Appl. Catal. A Gen. 210 (2001) 45–53.

[197] A. Cabello, P. Gayán, F. García-Labiano, L.F. de Diego, A. Abad, M.T. Izquierdo, et al., Relevance of the catalytic activity on the performance of a NiO/CaAl2O4 oxygen carrier in a CLC process, Appl. Catal. B Environ. 147 (2014) 980–987. doi:10.1016/j.apcatb.2013.10.034.

[198] P. Bolt, On the Role of a Nial2O4 Intermediate Layer in the Sintering Behavior of Ni/α-Al2O3, J. Catal. 151 (1995) 300–306. doi:10.1006/jcat.1995.1031.

[199] R. Villa, C. Cristiani, G. Groppi, L. Lietti, P. Forzatti, U. Cornaro, et al., Ni based mixed oxide materials for CH4 oxidation under redox cycle conditions, J. Mol. Catal. A Chem. 204–205 (2003) 637–646. doi:10.1016/S1381-1169(03)00346-7.

[200] C. Dueso, A. Abad, F. García-Labiano, L.F. De Diego, P. Gayán, J. Adánez, et al., Reactivity of a NiO/Al2O3 oxygen carrier prepared by impregnation for chemical-looping combustion, Fuel. 89 (2010) 3399–3409. doi:10.1016/j.fuel.2010.03.043.

[201] A. Cimino, M. Lo Jacono, M. Schiavello, Structural, magnetic, and optical properties of nickel oxide supported on .eta.- and .gamma.-aluminas, J. Phys. Chem. 75 (1971) 1044–1050. doi:10.1021/j100678a005.

[202] R.A. Robie, P.M. Bethke, K.M. Beardsley, X-ray Crystallographic Data, Molar

Volumes, and Densities of Minerals and Related Substances, in: R.C. Weast (Ed.), Handb. Chem. Phys., 49th ed., The Chemical Rubber Co., Cleveland, 1969: p. B-308.

[203] S. Rapagnà, M. Virginie, K. Gallucci, C. Courson, M. Di Marcello, A. Kiennemann, et al., Fe/olivine catalyst for biomass steam gasification: Preparation, characterization and testing at real process conditions, in: Catal. Today, Elsevier, 2011: pp. 163–168. doi:10.1016/j.cattod.2010.11.098.

[204] Marion Technologies, (n.d.). http://www.mariontechnologies.com/en/home/ (accessed October 9, 2017).

[205] S. Stendardo, P.U. Foscolo, Carbon dioxide capture with dolomite: A model for gas–solid reaction within the grains of a particulate sorbent, Chem. Eng. Sci. 64 (2009) 2343–2352. doi:10.1016/j.ces.2009.02.009.

[206] T. Numaguchi, K. Kikuchi, Intrinsic kinetics and design simulation in a complex reaction network; steam-methane reforming, Chem. Eng. Sci. 43 (1988) 2295–2301. doi:10.1016/0009-2509(88)87118-5.

Acknowledgements

I deeply thank my thesis directors, Prof. Pier Ugo Foscolo and Dr. Claire Courson, for letting me work and learn in their research teams. They both kindly leaded and supported me, becoming two fundamental points of reference.

It is also my pleasure to express heartfelt thanks to Dr. Katia Gallucci for her fundamental help, encouragement and enduring strength of spirit.

I am grateful to Prof. Emeritus Alain Kiennemann too, for devoting part of his precious time to give me very appreciated advices.

I thank Ing. Dipl. Giampaolo Antonelli for his technical support in L'Aquila laboratory, together with Yvan Zimmermann and Anne-Clémence Aun for the same reason in Strasbourg. Together with them, I take the opportunity to mention, for their availability, Fabiola Ferrante (TGA and porosimetry, L'Aquila), Lorenzo Arrizza (SEM and TEM, L'Aquila), Ksenia Parkhomenko (porosimetry, water pumps, and any other support in Strasbourg laboratory), Suzanne Libs (gas chromatography, Strasbourg), Corinne Ulhaq (TEM, Strasbourg).

I am glad to appreciate here the contribution from Andrea Romano, a person and a friend of exemplary trustworthiness, who hardly and fruitfully cooperated with DiGiPower s.r.l. on the automation of L'Aquila's packed-bed test rig. I also thank Andrea Di Carlo and Ilaria Aloisi for involving me in their activities about attrition tests and mathematical modelling, respectively. Moreover, I thank Umberto Pasqual Laverdura, for his availability in many occasions.

I am also grateful to my friend Fabrizio Giancaterino who, as a Master student before and as a researcher after, became a fundamental help for experimental research activities in L'Aquila. In this regard, I also want to thank all other Master students who joined and assisted me: Manuela Sciarra, Enrica Mattucci, Bassel Bazarbachi, Roberta Massacesi, and Jérémy Girr, the last needing a special thank you for his particularly fine work and his friendship.

Together with already mentioned people, I thank those who shared with me part of my PhD time between L'Aquila and Strasbourg and gave me a warm welcome, making me feel a member of laboratories' families. So, thanks to Tania Antonina, Giuseppe Spagnoli, Loredana Spera, and to Prof. Anne Cécile Roger, Kilian Köbl, Charlotte Lang, Valentin L'Hospital, Pauline Thibaudeau, Audrey Waldvogel, Marion Vingerder, Qinqin Ji and Qian Jiang, along with whoever spent some time with me in DIIIE (Dipartimento di

Ingegneria Industriale e dell'Informazione e di Economia) at L'Aquila and in ICPEES-ECED (Institut de Chimie et Procédés pour l'Énergie, l'Environnement et la Santé – Énergie et Carburants pour un Environnement Durable) at Strasbourg.

Before me, in the same research teams, three people had studied doctoral subjects similar to mine: Dr. Francesca Micheli, Dr. Ingrid Zamboni, and Dr. Moises Césario. I met only the first one, but I thank them all, because some of the knowledge they produced was my starting point.

A necessary but very important acknowledgement: *the research leading to these results has received funding from the European Union's Seventh Framework Program ASCENT grand agreement n° [608512]*. On this point, I'm grateful to Dr. Stefano Stendardo from ENEA (Agenzia nazionale per le nuove tecnologie, l'energia e lo sviluppo economico sostenibile) for scientific coordination of the whole project and helpful guidelines to the work of the research team where I have been working. Moreover, I express my gratification for cooperating with all other project partners: Dr. Julien Meyer and Dr. Luca Di Felice from IFE (Institutt For Energiteknikk, Norway), Dr. Gemma Grasa and Dr. Ramón Murillo from CSIC-ICB (Consejo Superior de Investigaciones Cientificas – Instituto de Carboquimíca, Spain), Delphine Maury and Christophe Voisin from Marion-Technologies (France).

Drawing to an end, let me thank my family and friends, particularly for backing me during my periods away from home.

Andrea DI GIULIANO

Synthesis, characterization and industrial applicability of Combined Sorbent-Catalyst Materials for Sorption Enhanced Steam Methane Reforming

Résumé

SESMR (Sorption Enhanced Steam Methane Reforming), SMR (Steam Methane Reforming) avec capture de CO_2 in-situ par un adsorbant solide, peut amener à une exploitation durable du gaz naturel pour la production de H_2. La thèse, partie du projet de recherche ASCENT (Advanced Solid Cycles with Efficient Novel Technologies), concerne le développement de matériaux combinés adsorbants-catalyseurs Ni-CaO-mayenite pour le SESMR, aux fins d'étudier les influences dues à la fraction de Ni, aux sels précurseurs du Ni (Ni-acétate ou Ni-nitrate), et à la fraction de CaO disponible. Les techniques ICP-AES, XRD, BET/BJH, SEM/EDS, TEM/EDS, TPR et TGA ont été utilisés pour caractériser les matériaux synthétisés. La réactivité a été évaluée par des tests en lit fixe à l'échelle du microréacteur, qui ont aussi permis une sélection des matériaux les plus prometteurs pour une étude de l'applicabilité industrielle par tests multi cycliques SESMR/régénération de solides par un réacteur automatisé à lit fixe.

Mots clés :
vaporeformage du méthane amélioré par absorption de CO_2 ; matériaux combinés adsorbants catalyseurs ; nickel ; oxide de calcium ; mayenite

Résumé en anglais

Sorption enhanced steam methane reforming (SESMR), steam methane reforming (SMR) with in situ CO_2 sorption by a solid sorbent, can lead to a sustainable exploitation of natural gas to produce H_2. (CSCM). This thesis, as a part of ASCENT (Advanced Solid Cycles with Efficient Novel Technologies) project, deals with Ni-CaO-mayenite combined sorbent-catalyst material for SESMR, to study the effect of Ni fraction, its precursor salt (Ni-nitrate or Ni-acetate), and free CaO fraction. ICP-AES, XRD, BET and BJH methods, SEM-EDS, TEM-EDS, TPR and TGA were used to characterize synthesized materials. Their reactivity was evaluated by tests in a packed-bed microreactor, which served also as a screening tool to choose the most promising materials. Their industrial applicability was assessed by multicycle SESMR/regeneration tests in an automated packed-bed bench scale rig.

Keywords :
Sorption enhanced steam methane reforming ; Combined sorbent-catalyst materials ; nickel ; calcium oxide ; mayenite